THESE DE DOCTORAT

Présentée à

L'Université de Lille

Université de Lille

Ecole Doctorale ENGSYS

Micro-nanosystèmes et capteurs

par

Yi ZHANG

Application of MXene-based composites for hydrogen production

by water electrolysis

Application de composites à base de MXenes pour la production de l'hydrogènepar

électrolyse de l'eau

Soutenue le 9 Septembre 2024 devant le jury composé de

Dr. Prashanth W. Menezes	Technische Universität Berlin	Rapporteur
Dr. Palaniappan Subramanian	University of West Bohemia	Rapporteur
Prof. Henri Happy	IEMN, Université de Lille	Président du jury
Dr. Yann Leroux	ISCR-CNRS, Rennes	Examinateur
Dr. Rabah BOUKHERROUB	IEMN, Université de Lille	Directeur
Prof. Sabine SZUNERITS	IEMN, Université de Lille	Co-directrice

Abstract

The global energy crisis and environmental degradation are exacerbated by extensive fossil fuel consumption, still comprising 80 % of global energy usage. Carbon-free hydrogen (H_2) emerges as a sustainable energy solution, due to its high energy density (142.351 MJ kg^{-1}) and zero pollution. Water splitting, powered by renewable energy, offers a cleaner and more sustainable alternative to fossil fuel methods like steam methane reforming and coal gasification. However, challenges, such as high cost, low efficiency and instability of catalysts, hinder electrolytic hydrogen generation from water. Developing multifunctional electrocatalysts with high performance, low cost, and durability is crucial for future integrated energy systems. Noble metals (Pt, Ru, Ir) exhibit excellent catalytic activity, but are costly and scarce. Transition metal-based (Fe, Co, Ni) catalysts represent an interesting alternative, but face issues like agglomeration and insufficient active site exposure. Discovering a nanomaterial with large surface area and conductivity to support both noble and transition metal particles could significantly reduce catalyst costs and enhance performance. MXenes, a new class of two-dimensional transition metal-based carbides or nitrides, have gained attention in electrochemistry and hold promise as a support material for catalysts for electrolytic water splitting, owing to their high conductivity, corrosion resistance, surface hydrophilicity and chemical stability.

The objective of my PhD thesis is to prepare stable, efficient, and affordable MXene-based catalysts for producing H_2 through water electrolysis. On this basis, the catalyst materials would be also used to electrolyze seawater, addressing energy shortages in regions with limited freshwater resources. Further, their potential to

electrolyze impurity-containing (urea, formaldehyde and so on) wastewater is explored, generating H_2 with the lowest possible energy consumption while removing contaminants. Considering that objective, my overall doctoral journey is summarized in the following manner:

Firstly, tiny RuO_2 particles were electrodeposited onto single- or few-layered Ti_3C_2 sheets loaded on nickel foam (RuO_2-Ti_3C_2/NF). This created an open nanostructure, enhancing charge and mass transport, boosting catalytic activity and reducing overpotential, crucial for preventing chlorine poisoning in seawater conditions. RuO_2-Ti_3C_2/NF showed enhanced performance in hydrogen evolution reaction (HER), oxygen evolution reaction (OER), and overall water splitting, even in simulated and real seawater. With a stability of 25 hours in seawater splitting and nearly 100% Faradaic efficiency, it proved effective for seawater electrolysis, offering a solution for energy scarcity in areas with limited freshwater.

Secondly, a novel Co_3O_4/Ti_3C_2 MXene composite, synthesized under mild conditions, serves as a highly efficient and stable electrocatalyst for both urea oxidation reaction (UOR) and HER in basic conditions. It surpasses pure Ti_3C_2 MXene and Co_3O_4, overcoming issues like inadequate active site exposure and particle agglomeration. This work provided a new strategy for the application of transition metal-based materials for energy-saving H_2 production coupled with urea containing wastewater purification.

Finally, a Mo_2TiC_2 MXene cluster complex supported by Cu_2O nanoflowers was synthesized by a simple immersion method. It was used as an electrocatalyst for HER coupled with formaldehyde oxidation reaction. This coupling strategy realizes H_2 production at both cathode and anode, while reducing the overall electrical energy consumption of the cell for more efficient H_2 synthesis. At each stage, the obtained new

materials were deeply characterized by several techniques (X-ray diffraction, X-ray photoelectron spectroscopy, scanning and transmission electron microscopies, Raman spectroscopy.).

Résumé

La crise énergétique mondiale et la dégradation de l'environnement sont exacerbées par la consommation importante de combustibles fossiles. L'hydrogène (H_2) apparaît comme une solution énergétique durable en raison de sa densité énergétique élevée (142,351 MJ kg^{-1}) et sa faible empreinte environnementale. Le fractionnement électrochimique de l'eau, alimenté par une énergie renouvelable, offre une alternative plus propre et plus durable aux méthodes utilisant des combustibles fossiles. Toutefois, des difficultés telles que le coût élevé, la faible efficacité et l'instabilité des catalyseurs entravent la production électrolytique d'hydrogène à partir de l'eau. Le développement d'électrocatalyseurs multifonctionnels à haute performance, à faible coût et durables est alors crucial pour les futurs systèmes énergétiques intégrés. Les MXènes, une nouvelle classe de carbures ou nitrures bidimensionnels à base de métaux de transition, ont attiré l'attention en électrochimie et sont prometteurs en tant que matériaux de support pour les catalyseurs en raison de leurs propriétés telles qu'une conductivité élevée, une résistance à la corrosion et de bonnes propriétés de surface (hydrophilie).

L'objectif de ma thèse de doctorat est de préparer des catalyseurs stables, efficaces et bon marché à base de MXènes pour produire de l'hydrogène par électrolyse de l'eau. Sur cette base, ces matériaux catalytiques pourraient être aussi utilisés pour l'électrolyse de l'eau de mer, ce qui permettrait de remédier aux pénuries d'énergie dans des régions où les ressources en eau douce sont limitées. En outre, le potentiel de ces catalyseurs pour l'électrolyse des eaux usées contenant des impuretés (urée, formaldéhyde, etc.) a été exploité, afin de produire de l'H_2 en utilisant le moins d'énergie possible tout en éliminant les contaminants organiques. Compte tenu de cet objectif,

l'ensemble de mon parcours doctoral se résume de la manière suivante.

Tout d'abord, des nanoparticules de RuO_2 ont été déposées par voie électrochimique sur des feuillets de Ti_3C_2 chargés sur une mousse de nickel (RuO_2-Ti_3C_2/NF). Le composite ainsi préparé a une structure poreuse qui est favorable pour le transport de charges et de la matière, stimulant l'activité catalytique et réduisant la surtension, ce qui est crucial pour prévenir l'empoisonnement par le chlore lors de l'électrolyse de l'eau de mer. Le RuO_2-Ti_3C_2/NF a démontré de bonnes performances dans la réaction de dégagement de l'hydrogène (HER), la réaction de dégagement de l'oxygène (OER) et d'électrolyse de l'eau, même de l'eau de mer simulée ou réelle.

Dans la deuxième partie de mon travail, un nouveau composite Co_3O_4/Ti_3C_2 MXene, synthétisé dans des conditions douces, a été utilisé comme électrocatalyseur très efficace et stable pour la réaction d'oxydation de l'urée (UOR) et l'HER dans un milieu alcalin (1 M KOH). Le Co_3O_4/Ti_3C_2 MXene est plus efficace que ses constituants i.e. Ti_3C_2 MXene et Co_3O_4, surmontant des problèmes tels que l'exposition inadéquate de sites actifs et l'agglomération des particules. Ces résultats ont permis de développer une nouvelle stratégie pour l'application de matériaux abondants pour la production d'H_2 à faible consommation d'énergie couplée à la purification des eaux usées contenant de l'urée. Enfin, un matériau hybride à base de MXène, Mo_2TiC_2, et de nano-fleurs de Cu_2O a été synthétisé par une méthode d'immersion. Il a été utilisé comme électrocatalyseur pour la génération de H_2 couplée à la réaction d'oxydation du formaldéhyde. Cette stratégie de couplage permet de produire de l'hydrogène à la fois à la cathode et à l'anode tout en réduisant la consommation globale d'énergie électrique de la cellule d'électrolyse. À chaque étape, les nouveaux matériaux préparés ont été systématiquement caractérisés par plusieurs techniques (XRD, XPS, microscopie

électronique à balayage et à transmission, spectroscopie Raman).

Mots clés : MXenes, Nanoparticules de RuO_2, Nanoparticules de Co_3O_4, Nano-fleurs de Cu_2O, Electrolyse d'eau, Hydrogène.

Acknowledgements

Completing a doctoral dissertation is a monumental task that would not have been possible without the support, guidance, and encouragement of many individuals. I would like to take this opportunity to express my deepest gratitude to those who have helped me throughout this journey.

First and foremost, I would like to extend my sincere appreciation to my supervisors, Dr. Rabah Boukherroub and Prof. Sabine Szunerits. Your unwavering support, insightful guidance, and invaluable feedback have been the cornerstone of my research. Both supervisors not only gave me professional guidance in academics, but also set an example for me in every aspect. I am deeply grateful for the opportunity to learn from you and for the countless hours you dedicated to my development as a researcher.

I am also profoundly grateful to the members of my dissertation committee: Dr. Prashanth W. Menezes, Dr. Palaniappan Subramanian, Prof. Henri Happy, and Dr. Yann Leroux. Your expertise, critical insights, and constructive criticism have greatly enriched my research. Each of you has played a crucial role in shaping the direction and quality of this dissertation, and I am thankful for the time and effort you invested in my work.

Special thanks go to my colleagues and friends in the NanoBioInterfaces group. Your camaraderie, support, and intellectual exchange have made my time here both productive and enjoyable. Special thanks to Dr. Alexandre Barras for his reliable and timely support during my PhD and his efforts to maintain the lab.

I would like to acknowledge Amar Abderrahmani, Emerson Giovanelli, Yuanyuan

Contents

Chapter 4. 0D/2D Co$_3$O$_4$/Ti$_3$C$_2$ MXene Composite: A Dual-Functional Electrocatalyst for Energy-Saving Hydrogen Production and Urea Oxidation 118

Chapter 1. General Introduction

Global energy demand and consumption are steadily increasing, due to population growth, rising living standards, and the industrial expansion of developing countries.[1] According to the International Energy Agency's predictions, global energy demand is expected to rise by 50% by 2030.[2] Presently, over 95 % of this substantial energy demand is fulfilled by using fossil fuels,[2] leading to the release of high concentrations of greenhouse gas emissions and exacerbating global warming and environmental pollution. Consequently, rapid development of alternative green energy technologies is crucial to meet global energy demands sustainably. In this context, various research institutions and organizations worldwide have directed their efforts towards developing innovative technologies utilizing renewable sources to generate green energy and fuels.

Hydrogen (H_2) emerges as one such promising environmentally-friendly renewable energy carrier, being the most abundant element in the universe.[3] Composed of one proton and one electron, the hydrogen atom is the lightest element in the universe, possessing unique properties, such as high energy density (120 MJ/kg) and lower volumetric energy density (8 MJ/L).[4] Although not readily available in its pure form on Earth, hydrogen exists in chemically combined forms within water, fossil fuels, and biomass. When hydrogen is used as a fuel, it only produces water as a byproduct, with no harmful emissions such as carbon dioxide, making it a crucial pathway toward achieving carbon neutrality. Additionally, hydrogen can be stored and transported, providing a storage solution for intermittent renewable energy sources like wind and solar, thereby enhancing the stability and flexibility of energy systems. Consequently, the advancement of hydrogen technology is expected to drive the green transformation of industries, transportation, and power sectors, contributing to global energy structure

optimization and environmental protection.

1.1 An overview of water electrolysis

1.1.1 Current method of hydrogen production

Hydrogen production can stem from diverse raw material sources, encompassing both renewable and non-renewable origins, totaling approximately 87 million tons/year.[5] The main production methods and consumptions are shown in **Figure 1.1**. Nonetheless, as of 2020, the predominant source of hydrogen (95 %) derived from non-renewable fossil fuels, particularly through steam reforming of natural gas, resulting in the emission of 830 million tons/year of CO_2.[6] Conversely, the remaining hydrogen production stemmed from renewable resources, including water electrolysis.[7]
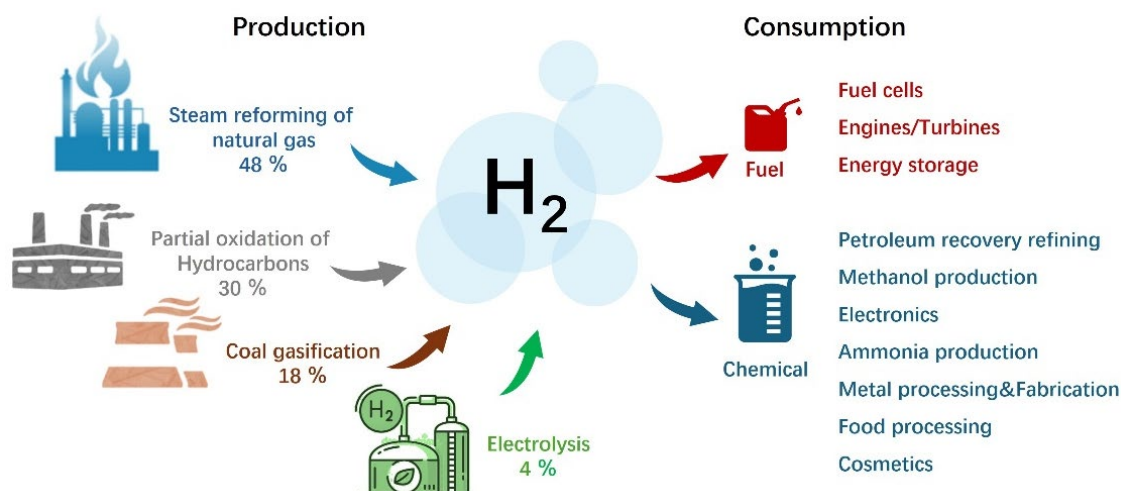
Figure 1.1. Major hydrogen production methods and applications.

Hydrogen is classified into different color shades i.e., blue, gray, brown, black, and green based on its production technology, energy source, and environmental impact,[8-10] as shown in **Table 1.1**. Blue hydrogen is produced by improving the

production process of gray hydrogen by utilizing carbon capture and storage technology. Although it can increase the hydrogen yield and reduce harmful gas emissions to a certain extent, it still emits a certain amount of carbon.[11] The gray hydrogen is produced from non-renewable fossil fuels, such as natural gas or coal, by steam reforming/auto-thermal reforming process;[12] this process is similar to the blue hydrogen process, but the produced CO_2 is not being captured, it is directly released into the atmosphere. In addition, the production process is unsustainable as it does not source away from dependence on fossil energy sources.[13] Brown hydrogen is most abundant in use today, which is produced from hydrocarbon-rich feedstock (brown coal or methane) *via* the gasification process. But as a result, every ton of brown hydrogen releases 10-12 tons of CO_2 into the atmosphere.[14] Black hydrogen is produced by coal gasification, in which syngas is produced in the gasifier. Hydrogen can be separated from the other gases by an absorber or a special membrane, and the remaining gas can be released into the atmosphere.[15] Green hydrogen is mainly produced by coupling with renewable energy sources,[16] such as solar, wind, and tidal energy and adopting electrolysis of water technology, which basically does not produce any environmental pollution during the whole production process.

Table 1.1 Hydrogen shades, their technology, costs, and CO_2 emissions.

Hydrogen color	Technology	Source	Products	Cost ($ kg/H_2)	CO_2 emissions
Brown	Gasification	Bron coal (lignite)	H_2+CO_2	1.2-2.1	High
Black	Gasification	Black coal	H_2+CO_2	1.2-2.1	High

		(Bituminous)			
Grey	Reforming	Natural gas	H_2+CO_2	1.2-2.1	Medium
Blue	Reforming+ carbon capture	Natural gas	H_2+CO_2	1.5-2.9	Low
Green	Electrolysis	Water	H_2+CO_2	3.6-5.8	Minimal

Currently, the world's main sources of hydrogen are still gray and blue hydrogen,[17] of which the share of blue hydrogen is gradually expanding, but it is ultimately only a transitional means. In the long run, with the increase of carbon tax and the gradual progress of carbon reduction target, the cost of hydrogen production of grey and blue hydrogen will gradually increase. Green hydrogen is widely viewed as a promising fuel for future sustainable development and energy transition, due to fact that green hydrogen can be produced from water and renewable energy sources through the electrolysis process, in this process there are no greenhouse gas emissions. Therefore, green hydrogen is increasingly being promoted to address climate change issues and meet the global net-zero challenges over the next decade.[18]

1.1.2 Water electrolysis

Since the 18th century, water electrolysis is a well-known technology for green hydrogen production.[19] However, globally only 4 % of hydrogen (65 million tons) can be produced from water electrolysis due to economic issues.[20] Water electrolysis technologies are being continuously developed and used in industrial applications, during this journey different trends have affected its development. During these developments, four types of water electrolysis technologies were introduced based on their electrolyte,[21] operating conditions, and their ionic agents (OH^-, H^+, O_2^-), such as

(i) alkaline water electrolysis (AWE), (ii) anion exchange membrane water electrolysis (AEMWE), (iii) proton exchange membrane water electrolysis (PEMWE), and (iv) solid oxide water electrolysis (SOWE).[22] The four types of water electrolysis technologies and their advantages, disadvantages are described in the following subsections and **Table 1.2**.[14]

Table 1.2. Advantages and disadvantages of typical water electrolysis technologies.

Electrolysis technology	Advantages	Disadvantages
AWE	• Well-established technology • Commercialized for industrial applications • Noble metal-free electrocatalysts • Relatively low cost • Long-term stability	• Limited current densities • Crossover of the gases • High concentrated (5 M KOH) liquid electrolyte
AEMWE	• Noble metal-free electrocatalysts • Low concentrated (1 M KOH) liquid electrolyte	• Limited stability • Under development
PEMWE	• Commercialized technology • Operates at higher current densities • High purity of the gases • Compact system design • Quick response	• Cost of the cell components • Noble metal electrocatalysts • Acidic electrolyte
SOWE	• High working temperature • High efficiency	• Limited stability • Under development
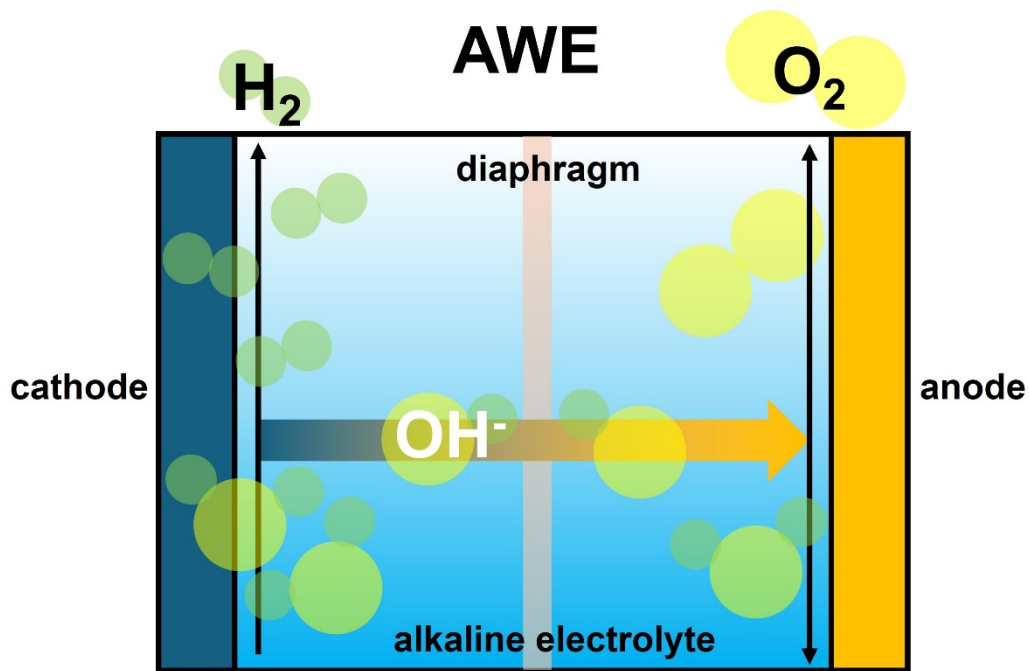
Figure 1.2. Schematic of an alkaline water electrolysis device.

However, the operating principles are the same for all the cases.[22] Take AWE, for example, which is the most well-developed in the industry with the advantages of low cost, long service time and large scale. As shown in **Figure 1.2**, the alkaline water electrolysis device is mainly composed of four parts: cathode, anode, electrolyte and diaphragm. Water undergoes a reduction reaction at the cathode to produce hydrogen and an oxidation reaction at the anode to produce oxygen. Therefore, the whole process of water electrolysis is two half-reactions: hydrogen evolution reaction (HER) at the cathode and oxygen evolution reaction (OER) at the anode.[23] For the cathode and anode materials, it is required to have good conductivity, high porosity and good stability. For the diaphragm, it is required to have good water absorption, poor permeability and low resistance, and asbestos is commonly used at present.[24] Electrolyte mainly plays a

conductive role, the requirements of a high conductivity and does not introduce impurities. At present, alkaline water electrolysis hydrogen production technology is very mature, but still faces the problem of insufficiently high operating pressure and poor adaptability to fluctuating power supply.[25]

1.1.3 Fundamentals of hydrogen evolution reaction (HER)

To address these issues and challenges, the mechanism of HER should be understood. Theoretically, the thermodynamic voltage required for a water cracking reaction to occur is 1.23 V, which corresponds to an energy dissipation of 237.2 kJ mol^{-1} at 25 °C, 1 atm;[26] however, the slow kinetics and energy inefficiencies induced by complex electron and ion transport processes make it so that actual water cracking reactions require a higher voltage than 1.23 V. The additional potential above the theoretical reaction voltage is called overpotential and is caused by activation energy, electrolyte diffusion resistance, ion and gas diffusion, wire and electrode resistance, and bubble resistance. The electrochemical water splitting reaction consists of an oxygen evolution reaction at the anode (OER, equations 1.1 and 1.3) and a hydrogen evolution reaction at the cathode (HER, equations 1.2 and 1.4).[25, 27, 28]

In acidic media:

$$\text{Anode: } 2H_2O\,(l) \;\rightarrow\; O_2\,(g) + 4H^+\,(aq) + 4e^- \tag{1.1}$$

$$\text{Cathode: } 4H^+\,(aq) + 4e^- \;\rightarrow\; 2H_2\,(g) \tag{1.2}$$

In alkaline media:

$$\text{Anode: } 4OH^-\,(aq) \;\rightarrow\; O_2\,(g) + 2H_2O\,(l) + 4e^- \tag{1.3}$$

$$\text{Cathode: } 4H_2O\,(aq) + 4e^- \;\rightarrow\; 2H_2(g) + 4OH^- \tag{1.4}$$
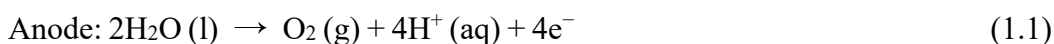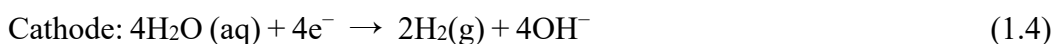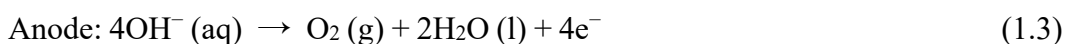
The understanding of the HER process in water decomposition is important for the synthesis and design of superior electrocatalysts. HER may consist of a two-step

reaction pathway: the formation of adsorbed hydrogen on the catalyst surface — the Volmer step, and the formation of hydrogen molecules — the Tafel step or the Heyrovsky step or both. The HER process can occur by either the Volmer-Heyrovsky mechanism or the Volmer-Tafel mechanism.[29]

The details are as follows: in an acidic electrolyte (equations 1.5 – 1.7), a hydrated proton (H_3O^+) first combines with an electron and chemically attaches to a catalyst (*) in the Volmer reaction; next, the adsorbed H* forms H_2 *via* the Heyrovsky or Tafel route and desorbs sequentially. The Tafel reaction involves the direct binding of two H*s to produce H_2, whereas the Heyrovsky reaction involves the generated H* binding to a hydrated proton and then gaining an electron from the catalyst surface to form H_2.

$$H_3O^+ + e^- + * \ \rightarrow \ H* + H_2O \quad (120\,\mathrm{mV\,dec^{-1}}) \qquad\qquad \text{Volmer (1.5)}$$

$$H_3O^+ + e^- + H* \ \rightarrow \ H_2 + H_2O \quad (40\,\mathrm{mV\,dec^{-1}}) \qquad\qquad \text{Heyrovsky (1.6)}$$

$$H* + H* \ \rightarrow \ H_2 \qquad\qquad (30\,\mathrm{mV\,dec^{-1}}) \qquad\qquad \text{Tafel (1.7)}$$
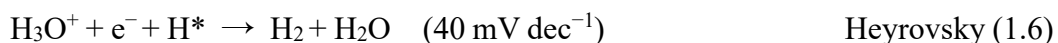
In alkaline electrolytes (equations 1.8 – 1.10), the catalyst needs to break the H-O-H bond to form adsorbed H* and OH⁻ before adsorbing H*, which is more difficult to achieve compared to the reduction of H_3O^+, as shown in **Figure 1.3**.
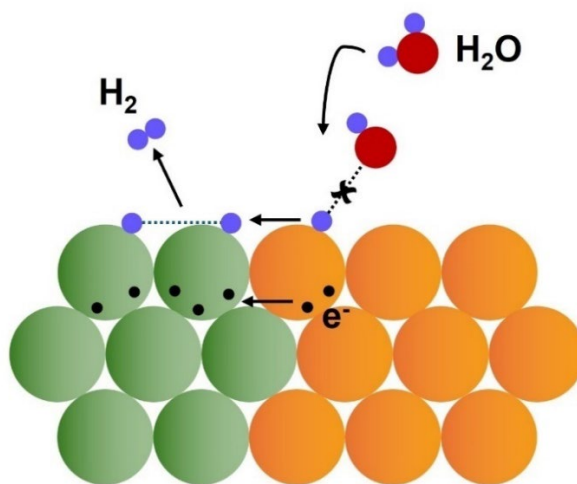
Figure 1.3 Alkaline HER mechanism.

$$H_2O + e^- \rightarrow H^* + OH^- \qquad (120 \text{ mV dec}^{-1}) \qquad \text{Volmer (1.8)}$$

$$H_2O + e^- + H^* \rightarrow H_2 + OH^- \quad (40 \text{ mV dec}^{-1}) \qquad \text{Heyrovsky (1.9)}$$

$$H^* + H^* \rightarrow H_2 \qquad\qquad (30 \text{ mV dec}^{-1}) \qquad \text{Tafel (1.10)}$$
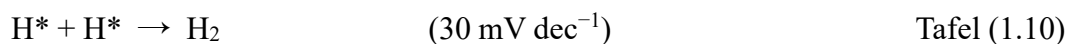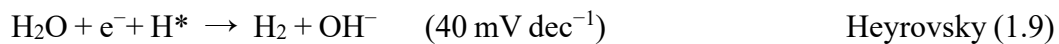
In general, the rate-controlling step in the electrocatalytic HER process is related to the affinity between the reaction intermediate and the catalyst surface. If the binding strength of the catalyst to the adsorbed H* is weak, the adsorption process will dominate the HER process; if the binding strength of the catalyst to the adsorbed H* is too strong, the desorption process will be the rate-limiting step.
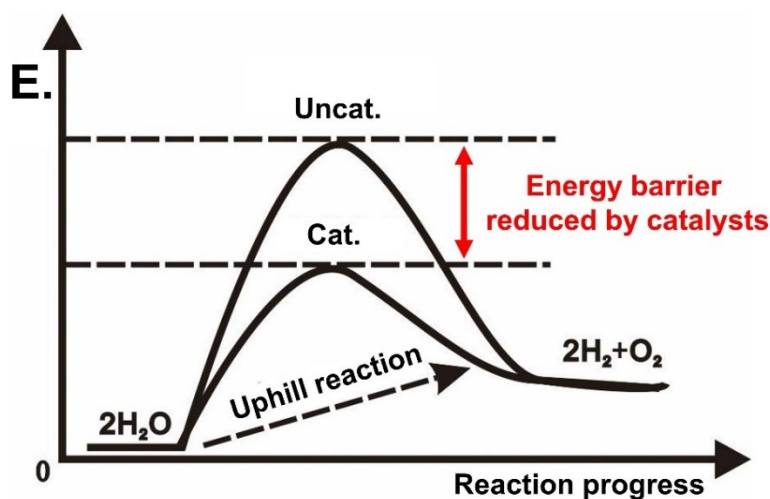
Figure 1.4. Schematic diagram of water decomposition reaction energy barrier reduction by catalyst.

Many studies have been conducted to reduce the overpotential by ameliorating the unfavorable factors. Among the different research approaches, the search for suitable electrocatalysts that are closely related to hydrogen and water molecules has attracted great attention, because suitable catalysts can significantly reduce the overpotential, lower the reaction energy barriers and increase the reaction rate (**Figure 1.4**).[30]

1.1.4 Fundamentals of oxygen evolution reaction (OER)

OER at the anode is a 4-electron process and is usually considered to have two possible mechanisms, which are the adsorbate evolution mechanism (AEM) and the lattice oxygen mediate mechanism (LOM).[31] The AEM is a traditional mechanism in which the magnitude of the overpotential is determined mainly by the adsorption energy between the oxygen-containing intermediate and the catalyst. Although many highly active catalysts can be quickly screened based on the AEM, the activity limitation of OER catalysts still cannot be overcome. The LOM was formalized through simulations of numerous theoretical calculations and the application of isotope tracer techniques, and the main difference between the two mechanisms lies in the involvement or not of lattice oxygen in the formation of oxygen molecules. As shown in **Figure 1.5(a)**, in the AEM, lattice oxygen is not involved in the reaction, and there is no exchange of material between the catalyst and the electrolyte during the entire process. In the LOM, the oxygen atoms in the catalyst are directly coupled to the O* formed by water oxidation to form O_2, and oxygen vacancies are generated on the surface of the catalyst, which are then filled by water molecules in the electrolyte. The proposed LOM provides a new way to overcome the activity limitation of the AEM and helps to design catalysts with higher activity, but the catalysts are less stable due to the participation of oxygen in the catalyst in the lattice oxygen mechanism.
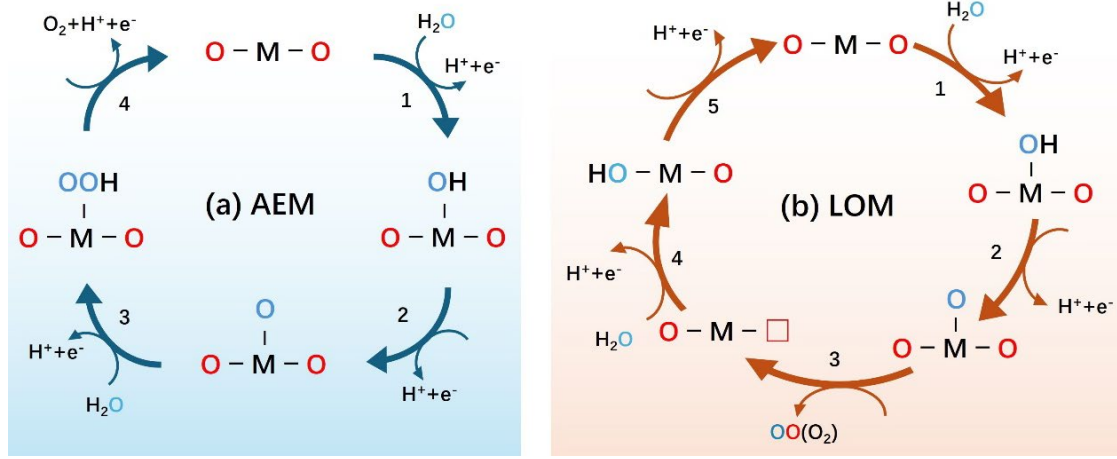
Figure 1.5. Schematic diagram of AEM and LOM.

In the AEM, as shown in equations (1.11-1.14),[32] a water molecule is first adsorbed at the metal site to form an *OH intermediate through the process of transfer of an electron, the *OH intermediate next forms *O through the process of deprotonation and the transfer of an electron. Then *O reacts with another water molecule and undergoes the process of deprotonation and charge transfer to form *OOH, and finally, *OOH continues to undergo the deprotonation and charge transfer to form an oxygen molecule and release the active site.

$$H_2O + * \rightarrow *OH + H^+ + e^- \qquad \Delta G_1 \qquad (1.11)$$

$$*OH \rightarrow *O + H^+ + e^- \qquad \Delta G_2 \qquad (1.12)$$

$$*O + H_2O \rightarrow *OOH + H^+ + e^- \qquad \Delta G_3 \qquad (1.13)$$

$$*OOH \rightarrow * + O_2 + H^+ + e^- \qquad \Delta G_4 \qquad (1.14)$$
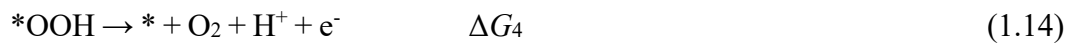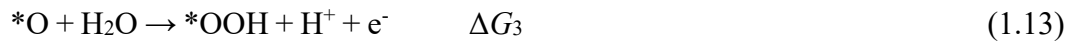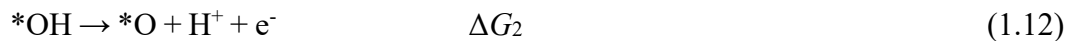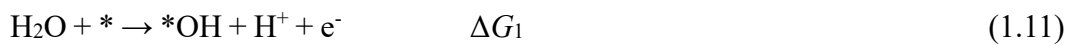
$$\eta = \max[\Delta G_2, \Delta G_3]/e - 1.23 \text{ V}$$

$$= \max[(\Delta G_{*O} - \Delta G_{*OH}), (\Delta G_{*OOH} - \Delta G_{*O})]/e - 1.23 \text{ V}$$

$$= \max[(\Delta G_{*O} - \Delta G_{*OH}), 3.2 \text{ eV} - (\Delta G_{*O} - \Delta G_{*OH})]/e - 1.23 \text{ V} \qquad (1.15)$$
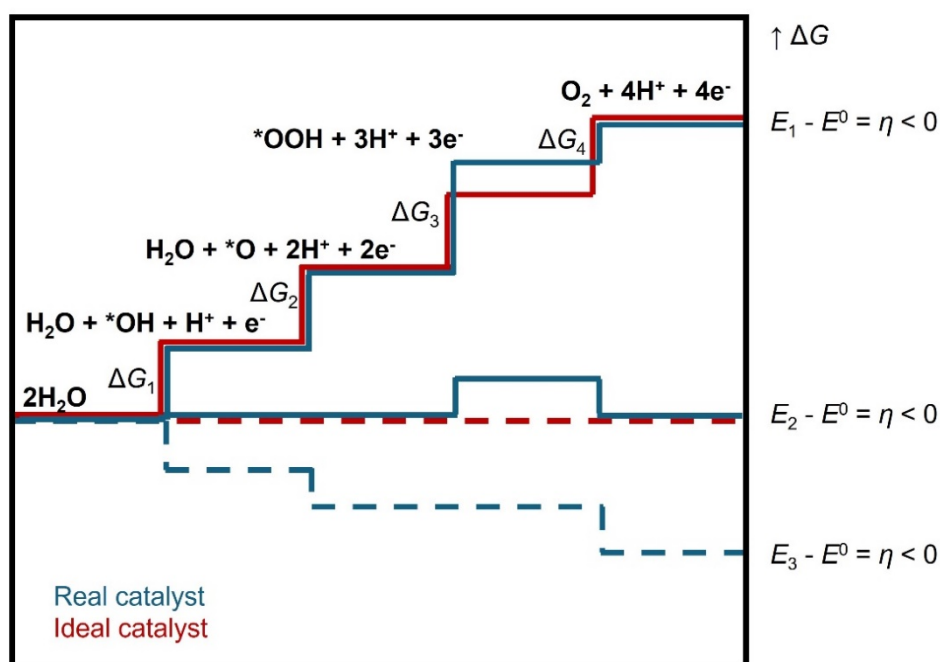
Figure 1.6. Diagram of energy steps in OER process.

As shown in **Figure 1.6**, each step of the process corresponds to a chemical reaction activation energy G_1, G_2, G_3, and G_4, respectively, and the decisive step of the process is determined by the one with the highest activation energy among these four reactions. Ideally, the activation energies of the four steps of an OER catalyst should be the same to ensure that the adsorption of each step is maintained at a moderate value, but in reality, the catalysts often do not behave in this way. In order to clarify the decisive step reaction of OER, an interesting phenomenon has been found through a large number of theoretical calculations that *OH and *OOH are linearly correlated, resulting in an energy difference of about 3.2 eV between them, which is independent of the interaction between the intermediates and the catalyst.[33] Based on these calculations, it was hypothesized that the second or third step is a decisive step reaction.

As shown in equation (1.15), using the fixed energy difference of 3.2 eV between *OH and *OOH for substitution, it was finally found that the overpotential was only related to ΔG_{*O}-ΔG_{*OH}, and thus ΔG_{*O} - ΔG_{*OH} was considered as the descriptor of the OER reaction.[34]

The limitation of the linear relationship between the intermediates of the adsorption mechanism results in a theoretical overpotential of 0.37 V. However, the reality is that a few catalysts have been found to have overpotentials lower than 0.37 V. It is then inevitable that there must exist other reaction mechanisms that are different from the adsorption mechanism. Inspired by the discovery that O_2 produced on some highly reactive oxides during OER may be derived from lattice oxygen by *in situ* ^{18}O isotope labeling, the now more widely studied mechanism of lattice oxygen evolution has been proposed. As shown in **Figure 1.5(b)**, in the LOM, the first two steps are similar to the adsorption mechanism with the formation of O* intermediate species, next O* couples directly with the lattice O to form O_2 and vacancies are formed on the surface of the catalyst, next the water molecules in the electrolyte attack the oxygen vacancies to re-form the adsorbed OH*.[35] Unlike the adsorption mechanism, the lattice oxygen evolution mechanism will have the O-O direct coupling process, which can directly transgress the formation of OOH* intermediate species, thus breaking the theoretical activity of the adsorption mechanism.

1.2 Electrolysis of non-pure water

The existing research on hydrogen production through water electrolysis primarily focuses on using pure water as the electrolyte, encompassing both theoretical and applied studies. To explore the potential of electrolyzing water with various electrolytes, I have conducted studies on the electrolysis of seawater, urea-, and formaldehyde-

containing water.

1.2.1 Seawater electrolysis

Presently, the primary commercial technologies for water splitting, such as proton exchange membrane (PEM) and alkaline electrolyzers, predominantly utilize high-purity water as a reactant.[36] However, utilizing substantial quantities of fresh water for global energy needs *via* water splitting might lead to water scarcity. In contrast, hydrogen production *via* seawater splitting presents significant benefits over freshwater splitting. First, seawater constitutes 96.5 % of all water resources on Earth. Additionally, integrating seawater electrolysis with fuel cells is advantageous for arid areas, providing both clean drinking water and efficient energy conversion and storage. Second, seawater's inherent electrolyte properties confer higher conductivity (5 S m^{-1}) compared to pure water (5.5×10^{-6} S m^{-1}).[37] Lastly, combining marine offshore hydrogen production with marine renewable energies could offer a sustainable approach for industrialized nations. The U.S. Department of Energy's Wind Energy Technologies Office reports over 2000 gigawatts of capacity, or 7200 terawatt hours annually, in U.S. coastal and Great Lakes' waters.[38] Consequently, direct hydrogen production from seawater electrolysis using offshore wind energy hold considerable promise. Thus, efficient and cost-effective hydrogen production from seawater splitting is essential for the widespread adoption of hydrogen energy.

Based on the principle of pure water electrolysis, the hydrogen evolution reaction (HER) on the cathode encounters several challenges in seawater splitting. As depicted in **Figure. 1.7**, seawater contains numerous dissolved cations (such as Ca^{2+}, Mg^{2+}, etc.), bacteria, microorganisms, and small particles, which can impact the performance of the electrocatalyst.[39-41] Notably, the pH of the solution increases during seawater splitting,

27

leading to the formation of calcium hydroxide and other precipitates on the electrode surface, which can block the active sites.[42] To address these issues, buffer media can be added to seawater to adjust the pH and prevent the formation of precipitates.[43] Additionally, an appropriate membrane and electrolyzer can be used to isolate the catalyst from interfering ions, and a catalyst with corrosion resistance or selectivity can be developed, from which perspective this thesis is dedicated to.
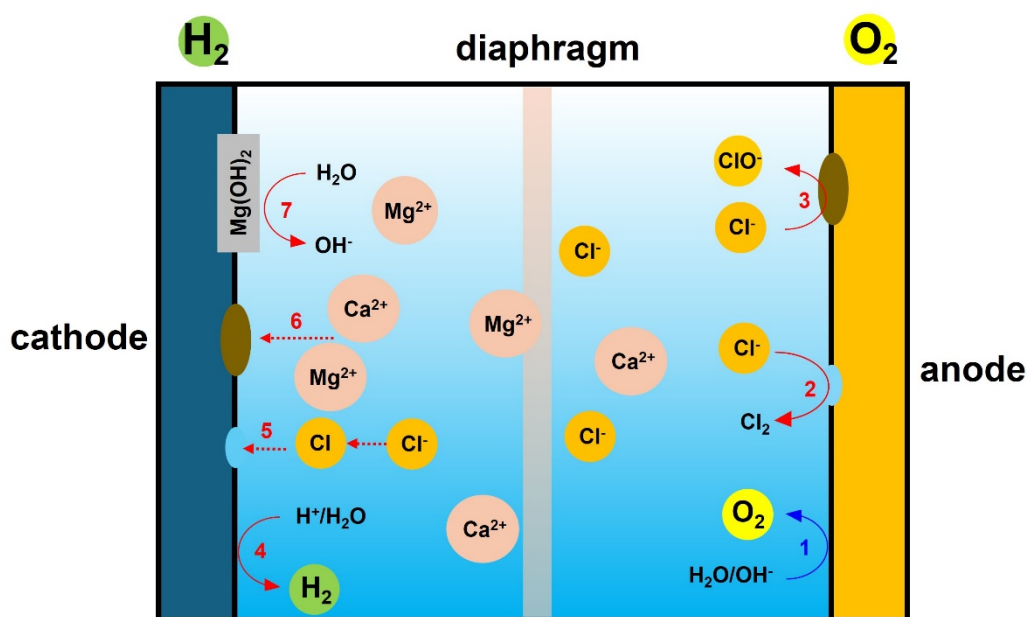
Figure 1.7. Challenges for designing seawater-based electrocatalysts.

In addition to cation-rich, numerous anions in seawater interfere with the oxygen evolution reaction (OER), with chlorine (Cl^-) being particularly significant. A minimal amount of Cl^- can migrate and accumulate at the anode, enhancing the reaction due to its strong de-passivation capability. However, excessive Cl^- impedes the anodic reaction.[44] In **Figure 1.7**, the chlorine evolution reaction (CER) and the formation of hypochlorite compete with the OER. Both CER and hypochlorite formation are two-

electron reactions, as shown in Equations (1.16-17), offering a kinetic advantage over the four-electron OER. Nonetheless, OER holds a thermodynamic edge, with the potential being 480 mV lower than hypochlorite formation when the pH exceeds 7.5.[45, 46]

$$CER: 2Cl^- \rightarrow Cl_2 + 2e^- \tag{1.16}$$

Hypochlorite formation:

$$Cl^- + 2OH^- \rightarrow ClO^- + H_2O + 2e^- \tag{1.17}$$

Therefore, to address the above challenges, a catalyst material with a low overpotential and a surface that is not easily blocked by precipitation to affect charge- and mass-transfer is urgently needed. The work in **Chapter 3** proposes two strategies to respond to these demands: acting on the surface morphology to create micro-nanostructures with high specific surface area may not only increase active sites and enhance the electrochemical active area, but it can also help with desorption of gas product and solid precipitation; constructing a heterojunction to create a phase interface with strong electrochemical activity with the aim to lower the reaction overpotential.

1.2.2 Urea water electrolysis

As described in Section 1.1.4, in electrolysis of water for hydrogen production, the OER at the anode is a slow 4-electron transfer process that requires high energy to promote the dissociation of water molecules, leading to high energy consumption for water electrolysis. At the same time, since the anode is at a higher potential, the metal active sites in the catalyst will inevitably dissolve, resulting in a less stable catalyst. These are the two reasons that have led to the fact that only commercial RuO_2 or IrO_2 can be successfully used in OER at the anode. In fact, the more energy-demanding OER produces O_2 as a low-value product at the anode, while H_2 is only produced at the

cathode. A preferred approach is to replace the anodic OER reaction with a thermodynamically more favorable reaction to reduce the overpotential of the anodic electrooxidation reaction and thus decrease the energy consumption of electrolytic hydrogen production. Therefore, small organic molecules, such as urea and formaldehyde, are used as sacrificial agents to replace the OER reaction at the anode. In the electrooxidation of these small molecules, the onset and overpotentials are often lower than those of OER, and the choice of catalysts is not only limited to noble metal catalysts, but also some transition metal catalysts can provide a good catalytic activity.
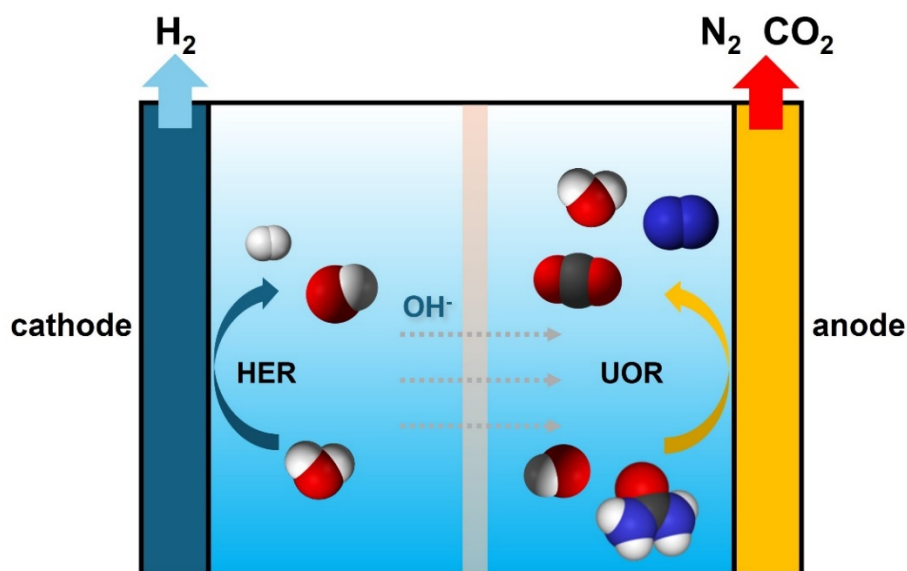
Figure 1.8. Schematic diagram of hydrogen production *via* urea electrolysis.

In 2009, Boggs et al.[47] conducted an experiment where they extracted hydrogen from one part of a solution and nitrogen from another using a urea-containing alkaline solution. This extraction was achieved by applying a voltage of 1.5 V in a Hoffman apparatus. Under standard conditions, the theoretical thermodynamic potential for extracting urea into its components is about -0.46 V compared to the standard hydrogen

electrode (SHE) and -0.83 V compared to the SHE for the hydrogen extraction. Consequently, the theoretical thermodynamic overall cell voltage for urea electrolysis is calculated to be 0.37 V, which is significantly lower than that required for electrolyzing water (1.23 V). The mechanism behind urea electrolysis in alkaline environments is illustrated in **Figure 1.8**. This process involves two half-reactions: the extraction of hydrogen at the cathode and the decomposition of urea at the anode. At the anode, one mole of urea reacts with six moles of hydroxyl ions (OH⁻) to yield nitrogen gas, water, and bicarbonate ions (CO_3^{2-}), while water molecules undergo reduction at the cathode to produce hydrogen gas. In general, the overall reactions during urea electrolysis generate nitrogen gas, hydrogen gas, and bicarbonate ions in alkaline environments. These reactions, including the urea oxidation reaction (UOR), the HER, and the overall urea electrolysis, are represented in equations (1.18-20).[48]

Anode: $CO(NH_2)_2 + 6OH^- \rightarrow N_2 + 5H_2O + CO_3^{2-} + 6e^-$

$$\varphi = -0.46 \text{ V } \textit{vs.} \text{ SHE} \qquad (1.18)$$

Cathode: $6H_2O + 6e^- \rightarrow 3H_2 + 6OH^- \qquad \varphi = -0.83 \text{ V } \textit{vs.} \text{ SHE} \qquad (1.19)$

Overall: $CO(NH_2)_2 + H_2O \rightarrow N_2 + 3H_2 + CO_3^{2-} \qquad E = 0.37 \text{ V} \qquad (1.20)$
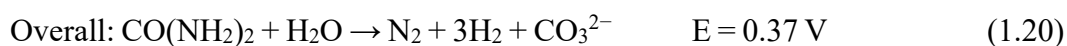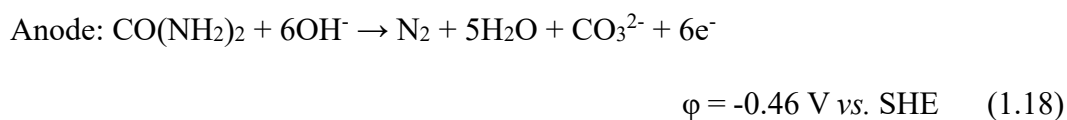
Besides, UOR can purify industrial, agricultural, and domestic wastewaters containing urea pollution, thereby achieving the dual purposes of producing clean energy and solving environmental problems.[49] Indeed, urea has many applications in industry and agriculture, and its production is an energy-intensive process. In addition, the production of every 1 kg of urea in manufacturing plants contributes to 0.75 kg of urea-containing wastewater, which has around 1 wt.% urea.[50] At the same time, humans and animals produce a great amount of urine every day, which contains about 2-2.5 wt.% urea. The urea in untreated wastewater will naturally decompose to form ammonia,

which can be easily oxidized to nitrates, nitrites, or nitrogen oxides after being released in the air. These substances are regarded as major contributors to the formation of acid rain, causing severe health problems for human beings. Therefore, it is necessary and urgent to remove urea in the urea-containing wastewater. However, the lack of inexpensive and efficient catalysts for UOR hinders the development of this approach. Researchers have developed a variety of materials and synthetic strategies to optimize the performance of catalysts for UOR, including morphology design,[51] defect engineering,[52] doping,[53] heterostructure construction,[54] and using noble metal-free materials. **Chapter 4** will look at catalyst design for the application of electrolysis of urea-containing water.

1.2.3 Formaldehyde water electrolysis

Considering the primary role of the anodic reaction is to synergize with cathodic hydrogen production, if the oxidation reaction also releases hydrogen, it would provide an ideal strategy for the co-production of H_2 at both the cathode and anode. In addition to its low overpotential and rapid reaction kinetics, formaldehyde oxidation reaction (FOR) offers another significant advantage: the generation of hydrogen through the decomposition of formaldehyde. This means that we can not only carry out the HER at the cathode, but also simultaneously produce hydrogen at the anode *via* the oxidation of formaldehyde. This dual hydrogen production strategy further enhances the efficiency of hydrogen production from water electrolysis.
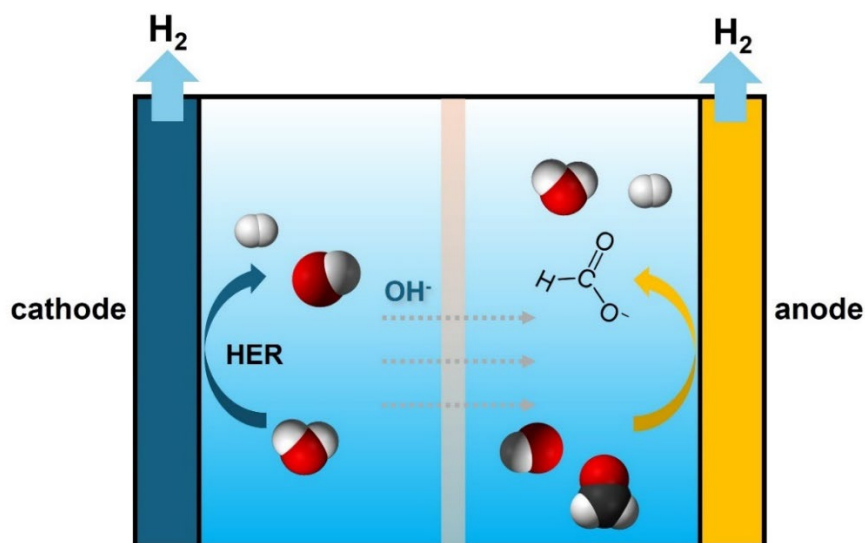
Figure 1.9. Schematic diagram of hydrogen production *via* formaldehyde electrolysis.

Similar to the UOR, formaldehyde oxidation reaction (FOR) has a very small thermodynamic theoretical potential (Equations 1.21-1.23).[55] And in the UOR process, the gaseous products contain CO_2, a greenhouse gas that is best avoided.[56] Unlike UOR, the gaseous product for FOR process is only hydrogen, as shown in **Figure 1.9**, which opens up the possibility for simultaneous hydrogen production at the cathode and anode. Furthermore, HCHO is a low-cost chemical feedstock with a gigantic annual yield, while its oxidation product formate (and later formic acid) is a more valuable chemical. Finally, coupling FOR with HER for H_2 production may also provide environmental benefits if toxic formaldehyde residues in wastewater pollutants could be adopted as the feedstock.

Anode: $2HCHO + 4OH^- \rightarrow 2HCOO^- + H_2 + 2H_2O + 2e^-$
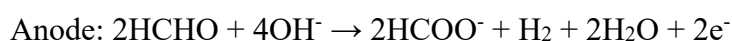
$$E_{anode} = -0.22 \text{ V} - 0.059(\text{pH}) \textit{ vs}. \text{ NHE} \qquad (1.21)$$

Cathode: $2H_2O + 2e^- \rightarrow H_2 + 2OH^-$ $\qquad E_{cathode} = -0.83 \text{ V } \textit{vs}. \text{ NHE} \qquad (1.22)$

Overall: $HCHO + OH^- \rightarrow HCOO^- + H_2$ $\qquad E_{cell} = 0.22 \text{ V} \qquad (1.23)$

Formaldehyde electrocatalytic oxidation similarly requires catalysts to possess good electrical conductivity, catalytic activity, and stability. It is particularly noteworthy that formaldehyde is highly corrosive, which can lead to the degradation and deactivation of catalyst materials, thereby affecting catalytic efficiency and lifespan.

1.3 Types of electrocatalysts

1.3.1 Precious metal-based catalysts

The performance of precious metal catalysts represented by Pt-based catalysts is excellent. Moreover, Pt, as a typical electrochemical hydrogen evolution catalyst, is more deeply investigated; its exchange current density is near the peak of the volcano relationship diagram (**Figure 1.10a**), and its excellent performance is directly related to the Pt-H chemical bonding energy. Pt, Pd, etc. as the representative elements of the noble metal group are expensive. Therefore, in recent years, the main focus of the research are: (a) surface modulation: reducing the size of noble metals, adjusting the crystal surface and geometrical configuration to increase the proportion of surface atoms or the exposure of high-activity surfaces, thereby improving the utilization and activity of noble metal atoms;[58] (b) alloying noble metals with abundant and inexpensive metals to reduce the amount of noble metal used, increase the number of active sites, improve performance, and lower costs; (c) compounding noble metals with other catalysts in the form of single atoms,[59] which will not be discussed in detail here.
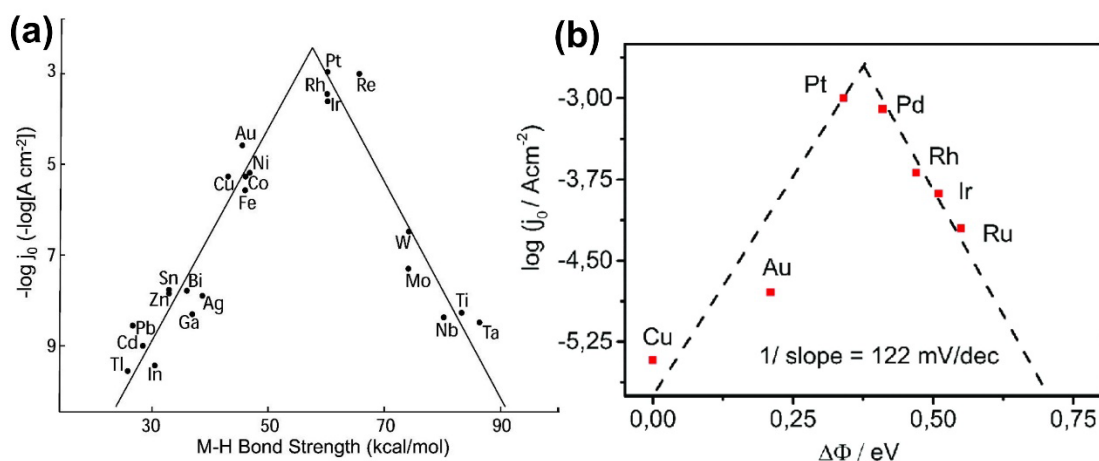
Figure 1.10.[57] (a) Volcano plot by Trasatti for pure metals in acidic solution. (b) Experimental volcano plot with the exchange current for HER values.

Among them, ruthenium (Ru), being the cheapest platinum-group metal with plentiful d-orbital electrons, has recently been shown to have adequate adsorption energies for adsorbed hydrogen (H_{ads}) and oxygen (O_{ads}),[60] although its application as a bifunctional catalyst in the field of overall water is hindered by its price and insufficient catalytic performance for HER.[61, 62] In the field of heterogeneous catalysis, the use of nanoparticles is common to attain a high performance. To address the agglomeration of nanoparticles occurring during the catalytic process, an efficient strategy is to support these nanoparticles on various substrates and particularly on 2D materials, owing to their high surface area and enhanced conductivity. Ti_3C_2 MXene, a 2D material with unique physicochemical properties, such as metallic conductivity,[63, 64] high intercalation capacitance,[65] selective adsorption capability,[66] and rich surface chemistry (-OH or -F termination)[67], is beneficial for the growth of other nanomaterials, like noble metals,[68] metal oxides,[62] and so on.[69] Given the small quantity of Ru required to achieve an electrocatalytic activity comparable to or even better than that of non-

noble metal catalysts, its cost performance is equivalent to that of other low-cost element catalysts. Taking these factors into consideration, growing fine and scattered RuO_2 nanoparticles on the surface of Ti_3C_2 MXene is expected not only to decrease the amount of Ru element to reduce cost, but also to enhance the active area of the catalyst to improve the HER performance. See **Chapter 3** for more details.

1.3.2 Transition metal-based catalysts

In addition to precious metal catalysts, researchers have developed a large number of various catalysts based on inexpensive transition metals: transition metals, transition metal alloys, transition metal oxides, transition metal nitrides, transition metal sulfides, transition metal phosphides, transition metal carbides, and others.

Among them, non-noble transition metal-based catalysts are competitive candidates for HER and UOR under alkaline conditions, owing to their excellent electrocatalytic performance. For instance, the catalytic performance of nickel-based nanomaterials has been demonstrated in numerous studies.[70-75] Inspired by nickel-based catalysts, there is no doubt that research on other transition metal catalysts for urea oxidation is also worth exploring. However, there is still a significant gap in this area. For these reasons, we chose cobalt, which, like nickel, is low-cost and has proven catalytic performance in other fields, as the subject of the study. We assessed the UOR and HER performances of cobalt oxide (Co_3O_4) with tunable morphological features and varying degrees of crystallinity.[76] Up to now, Co_3O_4 has been extensively studied in other energy-related fields and thus has a sound research background.[77-80] The main factors currently limiting the application of Co_3O_4 in the UOR and HER are poor electrical conductivity and insufficient exposure of active sites due to particle agglomeration. To address these problems, we introduced titanium carbide (Ti_3C_2)

MXene, which owns both high conductivity[81-83] and enhanced specific surface area[83] due to its layered structure, as a support material. On the other hand, Co_3O_4 was generally synthesized by a solvothermal reaction method at high temperature and high pressure in most reports,[84, 85] which brings safety concerns and limitations for large-scale preparation. Thus, a simple synthetic method, which is safe and convenient for industrialization is urgently needed. A nanocatalyst that combines Co_3O_4 and Ti_3C_2 MXene will be discussed in detail in **Chapter 4**.

1.4 Two-dimensional MXene-based catalysts

1.4.1 Overview of MXenes

In the 1960s-70s, Hans Nowotny's group discovered a new family of materials, ternary carbides and nitrides, known as H phases.[86] Little studied at the time, they received a major boost in the 1990s when Professor Michel Barsoum's group at Drexel University (Philadelphia, USA) undertook their systematic study.[87] They found that these materials formed a special class of ceramics with metallic properties.[88] Further research led to the synthesis and characterization of other materials of the same type.[89] These materials, which share the same crystallographic structure, have been grouped together under the generic term $M_{n+1}AX_n$ (n=1, 2, or 3), more commonly referred to as MAX phases, where M is a transition metal, A is an element from column 13 or 14 of the periodic table and the element X is either carbon or nitrogen.[90, 91] **Figure 1.11** depicts all the elements that can be used to create a MAX phase. One of the great advantages of MAX phases is their chemical versatility. To date, over than 150 different phases have been identified.[92]

Figure 1.11. Elements that may constitute the MAX phase.

Compared with their three-dimensional equivalents, two-dimensional materials have the advantage of a much higher ratio of surface to volume atoms, enabling us to limit the amount of material used in certain applications where the exposed surface plays a major role. In addition, they often exhibit unique electron properties.[93] Since the discovery of graphene, other 2D materials have been synthesized. These can generally be divided into two groups: materials with an elementary allotropic form (silicene, germanene,[94] etc) and compounds including graphane, transition metal dichalcogenides (MoS_2, WS_2, etc) or hexagonal boron nitride hBN.[95] However, the lack of flexibility of these materials and the impossibility of significantly varying their chemical compositions beyond a few atomic percent limit the possibility of optimizing their properties and, consequently, their field of application.

In this context, a new class of 2D materials with versatile chemistry was discovered in 2011 at Drexel University (Philadelphia, USA), the MXenes.[96] They are synthesized by removing the element A layer in the three-dimensional nano-lamellar

ceramic precursors that are MAX phases. MXenes are named by analogy with MAX phases and graphene. They are formed from transition metal carbide, nitride or carbonitride sheets. Given the compositional richness of MAX phases as described above, numerous MXenes of different M and X compositions can be obtained. In addition, when the element A layer is removed, end groups such as -F, -OH and/or -O, or even -Cl,[97] passivate the surface. This functionalization plays a key role in the surface properties of MXenes, providing another means of modulating them. Consequently, the formulation commonly encountered in the literature for MXenes is $M_{n+1}X_nT_x$ with M being the transition metal, n is the number of layers and X = C and/or N of the initial MAX phase. Finally, T_x represents the end groups formed during synthesis. Since their discovery, it has been accepted that the quantity of terminal groups x for a saturated MXene phase is close to 2,[98] although this value is still subject to debate. Given all these compositional levels, MXenes are potentially the largest family of 2D materials, with a wide range of properties offering a very broad spectrum of applications.

1.4.2 Synthesis of MXenes

MXenes are synthesized by exfoliation of the A element of the MAX phase. The first synthesis was carried out in 2011 by Naguib et al.[96] During this synthesis, a powder of Ti_3AlC_2 MAX phase was immersed in concentrated hydrofluoric acid (HF) to remove aluminum. The final suspension was then washed with ultrapure water *via* several centrifugation cycles until the pH of the supernatant was around 6. The final powder was filtered and dried. The $Ti_3C_2T_x$ MXene is synthesized in the form of a multilayer stack. The elimination of aluminum is explained by the anisotropic bonding forces at play in the MAX phases. Indeed, M-A bonds are weaker than M-X bonds, which explains why aluminum (A in the MAX phase) can be easily eliminated, leading to the

formation of $M_{n+1}X_n$ sheets linked together by weak hydrogen and/or van der Waals bonds. The process is shown in **Figure 1.12**.
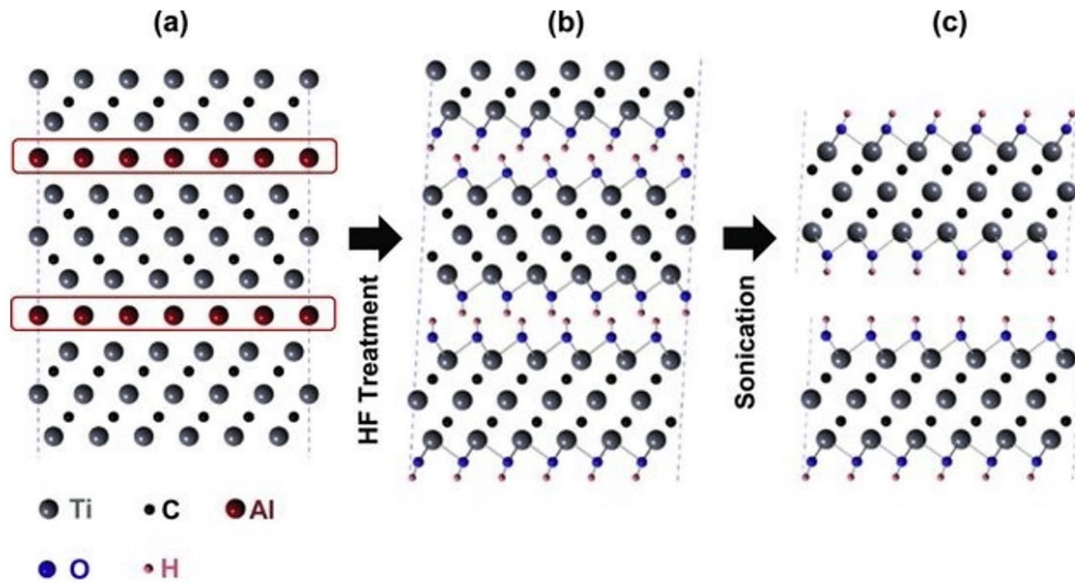
Figure 1.12.[96] Schematic of the exfoliation process for Ti₃AlC₂. (**a**) Ti₃AlC₂ structure. (**b**) Al atoms replaced by OH after reaction with HF. (**c**) Breakage of the hydrogen bonds and separation of nanosheets after sonication in methanol.

Figure 1.13 shows SEM images recorded for the MAX phase, Ti₃AlC₂, and the corresponding Ti₃C₂Tₓ MXene. The 2D character of this material can be clearly seen.

The proposed reaction mechanism for the exfoliation process leading to the formation of MXene is summarized below:

$$Ti_3AlC_2 + 3HF = AlF_3 + 3/2\ H_2 + Ti_3C_2 \qquad\qquad (1.24)$$

$$Ti_3C_2 + 2H_2O = Ti_3C_2(OH)_2 + H_2 \qquad\qquad (1.25)$$

$$Ti_3C_2 + 2HF = Ti_3C_2F_2 + H_2 \qquad\qquad (1.26)$$
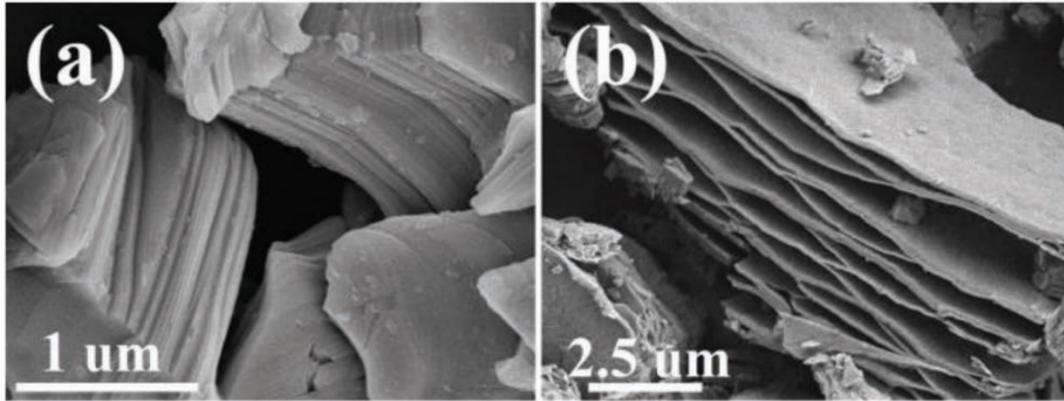
Figure 1.13.[99] Representative SEM images of (**a**) Ti_3AlC_2 MAX-phase raw particles;

(**b**) etched multilayered MXenes.

Aluminium fluoride (AlF_3) is formed during exfoliation (Equation.1.24). The solubility of this compound is relatively high, enabling it to be removed during the washing stages. However, in some cases, it can remain trapped between the MXene sheets. Its elimination and crystallization will depend on several parameters, resulting from the exfoliation treatment (duration, temperature and MAX/F phase mass ratio).[100] Equations 1.25-1.26 indicate that the surface of MXene sheets is passivated by various oxygenated (-OH or -O) and fluorinated (-F) end groups.[101, 102] However, in order to control the synthesis and properties of the obtained MXene, numerous parameters need to be taken into account, such as the mass ratio between the MAX phase and the exfoliating agent, the concentration of the exfoliating medium, the reaction time, the temperature and the particle size of the MAX phase used as precursor. All these parameters need to be adjusted to achieve significant yields in the conversion of MAX phase to MXene. Exfoliation conditions vary widely from one type of MAX phase to another, due to variations in M-A bond energy strength.

1.4.3 Properties and applications in electrocatalysis of MXene

MXenes have numerous properties, such as high electronic conductivity and hydrophilic properties.[103, 104] In addition, the many possible compositions of MXenes, whether at the core by changing the nature of the M and X elements of the MAX phase, or at the surface by playing on surface functionalization, depending on the exfoliating medium, offer new properties. This chemical richness makes it possible to adjust the properties of MXenes to suit the constraints of targeted applications. Below are discussed some of the main characteristics of 2D MXene materials:

High electrical conductivity: MXene materials exhibit metallic levels of electrical conductivity, with conductivity values reaching or even exceeding 10,000 S/cm.[105] This makes them highly promising as electrode materials in energy storage devices such as supercapacitors and lithium-ion batteries. Excellent mechanical properties: MXene materials possess high strength and good flexibility.[106] This makes them suitable for use in flexible electronic devices and nanocomposites. Rich surface chemistry: The surface of MXene materials typically contains various functional groups, such as -OH, -F, and -O.[107] These groups endow MXene with excellent chemical reactivity, enabling diverse surface modifications and functionalizations with other materials. High specific surface area: As 2D materials, MXene has a high specific surface area, which facilitates electrochemical reactions and enhances their efficiency in electrochemical energy storage and catalytic applications.[108] Outstanding thermal stability and conductivity: MXene materials exhibit good stability at high temperatures and have excellent thermal conductivity.[109] This makes them suitable for use in high-temperature electronic devices and thermal management systems. Optoelectronic properties: MXene materials demonstrate good light absorption characteristics and photoelectric conversion

efficiency, making them suitable for optoelectronic devices such as photodetectors and solar cells. These properties make MXene materials highly promising for applications in energy storage, electronic devices, sensors, catalysis, environmental remediation, and more.

In the field of electrocatalytic hydrogen production, MXene's high electrical conductivity can accelerate the electron transfer in the catalytic process and reduce the resistance loss, thus improving the catalytic efficiency; its abundant active sites (-OH,-F,-O and other functional groups) can help the generation and release of hydrogen molecules. In addition, it is possible to optimize the catalytic activity by complexing MXene with other catalytic materials (example: noble metal oxides− RuO_2; transition metals and their oxides− Co_3O_4 and Cu_2O) *via* functional groups on the surface of MXene.

Finally, MXene materials offer the possibility to introduce other elements, such as modification of "M" atoms (Ti, Mo, V, Cr, etc.) for elemental doping, which can further enhance the catalytic performance.

Seh et al.[110] were the first to publish a theoretical study of a series of M_2XT_x MXenes. To predict the HER performance of these materials, the authors used DFT (density functional theory) calculations, comparing energy changes before and after hydrogen adsorption on the MXene surface.[111] They then experimentally tested the electrochemical activities of Mo_2CT_x and Ti_2CT_x MXenes in acidic medium (0.5 M H_2SO_4). In line with theoretical results, Mo_2CT_x MXene exhibited a much higher activity towards HER than Ti_2CT_x. To deliver a current density of -10 mA cm^{-2}, a potential of -283 mV *vs*. RHE for Mo_2CT_x is required, whereas a potential of -609 mV *vs*. RHE is needed for Ti_2CT_x. The electrocatalytic performance of Mo_2CT_x derives

from the existence of catalytic active sites on the surface of the MXene sheets.[112, 113] Handoko et al.[114] also studied $Mo_2Ti_2C_3T_x$, $Mo_2TiC_2T_x$, Mo_2CT_x and Ti_2CT_x MXenes and found Mo_2CT_x to be the most promising catalyst among these MXenes, with a potential of -189 mV to achieve a current density of -10 $mA.cm^{-2}$.

So far, an atomic engineering approach involving the partial replacement of titanium (Ti) atoms in $Ti_3C_2T_x$ with molybdenum (Mo) atoms has been shown to effectively alter the kinetics of interfacial water adsorption. This affects vibrational modes, binding energies, and adsorption sites of water molecules. Adding molybdenum can also boost the chemical and thermal stability of MXenes, which is crucial for high temperature applications or in chemically aggressive environments. Meanwhile, the transition metal oxide Cu_2O nanoflowers mentioned in Section 1.3.2 possess favorable electronic properties for catalytic oxidation, numerous active sites, and redox properties. These characteristics facilitate the breaking of the C-H bond in formaldehyde molecules, while their ability to participate in the multiple electron transfer process further enhances conversion to formic acid.

The study in **Chapter 5** investigates the use of copper(I) oxide (Cu_2O) nanoflowers as a base to support Mo_2TiC_2 MXene nanoclusters with the goal of enhancing electrocatalysis. The Cu_2O nanoflowers not only serve as active sites for formaldehyde oxidation, but also increase the electrocatalyst's surface area when combined with Mo_2TiC_2 MXene nanoclusters. This combination introduces more active sites for the catalytic process, creating a potential synergy that leverages the high electrical conductivity and structural benefits of Cu_2O with the exceptional catalytic properties of Mo_2TiC_2 MXene, leading to a significantly improved electrocatalytic performance for both AFO and HER. This specific configuration ensures stability under

harsh conditions, optimizes electronic properties for effective charge transfer, and aligns with the growing demand for environmentally friendly energy technologies.

1.5 Objectives and structure of this thesis

The objective of my PhD thesis is to prepare MXenes and MXene-based catalysts with high stability, good performance and low cost for H_2 production by water electrolysis. I. The MXene-based nanomaterial will be designed and assessed as a catalyst for hydrogen evolution. II. Prepared MXene-based nanomaterials can catalyze the electrolysis of seawater to produce hydrogen, mitigating the energetic challenge in places where fresh water is scarce. III. Prepared MXene-based nanomaterials can electrolyze wastewater containing impurities (e.g. urea or formaldehyde) to generate hydrogen with low energy consumption and decompose contaminants in wastewater.

Chapter 1 covers current hydrogen production techniques, the fundamental mechanisms of hydrogen and oxygen evolution reactions, and the challenges of electrolysis using non-pure water sources such as seawater, urea, and formaldehyde solutions. It also discusses different types of electrocatalysts and their preparation strategies, highlighting the unique properties and synthesis of MXene materials with the aim to investigate the synthesis methods, catalytic mechanisms, and performance optimization of MXene catalysts in water electrolysis.

Chapter 2 outlines the materials and experimental techniques used in this research, including the synthesis of MXenes and related composites. It covers the methods for micromorphological characterization, such as scanning electron microscopy (SEM) and transmission electron microscopy (TEM), and chemical composition analysis techniques like X-ray diffraction (XRD), Raman spectroscopy, X-ray photoelectron spectroscopy (XPS), and inductively coupled plasma atomic emission spectroscopy

(ICP-AES). The chapter also details electrochemical characterization methods, including cell fabrication, cyclic voltammetry, polarization curve measurements, and electrochemical impedance spectroscopy, along with the evaluation criteria for water electrolysis reactions. Additionally, it discusses production determination techniques, such as the water displacement method and nuclear magnetic resonance (NMR).

In **Chapter 3**, an electrochemical method was applied for the deposition of ruthenium oxide nanoparticles onto Ti_3C_2 MXene nanosheets loaded on nickel foam (RuO_2-Ti_3C_2/NF) and assessed as a bifunctional electrocatalyst for the formation of H_2/O_2 in alkaline freshwater, simulated seawater, and real seawater electrolytes. The open, fine, and uniform nanostructure design enables intrinsically a high density of active sites to increase catalytic efficiency and prevents sediment build-up to mitigate damage to catalytic performance in seawater. With the optimized RuO_2 amount and structure achieved by adjusting the number of electrodeposition cycles, the RuO_2-Ti_3C_2/NF electrode achieved low overpotential values (85 and 351 mV to drive 100 mA cm^{-2} for, respectively, HER and OER in 1 M KOH) and fast current response toward both HER and OER. Owing to its excellent performance in both half-reactions, RuO_2-Ti_3C_2/NF acted as a bifunctional catalyst for the overall splitting of natural seawater (collected from North Sea, Dunkerque, France) and showed better activity than the benchmark RuO_2 || Pt/C pair. Moreover, the catalyst had long-term endurance (more than 25 h) and high Faradaic efficiency (about 100%).

In **Chapter 4**, we applied a mild method to synthesize a 0D/2D Co_3O_4/Ti_3C_2 MXene composite. The composite exhibited an excellent performance as an efficient and stable electrocatalyst for UOR and HER in basic medium. In this strategy, Co_3O_4 nanoparticles were uniformly and finely dispersed on Ti_3C_2 by *in situ* electrostatic

assembling of Co salt on Ti_3C_2 MXene nanosheet, followed by chemical reduction with $NaBH_4$, solving the problem of insufficient exposure of active sites caused by too large particle size and agglomeration of Co_3O_4 particles. As a result, the electrical conductivity, catalytic activity and stability of the 0D/2D Co_3O_4/Ti_3C_2 MXene composite were effectively enhanced. Co_3O_4/Ti_3C_2 MXene presented low overpotential values of $\eta = 1.40$ V (UOR) and $\eta = 0.124$ V (HER) to deliver ± 10 mA cm^{-2}, which were significantly improved compared to either pure Ti_3C_2 MXene or Co_3O_4 nanoparticles. More importantly, a two-electrodes (Co_3O_4/Ti_3C_2 ‖ Co_3O_4/Ti_3C_2) alkaline electrolyzer for overall urea electrolysis required a cell voltage of only 1.49 V to drive 50 mA cm^{-2}, which is 0.41 V lower compared to that for pure water splitting recorded at the same current density. Furthermore, the electrolyzer exhibited great stability with limited activity degradation after 40 h.

Chapter 5 introduces Cu_2O-supported Mo_2TiC_2 MXene clusters as a catalyst system for improved dual hydrogen production *via* coupled HER and FOR. The study demonstrates that for overall formaldehyde electrolysis, a cell voltage of only 0.36 V is required to achieve a current density of 50 mA cm^{-2}, which is 1.49 V lower than that required for pure water splitting at the same current density. The investigation focuses on catalytic efficiency, stability, and mechanistic pathways, aiming to advance both theoretical understanding and practical implementation in sustainable energy systems. The successful fabrication of Mo_2TiC_2/Cu_2O composites and their excellent catalytic activity for formaldehyde oxidation and hydrogen evolution reactions are highlighted, showcasing their potential for applications such as water splitting and environmental remediation. Future research will focus on collecting and analyzing the gaseous products produced by the positive and negative electrodes to evaluate the feasibility of

this strategy for dual hydrogen production.

References

(1) Dincer, I. Green Methods for Hydrogen Production. *International Journal of Hydrogen Energy* **2012**, *37* (2), 1954-1971.

(2) International Energy Outlook 2023. *EIA* **2023**.

(3) Vincent, I.; Bessarabov, D. Low Cost Hydrogen Production by Anion Exchange Membrane Electrolysis: A Review. *Renewable and Sustainable Energy Reviews* **2018**, *81*, 1690-1704.

(4) Ishaq, H.; Dincer, I.; Crawford, C. A Review on Hydrogen Production and Utilization: Challenges and Opportunities. *International Journal of Hydrogen Energy* **2022**, *47* (62), 26238-26264.

(5) Dawood, F.; Anda, M.; Shafiullah, G. M. Hydrogen Production for Energy: An Overview. *International Journal of Hydrogen Energy* **2020**, *45* (7), 3847-3869.

(6) Megía, P. J.; Vizcaíno, A. J.; Calles, J. A.; Carrero, A. Hydrogen Production Technologies: From Fossil Fuels toward Renewable Sources. A Mini Review. *Energy & Fuels* **2021**, *35* (20), 16403-16415.

(7) Mosca, L.; Medrano Jimenez, J. A.; Wassie, S. A.; Gallucci, F.; Palo, E.; Colozzi, M.; Taraschi, S.; Galdieri, G. Process Design for Green Hydrogen Production. *International Journal of Hydrogen Energy* **2020**, *45* (12), 7266-7277.

(8) Ajanovic, A.; Sayer, M.; Haas, R. The Economics and the Environmental Benignity of Different Colors of Hydrogen. *International Journal of Hydrogen Energy* **2022**, *47* (57), 24136-24154.

(9) Noussan, M.; Raimondi, P. P.; Scita, R.; Hafner, M. The Role of Green and Blue Hydrogen in the Energy Transition-A Technological and Geopolitical Perspective. *Sustainability* **2020**, *13* (1), 298.

(10) Incer-Valverde, J.; Korayem, A.; Tsatsaronis, G.; Morosuk, T. "Colors" of Hydrogen: Definitions and Carbon Intensity. *Energy Conversion and Management*

2023, *291*, 117294.

(11) Hermesmann, M.; Müller, T. E. Green, Turquoise, Blue, or Grey? Environmentally Friendly Hydrogen Production in Transforming Energy Systems. *Progress in Energy and Combustion Science* **2022**, *90*, 100996.

(12) Amin, M.; Shah, H. H.; Fareed, A. G.; Khan, W. U.; Chung, E.; Zia, A.; Rahman Farooqi, Z. U.; Lee, C. Hydrogen Production through Renewable and Non-renewable Energy Processes and their Impact on Climate Change. *International Journal of Hydrogen Energy* **2022**, *47* (77), 33112-33134.

(13) Nikolaidis, P.; Poullikkas, A. A Comparative Overview of Hydrogen Production Processes. *Renewable and Sustainable Energy Reviews* **2017**, *67*, 597-611.

(14) Shiva Kumar, S.; Lim, H. An Overview of Water Electrolysis Technologies for Green Hydrogen Production. *Energy Reports* **2022**, *8*, 13793-13813.

(15) Han, G.; Lee, W.; Kim, M.-K.; Lee, J. W.; Ahn, Y.-H. Hydrogen Separation from Hydrogen-compressed Natural Gas Blends through Successive Hydrate Formations. *Chemical Engineering Journal* **2024**, *483*, 149409.

(16) Olabi, A. G.; Abdelkareem, M. A.; Mahmoud, M. S.; Elsaid, K.; Obaideen, K.; Rezk, H.; Wilberforce, T.; Eisa, T.; Chae, K.-J.; Sayed, E. T. Green Hydrogen: Pathways, Roadmap, and Role in Achieving Sustainable Development Goals. *Process Safety and Environmental Protection* **2023**, *177*, 664-687.

(17) Le, P. A.; Trung, V. D.; Nguyen, P. L.; Bac Phung, T. V.; Natsuki, J.; Natsuki, T. The Current Status of Hydrogen Energy: An Overview. *RSC Advances* **2023**, *13* (40), 28262-28287.

(18) Sinsel, S. R.; Riemke, R. L.; Hoffmann, V. H. Challenges and Solution Technologies for the Integration of Variable Renewable Energy Sources-A Review. *Renewable Energy* **2020**, *145*, 2271-2285.

(19) Amini Horri, B.; Ozcan, H. Green Hydrogen Production by Water Electrolysis: Current Status and Challenges. *Current Opinion in Green and Sustainable Chemistry* **2024**, *47*, 100932.

(20) Yodwong, B.; Guilbert, D.; Phattanasak, M.; Kaewmanee, W.; Hinaje, M.; Vitale, G. AC-DC Converters for Electrolyzer Applications: State of the Art and Future Challenges. *Electronics* **2020**, *9* (6), 912-942.

(21) Pham, C. V.; Escalera-López, D.; Mayrhofer, K.; Cherevko, S.; Thiele, S. Essentials of High Performance Water Electrolyzers-From Catalyst Layer Materials to Electrode Engineering. *Advanced Energy Materials* **2021**, *11* (44), 2101998.

(22) Shiva Kumar, S.; Himabindu, V. Hydrogen Production by PEM Water Electrolysis - A Review. *Materials Science for Energy Technologies* **2019**, *2* (3), 442-454.

(23) Xu, H. G.; Zhang, X. Y.; Ding, Y.; Fu, H. Q.; Wang, R.; Mao, F.; Liu, P. F.; Yang, H. G. Rational Design of Hydrogen Evolution Reaction Electrocatalysts for Commercial Alkaline Water Electrolysis. *Small Structures* **2023**, *4* (8), 2200404.

(24) de Groot, M. T.; Kraakman, J.; Garcia Barros, R. L. Optimal Operating Parameters for Advanced Alkaline Water Electrolysis. *International Journal of Hydrogen Energy* **2022**, *47* (82), 34773-34783.

(25) El-Shafie, M. Hydrogen Production by Water Electrolysis Technologies: A Review. *Results in Engineering* **2023**, *20*, 101426.

(26) Yu, M.; Budiyanto, E.; Tuysuz, H. Principles of Water Electrolysis and Recent Progress in Cobalt-, Nickel-, and Iron-Based Oxides for the Oxygen Evolution Reaction. *Angewandte Chemie-international Edition* **2022**, *61* (1), e202103824.

(27) Sun, H.; Xu, X.; Kim, H.; Jung, W.; Zhou, W.; Shao, Z. Electrochemical Water Splitting: Bridging the Gaps Between Fundamental Research and Industrial Applications. *Energy & Environmental Materials* **2023**, *6* (5), e12441.

(28) Ifkovits, Z. P.; Evans, J. M.; Meier, M. C.; Papadantonakis, K. M.; Lewis, N. S. Decoupled Electrochemical Water-splitting Systems: A Review and Perspective. *Energy & Environmental Science* **2021**, *14* (9), 4740-4759.

(29) Lasia, A. Mechanism and Kinetics of the Hydrogen Eolution Reaction. *International Journal of Hydrogen Energy* **2019**, *44* (36), 19484-19518.

(30) Whitmore, S. A. Nytrox as "Drop-in" Replacement for Gaseous Oxygen in

SmallSat Hybrid Propulsion Systems. *Aerospace* **2020**, *7* (4), 7040043.

(31) Naito, T.; Shinagawa, T.; Nishimoto, T.; Takanabe, K. Recent Advances in Understanding Oxygen Evolution Reaction Mechanisms over Iridium Oxide. *Inorganic Chemistry Frontiers* **2021**, *8* (11), 2900-2917.

(32) Lin, L.; Fu, Q.; Wang, R.; Yao, T.; Wang, X.; Song, B. Spinel-Type Oxides for Acidic Oxygen Evolution Reaction: Mechanism, Modulation, and Perspective. *Advanced Energy and Sustainability Research* **2023**, *4* (12), 2300075.

(33) Man, I. C.; Su, H. Y.; Calle-Vallejo, F.; Hansen, H. A.; Martínez, J. I.; Inoglu, N. G.; Kitchin, J.; Jaramillo, T. F.; Nørskov, J. K.; Rossmeisl, J. Universality in Oxygen Evolution Electrocatalysis on Oxide Surfaces. *ChemCatChem* **2011**, *3* (7), 1159-1165.

(34) Exner, K. S. Why the Breaking of the OOH versus OH Scaling Relation Might Aause Decreased Electrocatalytic Activity. *Chem Catalysis* **2021**, *1* (2), 258-271.

(35) Yoo, J. S.; Rong, X.; Liu, Y.; Kolpak, A. M. Role of Lattice Oxygen Participation in Understanding Trends in the Oxygen Evolution Reaction on Perovskites. *ACS Catalysis* **2018**, *8* (5), 4628-4636.

(36) Xiao, X.; Yang, L.; Sun, W.; Chen, Y.; Yu, H.; Li, K.; Jia, B.; Zhang, L.; Ma, T. Electrocatalytic Water Splitting: From Harsh and Mild Conditions to Natural Seawater. *Small* **2022**, *18* (11), e2105830.

(37) Bradshaw, A.; Schleicher, K. E. Electrical Conductivity of Seawater. *IEEE Journal of Oceanic Engineering* **1980**, *5*, 50-62.

(38) Land-Based Wind Market Report: 2023 Edition. *U.S. Department of Energy* **2023**.

(39) Fu, C.; Hao, W.; Fan, J.; Zhang, Q.; Guo, Y.; Fan, J.; Chen, Z.; Li, G. Fabrication of Ultra-Durable and Flexible NiP_x -Based Electrode toward High-Efficient Alkaline Seawater Splitting at Industrial Grade Current Density. *Small* **2023**, *19* (11), e2205689.

(40) Wang, X.; Han, X.; Du, R.; Xing, C.; Qi, X.; Liang, Z.; Guardia, P.; Arbiol, J.; Cabot, A.; Li, J. Cobalt Molybdenum Nitride-Based Nanosheets for Seawater Splitting. *ACS Applied Materials & Interfaces* **2022**, *14* (37), 41924-41933.

(41) Dresp, S.; Dionigi, F.; Klingenhof, M.; Strasser, P. Direct Electrolytic Splitting of

Seawater: Opportunities and Challenges. *ACS Energy Letters* **2019**, *4* (4), 933-942.

(42) Qiu, Y.; Zhang, X.; Han, H.; Liu, Z.; Liu, J.; Ji, X. Advantageous Metal-atom-escape Towards Super-hydrophilic Interfaces Assembly for Efficient Overall Water Splitting. *Journal of Power Sources* **2021**, *499*, 229941.

(43) Tong, W.; Forster, M.; Dionigi, F.; Dresp, S.; Sadeghi Erami, R.; Strasser, P.; Cowan, A. J.; Farràs, P. Electrolysis of Low-grade and Saline Surface Water. *Nature Energy* **2020**, *5* (5), 367-377.

(44) Liu, X.; Gong, M.; Xiao, D.; Deng, S.; Liang, J.; Zhao, T.; Lu, Y.; Shen, T.; Zhang, J.; Wang, D. Turning Waste into Treasure: Regulating the Oxygen Corrosion on Fe Foam for Efficient Electrocatalysis. *Small* **2020**, *16* (24), e2000663.

(45) Maril, M.; Delplancke, J.-L.; Cisternas, N.; Tobosque, P.; Maril, Y.; Carrasco, C. Critical Aspects in the Development of Anodes for Use in Seawater Electrolysis. *International Journal of Hydrogen Energy* **2022**, *47* (6), 3532-3549.

(46) Cui, T.; Zhai, X.; Guo, L.; Chi, J.-Q.; Zhang, Y.; Zhu, J.; Sun, X.; Wang, L. Controllable Synthesis of a Self-assembled Ultralow Ru, Ni-doped Fe_2O_3 Lily as a Bifunctional Electrocatalyst for Large-current-density Alkaline Seawater Electrolysis. *Chinese Journal of Catalysis* **2022**, *43* (8), 2202-2211.

(47) Boggs, B. K.; King, R. L.; Botte, G. G. Urea electrolysis: Direct Hydrogen Production from Urine. *Chemical Communications* **2009**, *32* (32), 4859-4861.

(48) Modak, A.; Mohan, R.; Rajavelu, K.; Cahan, R.; Bendikov, T.; Schechter, A. Metal-Organic Polymer-Derived Interconnected Fe-Ni Alloy by Carbon Nanotubes as an Advanced Design of Urea Oxidation Catalysts. *ACS Applied Materials & Interfaces* **2021**, *13* (7), 8461-8473.

(49) Zhang, Q.; Kazim, F. M. D.; Ma, S.; Qu, K.; Li, M.; Wang, Y.; Hu, H.; Cai, W.; Yang, Z. Nitrogen Dopants in Nickel Nanoparticles Embedded Carbon Nanotubes Promote Overall Urea Oxidation. *Applied Catalysis B: Environmental* **2021**, *280*, 119436.

(50) Li, J.; Wang, S.; Sun, S.; Wu, X.; Zhang, B.; Feng, L. A Review of Hetero-

structured Ni-based Active Catalysts for Urea Electrolysis. *Journal of Materials Chemistry A* **2022**, *10* (17), 9308-9326.

(51) Yuan, M.; Wang, R.; Sun, Z.; Lin, L.; Yang, H.; Li, H.; Nan, C.; Sun, G.; Ma, S. Morphology-Controlled Synthesis of Ni-MOFs with Highly Enhanced Electrocatalytic Performance for Urea Oxidation. *Inorganic Chemistry* **2019**, *58* (17), 11449-11457.

(52) Zhang, L.; Wang, L.; Lin, H.; Liu, Y.; Ye, J.; Wen, Y.; Chen, A.; Wang, L.; Ni, F.; Zhou, Z.; et al. A Lattice-Oxygen-Involved Reaction Pathway to Boost Urea Oxidation. *Angewandte Chemie-international Edition* **2019**, *58* (47), 16820-16825.

(53) Li, P.; Zhuang, Z.; Du, C.; Xiang, D.; Zheng, F.; Zhang, Z.; Fang, Z.; Guo, J.; Zhu, S.; Chen, W. Insights into the Mo-Doping Effect on the Electrocatalytic Performance of Hierarchical CoxMoyS Nanosheet Arrays for Hydrogen Generation and Urea Oxidation. *ACS Applied Materials & Interfaces* **2020**, *12* (36), 40194-40203.

(54) Ligani Fereja, S.; Li, P.; Zhang, Z.; Guo, J.; Fang, Z.; Li, Z.; He, S.; Chen, W. W-doping Induced Abundant Active Sites in a 3D NiS_2/MoO_2 Heterostructure as an Efficient Electrocatalyst for Urea Oxidation and Hydrogen Evolution Reaction. *Chemical Engineering Journal* **2022**, *432*, 134274.

(55) Xiao, L.; Dai, W.; Mou, S.; Wang, X.; Cheng, Q.; Dong, F. Coupling Electrocatalytic Cathodic Nitrate Reduction with Anodic Formaldehyde Oxidation at Ultra-low Potential Over Cu_2O. *Energy & Environmental Science* **2023**, *16* (6), 2696-2704.

(56) Han, G.; Li, G.; Sun, Y. Electrocatalytic Dual Hydrogenation of Organic Substrates with a Faradaic Efficiency Approaching 200%. *Nature Catalysis* **2023**, *6* (3), 224-233.

(57) Gutić, S.; Dobrota, A.; Fako, E.; Skorodumova, N.; López, N.; Pašti, I. Hydrogen Evolution Reaction-From Single Crystal to Single Atom Catalysts. *Catalysts* **2020**, *10* (3), 290.

(58) Ge, R.; Li, L.; Su, J.; Lin, Y.; Tian, Z.; Chen, L. Ultrafine Defective RuO_2 Electrocatayst Integrated on Carbon Cloth for Robust Water Oxidation in Acidic Media. *Advanced Energy Materials* **2019**, *9* (35), 1901313.

(59) Zhang, J.; Zhao, Y.; Guo, X.; Chen, C.; Dong, C.-L.; Liu, R.-S.; Han, C.-P.; Li, Y.; Gogotsi, Y.; Wang, G. Single Platinum Atoms Immobilized on an MXene as an Efficient Catalyst for the Hydrogen Evolution Reaction. *Nature Catalysis* **2018**, *1* (12), 985-992.

(60) Xiao, W.; Yan, D.; Zhang, Y.; Yang, X.; Zhang, T. Heterostructured $MoSe_2$/Oxygen-Terminated Ti_3C_2 MXene Architectures for Efficient Electrocatalytic Hydrogen Evolution. *Energy & Fuels* **2021**, *35* (5), 4609-4615.

(61) Qin, Y.; Yu, T.; Deng, S.; Zhou, X. Y.; Lin, D.; Zhang, Q.; Jin, Z.; Zhang, D.; He, Y. B.; Qiu, H. J.; et al. RuO_2 Electronic Structure and Lattice Strain Dual Engineering for Enhanced Acidic Oxygen Evolution Reaction Performance. *Nature Communications* **2022**, *13* (1), 3784.

(62) Asen, P.; Esfandiar, A.; Mehdipour, H. Urchin-like Hierarchical Ruthenium Cobalt Oxide Nanosheets on $Ti_3C_2T_x$ MXene as a Binder-free Bifunctional Electrode for Overall Water Splitting and Supercapacitors. *Nanoscale* **2022**, *14* (4), 1347-1362.

(63) Yue, Q.; Sun, J.; Chen, S.; Zhou, Y.; Li, H.; Chen, Y.; Zhang, R.; Wei, G.; Kang, Y. Hierarchical Mesoporous MXene-NiCoP Electrocatalyst for Water-Splitting. *ACS Applied Materials & Interfaces* **2020**, *12* (16), 18570-18577.

(64) Chen, W. Y.; Lai, S. N.; Yen, C. C.; Jiang, X.; Peroulis, D.; Stanciu, L. A. Surface Functionalization of $Ti_3C_2T_x$ MXene with Highly Reliable Superhydrophobic Protection for Volatile Organic Compounds Sensing. *ACS Nano* **2020**, *14* (9), 11490-11501.

(65) Chen, Z.; Xu, X.; Ding, Z.; Wang, K.; Sun, X.; Lu, T.; Konarova, M.; Eguchi, M.; Shapter, J. G.; Pan, L.; et al. Ti_3C_2 MXenes-derived $NaTi_2(PO_4)_3$/MXene Nanohybrid for Fast and Efficient Hybrid Capacitive Deionization Performance. *Chemical Engineering Journal* **2021**, *407*, 127148.

(66) Pang, S. Y.; Wong, Y. T.; Yuan, S.; Liu, Y.; Tsang, M. K.; Yang, Z.; Huang, H.; Wong, W. T.; Hao, J. Universal Strategy for HF-Free Facile and Rapid Synthesis of Two-dimensional MXenes as Multifunctional Energy Materials. *Journal of the American Chemical Society* **2019**, *141* (24), 9610-9616.

(67) Park, S.; Lee, Y.-L.; Yoon, Y.; Park, S. Y.; Yim, S.; Song, W.; Myung, S.; Lee, K.-S.; Chang, H.; Lee, S. S.; et al. Reducing the High Hydrogen Binding Strength of Vanadium Carbide MXene with Atomic Pt Confinement for High Activity toward HER. *Applied Catalysis B: Environmental* **2022**, *304*, 120989.

(68) Zhang, B.; Shan, J.; Wang, X.; Hu, Y.; Li, Y. Ru/Rh Cation Doping and Oxygen-Vacancy Engineering of FeOOH Nanoarrays@Ti$_3$C$_2$T$_x$ MXene Heterojunction for Highly Efficient and Stable Electrocatalytic Oxygen Evolution. *Small* **2022**, *18* (25), e2200173.

(69) Niu, R.; Han, R.; Wang, Y.; Zhang, L.; Qiao, Q.; Jiang, L.; Sun, Y.; Tang, S.; Zhu, J. MXene-based Porous and Robust 2D/2D Hybrid Architectures with Dispersed Li$_3$Ti$_2$(PO$_4$)$_3$ as Superior Anodes for Lithium-ion Battery. *Chemical Engineering Journal* **2021**, *405*, 127049.

(70) Wang, K.; Huang, W.; Cao, Q.; Zhao, Y.; Sun, X.; Ding, R.; Lin, W.; Liu, E.; Gao, P. Engineering NiF$_3$/Ni$_2$P Heterojunction as Efficient Electrocatalysts for Urea Oxidation and Splitting. *Chemical Engineering Journal* **2022**, *427*, 130865.

(71) Liu, D.; Liu, T.; Zhang, L.; Qu, F.; Du, G.; Asiri, A. M.; Sun, X. High-performance Urea Electrolysis Towards Less Energy-intensive Electrochemical Hydrogen Production using a Bifunctional Catalyst Electrode. *Journal of Materials Chemistry A* **2017**, *5* (7), 3208-3213.

(72) Yue, Z.; Zhu, W.; Li, Y.; Wei, Z.; Hu, N.; Suo, Y.; Wang, J. Surface Engineering of a Nickel Oxide-Nickel Hybrid Nanoarray as a Versatile Catalyst for Both Superior Water and Urea Oxidation. *Inorganic Chemistry* **2018**, *57* (8), 4693-4698.

(73) Xu, Q.; Yu, T.; Chen, J.; Qian, G.; Song, H.; Luo, L.; Chen, Y.; Liu, T.; Wang, Y.; Yin, S. Coupling Interface Constructions of FeNi$_3$-MoO$_2$ Heterostructures for Efficient Urea Oxidation and Hydrogen Evolution Reaction. *ACS Applied Materials & Interfaces* **2021**, *13* (14), 16355-16363.

(74) Feng, S.; Luo, J.; Li, J.; Yu, Y.; Kang, Z.; Huang, W.; Chen, Q.; Deng, P.; Shen, Y.; Tian, X. Heterogeneous Structured Ni$_3$Se$_2$/MoO$_2$@Ni$_{12}$P$_5$ Catalyst for Durable Urea

Oxidation Reaction. *Materials Today Physics* **2022**, *23*, 100646.

(75) Hu, S.; Wang, S.; Feng, C.; Wu, H.; Zhang, J.; Mei, H. Novel MOF-Derived Nickel Nitride as High-Performance Bifunctional Electrocatalysts for Hydrogen Evolution and Urea Oxidation. *ACS Sustainable Chemistry & Engineering* **2020**, *8* (19), 7414-7422.

(76) Nozari-Asbemarz, M.; Amiri, M.; Khodayari, A.; Bezaatpour, A.; Nouhi, S.; Hosseini, P.; Wark, M.; Boukherroub, R.; Szunerits, S. In Situ Synthesis of $Co_3O_4/CoFe_2O_4$ Derived from a Metal-Organic Framework on Nickel Foam: High-Performance Electrocatalyst for Water Oxidation. *ACS Applied Energy Materials* **2021**, *4* (3), 2951-2959.

(77) He, X.; Tan, J.; Yin, F.; Chen, B.; Liang, X.; Li, G.; Yin, H. Well-dispersed Co-Co_3O_4 Hybrid Nanoparticles on N-doped Carbon Nanosheets as a Bifunctional Electrocatalyst for Oxygen Evolution and Reduction Reactions. *International Journal of Hydrogen Energy* **2019**, *44* (44), 24184-24196.

(78) Khalid, M.; Honorato, A. M. B.; Ticianelli, E. A.; Varela, H. Uniformly Self-decorated Co_3O_4 Nanoparticles on N, S Co-doped Carbon Layers Derived from a Camphor Sulfonic Acid and Metal-organic Framework Hybrid as an Oxygen Evolution Electrocatalyst. *Journal of Materials Chemistry A* **2018**, *6* (25), 12106-12114.

(79) Baruah, K.; Deb, P. Enabling Methanol Oxidation by an Interacting Hybrid Nanosystem of Spinel Co_3O_4 Nanoparticle Decorated MXenes. *Dalton Transactions* **2022**, *51* (11), 4324-4337.

(80) Xu, M.; Xia, Q.; Yue, J.; Zhu, X.; Guo, Q.; Zhu, J.; Xia, H. Rambutan-Like Hybrid Hollow Spheres of Carbon Confined Co_3O_4 Nanoparticles as Advanced Anode Materials for Sodium-Ion Batteries. *Advanced Functional Materials* **2018**, *29* (6), 1807377.

(81) Wang, Y.; Cui, Y.; Kong, D.; Wang, X.; Li, B.; Cai, T.; Li, X.; Xu, J.; Li, Y.; Yan, Y.; et al. Stimulation of Surface Terminating Group by Carbon Quantum Dots for Improving Pseudocapacitance of $Ti_3C_2T_x$ MXene Based Electrode. *Carbon* **2021**, *180*, 118-126.

(82) Lim, K. R. G.; Handoko, A. D.; Nemani, S. K.; Wyatt, B.; Jiang, H. Y.; Tang, J.; Anasori, B.; Seh, Z. W. Rational Design of Two-Dimensional Transition Metal Carbide/Nitride (MXene) Hybrids and Nanocomposites for Catalytic Energy Storage and Conversion. *ACS Nano* **2020**, *14* (9), 10834-10864.

(83) Pan, F.; Yu, L.; Xiang, Z.; Liu, Z.; Deng, B.; Cui, E.; Shi, Z.; Li, X.; Lu, W. Improved Synergistic Effect for Achieving Ultrathin Microwave Absorber of 1D Co Nanochains/2D Carbide MXene Nanocomposite. *Carbon* **2021**, *172*, 506-515.

(84) Zhang, D.; Mi, Q.; Wang, D.; Li, T. MXene/Co_3O_4 Composite Based Formaldehyde Sensor Driven by ZnO/MXene Nanowire Arrays Piezoelectric Nanogenerator. *Sensors and Actuators B: Chemical* **2021**, *339*, 129923.

(85) Pang, M.; Long, G.; Jiang, S.; Ji, Y.; Han, W.; Wang, B.; Liu, X.; Xi, Y.; Wang, D.; Xu, F. Ethanol-assisted Solvothermal Synthesis of Porous Nanostructured Cobalt Oxides (CoO/Co_3O_4) for High-performance Supercapacitors. *Chemical Engineering Journal* **2015**, *280*, 377-384.

(86) Nowotny, V. H. Strukturchemie einiger Verbindungen der Übergangsmetalle mit den elementen C, Si, Ge, Sn. *Progress in Solid State Chemistry* **1971**, *5*, 27-70.

(87) Barsoum, M. W.; El-Raghy, T. Synthesis and Characterization of a Remarkable Ceramic: Ti_3SiC_2. *Journal of the American Ceramic Society* **2005**, *79* (7), 1953-1956.

(88) Barsoum, M. W.; Brodkin, D.; El-Raghy, T. Layered Machinable Ceramics for High Temperature Applications. *Scripta Materialia* **1997**, *36* (5), 535-541.

(89) Barsoum, M.; El-Raghy, T.; Procopio, A. Synthesis of Ti_4AlN_3 and Phase Equilibria in the Ti-Al-N System. *Metallurgical and Materials Transactions A* **2000**, *31*, 373-378.

(90) Barsoum, M. W. The $M_{N+1}AX_N$ phases: A new class of solids: Thermodynamically stable nanolaminates. *Progress in Solid State Chemistry* **2000**, *28* (1), 201-281.

(91) Barsoum, M. W.; El-Raghy, T.; Ali, M. M. Processing and Characterization of Ti_2AlC, Ti_2AlN, and $Ti_2AlC_{0.5}N_{0.5}$. *Metallurgical and Materials Transactions A* **2000**, *31*, 1857-1865.

(92) Sokol, M.; Natu, V.; Kota, S.; Barsoum, M. W. On the Chemical Diversity of the MAX Phases. *Trends in Chemistry* **2019**, *1* (2), 210-223.

(93) Cai, X.; Luo, Y.; Liu, B.; Cheng, H. M. Preparation of 2D Material Dispersions and Their Applications. *Chemical Society Reviews* **2018**, *47* (16), 6224-6266.

(94) Dávila, M. E.; Xian, L.; Cahangirov, S.; Rubio, A.; Le Lay, G. Germanene: A Novel Two-dimensional Germanium Allotrope Akin to Graphene and Silicene. *New Journal of Physics* **2014**, *16* (9), 095002.

(95) Wang, H.; Zhao, Y.; Xie, Y.; Ma, X.; Zhang, X. Recent Progress in Synthesis of Two-dimensional Hexagonal Boron Nitride. *Journal of Semiconductors* **2017**, *38* (3), 031003.

(96) Naguib, M.; Kurtoglu, M.; Presser, V.; Lu, J.; Niu, J.; Heon, M.; Hultman, L.; Gogotsi, Y.; Barsoum, M. W. Two-dimensional Nanocrystals Produced by exfoliation of Ti_3AlC_2. *Advanced Materials* **2011**, *23* (37), 4248-4253.

(97) Zhao, X.; Vashisth, A.; Prehn, E.; Sun, W.; Shah, S. A.; Habib, T.; Chen, Y.; Tan, Z.; Lutkenhaus, J. L.; Radovic, M.; et al. Antioxidants Unlock Shelf-Stable $Ti_3C_2T_X$ (MXene) Nanosheet Dispersions. *Matter* **2019**, *1* (2), 513-526.

(98) Halim, J.; Persson, I.; Eklund, P.; Persson, P. O. A.; Rosen, J. Sodium Hydroxide and Vacuum Annealing Modifications of the Surface Terminations of a Ti_3C_2 (MXene) Epitaxial Thin Film. *RSC Advances* **2018**, *8* (64), 36785-36790.

(99) Jiao, S.; Zhou, A.; Wu, M.; Hu, H. Kirigami Patterning of MXene/Bacterial Cellulose Composite Paper for All-Solid-State Stretchable Micro-Supercapacitor Arrays. *Advanced Science* **2019**, *6* (12), 1900529.

(100) Rajavel, K.; Ke T Fau - Yang, K.; Yang K Fau - Lin, D.; Lin, D. Condition Optimization for Exfoliation of Two Dimensional Titanium Carbide ($Ti_3C_2T_X$). *Nanotechnology* **2018**, *29* (9), 095605.

(101) Shi, C.; Beidaghi, M.; Naguib, M.; Mashtalir, O.; Gogotsi, Y.; Billinge, S. J. Structure of Nanocrystalline Ti_3C_2 MXene using Atomic Pair Distribution Function. *Physical Review Letters* **2014**, *112* (12), 125501.

(102) Naguib, M.; Mochalin, V. N.; Barsoum, M. W.; Gogotsi, Y. 25th anniversary article: MXenes: A New Family of Two-dimensional Materials. *Advanced Materials* **2014**, *26* (7), 992-1005.

(103) Anasori, B.; Lukatskaya, M. R.; Gogotsi, Y. 2D Metal Carbides and Nitrides (MXenes) for Energy Storage. *Nature Reviews Materials* **2017**, *2* (2), 16098.

(104) Gogotsi, Y.; Anasori, B. The Rise of MXenes. *ACS Nano* **2019**, *13* (8), 8491-8494.

(105) Jia, L.; Zhou, S.; Ahmed, A.; Yang, Z.; Liu, S.; Wang, H.; Li, F.; Zhang, M.; Zhang, Y.; Sun, L. Tuning MXene Electrical Conductivity towards Multifunctionality. *Chemical Engineering Journal* **2023**, *475*, 146361.

(106) Zhou, Y.; Yin, L.; Xiang, S.; Yu, S.; Johnson, H. M.; Wang, S.; Yin, J.; Zhao, J.; Luo, Y.; Chu, P. K. Unleashing the Potential of MXene-Based Flexible Materials for High-Performance Energy Storage Devices. *Advanced Science* **2024**, *11* (3), e2304874.

(107) Natu, V.; Barsoum, M. W. MXene Surface Terminations: A Perspective. *The Journal of Physical Chemistry C* **2023**, *127* (41), 20197-20206.

(108) Kumar, S.; Kumari, N.; Seo, Y. MXenes: Versatile 2D Materials with Tailored Surface Chemistry and Diverse Applications. *Journal of Energy Chemistry* **2024**, *90*, 253-293.

(109) Liu, R.; Li, W. High-Thermal-Stability and High-Thermal-Conductivity $Ti_3C_2T_x$ MXene/Poly(vinyl alcohol) (PVA) Composites. *ACS Omega* **2018**, *3* (3), 2609-2617.

(110) Seh, Z. W.; Fredrickson, K. D.; Anasori, B.; Kibsgaard, J.; Strickler, A. L.; Lukatskaya, M. R.; Gogotsi, Y.; Jaramillo, T. F.; Vojvodic, A. Two-Dimensional Molybdenum Carbide (MXene) as an Efficient Electrocatalyst for Hydrogen Evolution. *ACS Energy Letters* **2016**, *1* (3), 589-594.

(111) Handoko, A. D.; Steinmann, S. N.; Seh, Z. W. Theory-guided Materials Design: Two-dimensional MXenes in Electro- and Photocatalysis. *Nanoscale Horizons* **2019**, *4* (4), 809-827.

(112) Yan, Y.; Xia, B.; Xu, Z.; Wang, X. Recent Development of Molybdenum Sulfides as Advanced Electrocatalysts for Hydrogen Evolution Reaction. *ACS Catalysis* **2014**, *4*

(6), 1693-1705.

(113) Chaudhari, N. K.; Jin, H.; Kim, B.; San Baek, D.; Joo, S. H.; Lee, K. MXene: An Emerging Two-dimensional Material for Future Energy Conversion and Storage Applications. *Journal of Materials Chemistry A* **2017**, *5* (47), 24564-24579.

(114) Handoko, A. D.; Fredrickson, K. D.; Anasori, B.; Convey, K. W.; Johnson, L. R.; Gogotsi, Y.; Vojvodic, A.; Seh, Z. W. Tuning the Basal Plane Functionalization of Two-Dimensional Metal Carbides (MXenes) To Control Hydrogen Evolution Activity. *ACS Applied Energy Materials* **2018**, *1* (1), 173-180.

Chapter 2. Materials and experimental techniques

2.1 Products and materials

Cobalt(II) chloride anhydrous ($CoCl_2$), ruthenium(III) chloride ($RuCl_3 \times H_2O$), potassium hydroxide (KOH), sodium chloride (NaCl), urea, Nafion 117 solution (5 wt %), hydrochloric acid (HCl, 36.5-38.0%), platinum on carbon (Pt/C), ruthenium(IV) oxide (RuO_2), sodium hydroxide (NaOH, ＞98%), potassium hydroxide (KOH, 95%, GR), lithium fluoride (LiF) and formaldehyde solution (HCHO, 36.5-38 wt%, AR) were purchased from Sigma-Aldrich Chemical Reagent Co., Ltd., France. Sodium borohydride ($NaBH_4$), hydrofluoric acid (HF), ethanol, acetone and isopropanol were obtained from Fisher Scientific, France. Ammonium persulfate ((NH_4)$_2S_2O_8$, 98%, AR) were purchased from Thermo Scientific TM.

The nickel foam (100×100 mm^2, thickness = 1 μm) was obtained from Kunshan Lvchuang Electronic Technology Co., Ltd., China. The copper foam (100×100 mm^2, thickness = 1 μm) was purchased from Taiyuan Lizhiyuan Technology Co., China.

Titanium aluminum carbide (Ti_3AlC_2) MAX phase powder was procured from 11 Technology Co., Ltd., China.

Ag/AgCl reference electrode, platinum foil counter electrode, graphite counter electrode, glassy-carbon working electrode, platinum electrode clips, glass mono-electrolytic cell, H-type electrolytic cell were obtained from Shanghai Yueci Electronic Technology Co., China.

The water used throughout the experiments in this thesis is purified with a Milli-Q system.

2.2 Synthesis of MXenes and related composites

In this paper, three series of MXene-based electrocatalysts were prepared, namely:

RuO$_2$/Ti$_3$C$_2$/NF, Co$_3$O$_4$/Ti$_3$C$_2$ MXene and Mo$_2$TiC$_2$/Cu$_2$O composites. Details of all preparation methods are described in **Chapter 3.1**, **Chapter 4.1** and **Chapter 5.1**, respectively.

2.3 Micromorphological characterization techniques

2.3.1 Scanning electron microscopy (SEM)

Scanning Electron Microscope (SEM) collects the secondary electron signals generated by the reflection of an electron beam bombarding the surface of a sample to determine the morphology of the material surface.[1] It is characterized by simple sample preparation and large magnification, which can be used to observe the microscopic morphology of catalyst surface. In this thesis, the micromorphology of all materials was examined with the aid of a JEOL JSM-7800F field-emission scanning electron microscope (**Figure 2.1**) operating at 15 kV. The powder samples were ultrasonically dispersed in an alcohol-water solution (1:1), dropped onto silicon wafers, and allowed to dry thoroughly at room temperature before observation. The foam samples were observed directly.

Figure 2.1. Photo of JEOL JSM-7800F field-emission scanning electron microscope.

2.3.2 Transmission electron microscopy (TEM)

Transmission Electron Microscope (TEM) analyzes the compositional and structural information of materials by collecting transmission electrons generated by a high-speed stream of electrons bombarding a sample accelerated by an electric field, with ultra-high magnification and imaging capabilities at the nanometer or even atomic level.[2]

Figure 2.2. Photo of FEI Tecnai G2-20 field-emission transmission electron microscopy.

In this thesis, TEM images were recorded on a FEI Tecnai G2-20 WIN field-emission transmission electron microscopy (**Figure 2.2**). Samples were prepared by dispersing the material in ethanol (0.2 mg mL^{-1}) and then 5 µL of this solution was drop-coated on a 200 mesh Cu grid for the high-resolution transmission electron microscopy (HR-TEM) analysis.

2.4 Chemical composition characterization techniques

2.4.1 X-ray diffraction (XRD)

X-ray diffraction (XRD), a research tool for obtaining information on the composition of a material, the structure or morphology of atoms or molecules within

the material by X-ray diffraction of the material and analyzing its diffraction pattern.[3] It is a versatile non-destructive analytical technique used to analyze the phase composition, crystal structure, orientation and other physical properties of powder, solid and liquid samples.
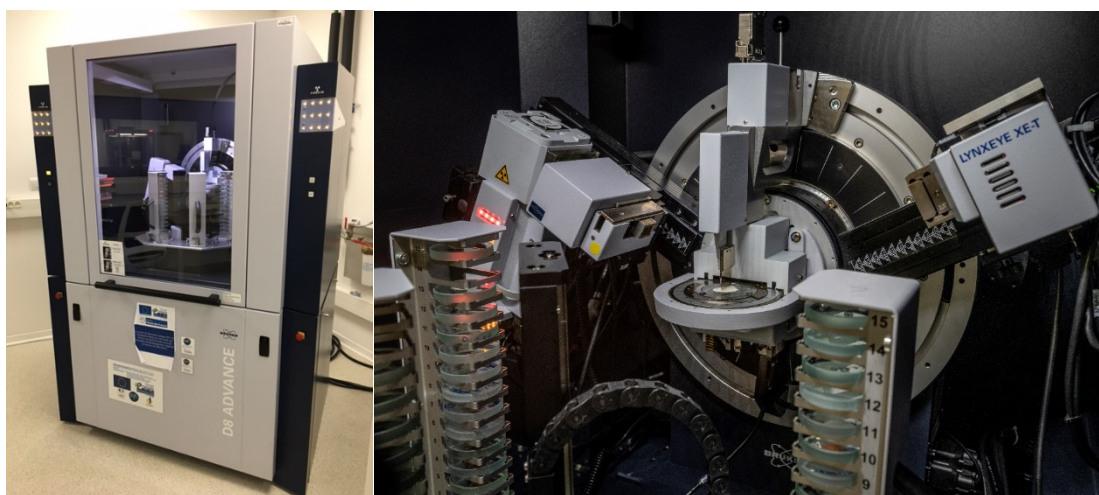

Figure 2.3. Photos of D8-PASSEUR.

In this thesis, the crystal structure of the synthesized nanomaterials was investigated by powder X-ray diffraction analysis. XRD patterns were recorded using a Bruker D8 Advance equipped with 1D LynxeEye detector and a 90-position robot-shifter (**Figure 2.3**). The scanning rate is 3° min^{-1} and *2θ* value ranges from 10 to 80° using Cu Kα (α = 1.54056Å) as the X-ray source and operates at a generator voltage of 40 kV and a current of 40 mA. Powder samples are prepared by grinding and sieving to obtain uniform fine powder, which is then loaded onto the XRD sample holder. The surface is flattened, and the sample holder is placed in the X-ray diffractometer for testing. The foam samples were tested directly.

2.4.2 Raman spectroscopy

Micro-Raman spectroscopy[4] measurements were performed on a Horiba Jobin

Yvon LabRam HR Micro-Raman system combined with a 473-nm laser diode as excitation source. Visible light was focused by a 100× objective. The scattered light was collected by the same objective in backscattering configuration, dispersed by a 1800-mm focal length monochromator and detected by a CCD. Samples were prepared by casting 50 µL aqueous or ethanol suspension of MXene composite on a clean silicon wafer or ITO surface followed by drying in an oven at 80° C to remove the solvent.

2.4.3 X-ray photoelectron spectroscopy (XPS)

X-ray photoelectron spectroscopy[5] experiments were performed on a PHI 5000 VersaProbe-Scanning ESCA Microprobe (ULVAC-PHI. Japan/USA) instrument, as shown in **Figure 2.4,** at a base pressure below 5×10^{-10} mbar. Monochromatic Al Kα radiation was used and the X-ray beam, focused to a diameter of 100 µm, was scanned on a 250 = 250 µm surface, at an operating power of 25 W (15 kV). Photoelectron survey spectra were acquired using a hemispherical analyzer at pass energy of 117.4 eV with a 0.4 eV energy step. Core-level spectra were acquired at pass energy of 23.5 eV with a 0.1 eV energy step. All spectra were recorded with 90° between X-ray source and analyzer and with the use of low energy electrons and low energy argon ions for charge neutralization. After subtraction of the linear-type background, the core-level spectra were decomposed into their components with mixed Gaussian-Lorentzian (30:70) shape lines using the CasaXPS software. Quantification calculations were performed using sensitivity factors supplied by PHI. The powder samples are dispersed in an alcohol solution and then coated onto silicon wafers. After drying, they are placed on the sample stage for testing, while block-like samples such as foam are tested directly.
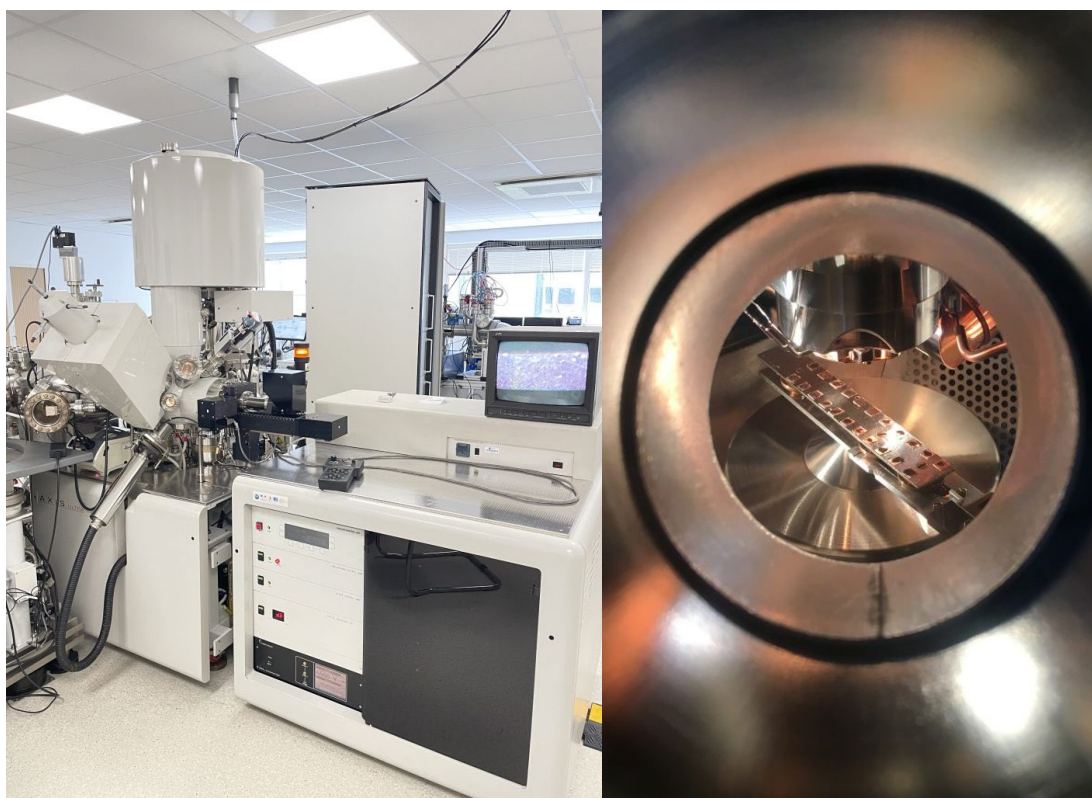
Figure 2.4. Photos of XPS and analysis chamber.

2.4.4 Inductively coupled plasma atomic emission spectroscopy (ICP-AES)

The amount of metal elements in prepared samples was determined with a Varian (liberty II axial view) inductively coupled plasma-atomic emission spectrometer (ICP-AES). The spectrometer was equipped with a pneumatic V-groove nebulizer and Sturmun-Master inert PTFE spray chamber. Sample solutions were driven through columns of resin by means of a multi-channel Gilson peristaltic pump equipped with 2.28 mm i.d. tubing. Teflon tubing. polyethylene bottles, and a pH meter (WTW) with glass electrode were also used. For ICP-AES analysis of solid metal samples, they need to be dissolved into a liquid form. Firstly, the RuO_2-Ti_3C_2/NF and Pt/C/NF samples are pre-treated to clean the surface and remove impurities, then dissolved in nitric acid. Next, the solution is diluted to ensure that the concentration of metal ions falls within

the detection range of the instrument. Finally, the sample solution is mixed thoroughly, and quality control checks are performed to ensure accuracy.

2.5 Electrochemical characterization methods

2.5.1 Cell fabrication

In tests using a three-electrode system for only half-reactions, a glass electrolytic single cell with a PTFE lid is used (**Figure 2.5a**). In two-electrode electrochemical tests where gases are collected, a hermetically sealed H-type electrolytic cell with a threaded lid **(Figure 2.5b)** is used.
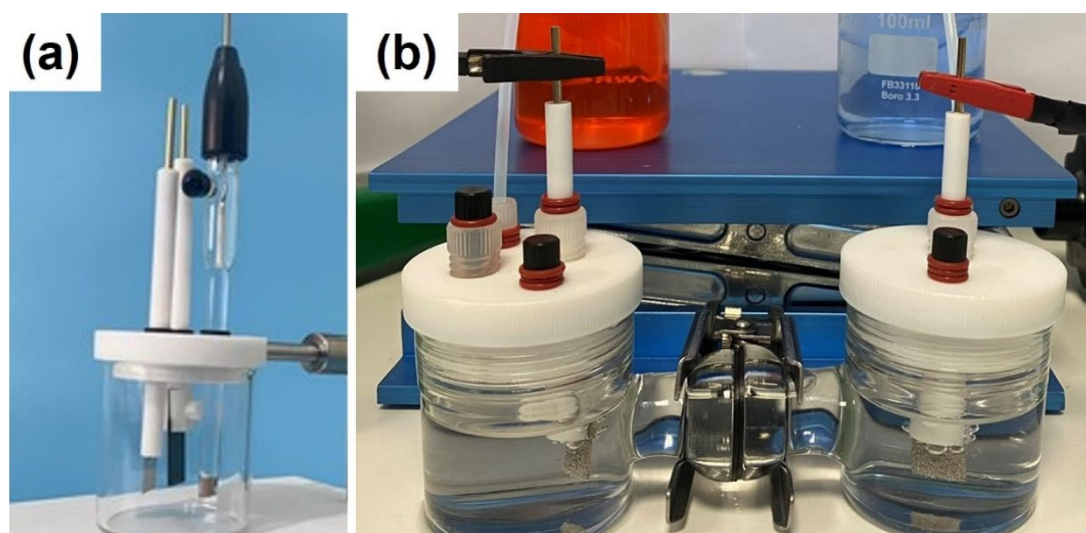

Figure 2.5. Photographs of (**a**) three-electrode system and (**b**) H-type electrolytic cell.

The three-electrode system consisted of a working electrode (3 mm diameter glassy carbon electrode or 1×1 cm^2 prepared sample plate), a counter electrode (graphite rod) and a reference electrode (Ag/AgCl, saturated KCl solution), respectively. A two-electrode test system (cathode and anode as working electrodes) was used in the total electrolyzed water test, urea- or formaldehyde-assisted total electrolyzed water using an electrochemical workstation.

The preparation of the working electrode for each chapter is detailed in the

experimental section of each chapter.

2.5.2 Cyclic voltammetry with linear potential variation

(1) Linear Sweep Voltammetry (LSV): Linear Sweep Voltammetry is the most basic electrochemical test method in water electrolysis test, which can show the catalytic activity of the electrocatalyst and its overpotential under different current densities most intuitively. The line scanning voltammetry curves of different electrocatalysts can be used to directly compare their catalytic performance. In this thesis, the line-scanning voltammetric curve tests were carried out at room temperature using the ModuLab-MTS electrochemical Test Station (Solartron, France), and the voltage range for the HER reaction were $0.9 \sim -2.9$ V (*vs.* Ag/AgCl reference electrode), and the voltage range for the OER reaction was $0 \sim 2$ V (*vs.* Ag/AgCl reference electrode) at a scanning rate of 5 mV s^{-1}. The voltage values obtained from the LSV curves were converted for use as a reversible hydrogen electrode (RHE) according to equation 2.1, where E_{RHE} denotes the voltage relative to a standard reversible hydrogen electrode, and $E_{Ag/AgCl}$ represents the voltage obtained from the line scan voltammetry curves relative to the Ag/AgCl reference electrode in the actual test. 0.198 V is the standard electrode potential for the Ag/AgCl reference electrode containing saturated potassium chloride solution as the electrolyte. The pH was 14 in a 1.0 mol L^{-1} solution of potassium hydroxide.

$$E_{RHE} = E_{Ag/AgCl} + 0.198 + 0.0591 \times pH \qquad\qquad (2.1)$$

(2) Cyclic Voltammetry (CV): Cyclic voltammetry is one of the most commonly used methods in electrochemical studies, in which the electrode can be controlled to scan repeatedly at different scanning rates within a certain potential, enabling different oxidation and reduction reactions to occur alternately on the electrode, and the current-voltage curve is recorded. According to the shape of the curve, the degree of

reversibility of the electrode reaction can be judged. It is also possible to integrate the corresponding peak area of the curve to obtain the real active area of the electrochemical reaction. In this thesis, cyclic voltammetry is used to test the catalytic activity and electrochemical active area of the electrocatalysts.

2.5.4 Electrochemical impedance spectroscopy (EIS)

Electrochemical Impedance Spectroscopy (EIS): Electrochemical Impedance Spectroscopy (EIS) is a relatively new electrochemical measurement technique that does not have a long history of development, but is now widely used in electrochemical fields, such as secondary batteries, fuel cells, corrosion protection and electrocatalysis. The response of an electrochemical system is observed by applying a small amplitude AC sinusoidal potential wave at different frequencies to the system, i.e., the ratio of the AC potential to the current signal, and this response is used to analyze the electrochemical properties of the system. The electrochemical system is regarded as an equivalent circuit, which is formed by combining various basic circuit elements in series or parallel, etc. By electrochemical impedance spectroscopy, the composition of the equivalent circuit as well as the size of the elements can be determined, and the electrochemical meanings of the elements can be utilized to analyze the structure of the electrochemical system and the electrode processes. The test is performed over a frequency range of 0.01 ~ 100000 Hz with an AC voltage amplitude of 5 mV and a corresponding test voltage of 0 or -100 mV (*vs.* RHE) for the HER reaction.

2.5.5 Evaluation criteria for electrolytic water reactions

Criteria for evaluating the reactivity of HER and OER include, among others, overpotential (especially at specific exchange current densities, e.g., 10, 100 mA cm^{-2}), Tafel slope, electrochemical surface area (ECSA), electrochemical impedance spectroscopy (EIS) and stability tests.

(1) Overpotential (η): Due to the additional potential barriers to be overcome during the reaction process, the actual working voltage is always higher than the theoretical decomposition voltage when the water electrolysis reaction is in progress (the theoretical decomposition voltages for the HER and OER are 0 and 1.23 V, respectively, with respect to a standard hydrogen electrode). Therefore, the overpotential at a specific current density is the most intuitive indicator for evaluating the activity of the HER and OER reactions, and the lower the overpotential, the better the electrochemical activity of the catalyst and the higher the energy utilization efficiency.

(2) Tafel slope: Tafel slope is an important kinetic parameter, calculated according to Tafel's formula, which can be used to determine the kinetic rate and reaction mechanism of the reaction. According to the description of the HER reaction mechanism in the previous section, the HER reaction usually involves three different reaction steps, and the step that determines the reaction rate can be inferred by calculating the Tafel slope. Specifically, the Tafel slopes are 30, 40, and 118 mV dec^{-1} when the reaction consists of the Tafel, the Heyrovsky and the Volmer steps as the rate-determining steps, respectively.

(3) Electrochemical impedance spectrum: By observing the shape of the electrochemical impedance spectrum in the high-frequency and low-frequency regions, we can analyze the controlling steps in the electrochemical reaction, such as semicircular or nearly semicircular curves appearing in the high-frequency region, indicating that the most probable controlling step is the charge-transferring step in the reaction; if the quantities of the real part and the imaginary part in the low-frequency region are linearly correlated, it indicates that the reaction is controlled by diffusion

steps at this voltage. The value of the charge transfer impedance can be obtained by fitting, and the smaller the value of this impedance in the electrocatalytic reaction, the faster the reaction proceeds. EIS data were gathered in the frequency range of 10^5 and 0.01 Hz.

(4) Double layer capacitance (double layer capacitance, C_{dl}): In the non-Faraday current region to test the double layer capacitance, using the CV curve in a small window of potential (0.1 V) between the scan rate of 5 ~ 100 mV s^{-1}, respectively. The current density value of the potential at the midpoint at different scanning rates was taken as the horizontal coordinate of the scanning rate and the corresponding current density value as the vertical coordinate, and the slope obtained was the capacitance value of the double layer.

(5) Electrochemical surface area (ECSA): ECSA represents the real active area of the electrocatalyst, which gives a clear indication on the catalytic activity of the catalyst. The electrochemical active surface area is generally measured by indirect way (equation 2.2), which needs requires first the determination of the double layer capacitance value (C_{dl}) in the non-Faraday current region. Where C_s is the specific capacitance, which represents the capacitance of a flat metal without defects in the ideal state, here C_{dl} is the double electric layer capacitance value in the non-Faradaic current region.

$$ECSA = C_{dl}/C_s \tag{2.2}$$

(6) Stability testing: Stability can be assessed by cyclic voltammetry at faster scan rates, or by applying a constant voltage or current to the electrode system. After a certain period of time, the stability can be judged by the curve fluctuation condition or comparing the linear scanning voltammetric curve before and after the cyclic test.

(7) iR compensation: The electrochemical data in **Chapters 4** and **5** were not iR compensated. In **Chapter 3**, all the LSV curves were iR-corrected (85 %) using

equation (2.3):[6, 7]

$$E_{compensated} = E_{measured} - I \times R_s \times 85\,\% \qquad (2.3)$$

$E_{compensated}$ is the potential after iR-compensation (V), $E_{measured}$ is the actual measured potential value (V), I is the actual measured current (A), R_s is the solution resistance, which can be obtained by the EIS.

2.6 Quantification of hydrogen

2.6.1 Water displacement method

Displacement of water is a commonly used, simple, and effective method for collecting gases in the laboratory. It is suitable for collecting gases that are insoluble or only slightly soluble in water, such as oxygen, hydrogen, and nitrogen. The principle of this method is illustrated in **Figure 2.6**.

Two gas collection tubes were filled with water and inverted in a water basin. One end of a tube was connected to the sealed cathode compartment of the H-type electrolytic cell, and the other end was inserted into the mouth of the collection tube. Similarly, another tube was used to collect the gas product from the anode compartment. Observe the volume change of the gas products in the collection tubes and record the gas production.
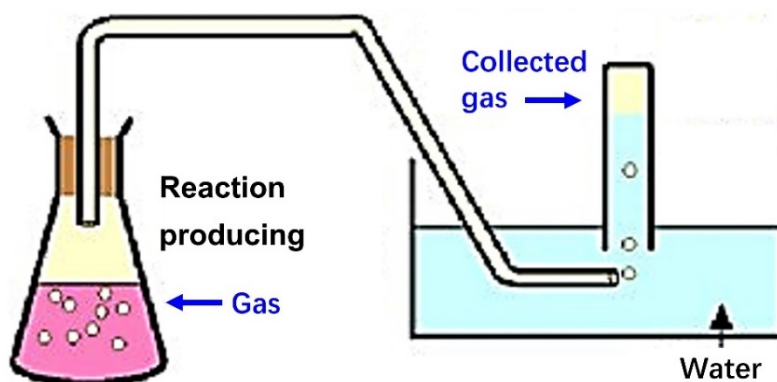

Figure 2.6. Schematic diagram of the drainage method.

2.6.2 Nuclear magnetic resonance (NMR)

Liquid-phase NMR can be used to characterize the molecular structure and dynamic behavior of liquid catalytic products. For example, through hydrogen spectra (^{1}H NMR) and carbon spectra (^{13}C NMR), the molecular structure, functional group positions, and coordination environment of the substance being measured can be determined, allowing for both qualitative and quantitative analysis of the products. By comparing the chemical shifts and coupling patterns in the NMR spectra, the structure and composition of the products can be identified. Comparing these with standard spectra can confirm the type of products. The non-destructive nature of NMR technology makes it highly suitable for quantitative analysis. By integrating peak areas, the concentrations of different components can be directly measured, enabling precise quantitative analysis.


Figure 2.7. Photo of a Bruker 300 MHz.

In this thesis, the ^{1}H NMR and ^{13}C spectra was collected on a Bruker 300 MHz liquid NMR spectrometers (**Figure 2.7**). The NMR samples were prepared by mixing 0.55 mL of electrolyte with 0.05 mL of D_2O containing 1% (w/w) 3-(trimethylsilyl)-1-propanesulfonic acid, sodium salt (DSS). DSS is used as an internal standard. All 1H NMR experiments were conducted using the Water suppression method.

References

(1) Akhtar, K.; Khan, S. A.; Khan, S. B.; Asiri, A. M. Scanning Electron Microscopy: Principle and Applications in Nanomaterials Characterization. In *Handbook of Materials Characterization*, Sharma, S. K. Ed.; Springer International Publishing, 2018; pp 113-145.

(2) Franken, L. E.; Grunewald, K.; Boekema, E. J.; Stuart, M. C. A. A Technical Introduction to Transmission Electron Microscopy for Soft-Matter: Imaging, Possibilities, Choices, and Technical Developments. *Small* **2020**, *16* (14), e1906198.

(3) Holder, C. F.; Schaak, R. E. Tutorial on Powder X-ray Diffraction for Characterizing Nanoscale Materials. *ACS Nano* **2019**, *13* (7), 7359-7365.

(4) Jimenez-Sandoval, S. Micro-Raman Spectroscopy: A Powerful Technique for Materials Research. *Microelectronics Journal* **2000**, *31* (6), 419-427.

(5) Krishna, D. N. G.; Philip, J. Review on Surface-characterization Applications of X-ray Photoelectron Spectroscopy (XPS): Recent Developments and Challenges. *Applied Surface Science Advances* **2022**, *12*, 100332.

(6) Xu, Q.; Yu, T.; Chen, J.; Qian, G.; Song, H.; Luo, L.; Chen, Y.; Liu, T.; Wang, Y.; Yin, S. Coupling Interface Constructions of $FeNi_3$-MoO_2 Heterostructures for Efficient Urea Oxidation and Hydrogen Evolution Reaction. *ACS Applied Materials & Interfaces* **2021**, *13* (14), 16355-16363.

(7) Kong, A.; Peng, M.; Gu, H.; Zhao, S.; Lv, Y.; Liu, M.; Sun, Y.; Dai, S.; Fu, Y.; Zhang, J.; et al. Synergetic Control of Ru/MXene 3D Electrode with Superhydrophilicity and Superaerophobicity for Overall Water Splitting. *Chemical Engineering Journal* **2021**, *426*, 131234.

Chapter 3. Ruthenium Oxide Nanoparticles Immobilized on Ti$_3$C$_2$ MXene Nanosheets for Boosting Seawater Electrolysis
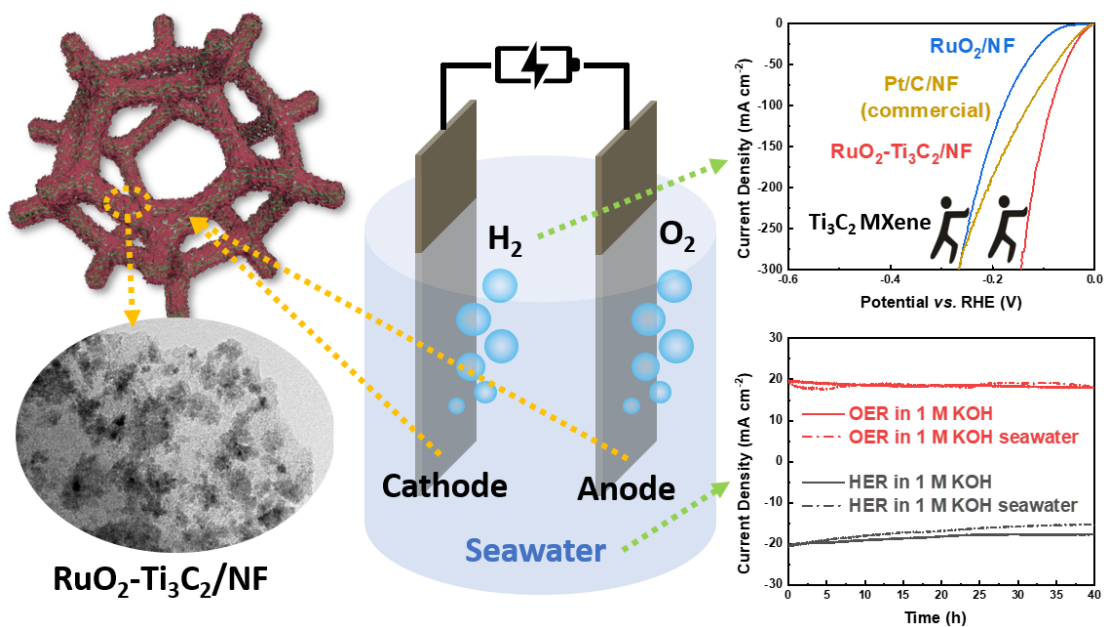
This chapter has been published in ACS Applied Materials & Interfaces.

Abstract

Seawater electrolysis represents a viable alternative for large-scale synthesis of hydrogen (H_2), which is recognized as the most promising clean energy source, without relying on scarce fresh water. However, high energy cost and harmful chlorine chemistry in seawater limited its development. Herein, an effective catalyst based on a ruthenium nanoparticles-Ti_3C_2 MXene composite loaded on nickel foam (RuO_2-Ti_3C_2/NF) with an open, fine, and homogeneous nanostructure was devised and synthesized by electrodeposition for high performance and stable overall seawater splitting. To drive a current density of 100 mA cm^{-2}, the RuO_2-Ti_3C_2/NF electrode required a small overpotential of 85 and 351 mV for HER and OER in 1 M KOH with only a slight increase in 1 M KOH seawater (156 and 378 mV for, respectively, HER and OER). An assembled RuO_2-Ti_3C_2/NF-based two-electrode cell required an overpotential of only 1.84 V to acquire 100 mA cm^{-2} in 1 M KOH seawater and maintained its activity for over 25 h. This low cell voltage effectively prevented chlorine electrochemical evolution without anode protection. These promising results open up new avenues for the effective conversion of abundant seawater resources to hydrogen fuel.

In this chapter, we aim to provide a solution, seawater splitting, for the sustainable development of H_2 energy in coastal arid regions, as illustrated in **Figure 3.1**.
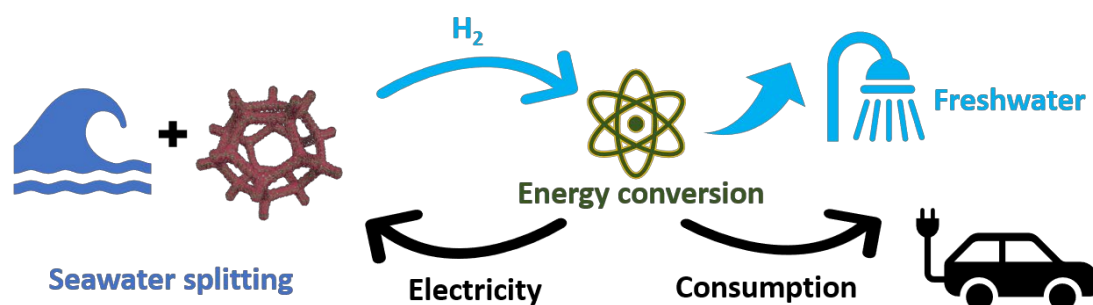

Figure 3.1. Hydrogen energy cycle model in areas without sufficient freshwater resources.

3.1 Experimental section

3.1.1 Synthesis of Titanium Carbide (Ti_3C_2) MXene Nanosheets.

Delaminated Ti_3C_2 MXene nanosheets were obtained by liquid etching of the pristine Ti_3AlC_2 bulk phase. First, lithium fluoride (LiF, 1 g) was added to a 9 M hydrochloric acid (HCl, 20 mL) solution and stirred (rotation speed was 400 rpm) in a Teflon beaker (volume was 100 mL) for 30 min until complete dissolution. Then, Ti_3AlC_2 (1 g) was slowly dropped to the above solution under stirring. Finally, the mixed solution was heated to 35 °C for 48 h under stirring. The resulting suspension was centrifuged (3500 rpm, 10 min), and the supernatant was poured off after centrifugation. Then, deionized water was added, and the suspension was thoroughly shaken and sonicated for 10 min. The precipitate was separated by centrifugation, and the above cleaning operation was repeated until the pH was close to neutral.

The obtained precipitate (accordion-shaped MXene) was dispersed in ethanol (as an intercalation agent) and sonicated for 1 h. The precipitate, collected by centrifugation at high speed (10000 rpm, 10 min), was redispersed ultrasonically in deionized water; the supernatant suspension obtained by centrifugation at low speed (3500 rpm, 10 min) was single-layer or few-layer MXene nanosheets. After concentration calibration, the prepared delaminated MXene nanosheets were kept in nitrogen-saturated deionized water to inhibit their oxidation.

3.1.2 Preparation of Ti_3C_2/NF.

Nickel foam (NF, 1.0×1.5 cm^2) was rinsed with acetone, diluted HCl (6 M), deionized water, and ethanol to limit the oxidized layer thickness. In short, Ti_3C_2-MXene/ nickel foam (Ti_3C_2/NF) was synthesized by adopting the following procedure. A piece of clean NF was completely soaked in few-layer Ti_3C_2 solution (1 mg mL^{-1}) for 30 min and then dried for 10 min at 60 °C in an oven; this process was repeated 2 times, and the resulting Ti_3C_2/NF was rinsed with water thoroughly and dried at 60 °C for 2 h.

3.1.3 Synthesis of RuO_2/NF and RuO_2/Ti_3C_2/NF Composites.

11 mg of $RuCl_3 \cdot \times H_2O$ and 117 mg of NaCl were placed in 20 mL of DI water and stirred magnetically for 5 min to form a dark brown solution, which was used as the electrolyte for electrochemical deposition. Electrochemical deposition was carried out in a three-electrode cell comprising a Pt foil (counter electrode), a Ag/AgCl electrode (reference electrode), and Ti_3C_2/NF (working electrode). Cyclic voltammetry was adopted in this electrodeposition process, in which the highest voltage was 1 V, the lowest voltage was -1.4 V, the scanning speed was 5 mV s^{-1}, and the number of cycles was 1, 3, or 5. As-prepared RuO_2-1/Ti_3C_2/NF, RuO_2-3/Ti_3C_2/NF, and RuO_2-5/Ti_3C_2/NF electrodes were rinsed with deionized water and air-dried. The control sample (RuO_2/NF) was prepared using bare NF as the working electrode.

3.1.4 Electrochemical Measurements

Hydrogen evolution reaction (HER) and oxygen evolution reaction (OER) experiments were conducted in a conventional three-electrode system by linear sweep voltammetry (LSV) at a sweep rate of 5 mV s^{-1} in electrolytes consisting of 1M KOH, 1M KOH + 1M NaCl or 1M KOH + seawater. The counter electrode was a graphite rod, while the reference electrode was an Ag/AgCl (saturated KCl). The working electrodes are the prepared composite materials. As benchmark, the commercial Pt/C/NF and RuO$_2$/NF were prepared by the coating method. A slurry (10 mg of commercial Pt/C or RuO$_2$ catalyst, 500 μL of DI, 450 μL of isopropanol, and 50 μL of Nafion) was deposited on a 1 × 1 cm^2 piece of clean NF with a mass loading of 1.6 mg cm^{-2} (optimum load for performance in line with literature reports).[1] After adding KOH and filtering the precipitate, which was mostly generated by magnesium hydroxide (~ 1.31 g/L Mg^{2+} in seawater),[2] natural seawater that had been collected from the North sea in Dunkerque, France, was utilized as the electrolyte with a final pH of 14.

3.1.5 Faradaic Efficiency Measurements for the HER.

The ratio of an experimentally evolved gas amount to the theoretically predicted one is known as the Faradaic efficiency (FE), which can be calculated using equation (3.1):[3]

$$FE = V_m / V_t \times 100\% \tag{3.1}$$

V_m is the measured amount of gas produced (mL), and V_t is the theoretical amount (mL), which can be calculated using the following equation (3.2-3.4):

$$V_t = n \times M / \rho \tag{3.2}$$

$$n = Q / (a \times F) \tag{3.3}$$

$$Q = It \tag{3.4}$$

n is the theoretical amount (mol) of produced gas; M is the molar mass of the gas

(g/mol); ρ is the density at normal temperature and pressure (g/mL); Q is the accumulated charge (C); a is the number of electrons transferred (n = 2 for HER and n = 4 for OER); F is the Faraday constant (96485 C mol^{-1}); I is the current (A); and t is the time (s). A water drainage method was used to capture the generated gas.

3.2 Results and discussion

3.2.1 Synthesis and Structural Characterization of RuO$_2$-Ti$_3$C$_2$/NF.

It is necessary to characterize the major electrocatalytic interface of the electrocatalysts in order to confirm that RuO$_2$-Ti$_3$C$_2$ was successfully formed on the surface of NF. The formation process of RuO$_2$-Ti$_3$C$_2$/NF is depicted in **Figure 3.2**. First, the stonelike Ti$_3$AlC$_2$ MAX precursor was etched selectively by strong acid (LiF/HCl) to remove Al atomic layers, yielding accordion-type Ti$_3$C$_2$ MXene nanosheets. **Figure 3.3(a)** depicts the scanning electron microscopy (SEM) image of the compact bulk morphology of the MAX raw material. This morphology contrasts with the loosely stacked structure of Ti$_3$C$_2$ **(Figure 3.3b)**, revealing the successful etching of the Al layers. After the washing and exfoliation procedures, a few-layered Ti$_3$C$_2$ MXene was subsequently produced as an aqueous dispersion. According to **Figure 3.3(c)**, the formation of 2D single- or few-layered Ti$_3$C$_2$ MXene with a lateral size of approximately 3 μm is clearly evidenced. During this process, numerous hydrophilic (-F and -OH) functional groups might theoretically be generated on the surface of Ti$_3$C$_2$.
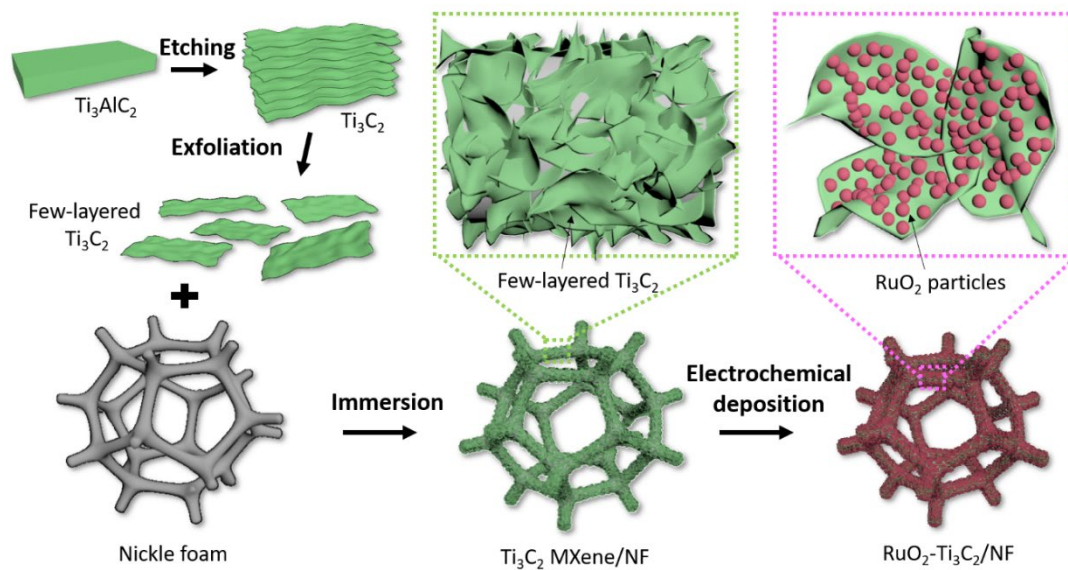
Figure 3.2. Schematic illustration of the preparation of RuO$_2$-Ti$_3$C$_2$/NF.
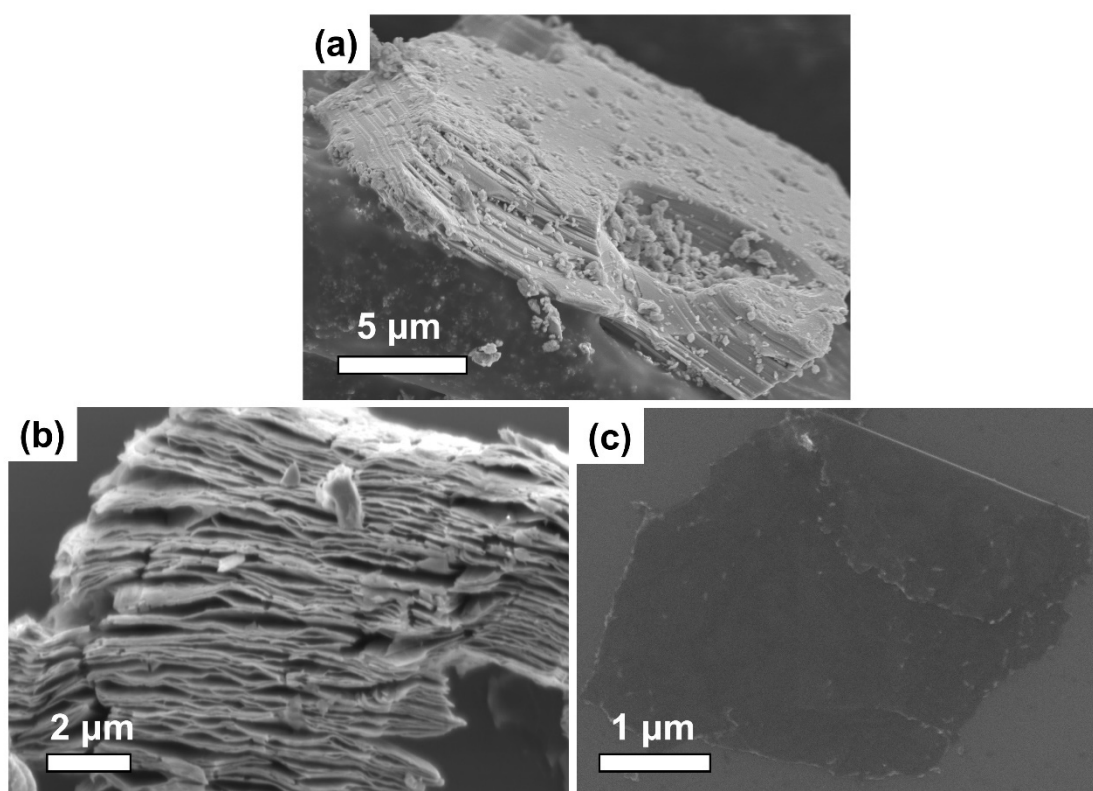
Figure 3.3. SEM images of (**a**) bulk Ti$_3$AlC$_2$ MAX phase, (**b**) accordion-like Ti$_3$C$_2$

MXene and (**c**) single or few-layer Ti$_3$C$_2$ MXene.

At the same time, a significant amount of positively charged Ni^{2+} was generated on the NF surface during cleaning by HCl. Therefore, when the cleaned NF was immersed in the Ti_3C_2 aqueous suspension, the negatively charged Ti_3C_2 and the positively charged NF attract and combine with each other, forming Ti_3C_2/NF through electrostatic interactions.

The electrochemical deposition of RuO_2 particles, which involves cathodic and anodic scans, is the last stage. During this process, Ru^{3+} species are converted to low valence before changing to high valence. **Figure 3.4** depicts a characteristic CV for the development of the RuO_2-Ti_3C_2/NF composites after 3 cycles. The reduction of Ru^{3+} species is evidenced by the existence of peak R1 on the negative sweep, in which Ru (Ru metal or oxy-chloro-ruthenium species) deposits onto Ti_3C_2/NF, generating Ru nanoparticles.
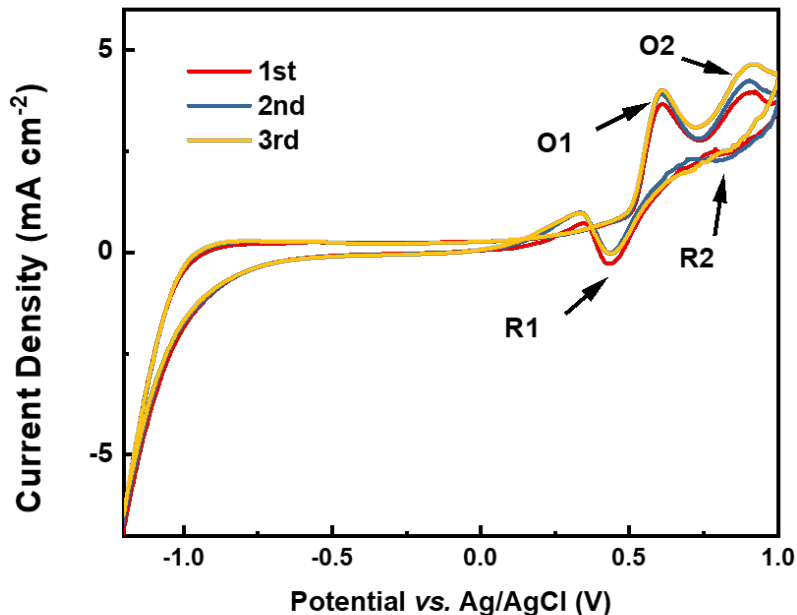
Figure 3.4. CV behavior of RuO_2 nanoparticles' growth on Ti_2C_3/NF (scan rate = 5 mV s^{-1}).

In the subsequent positive scanning process, Ru species are oxidized to hydrous oxides ($RuO_x \cdot nH_2O$) and then further oxidized to a higher oxidation state (i.e., hydroxyl Ru^{6+} species).[4] The two-step oxidation process is evidenced by the presence in **Figure 3.4** of the redox peaks of the O1 and the O2 redox peaks, respectively. During the next negative scan, these hydroxyl Ru^{6+} components are converted back to hydroxyl Ru^{4+} ($RuO_x \cdot nH_2O$) at peak R2's potential and then are gradually reduced to lower oxidation states. Finally, the Ru^{3+} species in the plating solution are once more deposited at greater negative potentials.

The microscopic morphology of RuO_2-Ti_3C_2/NF was studied by SEM (**Figure 3.5**) and TEM (**Figure 3.6**), in which the dark spots are RuO_2 particles and the light sheets correspond to Ti_3C_2 MXene. The ultrafine RuO_2 nanoparticles (mean size of ~ 15 nm) are uniformly deposited on relatively large Ti_3C_2 layers. Unlike RuO_2 particles grown on Ti_3C_2 nanosheets, which have an exceptionally tiny size and a greater distribution area, when RuO_2 particles are directly deposited on the surface of NF, as illustrated in **Figure 3.7**, RuO_2 particles not only easily agglomerate, disrupting charge transfer, but also form larger crystalline particles with a size of 2 μm, reducing the active area. That was expected, as the use of Ti_3C_2 MXene as a support material could dramatically expand the active area of the catalyst and expose more RuO_2 sites, hence promoting electrolyte transport and improving catalytic activity.
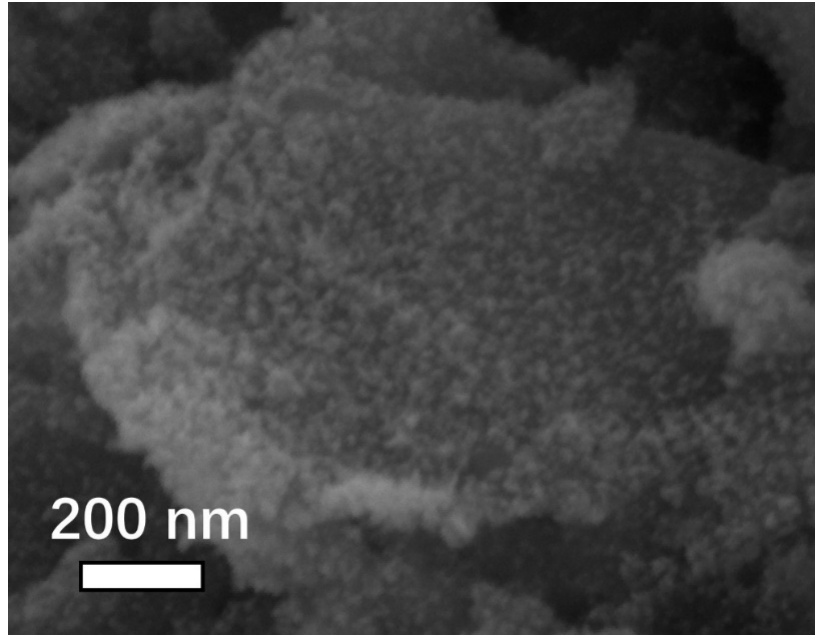
Figure 3.5. SEM micrographs of RuO$_2$-Ti$_3$C$_2$/NF.
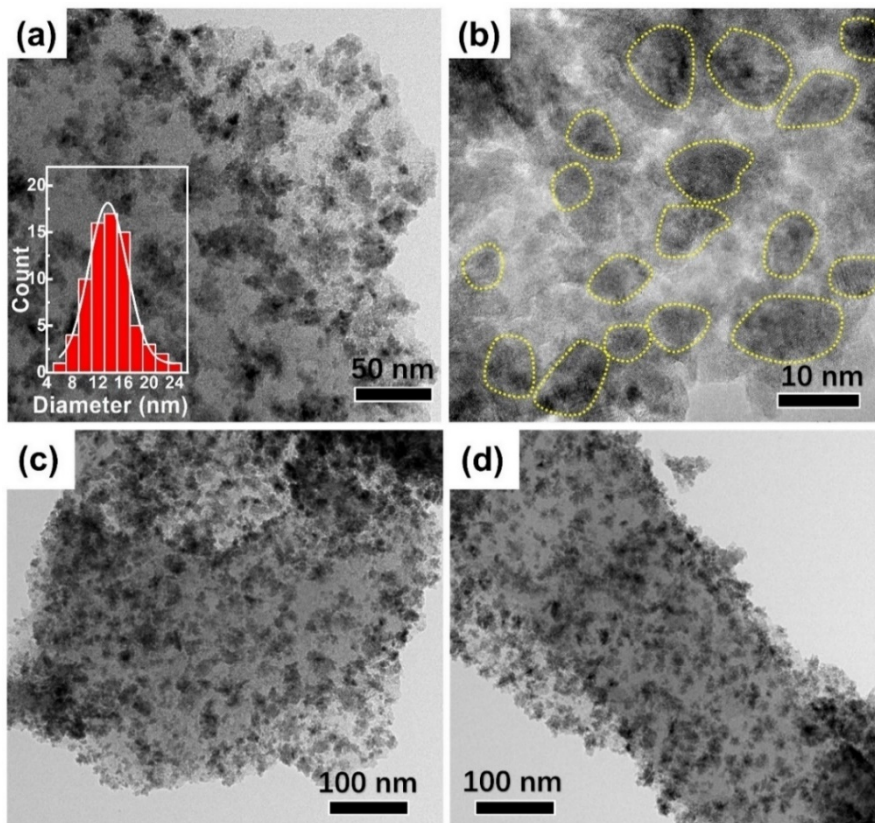

Figure 3.6. (a-d) TEM images of RuO$_2$-Ti$_3$C$_2$ (inset in **a** is the particle size

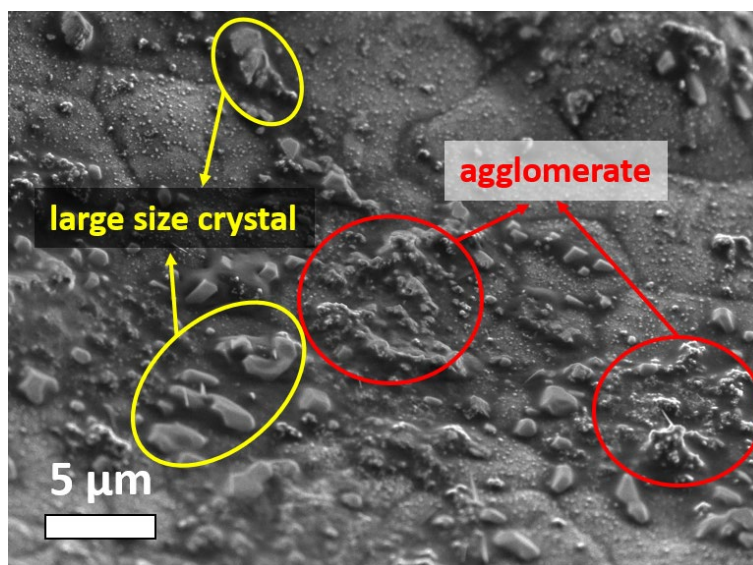distribution histogram of RuO$_2$ nanoparticles).

Figure 3.7. SEM image of RuO_2/NF.

Obviously, diffraction rings of Ti_3C_2 (006), Ni (111), and RuO_2 (211), (301), (202), and (321) could be easily evidenced in the selected area electron diffraction (SAED) plot (**Figure 3.8a**). High-resolution TEM (HRTEM) further revealed the phase structure of RuO_2-Ti_3C_2/NF. The typical fringe spacings of 0.25 nm in **Figure 3.8b** and 0.95 nm in **Figure 3.9** could be assigned to the (006) and (002) planes of Ti_3C_2 and 0.32 nm to the (110) diffraction plane of RuO_2.[5-7] The above results are corroborated by the XRD data, which will be analyzed in detail later. Moreover, the TEM dark-field image and corresponding element mapping analysis (**Figure 3.8c**) of RuO_2-Ti_3C_2/NF revealed uniform dispersion of Ru, O, Ti, and C, evidencing the effective integration of RuO_2 on the NF surface. A tiny loading quantity of Ru was confirmed by its content of merely 4.09 atom % determined by EDX analysis (**Figure 3.10**).
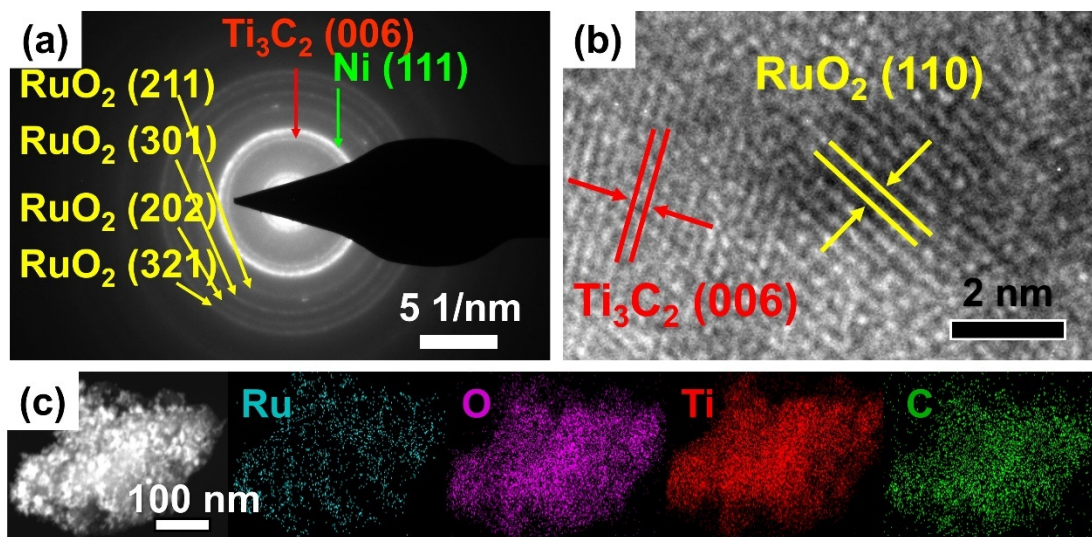
Figure 3.8. (**a**) SAED pattern, (**b**) HRTEM image and (**c**) HAADF-STEM image and EDS elemental (Ru, O, Ti and C) mappings of RuO_2-Ti_3C_2/NF.
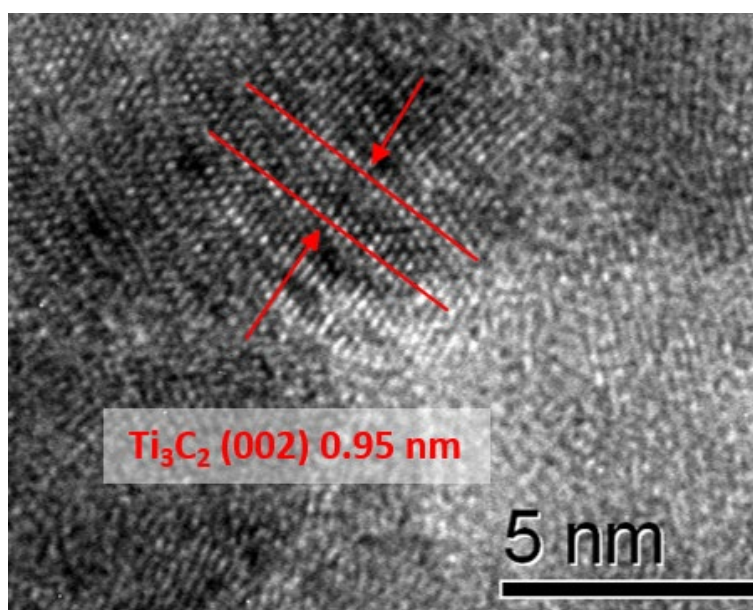

Figure 3.9. HRTEM image of RuO_2-Ti_3C_2/NF.

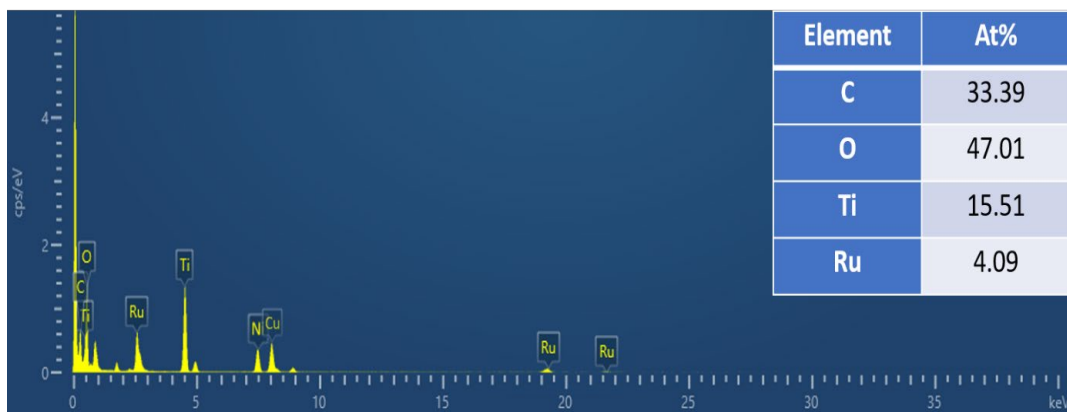| Element	At%
C	33.39
O	47.01
Ti	15.51
Ru	4.09

Figure 3.10. EDX spectrum of RuO_2-Ti_3C_2/NF; the inset corresponds to elemental composition.

The composition and crystal structure of Ti_3C_2/NF, RuO_2/NF, and RuO_2-Ti_3C_2/NF were examined by XRD analysis. As shown in **Figure 3.11**, the raw Ti_3AlC_2 MAX phase featured sharp peaks that match the standard 2θ degrees stated in the literature.[8] The strongest peak at $2\theta = 39°$ vanished after selective etching, indicating that all of the Al atoms in the lattice have been removed, and the peaks at (002) and (004) shifted to lower angles, suggesting that the interplanar spacing has increased, implying that Ti_3AlC_2 was fully transformed into Ti_3C_2 upon etching. Furthermore, the peak intensities of Ti_3C_2 MXene became substantially weaker, which can be attributed to the existence of thin layers.
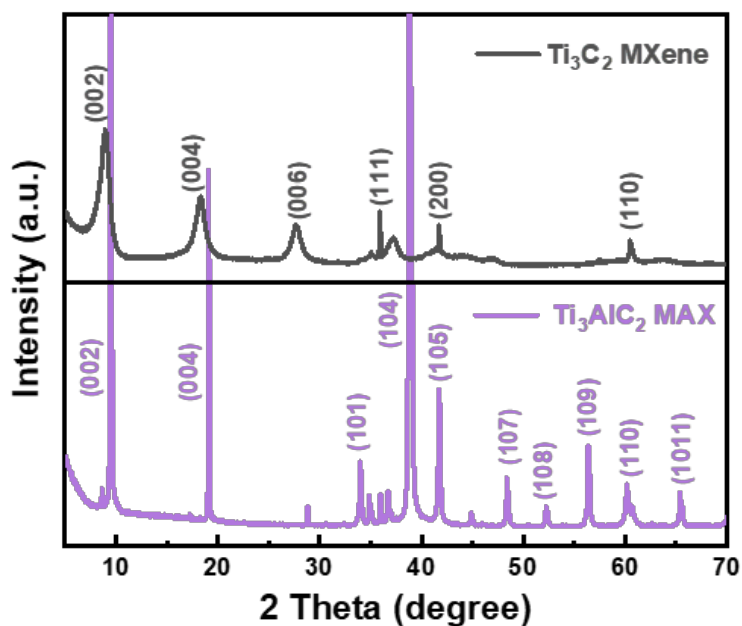
Figure 3.11. XRD patterns of Ti$_3$AlC$_2$ MAX and Ti$_3$C$_2$ MXene powder samples.

In addition, **Figure 3.12(a)** depicts also the XRD plots of Ti$_3$C$_2$/NF, RuO$_2$/NF and RuO$_2$-Ti$_3$C$_2$/NF, displaying diffraction peaks at 28.02° and 35.07° ascribed, respectively, to the (110) and (101) planes of RuO$_2$ (PDF #431027). The diffraction peaks of RuO$_2$ can still be identified, although their relative intensities are weak due to its presence in a low amount. The diffraction peaks were essentially undetectable (gray line in **Figure 3.12a**) when few-layer Ti$_3$C$_2$ MXene nanosheets were loaded on the surface of the NF framework. This is most likely due to the Ti$_3$C$_2$ nanosheets being excessively thin and considerably smaller than the distinctive Ni characteristic peaks. X-ray photoelectron spectroscopy (XPS) was utilized to validate the surface elemental composition of the Ti$_3$C$_2$/NF, RuO$_2$/NF, and RuO$_2$-Ti$_3$C$_2$/NF. The survey spectrum of Ti$_3$C$_2$ MXene powder obtained after Al etching, as shown in **Figure 3.13,** displayed peaks corresponding to F, O, Ti, C, and Cl elements.[9] Among them, F, O, and Cl originate from LiF and HCl etchants, which form -F, -OH, -Cl, and other polar functional groups on the surface of Ti$_3$C$_2$ MXene nanosheets, favoring electrostatic

interactions between Ti_3C_2 sheets and positively charged NF. Furthermore, there was no peak in the spectrum at the position corresponding to the Al element, indicating that the Al atomic layer has been totally removed. Core-level XPS plots of Ti 2p and Ru 3p of RuO_2-Ti_3C_2/NF are depicted in **Figure 3.12(c)** and **(d)** to verify the valence state of the elements on its surface. The Ti 2p spectrum was deconvoluted into four doublets representing Ti-C, Ti^{2+}, Ti^{3+}, and Ti^{4+}, whose 2p3/2 peaks are located at 455.8, 456.4, 457.2, and 458.2 eV, respectively, in accordance with the previous report on Ti_3C_2.[10] Likewise, the corresponding $2p_{1/2}$ orbital plots are also fitted with four species at 460.8, 461.8, 463.1, and 464.0 eV. On this basis, the components located at 462.5 and 485.1 eV corresponding to the $3p_{3/2}$ and $3p_{1/2}$ orbitals of Ru are also observed.[11, 12]
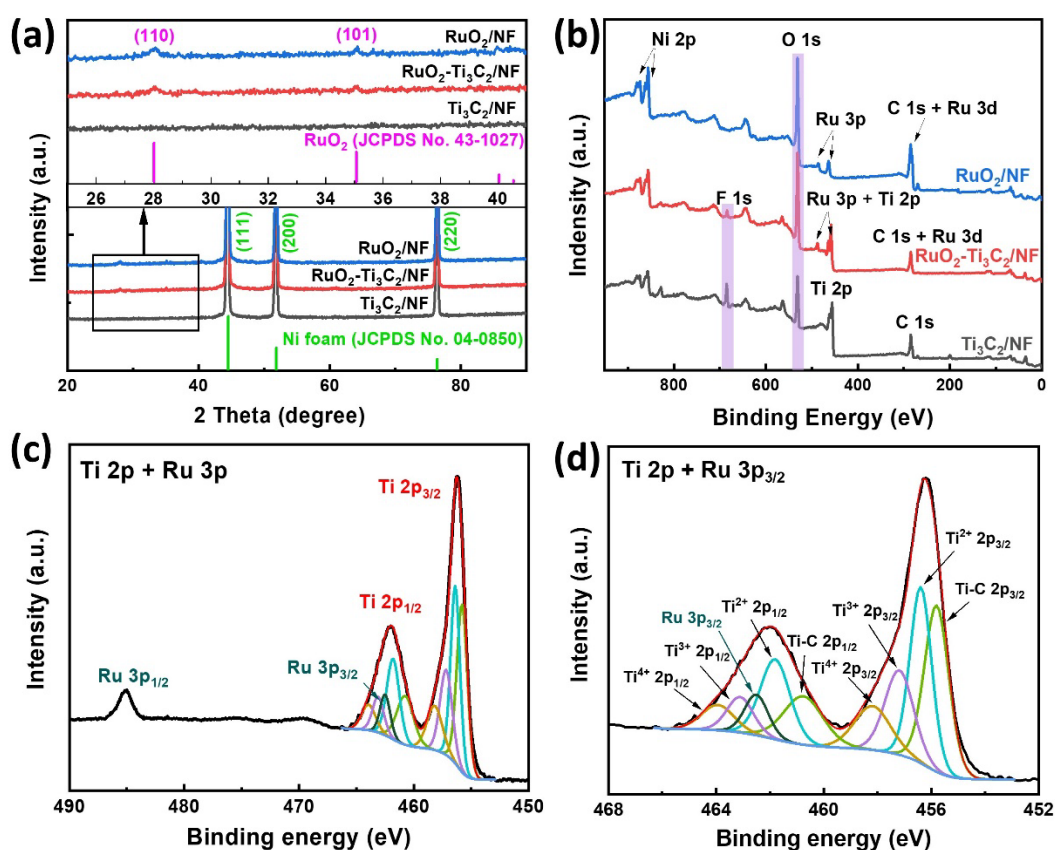

Figure 3.12. (a) X-ray diffractograms, **(b)** XPS survey spectra of Ti_3C_2/NF, RuO_2/NF and RuO_2-Ti_3C_2/NF, and core level XPS plots of **(c)** Ti 2p + Ru 3p and **(d)** Ti 2p + Ru

3p$_{3/2}$ of RuO$_2$-Ti$_3$C$_2$/NF.

According to the literature, these binding energies correspond to the +IV oxide valence state of ruthenium, further indicating that RuO$_2$ was synthesized on the Ti$_3$C$_2$ nanosheets.
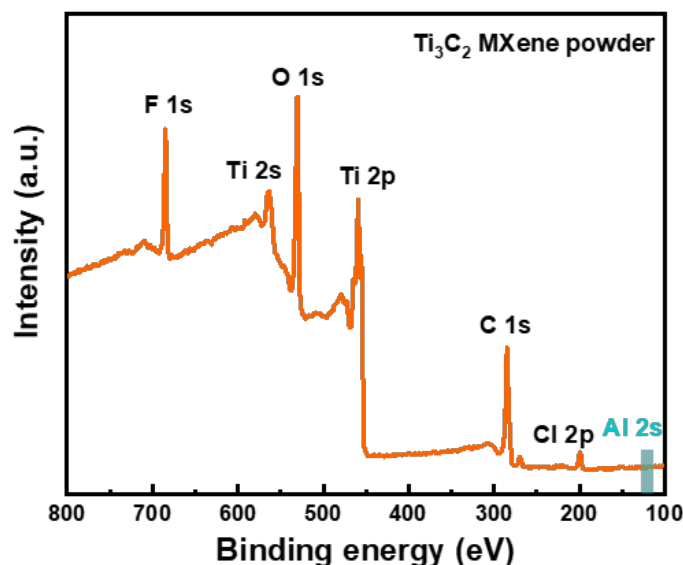

Figure 3.13. XPS survey scan of Ti$_3$C$_2$ MXene powder sample.

3.2.2 Hydrogen Evolution Reaction (HER).

A three-electrode device was applied to assess the electrocatalytic performance of NF, Ti$_3$C$_2$/NF, RuO$_2$/NF, and RuO$_2$-Ti$_3$C$_2$/NF. The performance of Pt/C (commercial catalyst) was also recorded as a supplementary benchmark for HER. **Figure 3.14(a)** shows the linear sweep voltammetry (LSV) curves with 85%-iR compensation performed in 1 M KOH solution of the above catalysts. The RuO$_2$-Ti$_3$C$_2$/NF electrocatalyst displayed remarkable HER activity, as compared with the others, even surpassing Pt/C (commercial). Inductively coupled plasma mass spectrometry (ICP-MS) analysis of RuO$_2$-Ti$_3$C$_2$/NF revealed that the content of ruthenium was only 0.02 wt.%, which was more than a hundred times lower than the loading mass of the Pt/C catalyst (1.6 mg/cm^2, 2.29 wt.%). This is the optimal loading mass with the highest activity for

commercial Pt/C/NF catalysts, and it is comparable with commercial catalytic performance reported in the literature.[1] In this work, RuO_2-Ti_3C_2/NF outperformed the Pt/C/NF activity with extremely minimal Ru loading, resulting in a low-cost catalyst.

As illustrated in **Figure 3.14(b)**, RuO_2-Ti_3C_2/NF required overpotentials of 20 and 85 mV to acquire, respectively, 10 and 100 mA cm^{-2}, which are significantly lower than those of Ti_3C_2/NF (150 and 299 mV) and RuO_2/NF (82 and 177 mV), demonstrating a notable increase of activity upon hybridization of Ti_3C_2 and RuO_2. RuO_2-Ti_3C_2/NF also featured the most favorable reaction kinetics among these electrocatalysts with a Tafel slope of 45.8 mV dec^{-1} (**Figure 3.16a**), outperforming Ti_3C_2/NF (141.5 mV dec^{-1}), RuO_2/NF (73.4 mV dec^{-1}), and Pt/C catalysts (62.6 mV dec^{-1}). The interfacial interaction of RuO_2 and Ti_3C_2 in the composite may shorten the electron/ion transport and mass diffusion channel, which is thought to be the cause of the rapid HER kinetics.
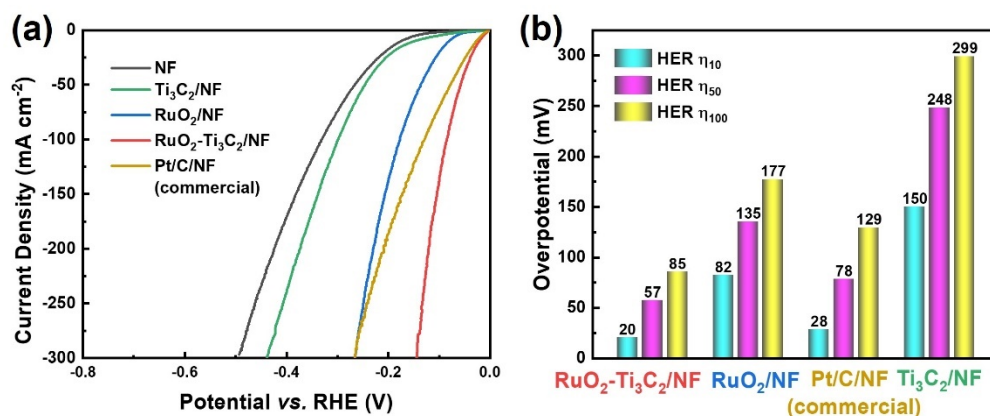

Figure 3.14. Electrocatalytic HER performance of the as-prepared catalysts: (**a**) LSV plots and (**b**) overpotentials at 10, 50, and 100 mA cm^{-2} for HER of NF, Ti_3C_2/NF, RuO_2/NF, RuO_2-Ti_3C_2/NF, and Pt/C/NF.

The HER performance of RuO_2-Ti_3C_2/NF composites, prepared using various electrochemical Ru deposition cycles, was evaluated as shown in **Figure 3.15(a,b)**, in

order to determine the loading mass of RuO_2 with the optimal activity. According to the LSV curves, the most prominent electrochemical signals for the HER were acquired for RuO_2-Ti_3C_2/NF with the same superiority for Tafel slopes. When the amount of deposited RuO_2 was insufficient (RuO_2-1/Ti_3C_2/NF), the nanoparticles were rarely detected on the Ti_3C_2 MXene sheets (**Figure 3.15c**), resulting in a lack of active sites for the catalytic process. In contrast, when the number of deposition cycles was above three (RuO_2-5/Ti_3C_2/NF), excessive development and accumulation of RuO_2 particles generated a thicker deposition layer, which not only blocked the transfer channel of charge and mass but also fell off, deteriorating durability. This was confirmed morphologically by SEM imaging, as shown in **Figure 3.15(d)**. The following electrochemical studies were thus performed on the optimal RuO_2-3/Ti_3C_2/NF.
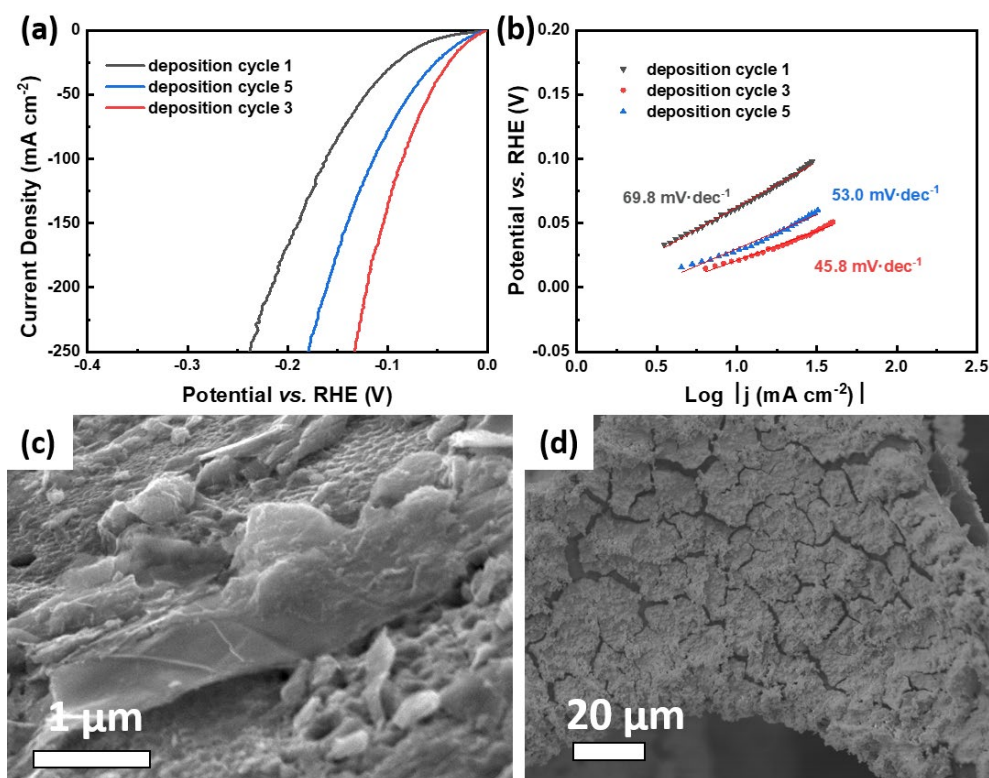

Figure 3.15. (**a**) LSV curves and (**b**) Tafel plots for HER of RuO_2-Ti_3C_2/NF prepared by 1, 3 or 5 deposition cycles of RuO_2 particles. SEM images of RuO_2-Ti_3C_2/NF prepared by (**c**) 1 and (**d**) 5 deposition cycles of RuO_2 particles.

In addition, as summarized in **Figure 3.16(b)** and **Table 3.1**, compared to the majority of other Ru- or Ti_3C_2-based electrocatalysts described thus far, the HER performance of RuO_2-Ti_3C_2/NF was not inferior. With the aim to understand the enhancement mechanism of RuO_2-Ti_3C_2/NF, the electron transport and transfer properties and electrochemically active surface area (ECSA) of various catalysts were investigated. The electrochemical impedance spectroscopy (EIS) was performed, and the Nyquist plots with a simplified equivalent circuit are displayed in **Figure 3.17**. According to this fitting model, RuO_2-Ti_3C_2/NF exhibited the most competitive charge-transfer kinetics as expected, which was inferred from the low charge transfer resistance (R_{ct}) of 1.21 Ω compared to Ti_3C_2/NF (15.06 Ω) and RuO_2/NF (3.67 Ω), as detailed in **Table 3.2**.
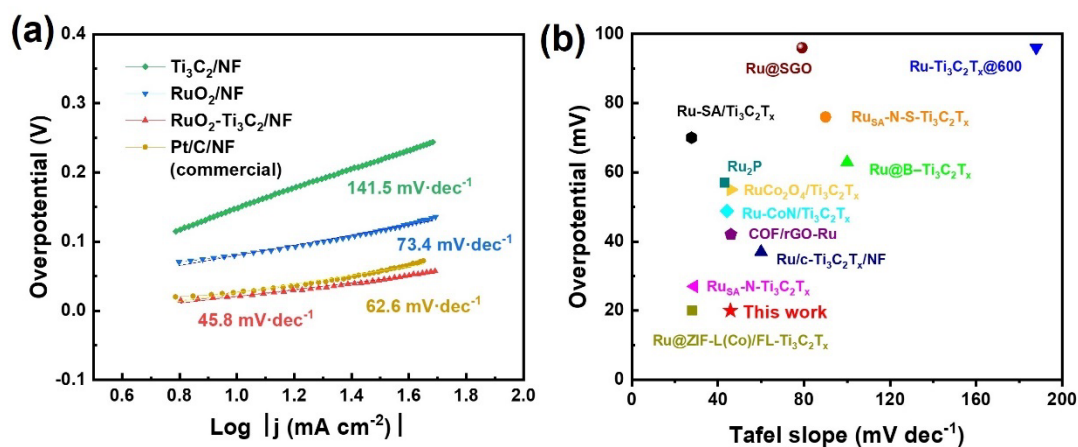

Figure 3.16. (**a**) Tafel plots of RuO_2-Ti_3C_2/NF, RuO_2/NF, Pt/C/NF and Ti_3C_2/NF. (**b**) Comparison of overpotentials (at 10 mA cm^{-2}) and Tafel slopes of RuO_2-Ti_3C_2/NF and other Ru-based HER catalysts (detailed in **Table 3.1**).

Table 3.1. Comparison of HER activity of RuO_2-Ti_3C_2/NF with recently reported Ru-based electrocatalysts in 1.0 M KOH electrolyte.

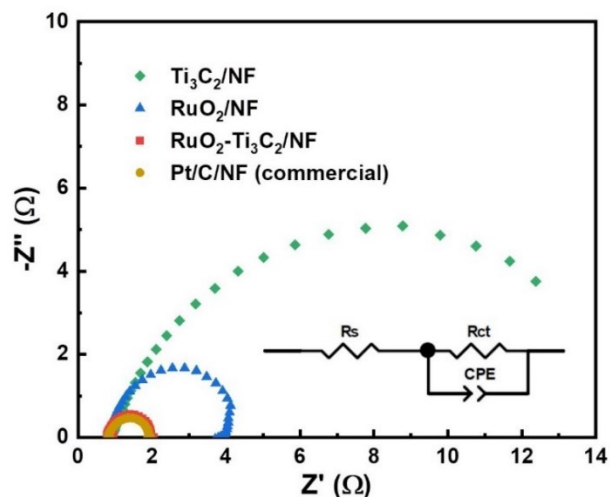| Electrocatalyst	Overpotential (mV) at 10 mA·cm^{-2}	Tafel slope (mV dec^{-1})	Reference
Ru@ZIF-L(Co)/FL-$Ti_3C_2T_x$	20	28	[13]
RuSA-N-S-$Ti_3C_2T_x$	76	90	[14]
Ru@B-$Ti_3C_2T_x$	62.9	100	[15]
Ru-$Ti_3C_2T_x$@600	96	187.9	[16]
Ru-CoN/$Ti_3C_2T_x$	48.8	44.1	[17]
RuSA-N-$Ti_3C_2T_x$	27	29	[18]
$RuCo_2O_4$/$Ti_3C_2T_x$	55	46	[19]
Ru-SA/$Ti_3C_2T_x$	70	27.7	[20]
Ru/c-$Ti_3C_2T_x$/NF	37	60	[21]
Ru@SGO	96	79	[22]
COF-rGO-Ru	42	46	[23]
Ru_2P	57	43	[24]
RuO_2-Ti_3C_2/NF	**20**	**45.8**	**This work**

Figure 3.17. Nyquist plots in the frequency range of 10^5 and 0.01 Hz

(detailed in **Table 3.2**) of Ti$_3$C$_2$/NF, RuO$_2$/NF, RuO$_2$-Ti$_3$C$_2$/NF, and Pt/C/NF.

Table 3.2. Solution resistance (R$_s$) and charge transfer resistance (R$_{ct}$) values of

Ti$_3$C$_2$/NF, RuO$_2$/NF, RuO$_2$-Ti$_3$C$_2$/NF and Pt/C.

Catalyst	R$_s$ (Ω)	R$_{ct}$ (Ω)
Ti$_3$C$_2$/NF	0.86	15.06
RuO$_2$/NF	0.83	3.67
RuO$_2$-Ti$_3$C$_2$/NF	0.78	1.21
Commercial Pt/C	0.82	1.12

As a measure of ECSA, **Figure 3.18(a)** depicts the double-layer capacitance (C$_{dl}$) values of Ti$_3$C$_2$/NF, RuO$_2$/NF, and RuO$_2$-Ti$_3$C$_2$/NF determined from the CV curves (**Figure 3.19**). After further calculation, RuO$_2$-Ti$_3$C$_2$/NF exhibited the largest ECSA among the tested catalysts up to 456.50 cm^{-2}, over four times greater than that of

Ti$_3$C$_2$/NF (110.75 cm^{-2}), considerably larger than that of RuO$_2$/NF (355.00 cm^{-2}) and higher than that of commercial Pt/C/NF catalysts (414.25 cm^{-2}). The values of C$_{dl}$ and ECSA are listed in **Table 3.3**. A catalyst is expected to perform well electrocatalytically if it owns a larger ESCA, as this measure is directly related to electrochemically active sites.[25] Even after normalizing the HER current density to the ECSA, the RuO$_2$-Ti$_3$C$_2$/NF electrocatalyst still featured the best performance (**Figure 3.18b**), which implies that RuO$_2$-Ti$_3$C$_2$/NF has the greatest intrinsic catalytic activity per unit ECSA. Additionally, during a 40 h galvanostatic study to assess catalytic durability, RuO$_2$-Ti$_3$C$_2$/NF revealed a minor drop of the current density in 1 M KOH (**Figure 3.20**). The LSV curve after the 40-h durability test almost overlapped with the original one, further testifying its stability.
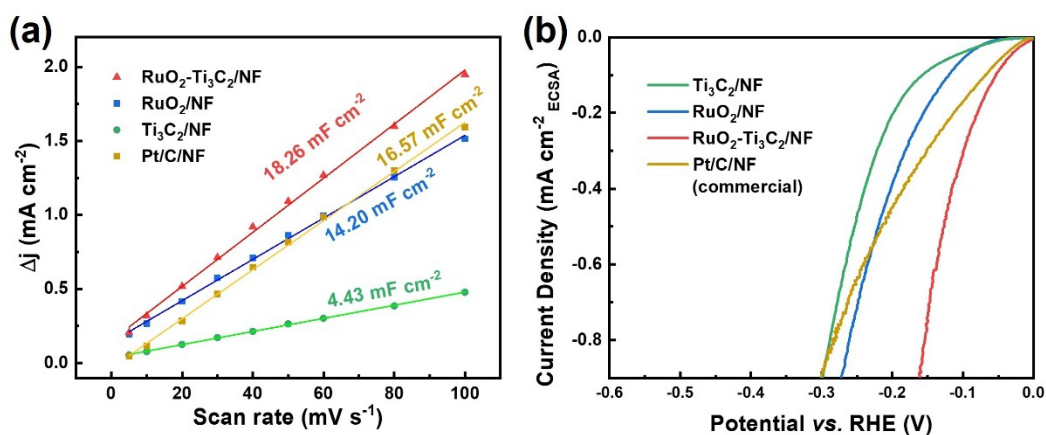

Figure 3.18 (**a**) Double layer capacitance (C$_{dl}$) and (**b**) ECSA-normalized HER polarization curves of Ti$_3$C$_2$/NF, RuO$_2$/NF, RuO$_2$-Ti$_3$C$_2$/NF, and Pt/C/NF..
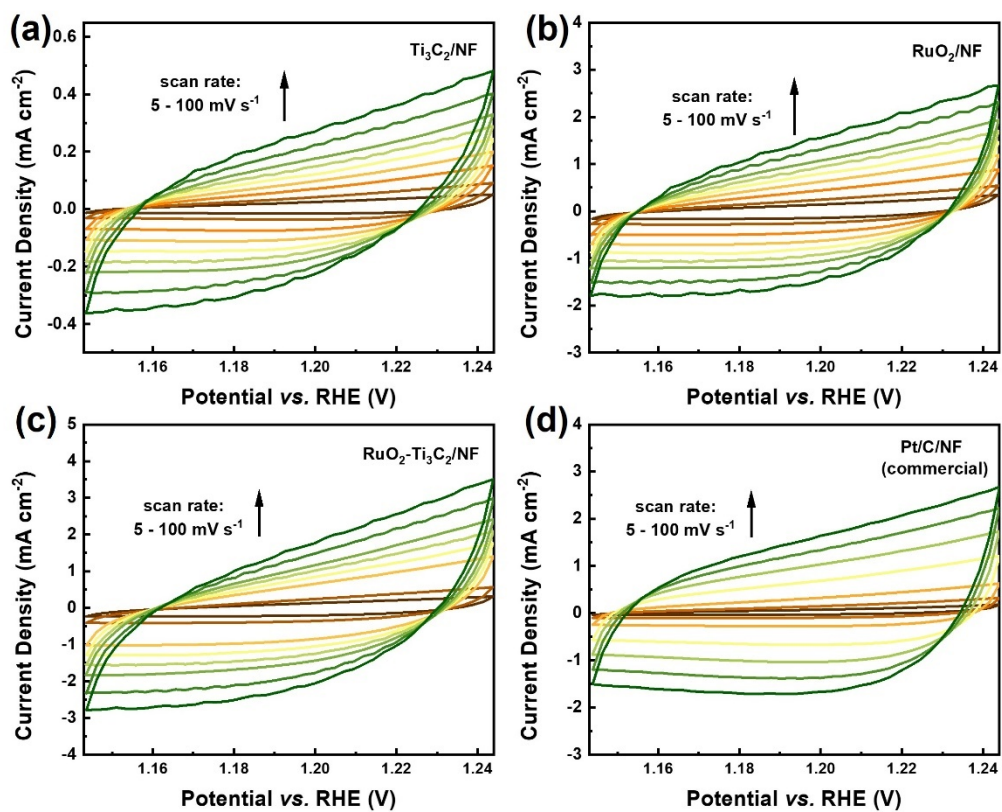
Figure 3.19. CV curves of (**a**) Ti_3C_2/NF, (**b**) Ti_3C_2/NF, (**c**) RuO_2-Ti_3C_2/NF and (**d**) Pt/C/NF in the non-Faradaic region of 1.145-1.245 V *vs.* RHE at various scan rates.

Table 3.3. C_{dl} and ECSAs of Ti_3C_2/NF, RuO_2/NF and RuO_2-Ti_3C_2/NF.

Catalyst	C_{dl} (mF cm^{-2})	ECSA (cm^{-2})
Ti_3C_2/NF	4.43	110.75
RuO_2/NF	14.20	355.00
RuO_2-Ti_3C_2/NF	18.26	456.50
Pt/C/NF	16.57	414.25
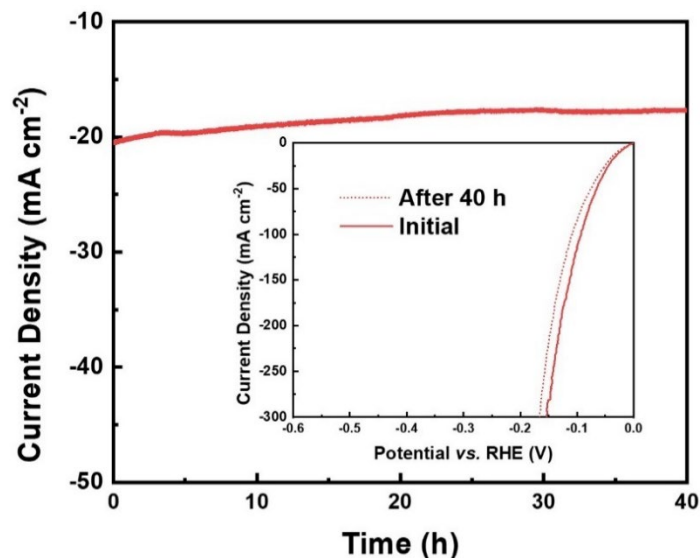
Figure 3.20. Chronoamperometry curves recorded at 20 mA cm^{-2} for 40 h. (**inset**: LSV curves of RuO$_2$-Ti$_3$C$_2$/NF before and after 40 h durability test).

3.2.3 Oxygen Evolution Reaction (OER).

As another essential half reaction, the oxygen evolution reaction (OER) performance of NF, Ti$_3$C$_2$/NF, RuO$_2$/NF, and RuO$_2$-Ti$_3$C$_2$/NF was also assessed and compared with commercial RuO$_2$ catalyst as the benchmark, as presented in **Figure 3.21(a)**.

As expected, RuO$_2$-Ti$_3$C$_2$/NF displayed the most enhanced activity with an overpotential of 351 mV to attain 100 mA cm^{-2}, which is smaller than that of Ti$_3$C$_2$/NF, RuO$_2$/NF, and even commercial RuO$_2$. More details about the overpotentials acquired at different current densities can be found in **Figure 3.21(b)**. Similar to the HER, their Tafel slopes for the OER were also determined, as shown in **Figure 3.21(c)**. The RuO$_2$-Ti$_3$C$_2$/NF showed better kinetics with a Tafel slope of 127.5 mV dec^{-1}, as compared to that of Ti$_3$C$_2$/NF (135.8 mV dec^{-1}) and RuO$_2$/ NF (129.4 mV dec^{-1}) and near that of commercial RuO$_2$ catalyst (98.3 mV de^{-1}). In terms of charge transfer capability, the

Nyquist plots, acquired for the above catalysts (**Figure 3.21d**), revealed a similar trend. The measured semicircle curve of RuO_2-Ti_3C_2/NF has the lowest diameter, meaning the smallest R_{ct} (1.40 Ω) among the prepared catalysts (the specific values of R_{ct} and R_s are summarized in **Table 3.4**). It is worth noting that an oxidation peak of up to 50 mA cm^{-2} is visible in the LSV curve. After examining the entire redox process (CV curves depicted in **Figure 3.22a**), a symmetrical reduction peak was observed in the reduction process, indicating that these peaks are in fact due to Ni(II)/Ni(III) redox peaks. A 40-h stability test at a current density of 20 mA cm^{-2} was performed according to the measured CV curve in **Figure 3.22(a)**. **Figure 3.22(b)** attests that the attenuation of the current after the durability test is negligible, and the LSV curve (inset in **Figure 3.22b**) remained practically the same as before, demonstrating the catalyst's stability.
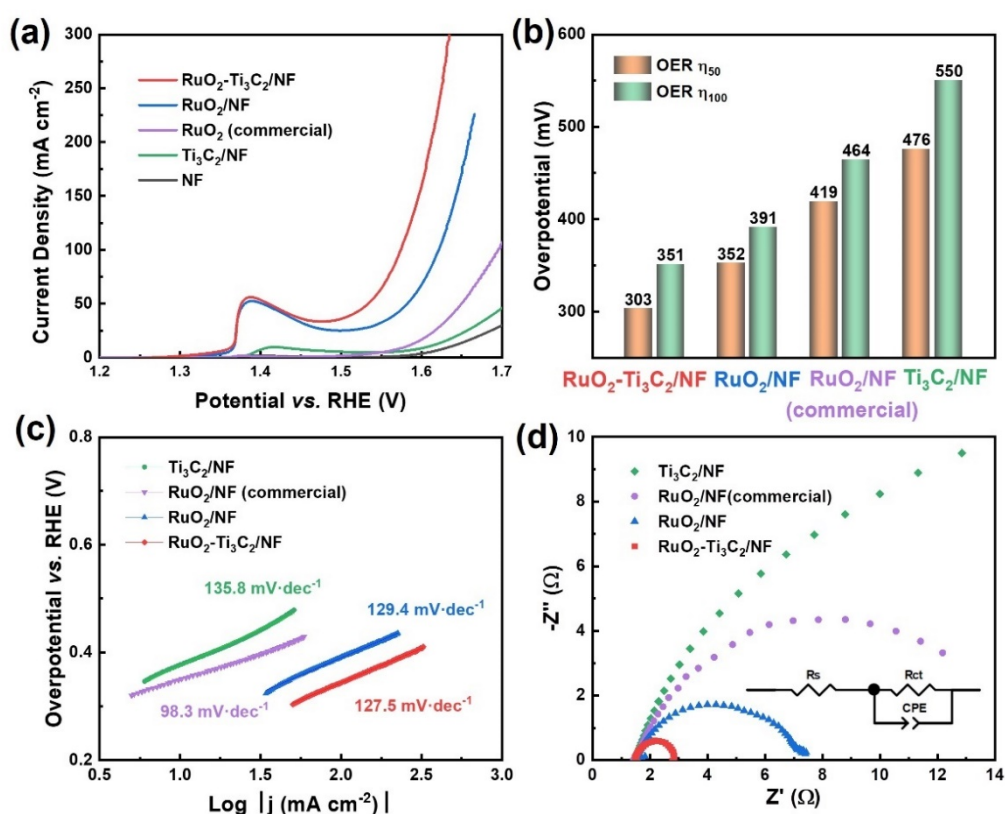

Figure 3.21. Electrocatalytic OER activity of the as-prepared catalysts: (**a**) LSV curves, (**b**) Overpotentials at 50 and 100 mA cm^{-2} for OER, (**c**) Tafel plots, (**d**)

Nyquist plots in the frequency range of 105 and 0.01 Hz of NF, Ti_3C_2/NF, RuO_2/NF, RuO_2, and RuO_2-Ti_3C_2/NF.

Table 3.4. Solution resistance (R_s) and charge transfer resistance (R_{ct}) values of Ti_3C_2/NF, RuO_2/NF, RuO_2-Ti_3C_2/NF and Pt/C.

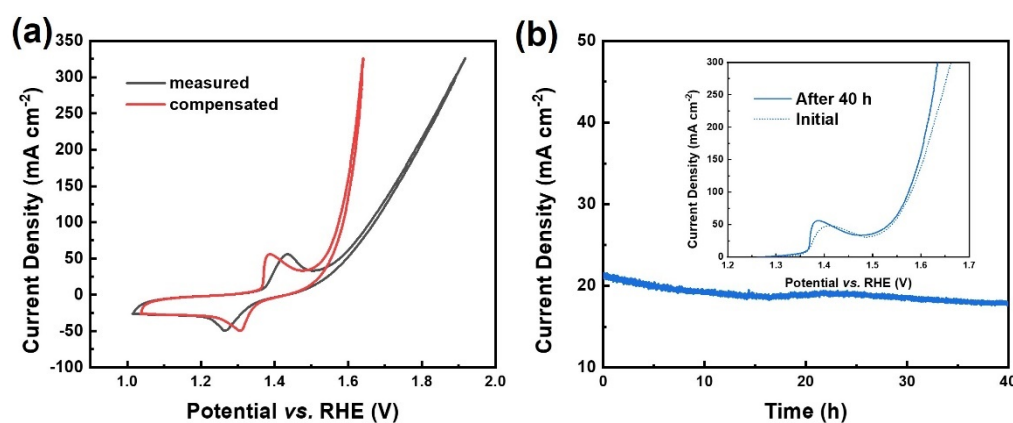| Catalyst	R_s (Ω)	R_{ct} (Ω)
Ti_3C_2/NF	1.46	31.51
RuO_2/NF	1.42	5.88
RuO_2-Ti_3C_2/NF	1.49	1.40
Commercial RuO_2	1.49	13.06

Figure 3.22. (**a**) The real measured CV curve (black) and the CV curve after iR-compensation (red) of RuO_2-Ti_3C_2/NF for OER. (**b**) Chronoamperometry curves recorded at 20 mA cm^{-2} for 40 h (inset: LSV curves of RuO_2-Ti_3C_2/NF before and after 40 h durability test).

3.2.4 Overall Water and Seawater Splitting.

To investigate the applicability of RuO_2-Ti_3C_2/NF for hydrogen generation from seawater splitting, LSV curves for HER and OER tests in 1 M KOH, 1 M KOH + 0.5 M NaCl (simulated seawater), and 1 M KOH seawater are recorded (**Figure 3.23a**). It could be observed that despite the LSV curves of RuO_2-Ti_3C_2/NF for HER and the OER experiencing a slight negative shift for HER and positive for OER in both simulated and actual seawater, the catalyst was able to achieve a high catalytic activity. Only low overpotentials of 156 mV for the HER and 378 mV for the OER were necessary for RuO_2-Ti_3C_2/NF to drive a current density of 100 mA cm^{-2} in seawater. Compared to its overpotentials in 1 M KOH (85 mV for HER and 351 mV for OER) and 1 M KOH + 0.5 M NaCl (117 mV for HER and 352 mV for OER), the incremental values are acceptable (**Figure 3.23b**). In particular, the overpotential for the OER was substantially lower than the theoretical value (480 mV) of the chlorine electro-oxidation reaction (ClOR), indicating that the RuO_2-Ti_3C_2/NF catalyst may efficiently avoid ClOR during the real seawater splitting process.

Additionally, **Figure 3.23(c)** displays the i-t curve of RuO_2-Ti_3C_2/NF for HER and OER at 20 mA cm^{-2} recorded for 40 h in seawater, which showed little current attenuation on both the anode and cathode, attesting the good electrochemical stability of the RuO_2-Ti_3C_2/NF bifunctional catalyst. Noteworthy is the fact that the attenuation of HER was more pronounced than OER, which could be ascribed to the twice gas production on the cathode.
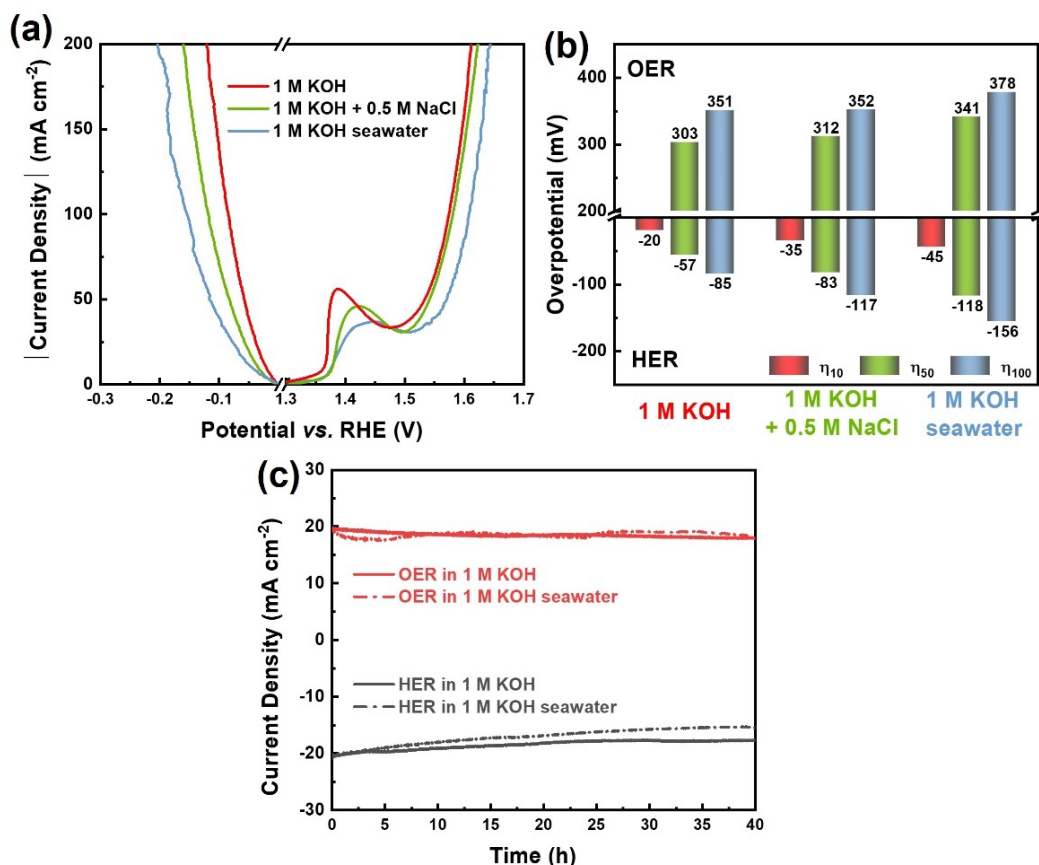
Figure 3.23. (**a**) LSV plots of RuO_2-Ti_3C_2/NF for HER and OER in 1 M KOH, 1 M KOH + 0.5 M NaCl, and 1 M KOH seawater electrolytes. (**b**) Overpotential of RuO_2-Ti_3C_2/NF in the above electrolytes at 10, 50, and 100 mA cm^{-2} for HER and OER. (**c**) Chronoamperometry i-t plots of 40 h for HER and OER in 1 M KOH and 1 M KOH seawater.

To scrutinize the corrosion resistance of the RuO_2-Ti_3C_2/NF electrode in saline environments, corrosion polarization curves were acquired before and after the extended stability tests for the HER and the OER, as illustrated in **Figure 3.24**. The initial corrosion potential (E_{corr}) of the RuO_2-Ti_3C_2/NF electrode was 0.55 V, accompanied by a corrosion current density (i_{corr}) of 1.21 mA cm^{-2}. Remarkably, no significant shift in E_{corr} and i_{corr} was observed after a 40-h catalytic process in seawater,

suggesting that the RuO$_2$-Ti$_3$C$_2$/NF electrode retained its corrosion resistance throughout the duration of the test.
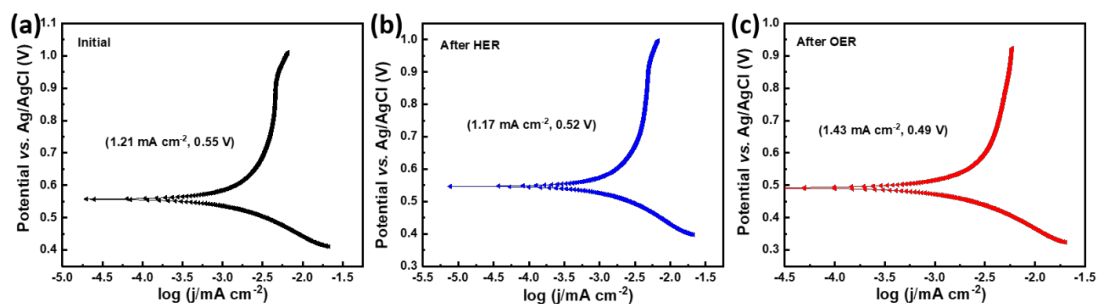

Figure 3.24. Corrosion polarization curves of RuO$_2$-Ti$_3$C$_2$/NF before (**a**), after HER (**b**) and OER (**c**) for 40 h in 1M KOH seawater.

The seawater electrolyte utilized during OER long-time stability test was further analyzed using the *N,N*-diethyl-phenylenediamine (DPD) reagent to check if any hypochlorite (ClO$^-$) was generated in order to further validate that no ClOR occurred. Iodide is converted to iodine by ClO$^-$, and iodine then oxidizes DPD to a species that is pink in color,[26] as shown in **Figure 3.25**, with visible color development even at very low concentrations (10^{-4} M) of ClO$^-$. Interestingly, the reagent did not manifest any color change in the seawater electrolyte upon a 40-h long-time stability OER test, testifying that the OER did not result in the formation of hypochlorite.
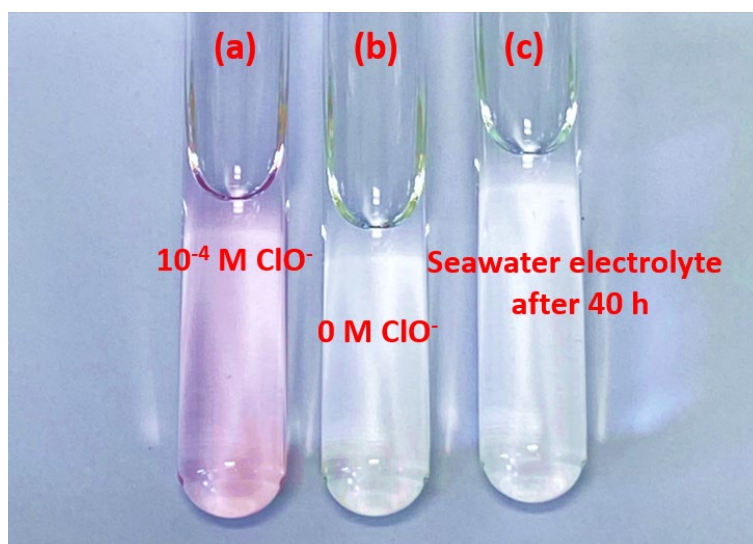
Figure 3.25. Photographs of (**a**) 10^{-4} M, (**b**) 0 M NaClO solution and (**c**) seawater electrolytes after a 40-h long-time stability OER test.

Considering the good HER and OER activities of RuO$_2$-Ti$_3$C$_2$/NF not only in 1 M KOH but also in 1 M KOH + 0.5 M NaCl and 1 M KOH seawater, its potential as a bifunctional catalyst for total seawater splitting deserves further investigation. In order to achieve total water splitting, a two-electrode electrolyzer was constructed employing RuO$_2$-Ti$_3$C$_2$/NF as both the anode and cathode (**Figure 3.26a**). As anticipated, the electrolyzer demonstrated good activity for total water splitting in alkaline pure water and seawater electrolytes, as depicted in **Figure 3.26(b)**. The RuO$_2$-Ti$_3$C$_2$/NF based electrolyzer required 1.82 V to drive a current density of 100 mA cm^{-2} in a 1 M KOH solution, a value significantly lower than the voltage necessary for the commercial Pt/C || RuO$_2$ cell (1.95 V). Moreover, the RuO$_2$-Ti$_3$C$_2$/NF (+, −) cell necessitated a voltage of 1.84 V to acquire 100 mA cm^{-2} in 1 M KOH saltwater for total seawater splitting (**Figure 3.26b**, **Table 3.5**). Furthermore, the durability for total seawater splitting was studied by multistage chronopotentiometry, as shown in **Figure 3.26c**. When the voltage was increased or decreased (from 1.5 to 1.9 V and back to 1.5 V), the current

responded in time and could remain almost constant in every stage within 10000 s. The whole stability test lasted up to 25 h, demonstrating the electrochemical stability of the RuO$_2$-Ti$_3$C$_2$/NF (+, −) cell for total water spitting in both alkaline pure water and saltwater.
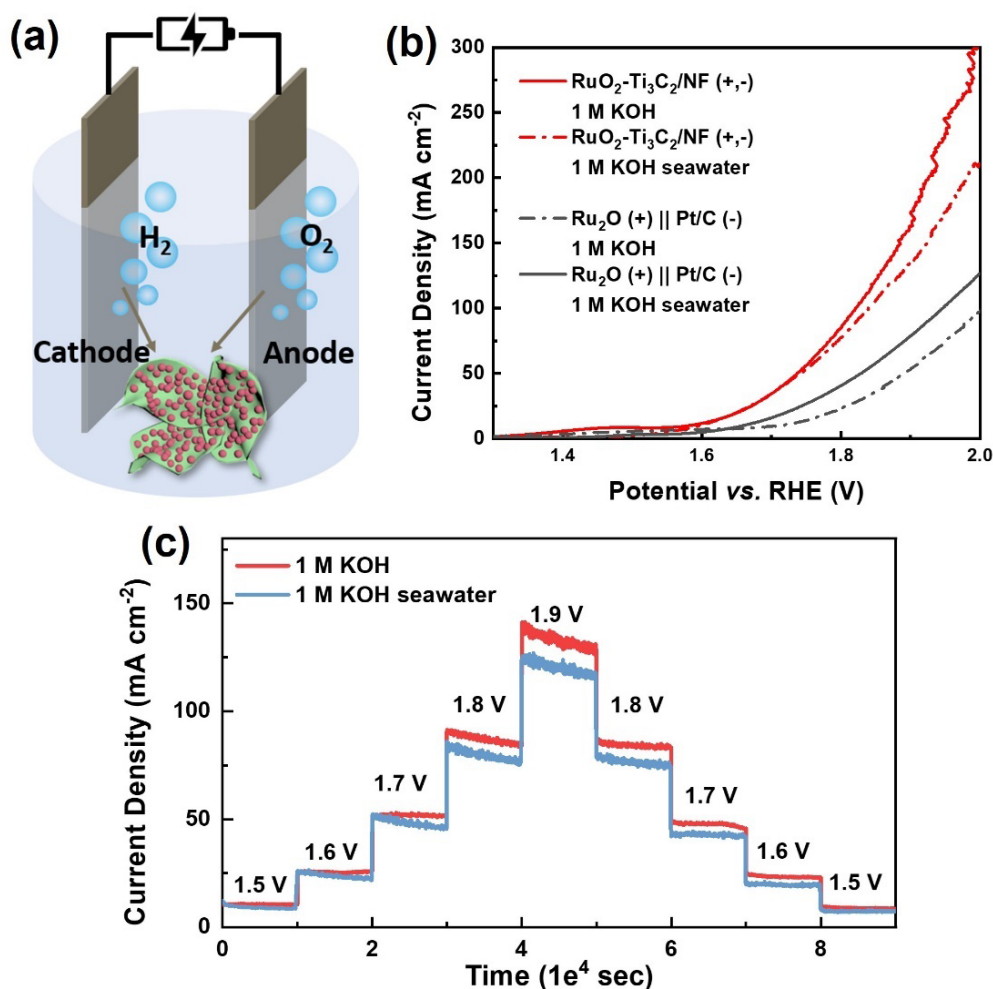

Figure 3.26. (**a**) Schematic of the overall water-splitting system. (**b**) Polarization curves of RuO$_2$-Ti$_3$C$_2$/NF (+, −) and commercial RuO$_2$ (+) || Pt/C (−) in 1 M KOH and 1 M KOH seawater in a two-electrode system for overall water splitting. (**c**) Multipotential stability test: i-t curves of RuO$_2$-Ti$_3$C$_2$/NF (+, −) in 1 M KOH and 1 M KOH seawater.

Table 3.5. Comparison of RuO_2-Ti_3C_2/NF for overall water splitting with previously reported electrocatalysts.

Electrocatalyst	Potential (V) for 100 mA·cm^{-2}	Electrolyte	Reference
$Ni_xB/B_4C/B$-C_{PR}/NF	1.88	1 M KOH	27
	1.95	1 M KOH seawater	
Mn-doped Ni_2P/Fe_2P	1.8	1 M KOH	28
	1.84	1 M KOH seawater	
Ru MOF CoFe	1.62	1 M KOH	29
	1.7	1 M KOH seawater	
asymmetric Co-N_3P_1	2.07	1 M KOH seawater	30
Er-MoO_2	2.2	1 M KOH seawater	31
CoB@MOF@CC	1.87	simulated seawater	32
RuO_2-C-300	1.7 for 33 mA·cm^{-2}	1 M KOH seawater	33
CoS_2-MoS_2/CC	> 2.5	simulated seawater	34
RuO_2-Ti_3C_2/NF	**1.82**	**1 M KOH**	**This work**
	1.84	**1 M KOH seawater**	

Last but not least, SEM and XPS were conducted to examine the stability of the RuO_2-Ti_3C_2/NF catalyst after a multipotential stability test in 1 M KOH seawater electrolyte in terms of microscopic morphology and chemical composition. The microstructure of the RuO_2 nanoparticle and Ti_3C_2 MXene nanosheet was well-

preserved following either the HER or the OER as seen in **Figure 3.27**, demonstrating its superior corrosion resistance and mechanical stability in saltwater. As shown in **Figure 3.28**, the Ru $3p_{1/2}$ peak location of the RuO_2-Ti_3C_2/NF catalyst did not change much over a protracted OER process, showing that its valence state was not affected. However, the peak intensity decreased slightly, and this, together with the fact that the peak intensity of lattice oxygen also diminished during the OER process (**Figure 3.29**), indicates that RuO_2 was dissolved to some extent. Of note, the peak intensity of oxygen vacancies, which participate actively in catalytic processes,[35, 36] in the high-resolution spectrum of the O 1s (**Figure 3.29**) was not affected after HER but rather increased dramatically after OER. As a result, the chemical composition stability of the RuO_2-Ti_3C_2/NF catalyst was confirmed further in seawater electrolyte.
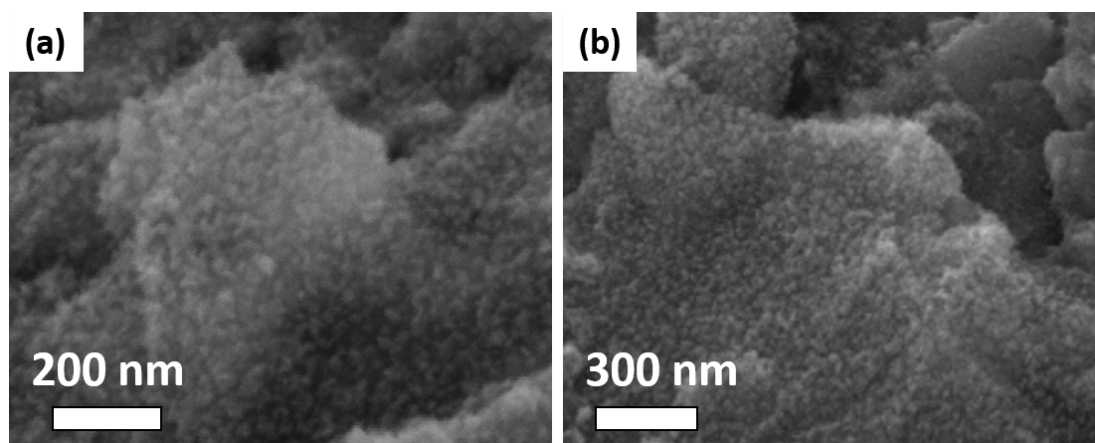

Figure 3.27. SEM images of RuO_2-Ti_3C_2/NF after (**a**) HER and (**b**) OER multipotential stability tests in 1M KOH seawater.

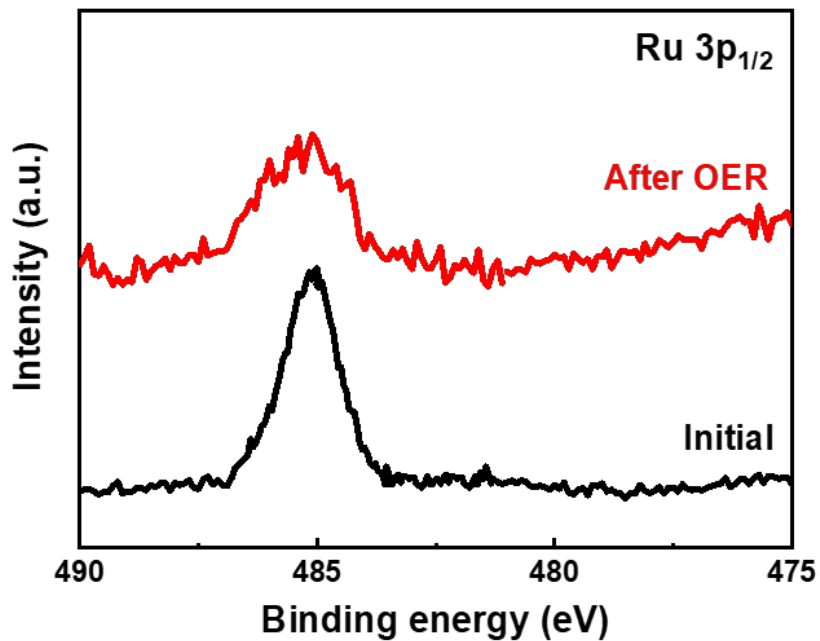**Figure 3.28.** XPS core level spectra of the Ru $3p_{1/2}$ of RuO_2-Ti_3C_2/NF before (black) and after (red) OER multipotential stability tests in 1 M KOH seawater.
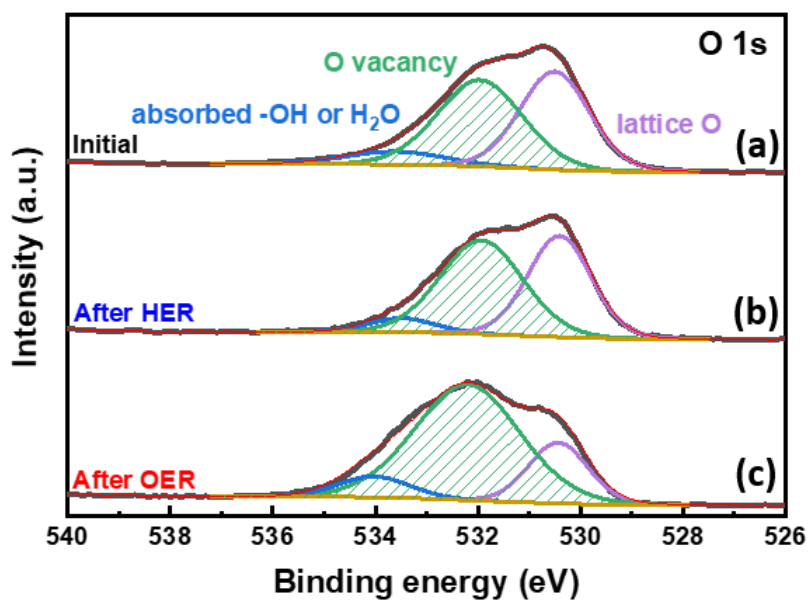

Figure 3.29. XPS core level spectra of the O 1s of RuO_2-Ti_3C_2/NF before (**a**), and after (**b**) HER and (**c**) OER multipotential stability tests in 1M KOH seawater.

From the above electrochemical results, it is critical to determine the Faradaic efficiency (FE) by measuring the real gas production rate if the catalyst can be used in practice. For this purpose, the gases produced on the anodic (O_2) and cathodic (H_2) electrodes were collected in alkaline seawater utilizing a drainage approach. **Figure 3.30(a)** depicts the setup, with purple-red liquid burets measuring the volume of generated H_2 and the orange one measuring O_2. The measurement period was 1800 s, and the input constant current density was 30 mA cm^{-2}.

Figure 3.30(b) depicts the quantities of O_2 and H_2 produced at various periods, whose corresponding specific values were charted in **Figure 3.30(c)**. At the end of the measurement, the volumes of H_2 and O_2 gas were 6.5 and 3.2 mL, respectively, with a ratio of 2.03:1, in line with the theoretical value of 2:1. After calculation, the FEs for HER and OER were 96.44% and ~100%, respectively, confirming the excellent dual-functional electrocatalytic activity of RuO_2-Ti_3C_2/NF and that no evident side reactions took place even in seawater electrolytes.
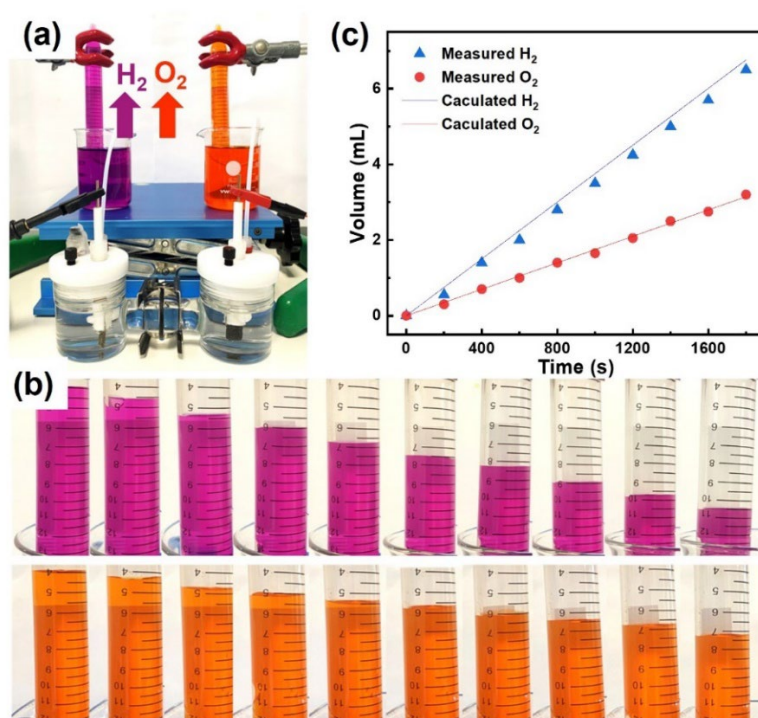

Figure 3.30. (a) Device for monitoring gas production *via* the drain method. **(b)** The

volume of gas produced at the anode and cathode at various periods. (**c**) A comparison of the quantities of experimental and theoretical H_2 and O_2 gaseous products *vs.* time.

Moreover, solar panels with a voltage of 2 V were used as the power source for the seawater electrocatalytic cells, and countless bubbles were generated on the surface of the electrodes (**Figure 3.31 a-b**). According to the above discussion, RuO_2-Ti_3C_2/NF is believed to be a reliable and effective electrocatalyst for overall seawater splitting.
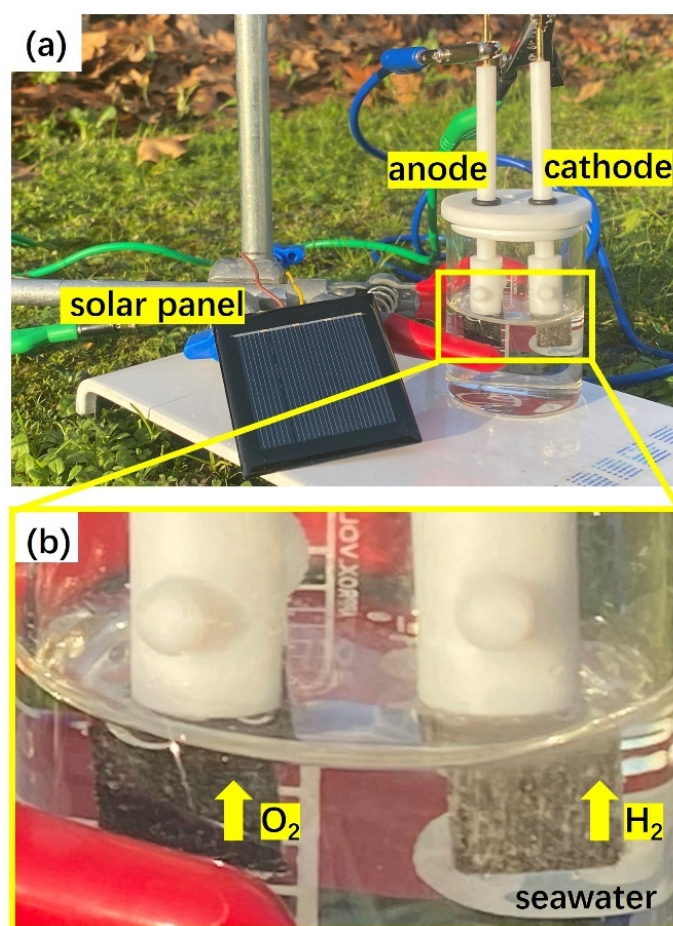

Figure 3.31. (**a**) The photo of overall seawater splitting powered by solar panels (2 V). (**b**) The enlarged view of (**a**) with obvious bubbles.

3.3 Conclusion

In summary, tiny RuO_2 particles were grown *via* an electrodeposition method on single- or few-layered Ti_3C_2 sheets loaded on nickel foam (RuO_2-Ti_3C_2/NF). The prepared RuO_2-Ti_3C_2/NF had an open nanostructure that promotes the transport of charge and mass, thereby improving the catalytic activity and reducing the overpotential and ultimately effectively avoiding chlorine poisoning in the complex ion condition of seawater. The RuO_2-Ti_3C_2/NF featured remarkable performance for HER, OER, and overall water splitting not only in KOH electrolyte, but also in simulated seawater and real seawater. Furthermore, with a stability of 25 h in overall seawater splitting and a Faradaic efficiency of almost 100%, the catalyst demonstrated its applicability in the field of seawater electrolysis. Owing to its high catalytic activity for hydrogen generation by saltwater electrolysis, it presents an effective solution to the energy problem in places with limited freshwater supplies.

References

(1) Yang, M.; Shi, B.; Tang, Y.; Lu, H.; Wang, G.; Zhang, S.; Sarwar, M. T.; Tang, A.; Fu, L.; Wu, M.; et al. Interfacial Chemical Bond Modulation of $Co_3(PO_4)_2$-MoO_{3-x} Heterostructures for Alkaline Water/Seawater Splitting. *Inorganic Chemistry* **2023**, *62* (6), 2838-2847.

(2) Hausmann, J. N.; Schlögl, R.; Menezes, P. W.; Driess, M. Is direct seawater splitting economically meaningful? *Energy & Environmental Science* **2021**, *14* (7), 3679-3685.

(3) Tang, Y.; Liu, Q.; Dong, L.; Wu, H. B.; Yu, X.-Y. Activating the Hydrogen Evolution and Overall Water Splitting Performance of NiFe LDH by Cation Doping and Plasma Reduction. *Applied Catalysis B: Environmental* **2020**, *266*, 118627.

(4) Hu, C.; Huang, Y. Cyclic Voltammetric Deposition of Hydrous Ruthenium Oxide for Electrochemical Capacitors. *Journal of the Electrochemical Society* **1999**, *146* (7), 2465-2471.

(5) Wu, Y.; Yao, R.; Zhao, Q.; Li, J.; Liu, G. La-RuO$_2$ Nanocrystals with Efficient Electrocatalytic Activity for Overall Water Splitting in Acidic Media: Synergistic Effect of La Doping and Oxygen Vacancy. *Chemical Engineering Journal* **2022**, *439*, 135699.

(6) Zhang, D.; Mi, Q.; Wang, D.; Li, T. MXene/Co$_3$O$_4$ Composite Based Formaldehyde Sensor Driven by ZnO/MXene Nanowire Arrays Piezoelectric Nanogenerator. *Sensors and Actuators B: Chemical* **2021**, *339*, 129923.

(7) Tie, L.; Li, N.; Yu, C.; Liu, Y.; Yang, S.; Chen, H.; Dong, S.; Sun, J.; Dou, S.; Sun, J. Self-Supported Nonprecious MXene/Ni$_3$S$_2$ Electrocatalysts for Efficient Hydrogen Generation in Alkaline Media. *ACS Applied Energy Materials* **2019**, *2* (9), 6931-6938.

(8) Cheng, L.; Chen, Q.; Li, J.; Liu, H. Boosting the Photocatalytic Activity of CdLa$_2$S$_4$ for Hydrogen Production using Ti$_3$C$_2$ MXene as a Co-catalyst. *Applied Catalysis B: Environmental* **2020**, *267*, 118379.

(9) Zhang, Y.; Zhang, Z.; Addad, A.; Wang, Q.; Roussel, P.; Amin, M. A.; Szunerits, S.; Boukherroub, R. 0D/2D Co$_3$O$_4$/Ti$_3$C$_2$ MXene Composite: A Dual-Functional Electrocatalyst for Energy-Saving Hydrogen Production and Urea Oxidation. *ACS Applied Energy Materials* **2022**, *5* (12), 15471-15482.

(10) Gao, X. T.; Xie, Y.; Zhu, X. D.; Sun, K. N.; Xie, X. M.; Liu, Y. T.; Yu, J. Y.; Ding, B. Ultrathin MXene Nanosheets Decorated with TiO$_2$ Quantum Dots as an Efficient Sulfur Host toward Fast and Stable Li-S Batteries. *Small* **2018**, *14* (41), e1802443.

(11) Zhang, B.; Shan, J.; Wang, X.; Hu, Y.; Li, Y. Ru/Rh Cation Doping and Oxygen-Vacancy Engineering of FeOOH Nanoarrays@Ti$_3$C$_2$T$_x$ MXene Heterojunction for Highly Efficient and Stable Electrocatalytic Oxygen Evolution. *Small* **2022**, *18* (25), e2200173.

(12) Hu, Y.; Zhou, J.; Sun, X.; Chen, J.; Li, B.; Wang, Y.; Wang, N. Ru-RuO$_2$ Nanoparticles Decorated on Various Substrates via Reduction-Hydrolysis Strategy for Boosting Overall Water-Splitting Performance. *ChemCatChem* **2022**, *14* (24), e202201010

(13) Luo, R.; Li, Z.; Li, R.; Jiang, C.; Qi, R.; Liu, M.; Lin, H.; Huang, R.; Luo, C.; Peng, H. Ultrafine Ru Nanoparticles Derived from Few-layered Ti$_3$C$_2$T$_x$ MXene Templated

MOF for Highly Efficient Alkaline Hydrogen Evolution. *International Journal of Hydrogen Energy* **2022**, *47* (77), 32787-32795.

(14) Ramalingam, V.; Varadhan, P.; Fu, H. C.; Kim, H.; Zhang, D.; Chen, S.; Song, L.; Ma, D.; Wang, Y.; Alshareef, H. N.; et al. Heteroatom-Mediated Interactions between Ruthenium Single Atoms and an MXene Support for Efficient Hydrogen Evolution. *Advanced Materials* **2019**, *31* (48), e1903841.

(15) Bat-Erdene, M.; Batmunkh, M.; Sainbileg, B.; Hayashi, M.; Bati, A. S. R.; Qin, J.; Zhao, H.; Zhong, Y. L.; Shapter, J. G. Highly Dispersed Ru Nanoparticles on Boron-Doped $Ti_3C_2T_x$ (MXene) Nanosheets for Synergistic Enhancement of Electrocatalytic Hydrogen Evolution. *Small* **2021**, *17*, e2102218.

(16) Liu, Y.; Bai, Y.; Yang, W.; Ma, J.; Sun, K. Self-supported Electrode of NiCo-LDH/$NiCo_2S_4$/CC with Enhanced Performance for Oxygen Evolution Reaction and Hydrogen Evolution Reaction. *Electrochimica Acta* **2021**, *367*, 137534.

(17) Yan, L.; Zhang, B. Rose-like, Ruthenium-modified Cobalt Nitride Nanoflowers Grown in Situ on an MXene Matrix for Efficient and Stable Water Electrolysis. *Journal of Materials Chemistry A* **2021**, *9* (36), 20758-20765.

(18) Liu, H.; Hu, Z.; Liu, Q.; Sun, P.; Wang, Y.; Chou, S.; Hu, Z.; Zhang, Z. Single-atom Ru Anchored in Nitrogen-doped MXene ($Ti_3C_2T_x$) as an Efficient Catalyst for the Hydrogen Evolution Reaction at All pH Values. *Journal of Materials Chemistry A* **2020**, *8* (46), 24710-24717.

(19) Asen, P.; Esfandiar, A.; Mehdipour, H. Urchin-like Hierarchical Ruthenium Cobalt Oxide Nanosheets on $Ti_3C_2T_x$ MXene as A Binder-free Bifunctional Electrode for Overall Water Splitting and Supercapacitors. *Nanoscale* **2022**, *14*, 1347-1362.

(20) Peng, X.; Zhao, S.; Mi, Y.; Han, L.; Liu, X.; Qi, D.; Sun, J.; Liu, Y.; Bao, H.; Zhuo, L.; et al. Trifunctional Single-Atomic Ru Sites Enable Efficient Overall Water Splitting and Oxygen Reduction in Acidic Media. *Small* **2020**, *16*, e2002888.

(21) Kong, A.; Peng, M.; Gu, H.; Zhao, S.; Lv, Y.; Liu, M.; Sun, Y.; Dai, S.; Fu, Y.; Zhang, J.; et al. Synergetic Control of Ru/MXene 3D Electrode with Superhydrophilicity and Superaerophobicity for Overall Water Splitting. *Chemical*

Engineering Journal **2021**, *426*, 131234.

(22) Jia, H.-L.; Guo, C.-L.; Chen, R.-X.; Zhao, J.; Liu, R.; Guan, M.-Y. Ruthenium Nanoparticles Supported on S-doped Graphene as an Efficient HER Electrocatalyst. *New Journal of Chemistry* **2021**, *45* (47), 22378-22385.

(23) Zhao, Q.; Chen, S.; Ren, H.; Chen, C.; Yang, W. Ruthenium Nanoparticles Confined in Covalent Organic Framework/Reduced Graphene Oxide As Electrocatalyst toward Hydrogen Evolution Reaction in Alkaline Media. *Industrial & Engineering Chemistry Research* **2021**, *60* (30), 11070-11078.

(24) Li, Y.; Chu, F.; Bu, Y.; Kong, Y.; Tao, Y.; Zhou, X.; Yu, H.; Yu, J.; Tang, L.; Qin, Y. Controllable fabrication of Uniform Ruthenium Phosphide Nanocrystals for the Hydrogen Evolution Reaction. *Chemical Communications* **2019**, *55* (54), 7828-7831.

(25) Li, M.; Wang, Y.; Li, T.; Li, J.; Huang, L.; Liu, Q.; Gu, J.; Zhang, D. Hierarchical Few-layer Fluorine-free $Ti_3C_2T_X$ (T=O,OH)/MoS_2 Hybrid for Efficient Electrocatalytic Hydrogen Evolution. *Journal of Materials Chemistry A* **2021**, *9* (2), 922-927.

(26) Wu, L.; Yu, L.; Zhang, F.; McElhenny, B.; Luo, D.; Karim, A.; Chen, S.; Ren, Z. Heterogeneous Bimetallic Phosphide Ni_2P-Fe_2P as an Efficient Bifunctional Catalyst for Water/Seawater Splitting. *Advanced Functional Materials* **2020**, *31* (1), 2006484.

(27) Liu, T.; Zhang, W.; Chen, T.; Liu, D.; Cao, L.; Ding, T.; Liu, X.; Pang, B.; Wang, S.; Wang, L.; et al. Regulating the Coordination Environment of Ruthenium Cluster Catalysts for the Alkaline Hydrogen Evolution Reaction. *Journal of Physical Chemistry Letters* **2021**, *12* (33), 8016-8023.

(28) Luo, Y.; Wang, P.; Zhang, G.; Wu, S.; Chen, Z.; Ranganathan, H.; Sun, S.; Shi, Z. Mn-doped Nickel-iron Phosphide Heterointerface Nanoflowers for Efficient Alkaline Freshwater/Seawater Splitting at High Current Densities. *Chemical Engineering Journal* **2023**, *454*, 140061.

(29) Muthurasu, A.; Chhetri, K.; Dahal, B.; Kim, H. Y. Ruthenium Nanoparticles Integrated Bimetallic Metal-organic Framework Electrocatalysts for Multifunctional Electrode Materials and Practical Water Electrolysis in Seawater. *Nanoscale* **2022**, *14*, 6557-6569.

(30) Wang, X.; Zhou, X.; Li, C.; Yao, H.; Zhang, C.; Zhou, J.; Xu, R.; Chu, L.; Wang, H.; Gu, M.; et al. Asymmetric Co-N_3P_1 Trifunctional Catalyst with Tailored Electronic Structures Enabling Boosted Activities and Corrosion Resistance in an Uninterrupted Seawater Splitting System. *Advanced Materials* **2022**, *34* (34), e2204021.

(31) Yang, T.; Lv, H.; Quan, Q.; Li, X.; Lu, H.; Cui, X.; Liu, G.; Jiang, L. Electronic Structure Modulation of MoO_2 via Er-doping for Efficient Overall Water/Seawater Splitting and Mg/Seawater Batteries. *Applied Surface Science* **2023**, *615*, 156360.

(32) Fan, J.; Fu, C.; Liang, R.; Lv, H.; Fang, C.; Guo, Y.; Hao, W. Mild Construction of "Midas Touch" Metal-Organic Framework-Based Catalytic Electrodes for Highly Efficient Overall Seawater Splitting. *Small* **2022**, *18*, e2203588.

(33) Fang, F.; Wang, Y.; Shen, L. W.; Tian, G.; Cahen, D.; Xiao, Y. X.; Chen, J. B.; Wu, S. M.; He, L.; Ozoemena, K. I.; et al. Interfacial Carbon Makes Nano-Particulate RuO_2 an Efficient, Stable, pH-Universal Catalyst for Splitting of Seawater. *Small* **2022**, *18*, e2203778.

(34) Wang, Q.; Tian, Z.-Y.; Cui, W.-J.; Hu, N.; Zhang, S.-M.; Ma, Y.-Y.; Han, Z.-G. Hierarchical Flower-like CoS_2-MoS_2 Heterostructure Spheres as Efficient Bifunctional Electrocatalyst for Overall Water Splitting. *International Journal of Hydrogen Energy* **2022**, *47* (25), 12629-12641.

(35) Zhu, K.; Shi, F.; Zhu, X.; Yang, W. The Roles of Oxygen Vacancies in Electrocatalytic Oxygen Evolution Reaction. *Nano Energy* **2020**, *73*, 104761.

(36) Zhu, J.; Guo, Y.; Liu, F.; Xu, H.; Gong, L.; Shi, W.; Chen, D.; Wang, P.; Yang, Y.; Zhang, C.; et al. Regulative Electronic States around Ruthenium/Ruthenium Disulphide Heterointerfaces for Efficient Water Splitting in Acidic Media. *Angewandte Chemie-international Edition* **2021**, *60* (22), 12328-12334.

Chapter 4. 0D/2D Co$_3$O$_4$/Ti$_3$C$_2$ MXene Composite: A Dual-Functional Electrocatalyst for Energy-Saving Hydrogen Production and Urea Oxidation
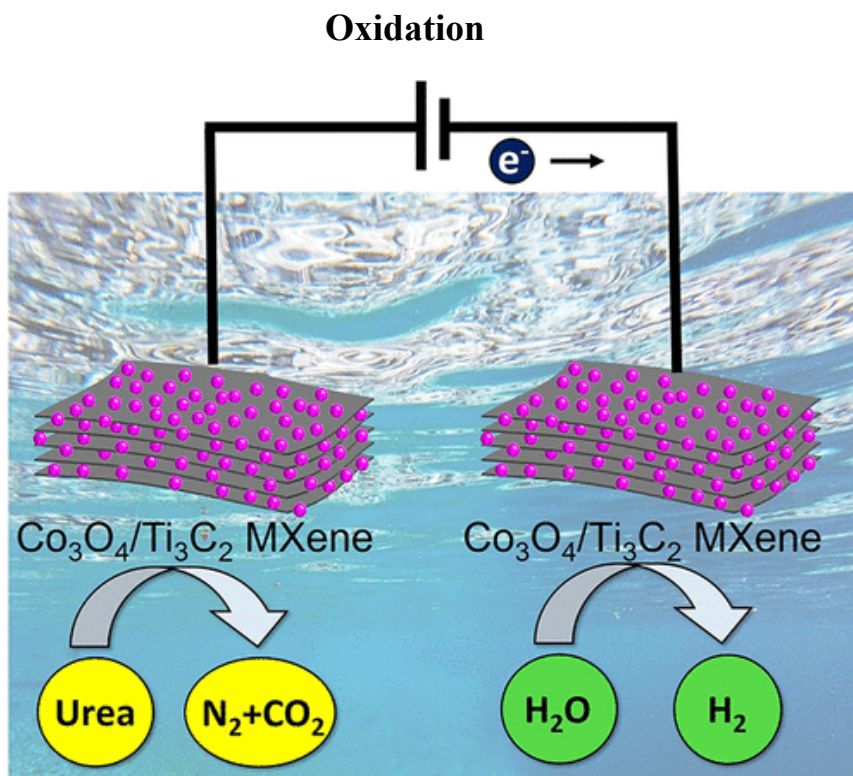
This chapter has been published in ACS Applied Energy Materials.

Abstract

Electrocatalytic water splitting to produce hydrogen (H_2) is a sustainable way of meeting energy demands at no environmental cost. However, the sluggish anodic reaction imposes a considerable overpotential requirement. By contrast, the electrocatalytic urea oxidation reaction offers the prospect of energy saving H_2 production together with urea-rich wastewater purification. In this work, a 0D/2D Co_3O_4/Ti_3C_2 MXene composite was synthesized by a simple solution reaction approach under mild conditions and applied as an efficient and stable electrocatalyst for hydrogen evolution reaction (HER) and urea oxidation reaction (UOR) in basic medium (1 M KOH + 0.5 M urea). The Co_3O_4/Ti_3C_2 MXene electrodes delivered a current density of 10 mA cm^{-2} at an overpotential of 124 mV for HER and required 1.40 V to reach 10 mA cm^{-2} for UOR. The hybrid catalyst could maintain high activity after 40 h continuous catalytic reaction for both UOR and HER. Its catalytic performance was significantly improved compared to that of pure Ti_3C_2 MXene and Co_3O_4 solving the problem of insufficient exposure of active sites caused by too large particle size and agglomeration of Co_3O_4 particles. Notably, Co_3O_4/Ti_3C_2 MXene was applied as a bifunctional catalyst for overall urea-containing water splitting, and showed certain energy saving advantages compared with other reported Co-based catalysts. This work provides a strategy for application other than noble metal-based electrode materials for urea-containing wastewater purification coupled with H_2 production.

4.1 Experimental section

4.2.1 Synthesis of Titanium Carbide (Ti_3C_2) MXene

The layered Ti_3C_2 was synthesized by liquid etching of the pristine Ti_3AlC_2. The etching was carried out by immersing the Ti_3AlC_2 powder in 40% HF aqueous solution and stirred for 24 h at room temperature. In this process, Al layers were removed, producing multilayered Ti_3C_2 MXene nanosheets. The chemical reaction processes of HF etching are summarized below (equation 4.1-4.3):[1, 2]

$$Ti_3AlC_2 + 3HF = AlF_3 + 3/2H_2 + Ti_3C_2 \tag{3.1}$$

$$Ti_3C_2 + 2H_2O = Ti_3C_2(OH)_2 + H_2 \tag{3.2}$$

$$Ti_3C_2 + 2HF = Ti_3C_2F + H_2 \tag{3.3}$$

Then, the precipitate was repeatedly ultrasonicated, centrifuged, and rinsed with deionized water until the pH of the supernatant reached 6. The prepared MXene was stored in nitrogen-saturated deionized water to prevent oxidation.

4.1.2 Synthesis of Cobalt Oxide (Co_3O_4) and Co_3O_4/Ti_3C_2

MXene composite. First, 40 mg of Ti_3C_2 MXene was uniformly dispersed in 40 mL of deionized water and ultrasonicated for 60 min at room temperature. Then, 2.17, 10.85, 21.70, and 43.40 mg of $CoCl_2$ were separately added into the MXene colloidal solution under stirring for 10 min. After that, the mixed solution was heated to 70 °C and an aqueous solution of $NaBH_4$ of different concentrations (20, 100, 200, and 400 mg $NaBH_4$ dispersed in 20 mL of deionized water) was slowly added into the MXene colloidal under stirring. After 10 min reaction, the resulting products were separated by centrifugation, washed with deionized water several times, and finally dried at 60 °C overnight. The samples were named as Co_3O_4/Ti_3C_2 (1:10), Co_3O_4/Ti_3C_2 (1:2), Co_3O_4/Ti_3C_2 (1:1), and Co_3O_4/Ti_3C_2 (1:0.5), where the ratio refers to the mass ratio. The Co_3O_4 was prepared using the same method without adding Ti_3C_2 MXene.

4.1.3 Fabrication of the Electrodes

The prepared sample (5 mg) and Nafion 117 solution (∼5 wt.%, 5 μL) were uniformly dispersed in ethanol (500 μL) by sonication. The slurry (2 μL) was drop-casted onto a polished glassy carbon disk (d = 3.0 mm, area: 0.071 cm^2) and dried at room temperature. The current density was calculated by dividing the actual current value, measured by the electrochemical workstation, by the area (j = I/S, where j is the current density, I refers to the current, and S corresponds to the surface area of the electrode). Similarly, Pt/C and RuO$_2$ electrodes were prepared under otherwise identical conditions. The glassy carbon (GC) electrodes loaded with different samples were used in UOR and HER electrochemical tests. For the overall water splitting test, the Co$_3$O$_4$/Ti$_3$C$_2$ MXene slurry was prepared by a similar process[3] (10 mg of Co$_3$O$_4$/Ti$_3$C$_2$ MXene catalyst, 500 μL of DI, 450 μL of isopropanol, and 50 μL of Nafion), and then deposited on a 0.5 × 0.5 cm piece of nickel foam (NF) with a mass loading of 1.6 mg cm^{-2}. Prior to Co$_3$O$_4$/Ti$_3$C$_2$ MXene loading, the NF was cleaned with acetone, diluted HCl (6 M), DI water, and ethanol to reduce the oxidized layer thickness. The benchmark precious metal catalysts Pt/C and RuO$_2$ were casted on NF at the same mass loading (1.6 mg cm^{-2}) and the same area (0.5 × 0.5 cm^2).

4.1.4 Electrochemical Measurements

UOR and HER electrochemical measurements were carried out by the linear sweep voltammetry (LSV) method in a standard three-electrode system in 1 M KOH + 0.5 M urea electrolyte at room temperature using a Metrohm potentiostat. A graphite rod and Ag/AgCl (saturated KCl) electrodes act as the counter and the reference electrodes, respectively. The sweep rate was set to 5 mV s^{-1} for LSV measurements. All values of potential were calculated with respect to the reversible hydrogen electrode (RHE) according to equation 4.4:[4]

$$E_{RHE} = E_{Ag/AgCl} + 0.197V + 0.059pH \qquad (4.4)$$

where E_{RHE} is the potential *versus* RHE and $E_{Ag/AgCl}$ is the measured potential against the saturated Ag/AgCl reference electrode. In this work, the pH of 1 M KOH solution is around 14 and that of 1 M KOH + 0.5 M urea is 13.9. All polarization curves were not IR-corrected. During the long-term test, a carbon rod acted as the counter electrode to avoid the influence of platinum deposition. The electrochemically active surface area (ECSA) was measured by the cyclic voltammetry (CV) method in a non-Faradaic region at various scan rates. The ECSA was estimated by equation 4.5:[5]

$$ECSA = C_{dl}/C_s \qquad (4.5)$$

where electrochemical double-layered capacitance (C_{dl}) was determined by extracting the slope of the fitted linear relationship between scan rate and charging current (equation 4.6). C_s is the specific capacitance for a flat surface.

$$C_{dl} = d(j_a-j_c)/2dv \qquad (4.6)$$

in which the j_a is the anodic current density, j_c is the cathodic current density, v is the scan rate, d/d is a derivative calculation.

4.1.5 Faradaic Efficiency Measurements for the HER

Gas chromatography (GC, Agilent 7890A gas chromatograph) was used to monitor the released H_2 using an automatic gas sampling valve that was pneumatically actuated. Custom sealed glass-to-metal adapters and 1/8 in. copper tubing were used to connect the electrolysis cell to the GC apparatus. Ar was used as the carrier gas, and the oven temperature was set to 45 °C. Ar flow rate was around 3 mL min^{-1}.

Gas chromatography (GC) was used to determine the volume of H_2 liberated under the employed experimental conditions (a controlled potentiostatic electrolysis (CPE); the electrode was held at -1.0 V *vs.* RHE for 1 h in 1 M KOH+0.5 M urea solution at 25 °C). This volume is referred to as $V_{measured}$. Equation 4.6 was used to estimate the

FE value:

$$FE = V_{measured}/V_{calculated} \qquad (4.6)$$

Where $V_{calculated}$ represents the theoretical volume of H_2 (the amount of the gas calculated from the charge passed through the WE during CA assuming 100% Faradaic efficiency). Measurements were conducted in a two-compartment bulk electrolysis cell with standard configuration. The cell consists of three electrodes: a working electrode, a counter electrode (a graphite rod, Sigma-Aldrich, 99.999%) and a Hg/HgO, NaOH (0.1 M) as the reference electrode. Equation 4.7 shown below was used to calculate the Faradaic efficiency values for the HER:

$$\text{Faradaic efficiency (\%)} = [F2\text{mol } H_2 \text{ (GC)}100]/Q(CPE) \qquad (4.7)$$

Where F is the Faraday's constant ($F = 96485$ C), mol H_2 (GC) refers to the amount of H_2 released during a controlled potential electrolysis (CPE) by GC, and Q(CPE) is the charge passed through the WE during the CPE. The factor (2) is the number of electrons transferred during the HER (n = 2 due to H^+ reduction, $2H^+ + 2e^- = H_2$).

4.2 Results and discussion

4.2.1. Fabrication and Characterization of the 0D/2D

Co_3O_4/Ti_3C_2 MXene Composite. The preparation of 0D/2D Co_3O_4/Ti_3C_2 MXene composite is illustrated in **Figure 4.1**. First, the bulk Ti_3AlC_2 MAX phase was selectively etched by hydrofluoric acid (HF) to remove Al layers, resulting in accordion-like layered Ti_3C_2 MXene nanosheets. On the surface of Ti_3C_2 MXene, many negative hydrophilic functional groups (-O, -F, and -OH) could be potentially produced upon etching by HF,[6] which can form strong electrostatic interactions with Co^{2+} ions, resulting in tight adsorption of Co cations on the surface of Ti_3C_2 MXene. Upon addition of the reducing agent ($NaBH_4$), the Co^{2+} ions adsorbed on the surface were *in situ* reduced to Co-CoO particles. The resulting Co-CoO/Ti_3C_2 MXene composite was

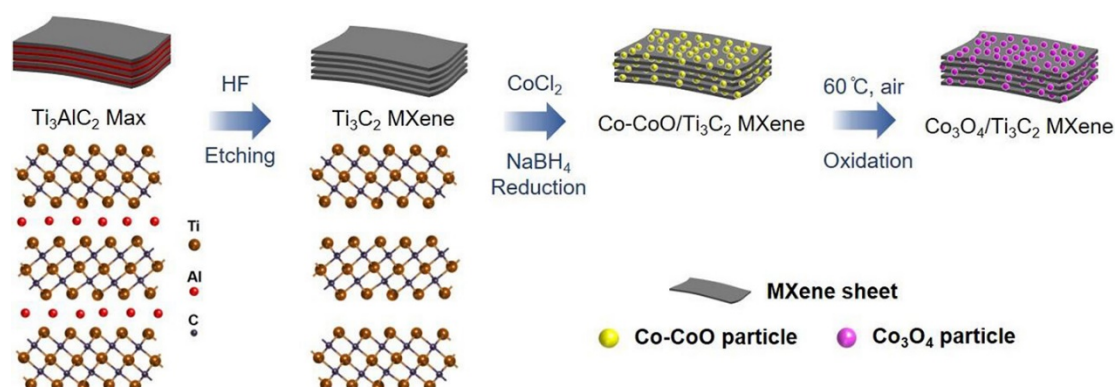further dried in air at 60 °C to produce 0D/2D Co_3O_4/Ti_3C_2 MXene composite.

Figure 4.1. Schematic illustration of the synthetic procedure of 0D/2D Co_3O_4/Ti_3C_2 MXene composite.

The morphology of Ti_3AlC_2 MAX, Ti_3C_2 MXene nanosheets, 0D/2D Co_3O_4/Ti_3C_2 MXene, and pure Co_3O_4 nanoparticles was assessed by scanning electron microscopy (SEM). **Figure 4.2** depicts the tightly stacked morphology of bulk Ti_3AlC_2 MAX with a width of the upper surface of about 10 μm. After removing the Al atomic interlayer by etching in HF, Ti_3C_2 MXene was well-delaminated and exhibited an accordion-like structure with a regular gap layer, as shown in **Figure 4.3(a)**. From the SEM micrographs in **Figure 4.3(b-c)**, it could be evidenced that a large number of fine and uniform 0D Co_3O_4 nanoparticles with a diameter of about 14 nm are not only dispersed on the Ti_3C_2 MXene surface, but also within the interlayer gap.

To estimate the size of 0D Co_3O_4 particles on Ti_3C_2 MXene, we obtained the particle size distribution histogram according to the SEM image in **Figure 4.4(a)**. The black line in **Figure 4.4(b)** is a simple GaussAMP fit showing size distribution, which reveals a mean diameter of Co_3O_4 particles of about 14.1 nm. In contrast, the Co_3O_4 particles synthesized without support material (**Figure 4.3d**) stuck together, causing

serious agglomeration. In addition, their size ($\sim$400 nm) is much larger than that of Co_3O_4 nanoparticles grown on the Ti_3C_2 MXene. As can be seen from **Figure 4.4(e)**, elemental mapping analysis highlighted the uniform distribution of Ti, C, Co and O elements in Co_3O_4/Ti_3C_2 MXene, implying the successful hybridization of Ti_3C_2 MXene with 0D Co_3O_4 nanoparticles. In addition to the above elements, the F element was also detected to be uniformly distributed (**Figure 4.5**), indicating that there are F-containing groups on the Ti_3C_2 MXene surface after HF etching. Loading Co_3O_4 nanoparticles on Ti_3C_2 MXene reduced the large particle size and inhibited the aggregation of Co_3O_4 particles, manifesting the strong interaction between Co_3O_4 and Ti_3C_2 MXene,[7] thus increasing the active sites involved in the catalytic reaction from the perspective of morphology.
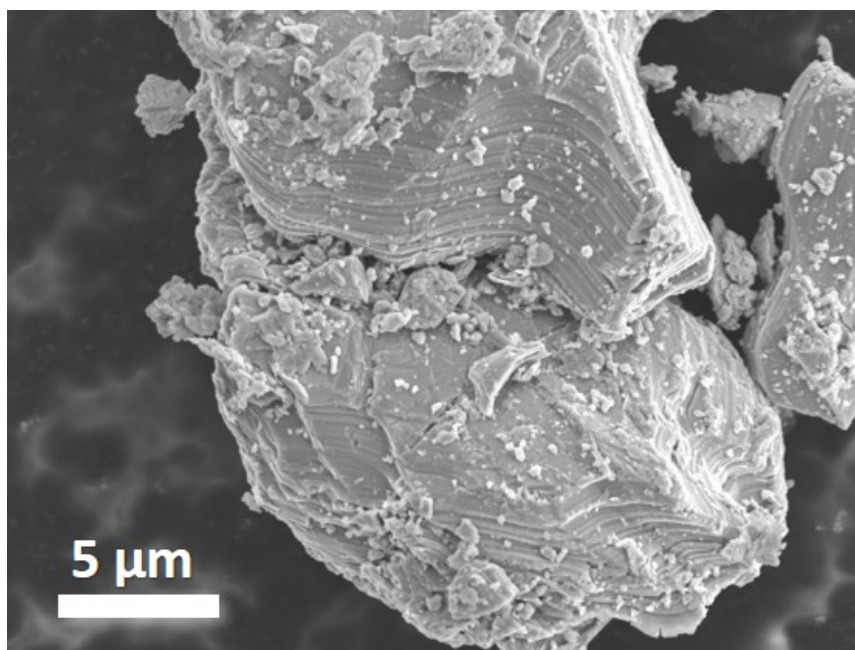
Figure 4.2. SEM image of the bulk Ti_3AlC_2 MAX phase.
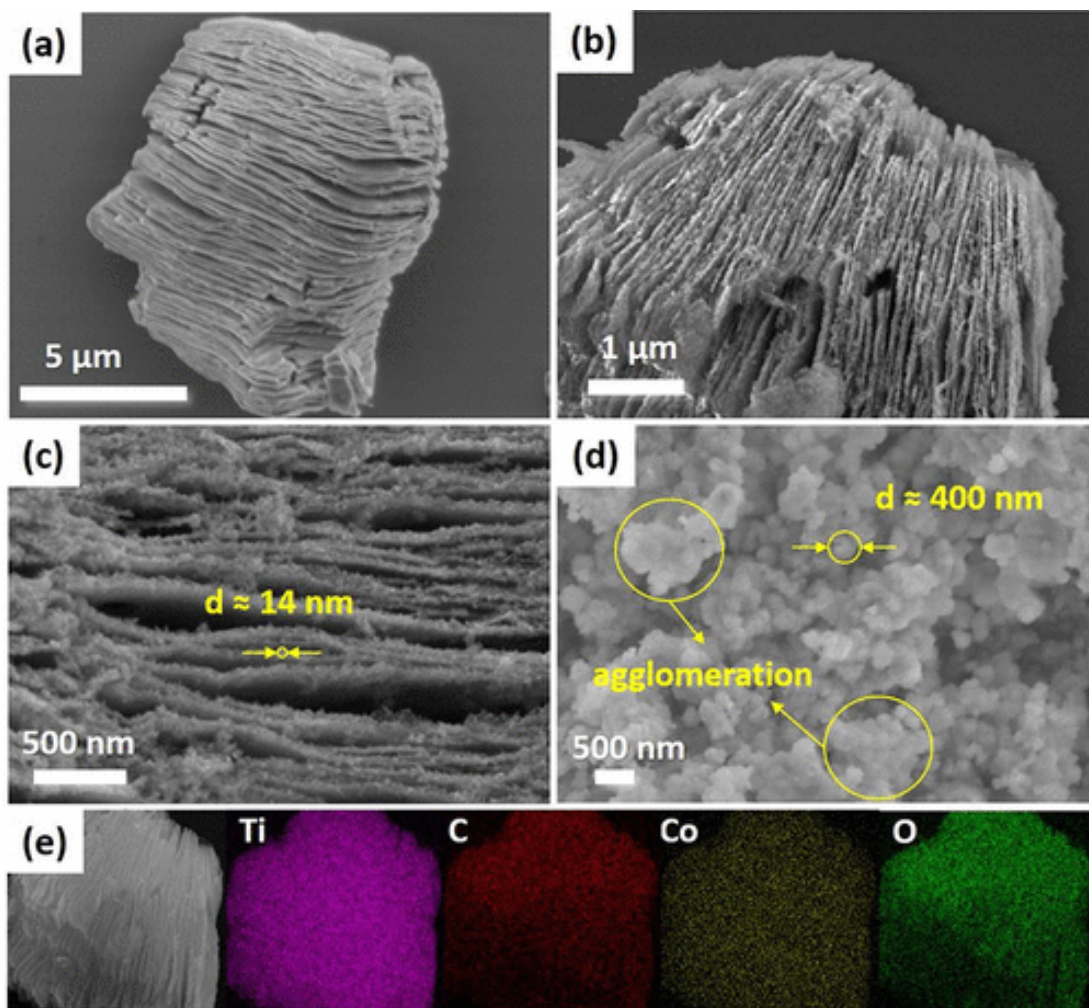
Figure 4.3. SEM images of (**a**) accordion-like layered Ti_3C_2 MXene nanosheets, Co_3O_4/Ti_3C_2 MXene composite at (**b**) low and (**c**) high magnifications, and (**d**) pure Co_3O_4 nanoparticles. (**e**) Elemental mapping of Co_3O_4/Ti_3C_2 MXene composite.
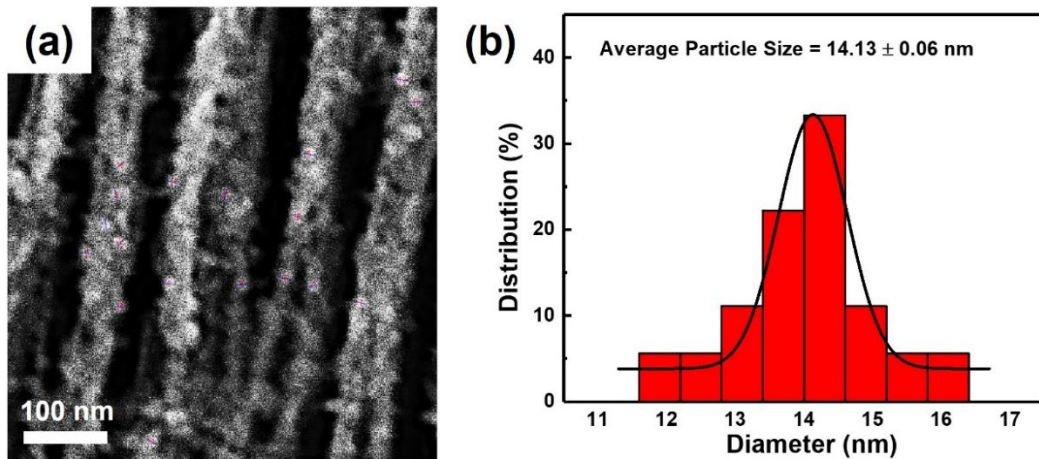
Figure 4.4. (**a**) SEM image Co_3O_4/Ti_3C_2 MXene composite and (**b**) the particle size distribution histogram of Co_3O_4 particles on Ti_3C_2 MXene.
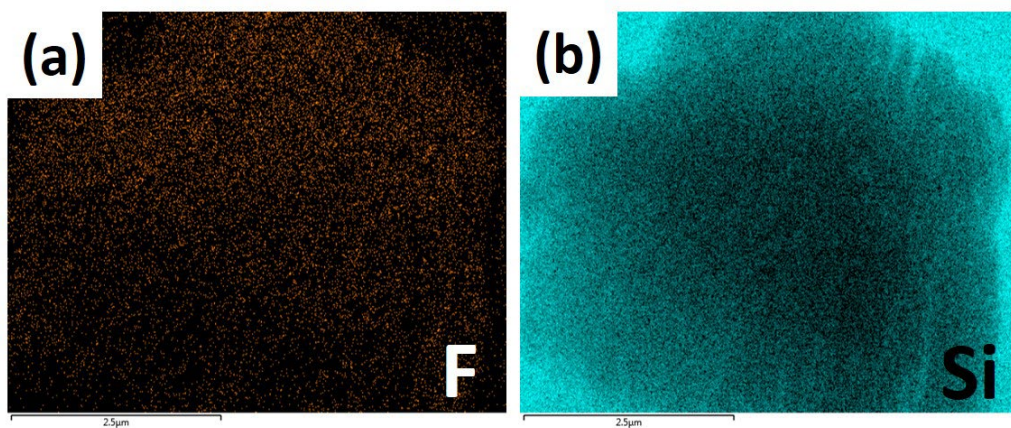

Figure 4.5. Element mapping of Co_3O_4/Ti_3C_2 MXene for F and Si (Si originates from the Si wafer base).

The phase structures of Ti_3AlC_2 MAX, Ti_3C_2 MXene nanosheets, 0D/2D Co_3O_4/Ti_3C_2 MXene and pure Co_3O_4 were determined by X-ray diffraction (XRD) analysis. **Figure 4.6(a)** displays the diffraction peaks of Ti_3AlC_2 MAX at *2θ* of 9.5°, 19.1°, 39.0°, 41.7°, and 56.4° corresponding respectively to the (002), (004), (104),

(105), and (109) planes of Ti_3AlC_2 MAX phase. These peaks are sharp and intense with their positions being consistent with those reported in the literature.[8] After HF chemical etching, a shift of the (00l) diffraction peak to low-angle position, indicating a c-cell parameter increase. The disappearance of the (104) peak of MAX, located at 39°, accompanied by the appearance of the characteristic (006) and (111) crystal planes at respectively $2\theta = 27.7$ and 35.8° suggest the formation of Ti_3C_2 MXene. These results proved that the Al atomic layers were effectively etched and the Ti_3AlC_2 MAX was transformed into Ti_3C_2 MXene.[2] Additionally, different from the diffraction peaks of Ti_3AlC_2, the peak intensities of Ti_3C_2 are much weaker and broader due to the thinner layered structure of Ti_3C_2.[9] In the XRD pattern of Co_3O_4/Ti_3C_2 MXene composite, diffraction peaks at 2θ of 19°, 31.2°, 36.9°, 44.8°, 59.4°, and 65.2° assigned to the (111), (220), (311), (400), (551), and (400) planes of Co_3O_4 (PDF #42−1467) are obvious. Compared with the XRD patterns of the prepared Co_3O_4 without MXene (**Figure 4.6b**), the characteristic peaks of Co_3O_4 in the Co_3O_4/Ti_3C_2 MXene composite are more evident, which can be ascribed to higher crystallinity of the grown Co_3O_4 particles after introducing Ti_3C_2 MXene as a support material. The reason behind the better crystallinity of Co_3O_4 nanoparticles upon their support on MXene sheets, as compared to pure Co_3O_4, is most likely due to the formation Co-CoO particles on MXene layers with relative larger surface energy, which are easier to be completely converted into Co_3O_4 upon thermal annealing at 60 °C. In contrast, pure Co-CoO particles are larger with a lower surface energy. Therefore, they are difficult to be fully transformed into Co_3O_4 and show poor crystallinity.
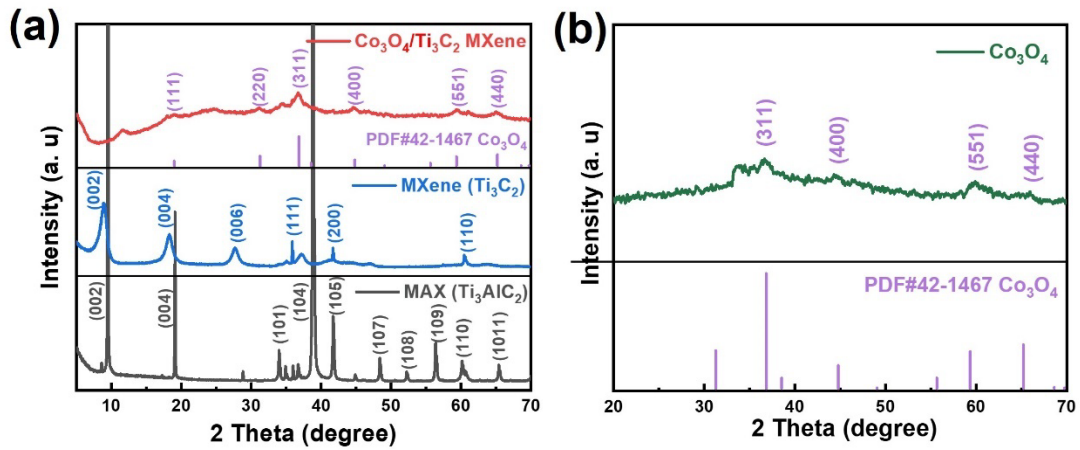
Figure 4.6. XRD patterns of (**a**) Ti_3AlC_2 MAX, Ti_3C_2 MXene, Co_3O_4/Ti_3C_2 MXene composite and (**b**) pure Co_3O_4.

The Raman spectra of Ti_3AlC_2 before and after HF etching also further proved that the Al element was removed completely, as shown in **Figure 4.7**. The four dominant Raman peaks of Ti_3AlC_2 could be assigned to Al-Ti vibrations (I and II), while bands III and IV involve Ti-C vibrations.[9][10] Peaks I and II of Al-Ti vibrations have almost disappeared in the Raman plot of Ti_3C_2 MXene, confirming the successful shedding of Al. At the same time, the peaks III and IV became broader with weaker intensities, which can be attributed to the formation of Ti_3C_2 thinner layers.[9]
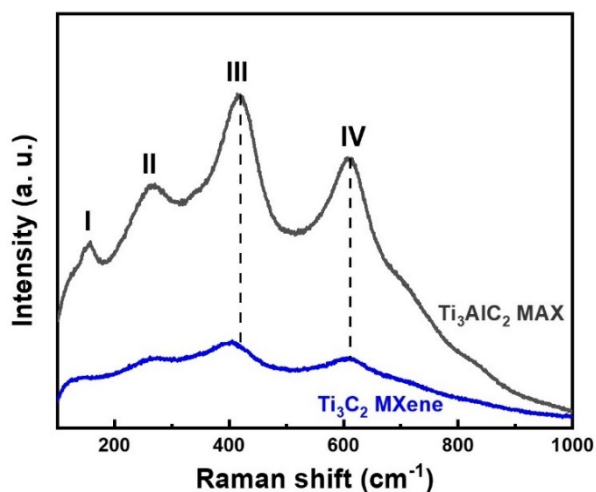
Figure 4.7. Raman spectra of Ti_3AlC_2 MAX and Ti_3C_2 MXene.

X-ray photoelectron spectroscopy (XPS) spectra were acquired to analyze the elemental composition and valence states of the pure Co_3O_4, Ti_3C_2 MXene and Co_3O_4/Ti_3C_2 MXene, as shown in **Figures 4.8, 4.9**. From the survey spectra of Ti_3C_2 MXene and Co_3O_4/Ti_3C_2 MXene (**Figure 4.8a**), except for Ti, C, O, F, and Co elements, no other chemical element was detected, suggesting the complete removal of Al layers, in good agreement with the XRD and Raman observations. Double checking this assumption, a high-resolution spectrum at the position corresponding to the binding energy of the Al did not show any obvious signal (**Figure 4.8b**), which further confirms the above results. Additionally, the intensity of the F 1s peak became weaker and the intensity of the peak O 1s increased after formation of Co_3O_4/Ti_3C_2 MXene (**Figure 4.8a**). This is due to the growth of Co_3O_4 particles covering the -F functional groups and likewise increasing the content of O element.
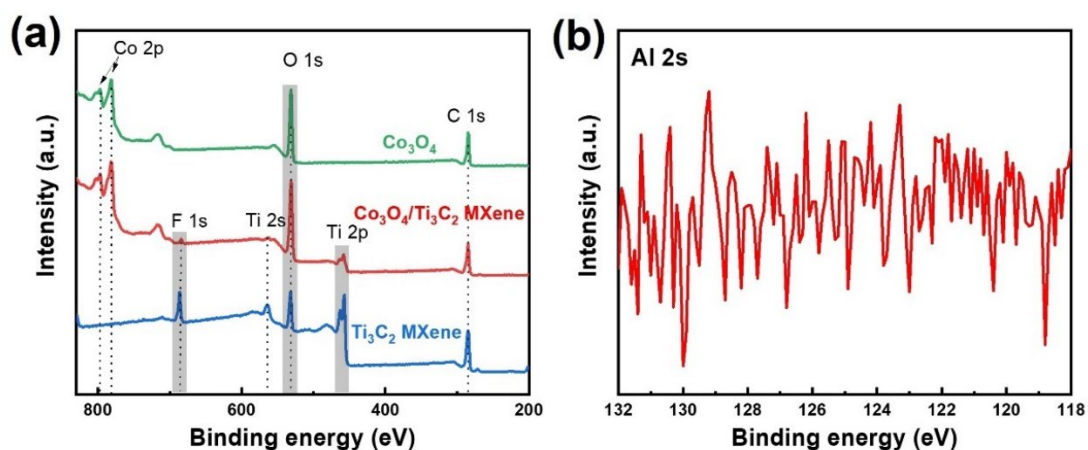
Figure 4.8. (**a**) XPS survey spectra of Ti$_3$C$_2$ MXene, pure Co$_3$O$_4$/Ti$_3$C$_2$ MXene composite, and Co$_3$O$_4$. (**b**) High-resolution XPS spectrum of the Al 2s of Co$_3$O$_4$/Ti$_3$C$_2$ MXene composite.

For Ti 2p spectrum of Co$_3$O$_4$/Ti$_3$C$_2$ MXene (**Figure 4.9a**), it was fitted with four doublets due to Ti 2p$_{3/2}$ and Ti 2p$_{1/2}$ with a peak area ratio of 2:1. The four peaks of 2p3/2 are located at 454.4, 455.5, 457.7, and 458.3 eV, corresponding to the Ti-C, Ti^{2+}, Ti^{3+}, and Ti^{4+}, respectively, consistent with reported data.[10, 11] Likewise, the corresponding 2p$_{1/2}$ orbital spectra are also deconvoluted into four components at 460.3, 461.5, 463.3, and 464.2 eV. Besides, the high-resolution Co 2p plot of Co$_3$O$_4$ (**Figure 4.9b**) exhibits two broad peaks at around 781 and 796 eV with a binding energy separation of 15 eV due to the spin−orbit splitting of the 2p orbital into 2p$_{3/2}$ and 2p$_{1/2}$, suggesting the formation of Co$_3$O$_4$.[12] Further, the four resulting peaks upon deconvolution analysis at 780.9 and 796.5 eV are assigned respectively to Co^{3+} 2p$_{3/2}$ and Co^{3+} 2p$_{1/2}$, while the components at 782.4 and 797.9 eV are ascribed to Co^{2+} 2p$_{3/2}$ and Co^{2+} 2p$_{1/2}$, respectively.[13] The other two peaks are the corresponding satellite peaks (786.8 and 803.5 eV). From **Figure 4.9(c)**, it could be seen that the peaks of Co 2p in

Co$_3$O$_4$/Ti$_3$C$_2$ MXene composite were slightly shifted to higher binding energies (781.0, 796.5, 782.6, and 798.1 eV) compared with those of Co$_3$O$_4$, revealing the charge transfer from the Co$_3$O$_4$ nanoparticles to Ti$_3$C$_2$ MXene.[7] All these aspects demonstrated the successful growth of zero-dimensional Co$_3$O$_4$ nanoparticles on two-dimensional Ti$_3$C$_2$ MXene nanosheets, forming a 0D/2D Co$_3$O$_4$/Ti$_3$C$_2$ MXene composite.
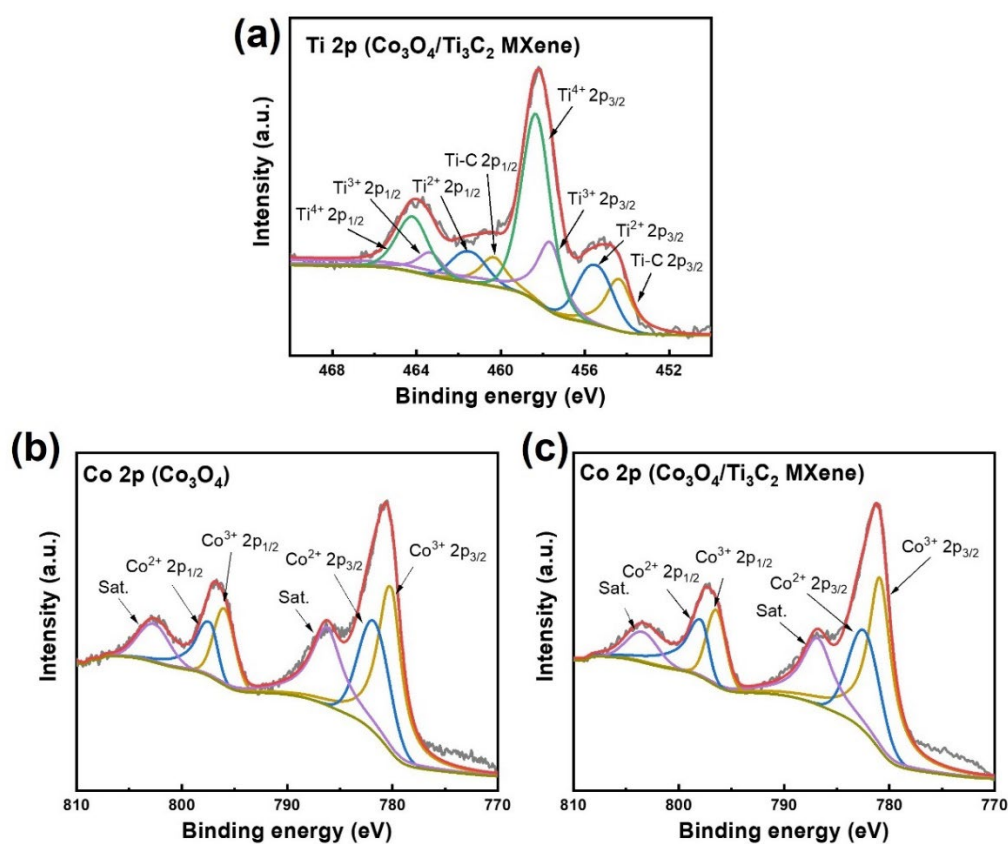
Figure 4.9. High-resolution XPS spectra for (**a**) Ti 2p of Co$_3$O$_4$/Ti$_3$C$_2$ MXene composite; Co 2p of (**b**) pure Co$_3$O$_4$ and (**c**) Co$_3$O$_4$/Ti$_3$C$_2$ MXene composite.

4.2.2. Electrocatalytic Performance of Co$_3$O$_4$/Ti$_3$C$_2$ MXene Composite for Urea Oxidation Reaction (UOR)

The electrocatalytic UOR performance of the Co$_3$O$_4$/Ti$_3$C$_2$ MXene composite was

surveyed in a typical three-electrode setup. As shown in **Figure 4.10**, the linear sweep voltammetry (LSV) curves of the Co_3O_4/Ti_3C_2 MXene composite, deposited on a glassy carbon electrode, were recorded in different electrolytes. The current response in 0.5 M urea without KOH is negligible compared to that in 1 M KOH, indicating that both OER and UOR need to be performed under alkaline conditions. Obviously, the anodic current density tested in 1 M KOH+0.5 M urea (corresponding to the UOR process) increased significantly compared to that recorded without urea (corresponding to the OER process). At the same time, Co_3O_4/Ti_3C_2 MXene required a drive potential of 1.69 V to attain 40 mA cm^{-2} during the process of OER, while it only demanded 1.49 V for UOR. This result revealed convincingly that Co_3O_4/Ti_3C_2 MXene is an excellent electrocatalyst for UOR in alkaline electrolyte and more energy efficient than for OER.
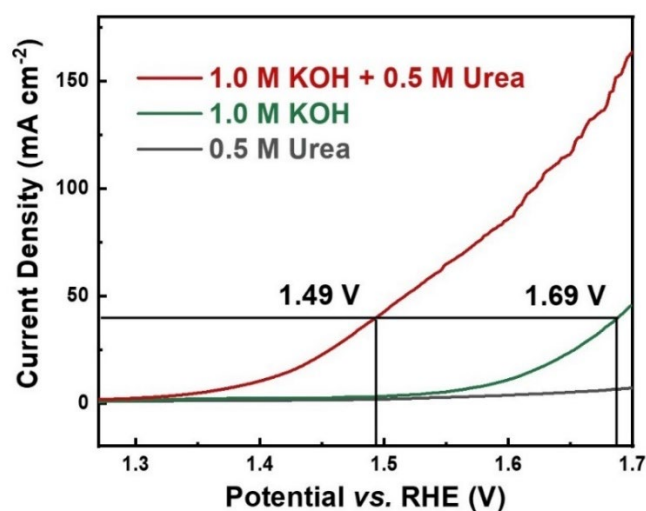
Figure 4.10. Electrocatalytic performance for urea oxidation reaction. LSV curves of the Co_3O_4/Ti_3C_2 MXene in 1.0M KOH with/without urea at a scan rate of 5 mV s^{-1}.

To assess the material ratio with the best performance, we carried out parameter optimization experiments: the UOR properties of composites with different

Co_3O_4/Ti_3C_2 MXene ratios were tested, as shown in **Figure 4.11(a-b).** As can be seen from the LSV curves, for UOR, Co_3O_4/Ti_3C_2 MXene (1:1) featured the most obvious electrochemical signals, corresponding to the results of the Tafel slopes. In addition, the electrocatalytic activity of Co_3O_4/Ti_3C_2 MXene was assessed in 1 M KOH containing different urea concentrations (0.1, 0.3, and 0.5 M). The results in **Figure 4.12** clearly indicate that the current density decreased upon decreasing the urea concentration below 0.5 M and approached that of OER for 1 M KOH+0.1 M urea. The catalytic properties of all materials are summarized in **Table 4.1**. From their SEM image (**Figure 4.13a-d**) analysis, when the Co salt amount was low (Co_3O_4/Ti_3C_2 MXene 1:10 and 1:2), Co_3O_4 particles were hardly seen to grow on the Ti_3C_2 MXene sheet surface (**Figure 4.13a**), resulting in insufficient active sites to participate in the catalytic reaction. On the contrary, when too much Co salt was introduced, a large number of flocculent agglomerates were formed (**Figure 4.13d**), blocking the gaps of the Ti_3C_2 MXene sheets which hindered the charge transfer, thus deteriorating the electrocatalytic performance. The subsequent electrochemical experiments were carried out on Co_3O_4/Ti_3C_2 MXene (1:1).
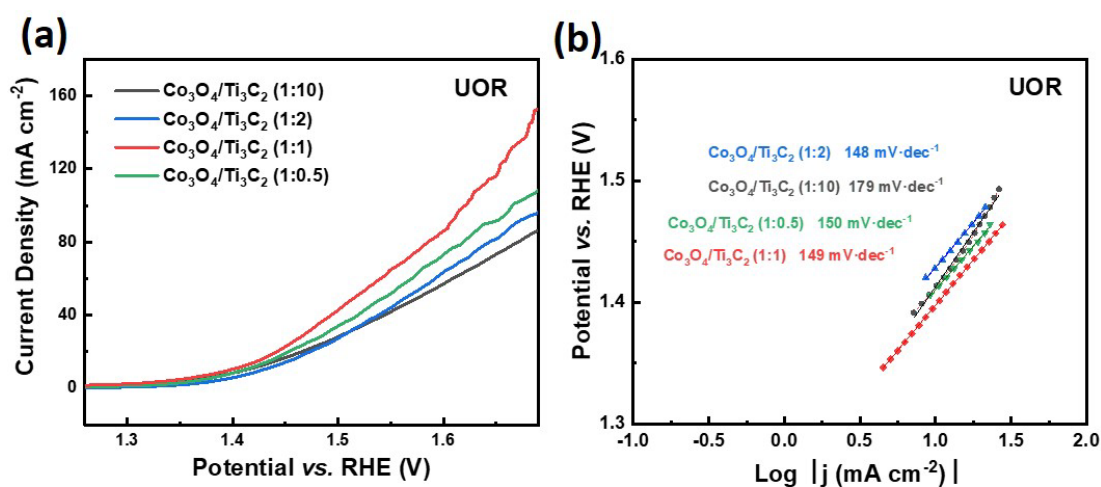

Figure 4.11. (a) LSV curves for UOR and **(b)** Tafel plots of Co_3O_4/Ti_3C_2 MXene

(1:10), Co_3O_4/Ti_3C_2 MXene (1:2), Co_3O_4/Ti_3C_2 MXene (1:1) and Co_3O_4/Ti_3C_2 MXene
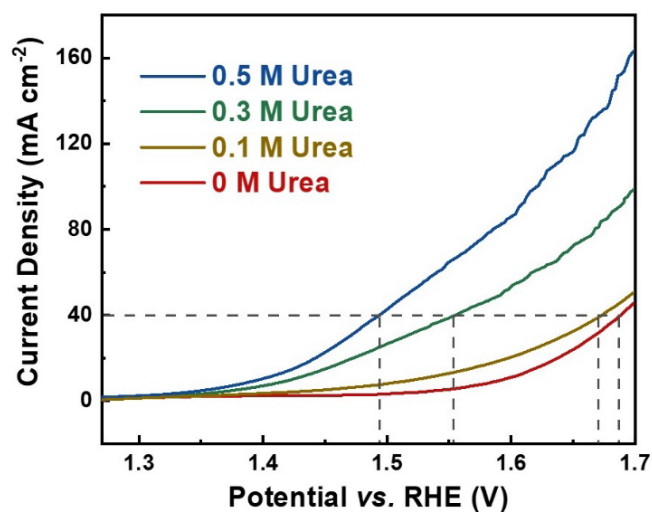
(1:0.5) in 1 M KOH + 0.5 M urea at the scan rate of 5 mV s^{-1}.

Figure 4.12. LSV curves of Co_3O_4/Ti_3C_2 MXene for UOR in 1M KOH containing

different urea concentrations.

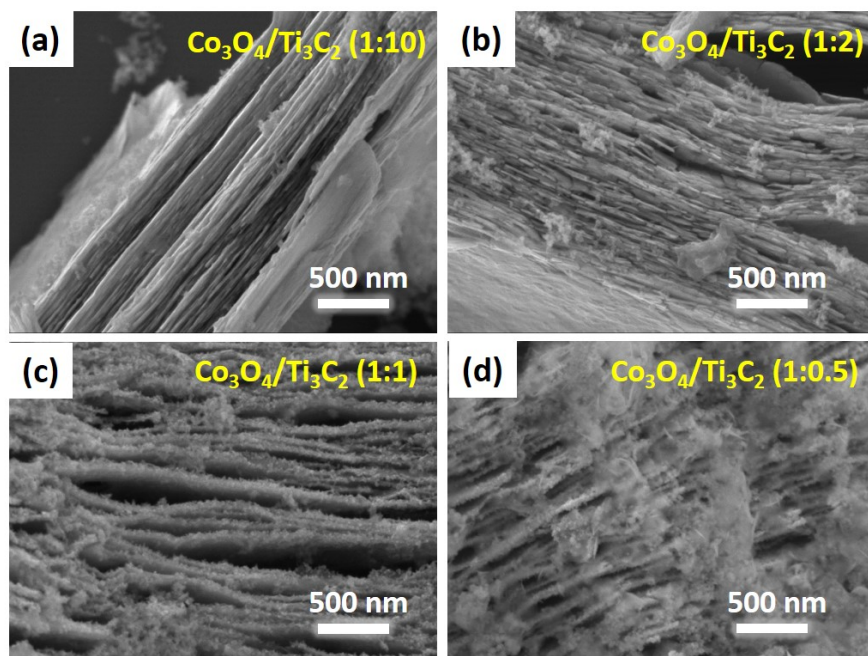**Figure 4.13.** SEM images of (**a**) Co_3O_4/Ti_3C_2 MXene (1:10), (**b**) Co_3O_4/Ti_3C_2 MXene

(1:2), (**c**) Co_3O_4/Ti_3C_2 MXene (1:1) and (**d**) Co_3O_4/Ti_3C_2 MXene (1:0.5).

Table 4.1. Comparison of UOR and HER properties of different materials in this work.

Catalyst	Potential (V *vs.* RHE) at 10 mA cm^{-2} for UOR	Tafel slope (mV dec^{-1}) for UOR	Overpotential (V *vs.* RHE) at 10 mA cm^{-2} for HER	Tafel slope (mV dec^{-1}) for HER
Pure Ti$_3$C$_2$ MXene	1.67	156	0.80	114
Pure Co$_3$O$_4$	1.50	256	0.44	150
Co$_3$O$_4$/Ti$_3$C$_2$ MXene (1:10)	1.42	179	0.34	165
Co$_3$O$_4$/Ti$_3$C$_2$ MXene (1:2)	1.43	148	0.26	140
Co$_3$O$_4$/Ti$_3$C$_2$ MXene (1:1)	**1.40**	**149**	**0.124**	**105**
Co$_3$O$_4$/Ti$_3$C$_2$ MXene (1:0.5)	1.42	150	0.22	121
RuO$_2$	1.58	119	-	-
Pt/C	-	-	0.054	29

In order to compare the UOR behaviors of various materials, **Figure 4.14(a)** presents the LSV curves of glassy carbon (GC) electrodes casted with different materials of the same amount (20 µg). As the voltage was increased, the bare GC electrode showed almost no current response, reflecting its lack of electrocatalytic activity, while Ti$_3$C$_2$ MXene merely exhibited slight activity. In addition, although pure Co$_3$O$_4$ was active for UOR and required a potential of 1.50 V to drive 10 mA cm^{-2},

Co_3O_4/Ti_3C_2 MXene displayed significantly improved catalytic activity, necessitating only a potential of 1.40 V to drive 10 mA cm^{-2}, which even outperformed commercial Ru_2O catalyst. **Figure 4.14(b)** details the potentials required for various materials to achieve different current densities of 10, 30, and 50 mA cm^{-2}, further illustrating the catalytic performance advantage of Co_3O_4/Ti_3C_2 MXene composite. **Table 4.2** compares the catalytic potentials for UOR of Co_3O_4/Ti_3C_2 MXene composite and other reported transition metal-based electrocatalysts, and our material still featured superiority.
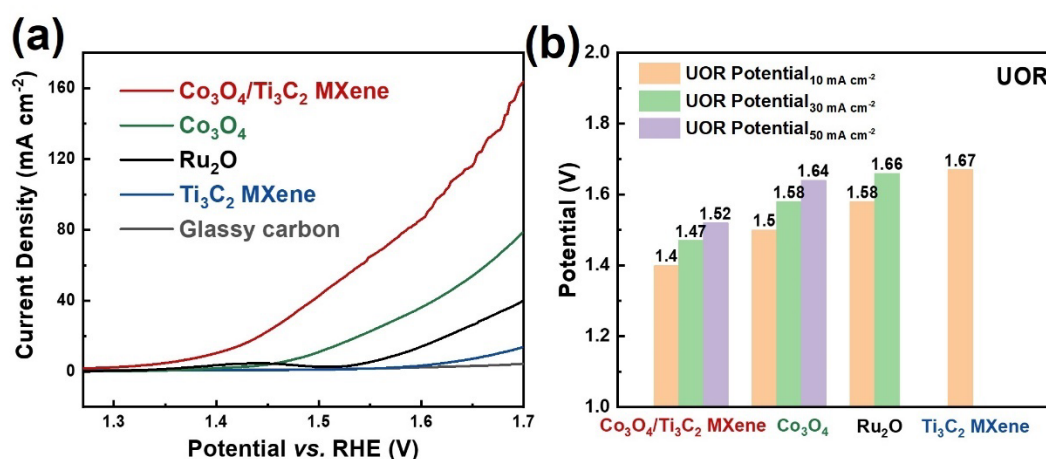
Figure 4.14 (**a**) LSV curves and (**b**) the required potentials of the Co_3O_4/Ti_3C_2 MXene, Co_3O_4, Ti_3C_2 MXene, commercial Ru_2O and bare glassy carbon electrode in 1M KOH+0.5M urea at a scan rate of 5 mV s^{-1}.

Table 4.2. Comparison of catalytic potentials for UOR of reported transition metal-based electrocatalysts.

	Onset potential (V *vs.* RHE)	η_{10} (V *vs.* RHE)	Reference
Ag/ZnO	1.43	1.56	[14]
CoS$_2$/Ti mesh	1.27	1.40	[15]
Ni-NiO	1.37	1.41	[16]
CoFe LDH/MOF	1.36	1.45	[17]
Co$_2$GeO$_4$	1.38	1.42	[18]
Co$_3$O$_4$/Ti$_3$C$_2$ MXene	**1.32**	**1.40**	**This work**

The reaction kinetics of UOR were studied through the analysis of the Tafel plots, **Figure 4.15(a)**. The Tafel slope of Co$_3$O$_4$/Ti$_3$C$_2$ MXene (149 mV dec^{-1}) was lower than that of Co$_3$O$_4$ (256 mV dec^{-1}) and Ti$_3$C$_2$ MXene (156 mV dec^{-1}), even close to that of benchmark Ru$_2$O catalyst (119 mV dec^{-1}), implying the competitive catalytic kinetics of Co$_3$O$_4$/Ti$_3$C$_2$ MXene. Notably, although the current density response of pure Co$_3$O$_4$ was more obvious than that of Ti$_3$C$_2$ MXene, its Tafel slope was much smaller compared to that of Ti$_3$C$_2$ MXene. The reason for this phenomenon is that Co$_3$O$_4$ has high intrinsic catalytic activity, but its catalytic kinetics are affected by particle agglomeration, hindering its electron transport. Ti$_3$C$_2$ MXene itself owned poor reactivity, but the multilayer structure accelerated the ion/electron transfer and finally achieved better kinetics. LSV curves of Co$_3$O$_4$/Ti$_3$C$_2$ MXene, acquired at different scan rates in **Figure 4.15(b)**, revealed that the current density changed only slightly as the scan rate was increased, indicating the efficient charge and mass transport of

Co_3O_4/Ti_3C_2 MXene composite.[19] To verify whether Co_3O_4/Ti_3C_2 MXene can be flexibly applied in practical catalytic reactions, a multistep chronopotentiometric curve was recorded in 1 M KOH+0.5 M urea, where the voltage increased from 1.49 to 1.66 V corresponding to a current density increase from 40 to 120 mA cm^{-2} with an increment of 10 mA cm^{-2} per 200 s. As shown in **Figure 4.15(c)**, each voltage step was straight and flat, implying that the voltage responded immediately (response time was less than 1 s) and could be maintained for 200 s without decay. This result confirmed the excellent mechanical robustness, conductivity, mass transport and electron transfer of Co_3O_4/Ti_3C_2 MXene.[20, 21] Last but not least, the LSV curves of Co_3O_4/Ti_3C_2 MXene before and after the continuous chronoamperometry test are depicted in **Figure 4.15(d)**, in which only a negligible positive shift was obvious, further supporting this point. All the above results proved that Co_3O_4/Ti_3C_2 MXene had superior catalytic performance as an electrocatalyst for UOR with high efficiency and durability.

Even though, the UOR oxidation produces CO_2 thereby making the hydrogen produced on the cathode dirty, this also applies for the traditional hydrogen evolution strategy (OER-HER) which produces O_2 and H_2. As the product of OER, O_2 is of limited value, and there is even a safety problem about the mixture of O_2 and H_2.[22] According to reports, the methods of purifying H_2 in industry and separating it from gases such as O_2, N_2, and CO_2 are the same, such as low temperature and temperature swing adsorption method, cryogenic separation and so on. Therefore, this issue should not limit the application of biomass oxidation methods such as UOR in the field of hydrogen production from water.
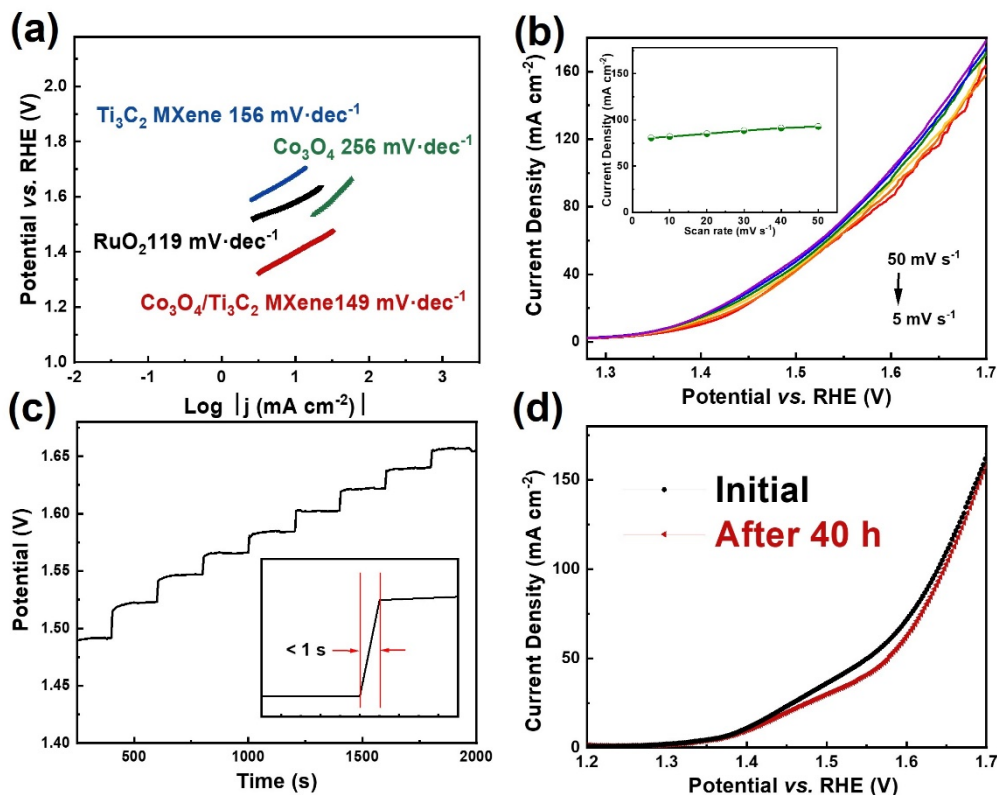
Figure 4.15 (**a**) Tafel plots of Co_3O_4/Ti_3C_2 MXene, Co_3O_4, Ti_3C_2 MXene and commercial Ru_2O. (**b**) LSV curves of the Co_3O_4/Ti_3C_2 MXene in 1M KOH+0.5M urea at various scan rates from 5 to 50 mV s^{-1} (inset: plot of the current density *vs.* scan rate at 1.6 V). (**c**) Multi-current process of the Co_3O_4/Ti_3C_2 MXene in 1M KOH+0.5M urea. The current density started from 40 mA cm^{-2} and ended at 120 mA cm^{-2} with an increment of 10 mA cm^{-2} per 200 s. (**d**) LSV curves of the Co_3O_4/Ti_3C_2 MXene before and after long-term stability test.

4.2.3. Electrocatalytic Performance of Co_3O_4/Ti_3C_2 MXene Composite for Hydrogen Evolution Reaction (HER)

In addition to electrocatalytic UOR performance, HER activity is another equally crucial factor for water splitting. First, to examine the influence of urea on HER process,

the LSV curves of Co_3O_4/Ti_3C_2 MXene in alkaline electrolyte with and without urea were recorded in **Figure 4.16(a)**. Interestingly, there was only a minuscule negative potential shift of 0.015 V at the current density of 100 mA cm^{-2} after adding 0.5 M urea, demonstrating the limited effect of urea addition on the HER process. Similar to UOR, different ratios of Co_3O_4/Ti_3C_2 MXene were also investigated for HER performance testing.

The results in **Figure 4.17(a,b)** also followed the same trend as he UOR test, and the details are recorded in **Table 4.1**. **Figure 4.16(b)** depicts the LSV curves of different materials for HER without iR correction, including the commercial Pt/C catalyst. Pt/C casted on glassy carbon exhibited superior activity, whereas bare glassy carbon displayed almost no activity and pure Ti_3C_2 MXene had poor HER activity with a barely visible current. Meanwhile, Co_3O_4/Ti_3C_2 MXene required an overpotential of 124 mV to attain a current density of 10 mA cm^{-2}, which is greatly enhanced as compared to pure Co_3O_4 (444 mV at 10 mA cm^{-2}) (**Figure 4.18**). Thus, similar to the UOR study, Ti_3C_2 MXene played a key role as an efficacious conductive framework or charge channels for HER.[23] Likewise, the reaction kinetics of the catalysts during the HER process were assessed through the determination of the slope values from the Tafel plots (**Figure 4.16c**). In line with the above results, Co_3O_4/Ti_3C_2 MXene recorded the smallest Tafel slope of 105 mV per decade (mV dec^{-1}), revealing fast HER kinetics following the Volmer-Heyrovsky mechanism.[5] The long-term stability of Co_3O_4/Ti_3C_2 MXene for HER is depicted in **Figure 4.16(d)**. After 40 h of continuous catalysis, the current density could still maintain 90% of its initial value and a little change in LSV, which further demonstrated its catalytic durability for HER.
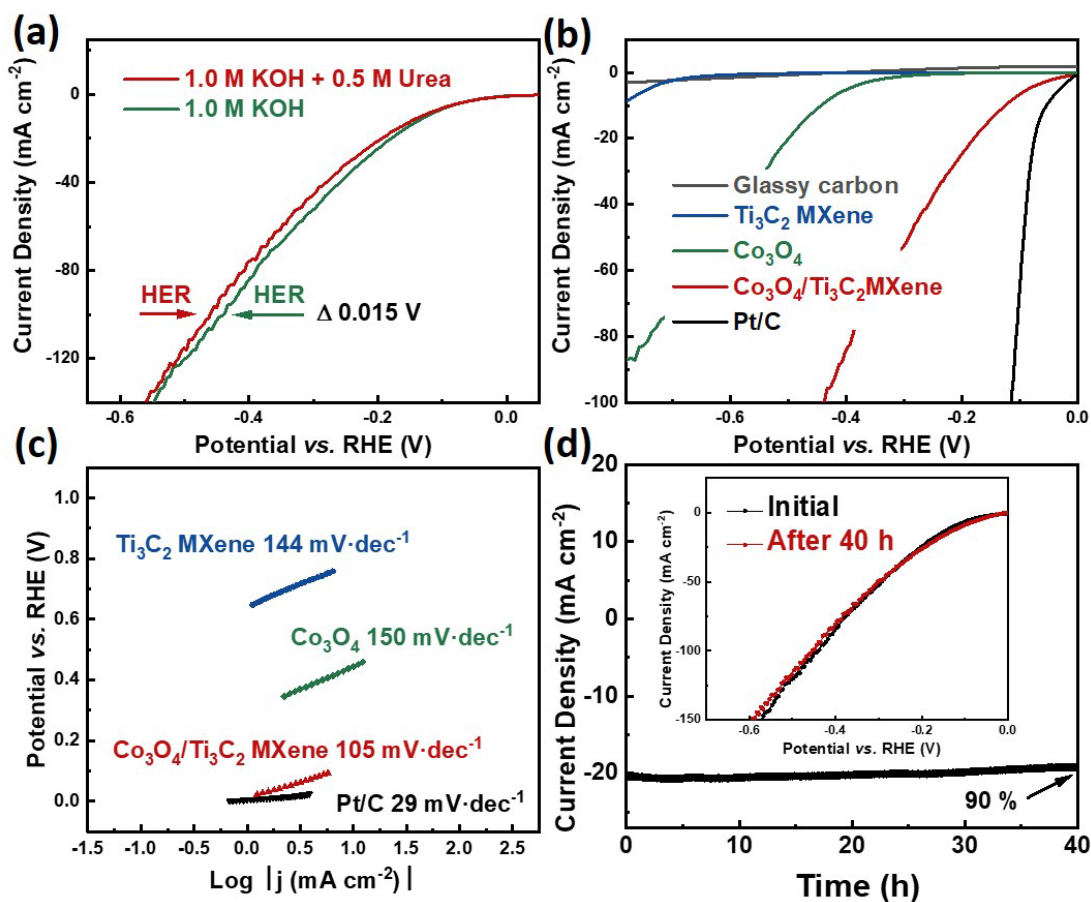
Figure 4.16. Electrocatalytic performance for hydrogen evolution reaction. **(a)** LSV curves of the Co_3O_4/MXene in 1M KOH with and without urea at a scan rate of 5 mV s^{-1}. **(b)** LSV curves of the Co_3O_4/Ti_3C_2 MXene, Co_3O_4, Ti_3C_2, commercial Pt/C and bare glassy carbon electrode in 1M KOH+0.5M urea at a scan rate of 5 mV s^{-1}. **(c)** Tafel plots of Co_3O_4/Ti_3C_2, Co_3O_4, Ti_3C_2 MXene and commercial Pt/C. **(d)** Current density $vs.$ time curve of the Co_3O_4/Ti_3C_2 MXene under the static potential of -0.2 V for 40 h (inset: LSV curves of the Co_3O_4/Ti_3C_2 MXene before and after long-term stability test).
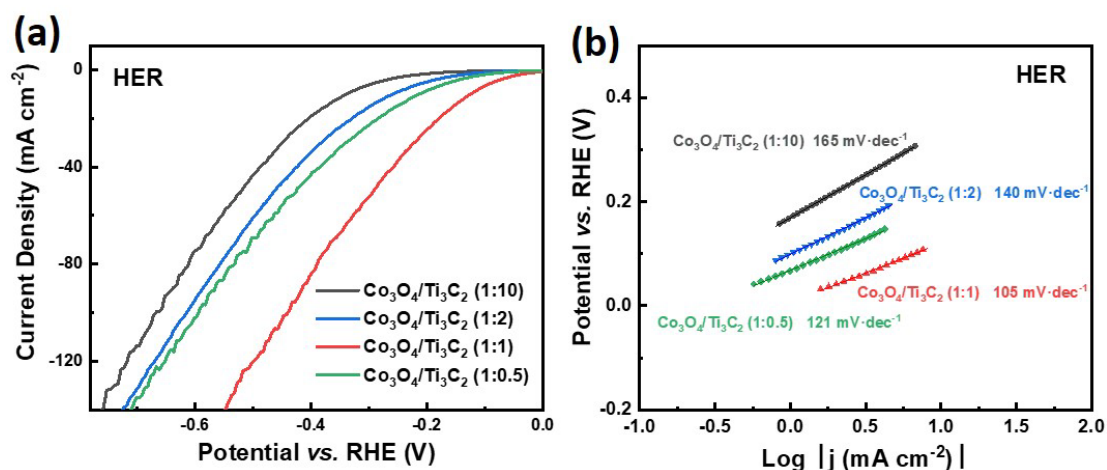
Figure 4.17. **(a)** LSV curves for HER and **(b)** Tafel plots of Co_3O_4/Ti_3C_2 MXene (1:10), Co_3O_4/Ti_3C_2 MXene (1:2), Co_3O_4/Ti_3C_2 MXene (1:1) and Co_3O_4/Ti_3C_2 MXene (1:0.5) in 1M KOH + 0.5M urea, scan rate=5 mV s^{-1}.
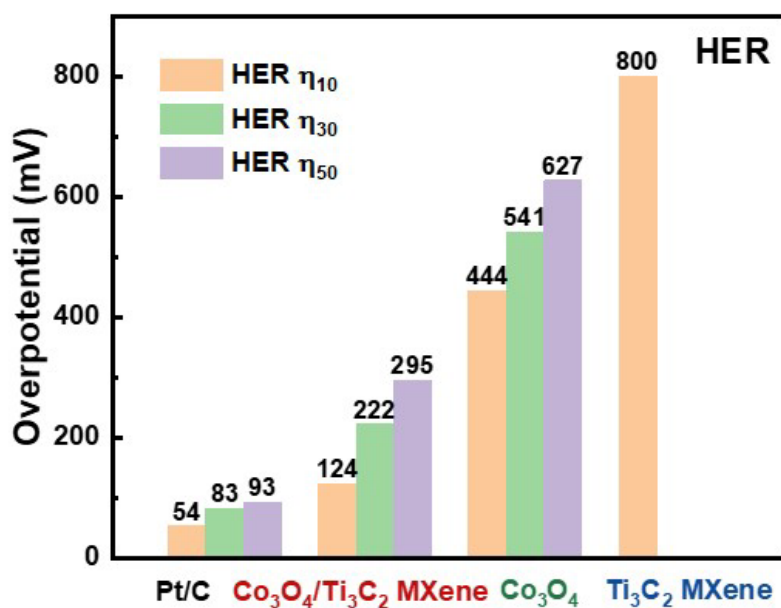
Figure 4.18. The overpotentials of Co_3O_4/Ti_3C_2 MXene, Co_3O_4, Ti_3C_2 MXene and commercial Pt/C at different current densities (10, 30, and 50 mA cm^{-2}) in 1M KOH + 0.5M urea, scan rate=5 mV s^{-1}.

4.2.4. Synergistic Mechanism Analysis

The catalytic activity of Co_3O_4/Ti_3C_2 MXene as an electrode material for UOR

143

and HER has been demonstrated. In order to deeply investigate the kinetic mechanism of the performance improvement of Co_3O_4/Ti_3C_2 MXene, we performed electrochemical impedance spectroscopy (EIS) tests. The semicircle at lower frequencies represents the charge transfer resistance (R_{ct}).[24, 25] It can be seen from the Nyquist plots in **Figure 4.19** that Co_3O_4/Ti_3C_2 MXene featured the smallest radius (R_{ct} = 20.7 Ω) compared with pure Co_3O_4 (R_{ct} = 156.7 Ω) and Ti_3C_2 MXene (R_{ct} = 365.5 Ω), revealing its remarkable electron transport capability (**Table 4.3**).
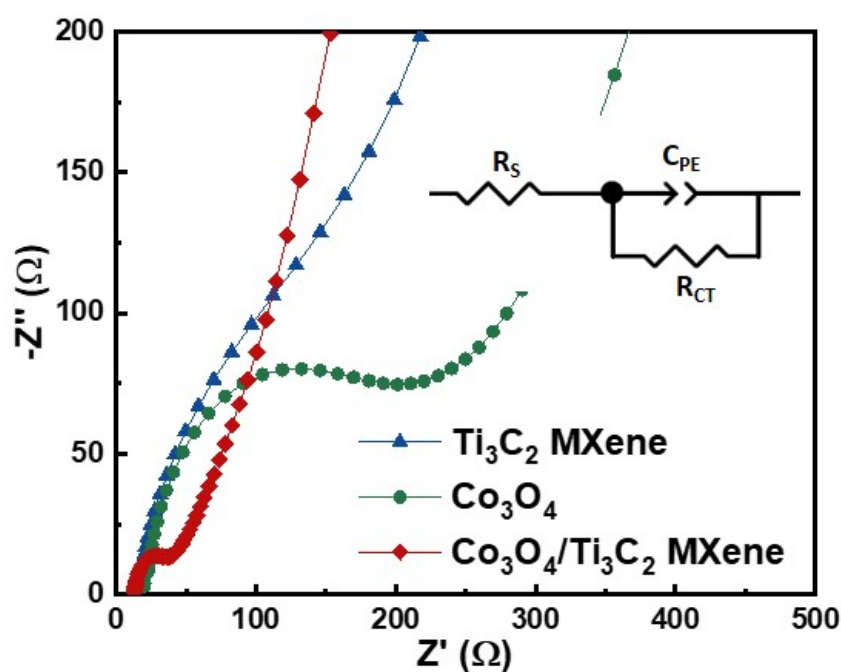
Figure 4.19. Nyquist plots of the Co_3O_4/Ti_3C_2 MXene, Co_3O_4 and Ti_3C_2 MXene from 100 kHz to 0.01 Hz frequency in 1M KOH + 0.5M urea. The insert is the equivalent circuit.

Table 4.3. Solution resistance (R_s) and charge transfer resistance (R_{ct}) values of pure Co_3O_4, Ti_3C_2 MXene and Co_3O_4/Ti_3C_2 MXene.

	R_s /Ω	R_{ct}/Ω
Pure Co_3O_4	15.72	156.7
Ti_3C_2 MXene	13.78	365.5
Co_3O_4/Ti_3C_2 MXene	12.07	20.7

Furthermore, the electrochemically effective surface area (ECSA) plays a key role in catalytic activity as it is related to the number of active sites.[23] ECSA has a linear relationship with the electrochemical double-layer capacitance (C_{dl}),[26] which can be estimated by a typical cyclic voltammetry (CV) method. The CV curves of Ti_3C_2 MXene, Co_3O_4, and Co_3O_4/Ti_3C_2 MXene were acquired at increased scan rates (20-120 mV s^{-1}) within the non-Faradaic region, and the results are displayed in **Figure 4.20(a-c)**. As expected, the C_{dl} of Co_3O_4/Ti_3C_2 MXene (2.3 mF cm^{-2}) is the highest, which is almost ten times larger than those of Ti_3C_2 MXene and Co_3O_4 (**Figure 4.20d**), indicating that more active sites are exposed in Co_3O_4/Ti_3C_2 MXene composite. The above results further confirmed that the 2D multilayer MXene sheets provided a huge surface area for Co_3O_4 nanoparticles, which increased the channels for charge transfer; this strategy reduced the size of Co_3O_4 particles, alleviating the severe agglomeration of Co_3O_4 nanoparticles and enabling more exposed active sites.
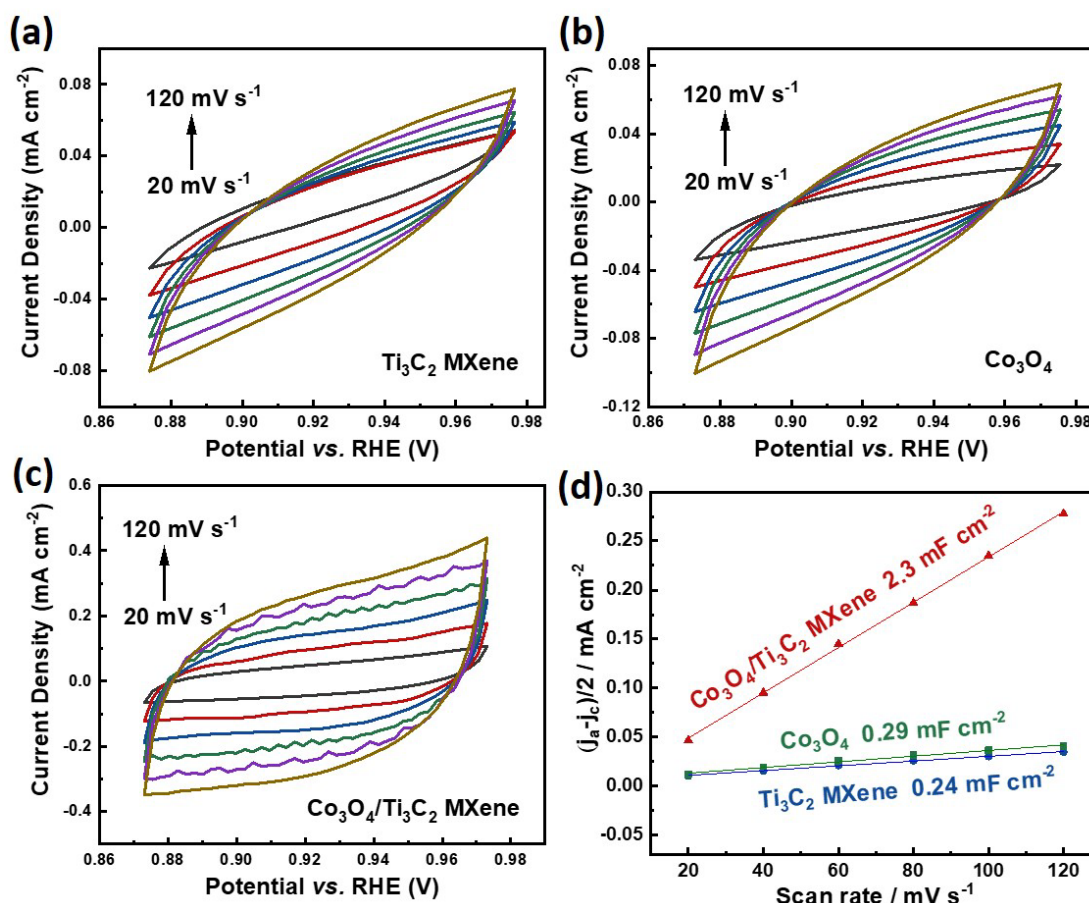
Figure 4.20. Determination of electrochemically effective surface area. Cyclic voltammograms of **(a)** Co_3O_4/Ti_3C_2 MXene, **(b)** Co_3O_4 and **(c)** Ti_3C_2 MXene in the 0.87 to 0.97 V *vs.* RHE potential range at various scan rates. **(d)** Double-layer charging currents of Co_3O_4/Ti_3C_2 MXene, Co_3O_4 and Ti_3C_2 MXene recorded at 0.92 V at various scan rates in 1M KOH + 0.5M urea.

4.2.5. Overall Urea Electrolysis

Taking the performance for UOR and HER into account, a dual-electrode system with Co_3O_4/Ti_3C_2 MXene as both cathode and anode (Co_3O_4/Ti_3C_2 MXene || Co_3O_4/Ti_3C_2 MXene) was constructed to study its practical performance as a catalyst for full urea-containing water splitting. In this way, the complexity of the device can be effectively solved to reduce the cost in practical industrial catalysis.[27] For the

convenience of testing, Co_3O_4/Ti_3C_2 MXene powder sample was dispersed into a uniform slurry and then drop-coated on Ni foam. As shown in the inset of **Figure 4.21a**, in the electrolyte containing urea, urea was oxidized at the anode to produce CO_2 and N_2, and hydrogen evolved at the cathode; without urea, the oxygen evolution reaction occurred at the anode replacing the urea oxidation reaction. **Figure 4.21a** depicts the LSV curves of Co_3O_4/Ti_3C_2 MXene || Co_3O_4/Ti_3C_2 MXene: a driving potential of 1.49 V was required when the current density reached 50 mA cm^{-2}, whereas 1.90 V was necessary in absence of urea (for OER and HER). The catalytic process required 0.41 V less to operate the overall urea-containing water electrolysis, and can effectively reduce the cost in practical applications. To eliminate the influence of Ni foam substrate on the performance, the electrocatalytic performance of bare Ni foam was also tested as cathode and anode (**Figure 4.21b**). It was clearly observed that there was no obvious signal on bare Ni foam, indicating the catalytic activity was attributed to the active materials coated on Ni foam.

In addition, compared with the performance of commercial Pt/C || RuO_2, Co_3O_4/Ti_3C_2 MXene || Co_3O_4/Ti_3C_2 MXene still displayed significant superiority, which validated its suitability as a bifunctional catalyst for overall urea-containing water splitting. For instance, the Co_3O_4/Ti_3C_2 MXene || Co_3O_4/Ti_3C_2 MXene required cell voltages of 1.04, 1.20, 1.32, and 1.41 V at respectively 10, 20, 30, and 40 mA cm^{-2}; these values are lower than 1.46, 1.71, 1.85, and 1.98 V recorded for Pt/C || RuO_2 at the same current densities (**Figure 4.21b**). To further explore this point, the LSV curves of Co_3O_4/Ti_3C_2 MXene, Pt/C, and Ru_2O for UOR and HER are illustrated in **Figure 4.21c**. The operation voltage of the cell at a current density of 10 mA cm^{-2} for Co_3O_4/Ti_3C_2 MXene || Co_3O_4/Ti_3C_2 MXene system was only 1.54 V, which surpassed that of the Pt/C || RuO_2 couple (1.63 V). Similarly, the activity of Co_3O_4/Ti_3C_2 MXene || Co_3O_4/Ti_3C_2 MXene can still maintain 93.56% after 40 h of continuous catalytic

reaction (**Figure 4.21d**). The LSV curve was almost unchanged, so the stability of the bifunctional catalyst was verified. Compared with the reported Co-based bifunctional catalysts, Co_3O_4/Ti_3C_2 MXene showed the smallest applied potential of 1.49 V at 50 mA cm^{-2} (**Figure 4.22** and **Table 4.4**).
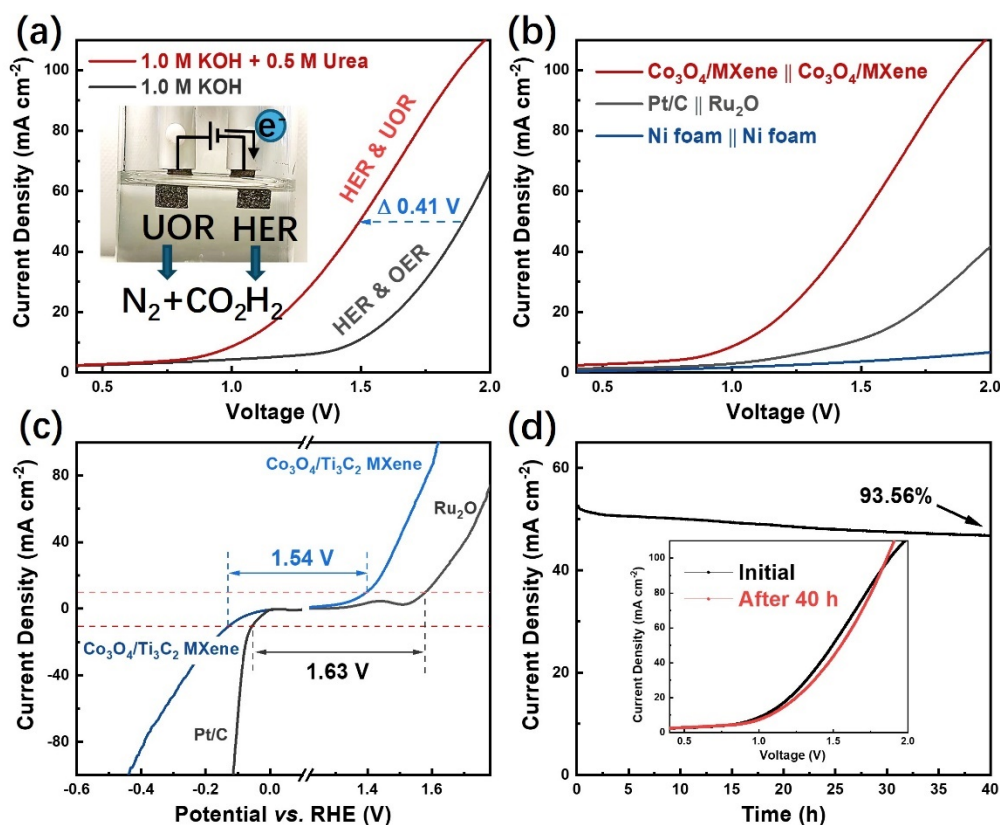

Figure 4.21. Electrocatalytic performance for overall water splitting. (**a**) Polarization curves for the $Co_3O_4/Ti_3C_2 \parallel Co_3O_4/Ti_3C_2$ in 1M KOH with and without 0.5M urea at a scan rate of 5 mV s^{-1} (inset: photograph of the overall water splitting reaction performed using the bifunctional Co_3O_4/Ti_3C_2 MXene catalyst). (**b**) Polarization curves for the $Co_3O_4/Ti_3C_2 \parallel Co_3O_4/Ti_3C_2$, Pt/C $\parallel$ RuO$_2$ and Ni foam $\parallel$ Ni foam in 1M KOH+0.5M urea. (**c**) LSV curves of the Co_3O_4/Ti_3C_2 MXene and Pt/C $\parallel$ RuO$_2$ for HER and UOR, respectively. (**d**) Current density *vs.* time curve of the $Co_3O_4/Ti_3C_2 \parallel Co_3O_4/Ti_3C_2$ under the static potential of 1.5 V for 40 h (inset: LSV curves of the $Co_3O_4/Ti_3C_2 \parallel Co_3O_4/Ti_3C_2$ before and after long-term stability test).
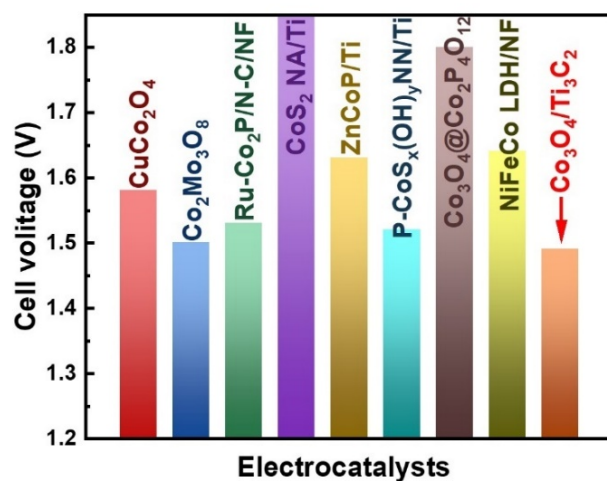
148

Figure 4.22 Comparison of cell voltage of different catalysts for overall urea-containing water splitting.

Table 4.4. Comparison of cell voltage at 50 mA cm^{-2} of reported transition metal-based bi-functional catalysts for urea overall splitting.

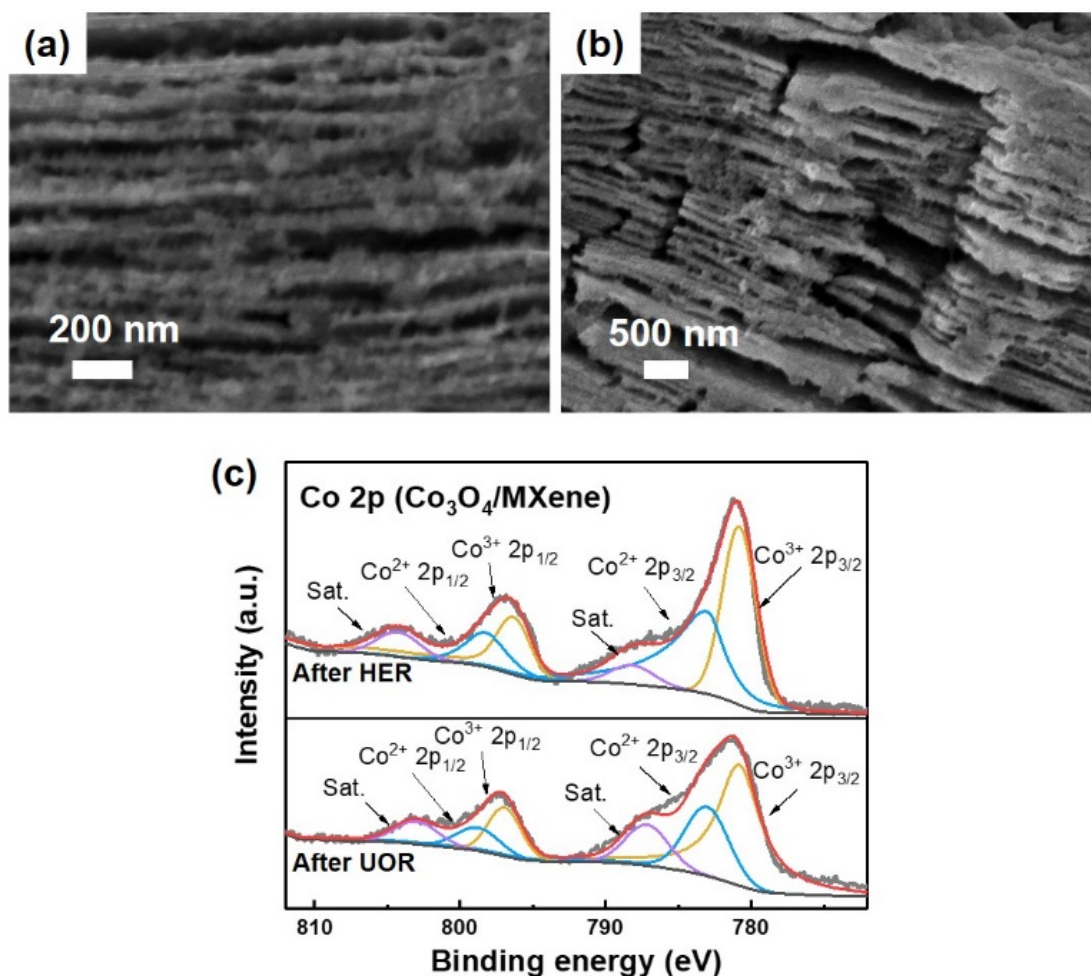|	Cell voltage at 50 mA cm^{-2}	Reference
CoS$_2$ NA/Ti	1.85 V	[15]
CuCo$_2$O$_4$	1.58 V	[28]
Co$_2$Mo$_3$O$_8$	1.50 V	[29]
Ru-Co$_2$P/N-C/NF	1.53 V	[30]
ZnCoP/Ti	1.63 V	[31]
P-CoS$_x$(OH)$_y$NN/Ti	1.52 V	[32]
Co$_3$O$_4$@Co$_2$P$_4$O$_{12}$	>1.80 V	[33]
NiFeCo LDH/NF	1.64 V	[34]
Co$_3$O$_4$/Ti$_3$C$_2$ MXene	**1.49 V**	**This work**

Figure 4.23. SEM image Co_3O_4/Ti_3C_2 MXene composite after (**a**) UOR and (**b**) HER for 40 h. (**c**) High-resolution XPS spectra for Co 2p of Co_3O_4/Ti_3C_2 MXene composite after UOR and HER for 40 h.

As shown in **Figure 4.23(a-b)**, the as-fabricated Co_3O_4/Ti_3C_2 MXene composite retained well the accordion structure with nanoparticles on the surface of sheets after the long-term catalytic process, which supports the stability of Co_3O_4/Ti_3C_2 MXene composite from the morphological point of view. In addition, to examine the change in the chemical composition of Co_3O_4/Ti_3C_2 MXene composite after the 40 h electrocatalytic process, high-resolution XPS spectra for Co 2p of Co_3O_4/Ti_3C_2 MXene

composite after UOR and HER are depicted in **Figure 4.23(c)**. The valence state of Co had no obvious change compared with that before long-time stability test (**Figure 4.9c**). It is worth mentioning that, after the UOR process, the intensity of the peak of Co 2p was slightly weakened and the relative peak area of Co^{3+} became larger. This shows that in the UOR catalytic process, Co_3O_4 was further oxidized to form more +3-valent Co ions, which will be more conducive to its adsorption of ^-OH in the alkaline electrolyte, thereby improving the catalytic activity. For HER, Co reduction was not that obvious. Indeed, the increase of Co^{2+} content after the HER test is about 1 at.%, as compared to about 10 at.% after the UOR test. Therefore, it is hard to conclude with accuracy the reduction of Co^{3+} during the HER process.

To further assess its electrocatalytic efficacy toward the HER and support electrochemical results, faradaic efficiency (FE) measurements were also carried out on the best-performing catalyst, Co_3O_4/Ti_3C_2. As shown in **Figure 4.24**, the H_2 amount measured by Co_3O_4/Ti_3C_2 MXene as cathode catalyst was almost in agreement with the calculated value, which presents a Faradaic efficiency (FE) of 97.9% close to 100%, demonstrating its real gas production performance.
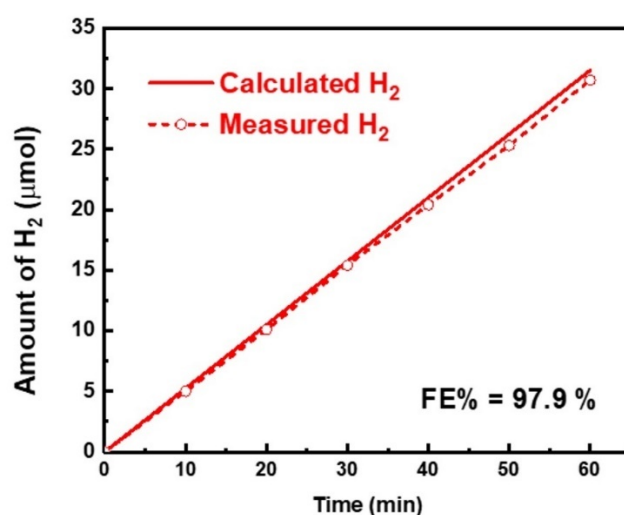

Figure 4.24. Amount of hydrogen *vs.* time for Co_3O_4/Ti_3C_2 MXene.

4.3 Conclusion

In summary, a novel 0D/2D Co_3O_4/Ti_3C_2 MXene composite was synthesized by a simple solution reaction under mild conditions. As an efficient and stable bifunctional electrocatalyst for urea oxidation reaction (UOR) and hydrogen evolution reaction (HER) in basic medium, it showed improved performance compared to pure Ti_3C_2 MXene and Co_3O_4, solving the problem of insufficient exposure of active sites caused by too large particle size and agglomeration of Co_3O_4 particles. It is worth mentioning that the overall water splitting cell constructed using Co_3O_4/Ti_3C_2 MXene as a catalyst could maintain its catalytic activity for over 40 h. Its high efficiency, stability, and practical applicability as a bifunctional electrocatalyst have been fully verified. This work provided a new strategy for the application of cheap abundant materials for energy-saving H_2 production coupled with urea containing wastewater purification. In a follow up study, it will be interesting to assess the catalytic performance of Co_3O_4 supported on single-layer or few-layer MXene nanosheets to gain further understanding on the influence of the MXene structure on the catalytic activity.

References

(1) Xiong, D.; Li, X.; Bai, Z.; Lu, S. Recent Advances in Layered $Ti_3C_2T_x$ MXene for Electrochemical Energy Storage. *Small* **2018**, *14* (17), e1703419.

(2) Liu, H.; Hu, R.; Qi, J.; Sui, Y.; He, Y.; Meng, Q.; Wei, F.; Ren, Y.; Zhao, Y.; Wei, W. One-Step Synthesis of Nanostructured CoS_2 Grown on Titanium Carbide MXene for High-Performance Asymmetrical Supercapacitors. *Advanced Materials Interfaces* **2020**, *7* (6), 1901659.

(3) Le, T. A.; Tran, N. Q.; Hong, Y.; Kim, M.; Lee, H. Porosity-Engineering of MXene as a Support Material for a Highly Efficient Electrocatalyst toward Overall Water Splitting. *ChemSusChem* **2020**, *13* (5), 945-955.

(4) Zhang, J.; Zhao, Y.; Guo, X.; Chen, C.; Dong, C.-L.; Liu, R.-S.; Han, C.-P.; Li, Y.;

Gogotsi, Y.; Wang, G. Single Platinum Atoms Immobilized on an MXene as an Efficient Catalyst for the Hydrogen Evolution Reaction. *Nature Catalysis* **2018**, *1* (12), 985-992.

(5) Ramalingam, V.; Varadhan, P.; Fu, H. C.; Kim, H.; Zhang, D.; Chen, S.; Song, L.; Ma, D.; Wang, Y.; Alshareef, H. N.; et al. Heteroatom-Mediated Interactions between Ruthenium Single Atoms and an MXene Support for Efficient Hydrogen Evolution. *Advanced Materials* **2019**, *31* (48), e1903841.

(6) Zou, H.; He, B.; Kuang, P.; Yu, J.; Fan, K. Metal-Organic Framework-Derived Nickel-Cobalt Sulfide on Ultrathin Mxene Nanosheets for Electrocatalytic Oxygen Evolution. *ACS Applied Materials & Interfaces* **2018**, *10* (26), 22311-22319.

(7) Lu, Y.; Fan, D.; Chen, Z.; Xiao, W.; Cao, C.; Yang, X. Anchoring Co_3O_4 Nanoparticles on MXene for Efficient Electrocatalytic Oxygen Evolution. *Science Bulletin* **2020**, *65* (6), 460-466.

(8) Jian, X.; He, M.; Chen, L.; Zhang, M.-m.; Li, R.; Gao, L.-j.; Fu, F.; Liang, Z.-h. Three-dimensional Carambola-like MXene/Polypyrrole Composite Produced by One-step Co-electrodeposition Method for Electrochemical Energy Storage. *Electrochimica Acta* **2019**, *318*, 820-827.

(9) Cheng, L.; Chen, Q.; Li, J.; Liu, H. Boosting the Photocatalytic Activity of $CdLa_2S_4$ for Hydrogen Production using Ti_3C_2 MXene as a Co-catalyst. *Applied Catalysis B: Environmental* **2020**, *267*, 118379.

(10) Zhuang, Y.; Liu, Y.; Meng, X. Fabrication of TiO_2 Nanofibers/MXene Ti_3C_2 Nanocomposites for Photocatalytic H_2 Evolution by Electrostatic Self-assembly. *Applied Surface Science* **2019**, *496*, 143647.

(11) Rakhi, R. B.; Ahmed, B.; Hedhili, M. N.; Anjum, D. H.; Alshareef, H. N. Effect of Postetch Annealing Gas Composition on the Structural and Electrochemical Properties of Ti_2CT_x MXene Electrodes for Supercapacitor Applications. *Chemistry of Materials* **2015**, *27* (15), 5314-5323.

(12) Xie, Q.; Song, R.; Zhao, P.; Zhang, Y.; Wu, S.; Xie, D. In-plane Porous Co_3O_4 Nanosheet Assembled 3D Hierarchical Clusters Grown on Stainless Steel Mesh as Binder-free Anodes for High Performance Lithium Ion Batteries. *Journal of Materials*

Chemistry A **2018**, *6* (18), 8388-8395.

(13) Deng, R.; Chen, B.; Li, H.; Zhang, K.; Zhang, T.; Yu, Y.; Song, L. MXene/Co_3O_4 Composite Material: Stable Synthesis and its Enhanced Broadband Microwave Absorption. *Applied Surface Science* **2019**, *488*, 921-930.

(14) Yoon, J.; Lee, D.; Lee, E.; Yoon, Y. S.; Kim, D.-J. Ag/ZnO Catalysts with Different ZnO Nanostructures for Non-enzymatic Detection of Urea. *Electroanalysis* **2019**, *31* (1), 17-21.

(15) Wei, S.; Wang, X.; Wang, J.; Sun, X.; Cui, L.; Yang, W.; Zheng, Y.; Liu, J. CoS_2 Nanoneedle Array on Ti Mesh: A Stable and Efficient Bifunctional Electrocatalyst for Urea-assisted Electrolytic Hydrogen Production. *Electrochimica Acta* **2017**, *246*, 776-782.

(16) Chen, Z.; Xu, X.; Ding, Z.; Wang, K.; Sun, X.; Lu, T.; Konarova, M.; Eguchi, M.; Shapter, J. G.; Pan, L.; et al. Ti_3C_2 MXenes-derived $NaTi_2(PO_4)_3$/MXene Nanohybrid for Fast and Efficient Hybrid Capacitive Deionization Performance. *Chemical Engineering Journal* **2021**, *407*, 127148.

(17) Huang, S.; Wu, Y.; Fu, J.; Xin, P.; Zhang, Q.; Jin, Z.; Zhang, J.; Hu, Z.; Chen, Z. Hierarchical CoFe LDH/MOF Nanorods Array with Strong Coupling Effect Grown on Carbon Cloth Enables Efficient Oxidation of Water and Urea. *Nanotechnology* **2021**, *32* (38), 385405.

(18) Choi, H.; Surendran, S.; Kim, D.; Lim, Y.; Lim, J.; Park, J.; Kim, J. K.; Han, M.-K.; Sim, U. Boosting Eco-friendly Hydrogen Generation by Urea-assisted Water Electrolysis using Spinel M_2GeO_4 (M=Fe,Co) as an Active Electrocatalyst. *Environmental Science: Nano* **2021**, *8* (11), 3110-3121.

(19) Liu, D.; Liu, T.; Zhang, L.; Qu, F.; Du, G.; Asiri, A. M.; Sun, X. High-performance Urea Electrolysis Towards Less Energy-intensive Electrochemical Hydrogen Production using a Bifunctional Catalyst Electrode. *Journal of Materials Chemistry A* **2017**, *5* (7), 3208-3213.

(20) Feng, S.; Luo, J.; Li, J.; Yu, Y.; Kang, Z.; Huang, W.; Chen, Q.; Deng, P.; Shen, Y.; Tian, X. Heterogeneous Structured Ni_3Se_2/MoO_2@$Ni_{12}P_5$ Catalyst for Durable Urea

Oxidation Reaction. *Materials Today Physics* **2022**, *23*, 100646.

(21) Hu, S.; Wang, S.; Feng, C.; Wu, H.; Zhang, J.; Mei, H. Novel MOF-Derived Nickel Nitride as High-Performance Bifunctional Electrocatalysts for Hydrogen Evolution and Urea Oxidation. *ACS Sustainable Chemistry & Engineering* **2020**, *8* (19), 7414-7422.

(22) Bi, J.; Ying, H.; Hao, J.; Li, Z. Application of Metal Chalcogenide-based Anodic Electrocatalyst toward Substituting Oxygen Evolution Reaction in Water Splitting. *Current Opinion in Electrochemistry* **2022**, *33*, 100963.

(23) Zuo, G.; Wang, Y.; Teo, W. L.; Xie, A.; Guo, Y.; Dai, Y.; Zhou, W.; Jana, D.; Xian, Q.; Dong, W.; et al. Enhanced Photocatalytic Water Oxidation by Hierarchical 2D-Bi_2MoO_6@2D-MXene Schottky Junction Nanohybrid. *Chemical Engineering Journal* **2021**, *403*, 126328.

(24) Li, M.; Wang, Y.; Li, T.; Li, J.; Huang, L.; Liu, Q.; Gu, J.; Zhang, D. Hierarchical Few-layer Fluorine-free $Ti_3C_2T_X$ (T=O,OH)/MoS_2 Hybrid for Efficient Electrocatalytic Hydrogen Evolution. *Journal of Materials Chemistry A* **2021**, *9* (2), 922-927.

(25) Liang, X.; Yun, J.; Xu, K.; Xiang, H.; Wang, Y.; Sun, Y.; Yu, Y. A Multi-layered Ti_3C_2/Li_2S Composite as Cathode Material for Advanced Lithium-sulfur Batteries. *Journal of Energy Chemistry* **2019**, *39*, 176-181.

(26) Lu, S.; Hummel, M.; Gu, Z.; Wang, Y.; Wang, K.; Pathak, R.; Zhou, Y.; Jia, H.; Qi, X.; Zhao, X.; et al. Highly Efficient Urea Oxidation via Nesting Nano-Nickel Oxide in Eggshell Membrane-Derived Carbon. *ACS Sustainable Chemistry & Engineering* **2021**, *9* (4), 1703-1713.

(27) Wu, L.; Zhang, M.; Wen, Z.; Ci, S. V_8C_7 Decorating CoP Nanosheets-assembled Microspheres as Trifunctional Catalysts toward Energy-saving Electrolytic Hydrogen Production. *Chemical Engineering Journal* **2020**, *399*, 125728.

(28) Zequine, C.; Wang, F.; Li, X.; Guragain, D.; Mishra, S. R.; Siam, K.; Kahol, P.; Gupta, R. Nanosheets of $CuCo_2O_4$ As a High-Performance Electrocatalyst in Urea Oxidation. *Applied Sciences* **2019**, *9* (4), 793.

(29) Zhang, K.; Liu, C.; Graham, N.; Zhang, G.; Yu, W. Modulation of Dual Centers on Cobalt-molybdenum Oxides Featuring Synergistic Effect of Intermediate Activation

and Radical Mediator for Electrocatalytic Urea Splitting. *Nano Energy* **2021**, *87*, 106217.

(30) Xu, Y.; Ren, T.; Ren, K.; Yu, S.; Liu, M.; Wang, Z.; Li, X.; Wang, L.; Wang, H. Metal-organic Frameworks-derived Ru-doped Co_2P/N-doped Carbon Composite Nanosheet Arrays as Bifunctional Electrocatalysts for Hydrogen Evolution and Urea Oxidation. *Chemical Engineering Journal* **2021**, *408*, 127308.

(31) Liu, T.; Liu, D.; Qu, F.; Wang, D.; Zhang, L.; Ge, R.; Hao, S.; Ma, Y.; Du, G.; Asiri, A. M.; et al. Enhanced Electrocatalysis for Energy-Efficient Hydrogen Production over CoP Catalyst with Nonelectroactive Zn as a Promoter. *Advanced Energy Materials* **2017**, *7* (15), 1700020.

(32) Jiang, Y.; Gao, S.; Xu, G.; Song, X. Porous and Amorphous Cobalt Hydroxysulfide Core-shell Nanoneedles on Ti-mesh as a Bifunctional Electrocatalyst for Energy-Efficient Hydrogen Production via Urea Electrolysis. *Journal of Materials Chemistry A* **2021**, *9* (9), 5664-5674.

(33) Du, X.; Zhang, X. Dual-functional Co_3O_4@$Co_2P_4O_{12}$ Nanoneedles Supported on Nickel Foams with Enhanced Electrochemical Performance and Excellent Stability for Overall Urea Splitting. *International Journal of Hydrogen Energy* **2019**, *44* (45), 24705-24711.

(34) Babar, P.; Lokhande, A.; Karade, V.; Pawar, B.; Gang, M. G.; Pawar, S.; Kim, J. H. Bifunctional 2D Electrocatalysts of Transition Metal Hydroxide Nanosheet Arrays for Water Splitting and Urea Electrolysis. *ACS Sustainable Chemistry & Engineering* **2019**, *7* (11), 10035-10043.

Chapter 5. Coupling with Anodic Formaldehyde Oxidation for Dual Hydrogen Production over Cu_2O-Supported Mo_2TiC_2 MXene Clusters
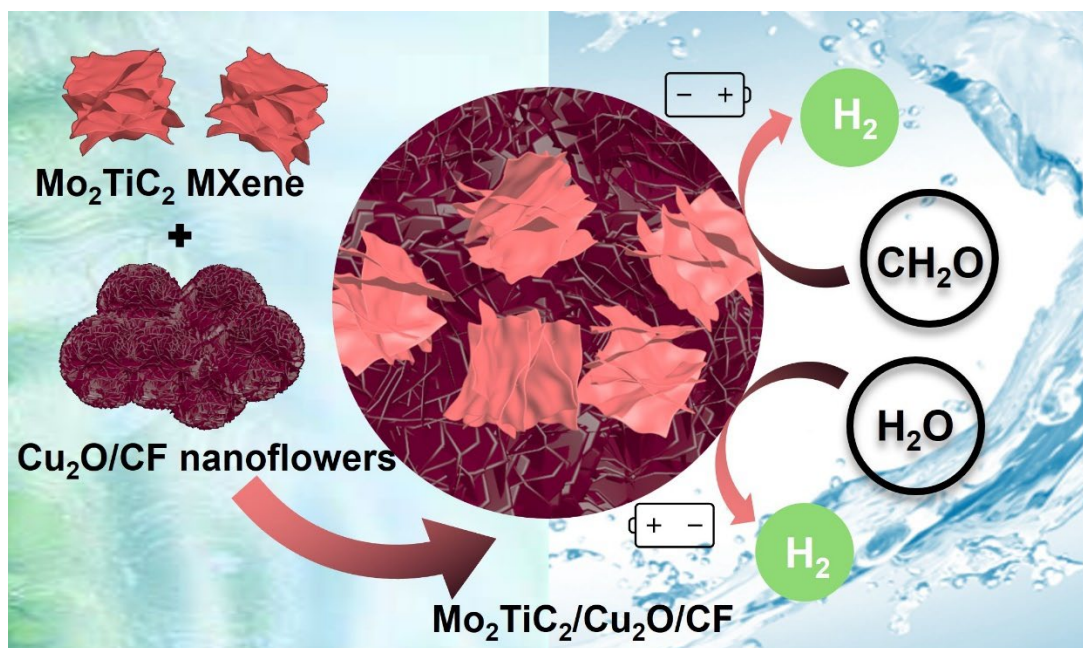
Abstract

As the global shift towards renewable energy accelerates, the quest for efficient hydrogen (H_2) production methods becomes increasingly urgent.[1] Electrolysis-based overall water splitting (OWS) holds promise for H_2 generation due to its environmental benefits, yet it faces challenges like high energy requirements, particularly from the oxygen evolution reaction (OER).[2] Anodic oxidation emerges as an alternative to traditional OER, offering low-voltage decomposition of various organics.[3] Notably, formaldehyde oxidation reaction (FOR) stands out for its dual hydrogen production capability, enhancing both cathodic hydrogen evolution reaction (HER) and anodic hydrogen release.[1, 4-7] By leveraging MXenes and Cu_2O nanoflowers, this study introduces Cu_2O-supported Mo_2TiC_2 MXene clusters as a catalyst system for improved dual hydrogen production *via* coupled HER and FOR. For overall formaldehyde electrolysis, it required a cell voltage of only 0.36 V to achieve a current density of 50 $mA\,cm^{-2}$, which is 1.49 V lower than the voltage required for pure water splitting at the same current density. The investigation focuses on catalytic efficiency, stability, and mechanistic pathways, aiming to advance both theoretical understanding and practical implementation in sustainable energy systems.

5.1 Experimental section

5.1.1 Synthesis of Molybdenum-Titanium Carbide (Mo$_2$TiC$_2$) MXene nanoclusters

The preparation of Mo$_2$TiC$_2$ MXene nanoclusters involved the liquid etching of the precursor Mo$_2$TiAlC$_2$ bulk phase. Initially, a solution was prepared by dissolving 1g of lithium fluoride (LiF) in 15 mL of 9M hydrochloric acid (HCl). This solution was stirred at 400 rpm for an hour at 55°C in a 100 mL Teflon beaker until LiF was fully dissolved. Then, 1 g of Mo$_2$TiAlC$_2$ was gradually added to the solution while stirring. The mixture was maintained at 55 °C for 72 hours with continuous stirring. The resulting suspension was centrifuged for 10 minutes at 3500 rpm. The supernatant was discarded by post-centrifugation, and deionized water was added to the suspension, followed by shaking and sonication for 10 minutes. The process of centrifugation and cleaning was repeated until the pH was neutral. The resulting precipitate, which was accordion-shaped Mo$_2$TiC$_2$ MXene, was dispersed in deionized water and sonicated for 1 hour. The precipitate was collected after high-speed centrifugation (10000 rpm, 10 minutes) and re-dispersed in deionized water using ultrasonication. The supernatant suspension obtained from low-speed centrifugation (3500 rpm, 10 minutes) contained Mo$_2$TiC$_2$ MXene nanoclusters. After adjusting the concentration, the resulting delaminated MXene nanoclusters were stored in nitrogen-saturated deionized water to prevent oxidation.

5.1.2 Preparation of Cu$_2$O/CF

Copper foam (CF, 1 × 1.5 × 0.1 cm^2) was ultrasonically cleaned with acetone, diluted HCl (0.5 M) and deionized water to remove oxidized layer thickness. 7.2 g NaOH and 2.74 g (NH$_4$)$_2$S$_2$O$_8$ were dissolved separately in 30 mL DI water; the two solutions were then mixed at 60 °C and stirred thoroughly. A piece of clean CF was

completely immersed in this mixture for 30 minutes at 60°C. It was turned over once halfway through. It was then rinsed several times sequentially with water and ethanol. At this point, the CF surface was oxidized to copper hydroxide ($Cu(OH)_2$) with the color change to blue-black ($Cu(OH)_2$ and CuO mixture). Subsequently, the piece of foam was dried in oven at 60°C overnight, and the lattice water was further stripped out to give CuO (totally black). To synthesize Cu_2O/CF nanosheets, the obtained CuO/CF was immersed in a solution containing 40 mL of 1 M KOH/HCHO for 1 hour and then rinsed 3 times with water and ethanol, followed by drying at room temperature.

5.1.3 Synthesis of Mo_2TiC_2/CF and Mo_2TiC_2/Cu_2O/CF

In short, Mo_2TiC_2/CF and Mo_2TiC_2/Cu_2O/CF were synthesized by adopting the following procedure. A piece of obtained Cu_2O/CF was completely soaked in Mo_2TiC_2 MXene nanoclusters solution (1 mg mL^{-1}) for 15 minutes and then dried for 10 minutes at 60 °C in oven; this process was repeated 2 times, and the resulting Mo_2TiC_2/CF was rinsed with water thoroughly and dried at 60 °C for 2 hours to yield Mo_2TiC_2/Cu_2O/CF. The control sample (Mo_2TiC_2/CF) was prepared using a piece of clean CF to replace the piece of Cu_2O/CF.

5.2 Results and discussion

5.2.1. Fabrication and Characterization of the Mo_2TiC_2/Cu_2O/CF

Mo_2TiC_2 nanosheets were synthesized by a top-down wet chemical etching combined with a liquid-phase exfoliation process, in which the aluminum layer in the Mo_2TiAlC_2 was first etched with a hydrofluoric acid (HF) solution, then delaminated by ultrasonic waves, as shown in **Figure 5.1**. The stone-like Mo_2TiAlC_2 MAX phase was selectively etched in HF to dissolve the atomic layer of aluminum. **Figure 5.2(a)** depicts the scanning electron microscope (SEM) image of the Mo_2TiAlC_2 MAX

precursor, in which its tightly packed laminar structure could be observed. After HF etching, Mo_2TiC_2 MXene was obtained as the Al element in Mo_2TiAlC_2 was removed, showing an accordion-like multilayer morphology, as shown in **Figure 5.2(b)**. Finally, after ultrasonic exfoliation, Mo_2TiC_2 MXene nanoclusters were prepared, as shown in **Figure 5.2(c,d)**. The clusters are approximately 500 nm in size and consist of layered single or few-layer Mo_2TiC_2 MXene nanosheets.
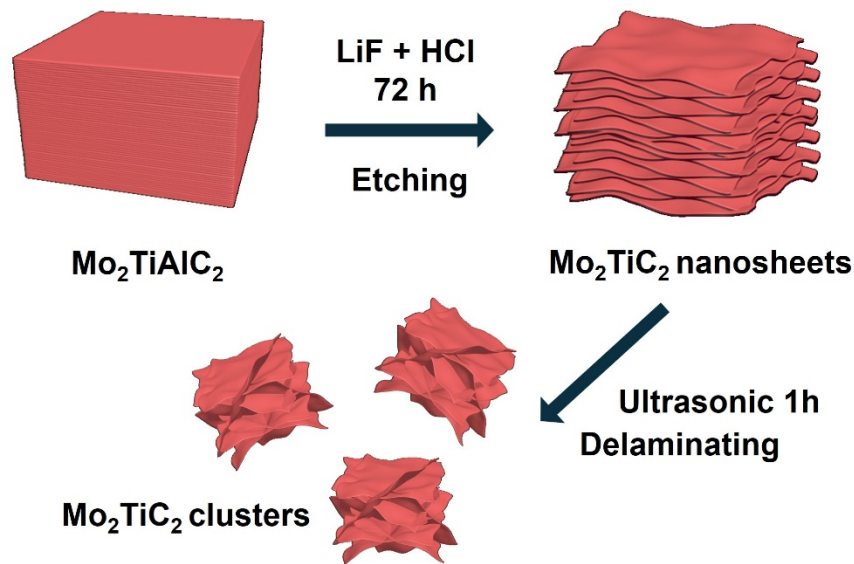

Figure 5.1. Schematic illustration of the preparation of $Mo_2TiC_2/Cu_2O/CF$.
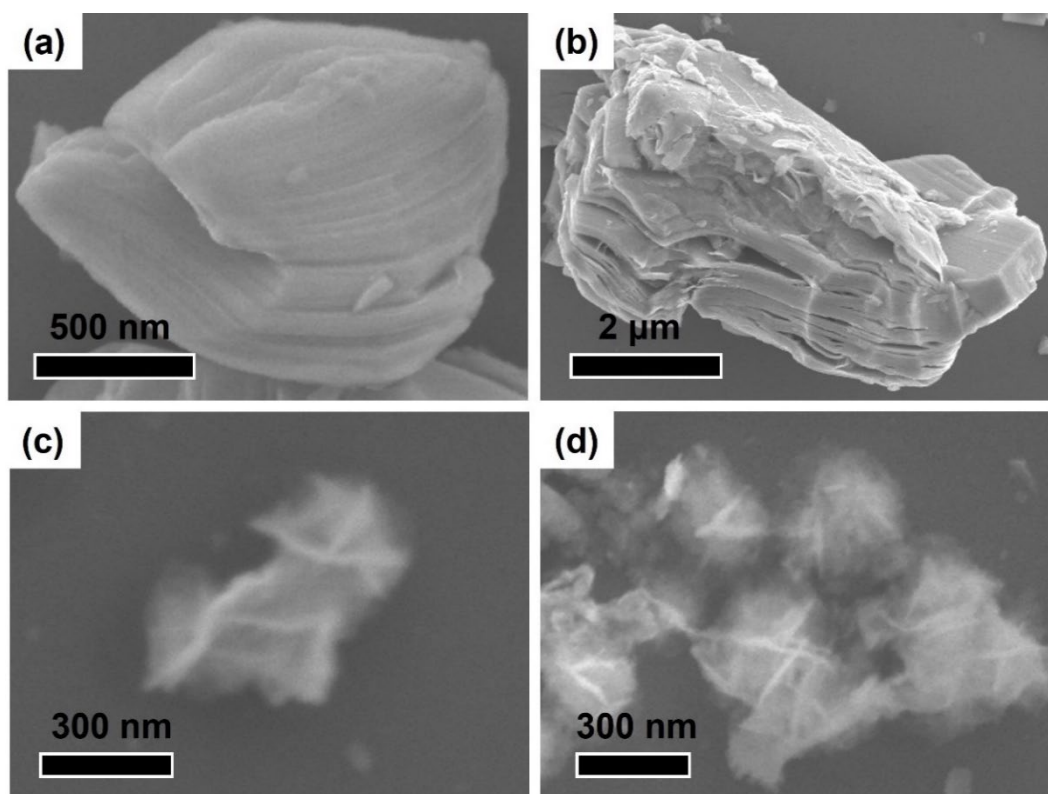
Figure 5.2. SEM images of (**a**) the bulk Mo_2TiAlC_2 MAX phase, (**b**) accordion-like layered Mo_2TiC_2 MXene nanosheets and (**c,d**) Mo_2TiC_2 nanoclusters.

The brief preparation process of Mo_2TiC_2/Cu_2O composites is shown in **Figure 5.3**. Copper foam (CF) has a porous 3D network structure (**Figure 5.4a,b**) with uniformly distributed pores, providing a high surface area. The cleaned CF surface is smooth and has a certain rough structure, which increases active reaction sites, making it suitable for electrochemical and catalytic applications.
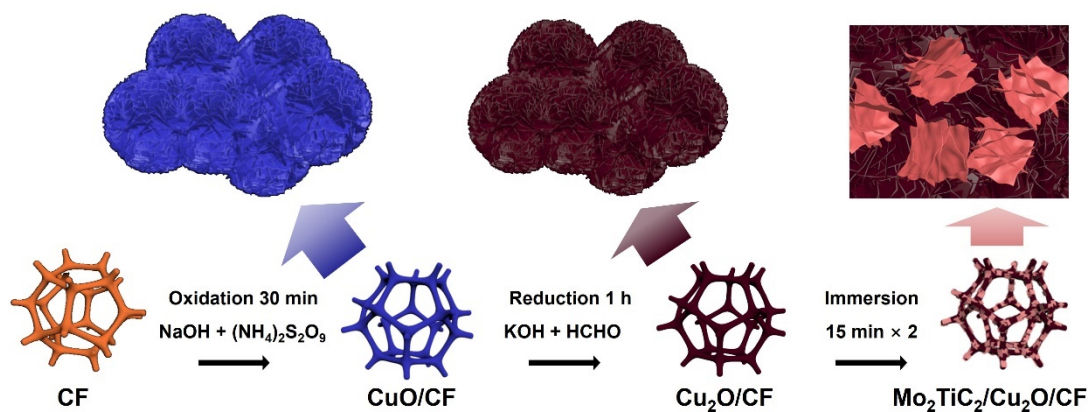
Figure 5.3. Schematic illustration of the preparation of $Mo_2TiC_2/Cu_2O/CF$ composites.
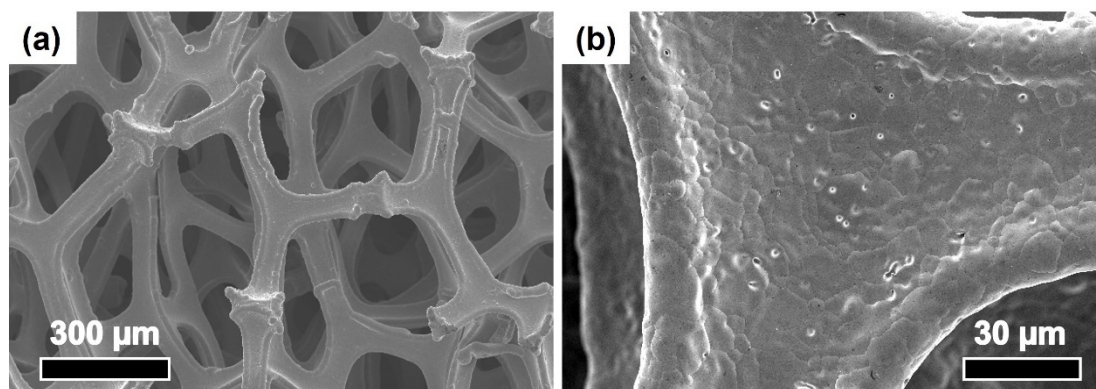
Figure 5.4. SEM images of bare copper foam (CF) at (**a**) low and (**b**) high magnifications.

Subsequently, a Cu_2O catalyst with a two-dimensional flake-like structure (**Figure 5.5c,d**) was prepared from CF using a two-step chemical method (**Figure 5.3**) to investigate the HCHO oxidation reaction. Firstly, the elemental copper on the CF surface was oxidized to divalent CuO, as shown in **Figure 5.5(a,b)**. Subsequently, the divalent copper was reduced to monovalent Cu_2O, with no significant change in morphology, retaining the nanoflower structure composed of two-dimensional

nanoflakes. The $Mo_2TiC_2/Cu_2O/CF$ composites were synthesized by a simple soaking method, which is attributed to the electrostatic effect due to the difference in surface charges of MXene and Cu_2O. After strong acid etching, many negatively charged functional groups, such as -F, -OH, and =O,[8] form on the surface of Mo_2TiC_2 MXene nanosheets, resulting in a strongly negatively charged surface. The Cu_2O surface carries a positive charge,[9] which can electrostatically attract the negatively charged MXene surface, thereby coupling the two to produce the $Mo_2TiC_2/Cu_2O/CF$ composite. **Figure 5.6** shows the final morphology of $Mo_2TiC_2/Cu_2O/CF$ composite. It could be seen that the basic morphology of Cu_2O on the CF framework was maintained, with additional clusters of Mo_2TiC_2 nanosheets loaded on top (as indicated by the red arrow).
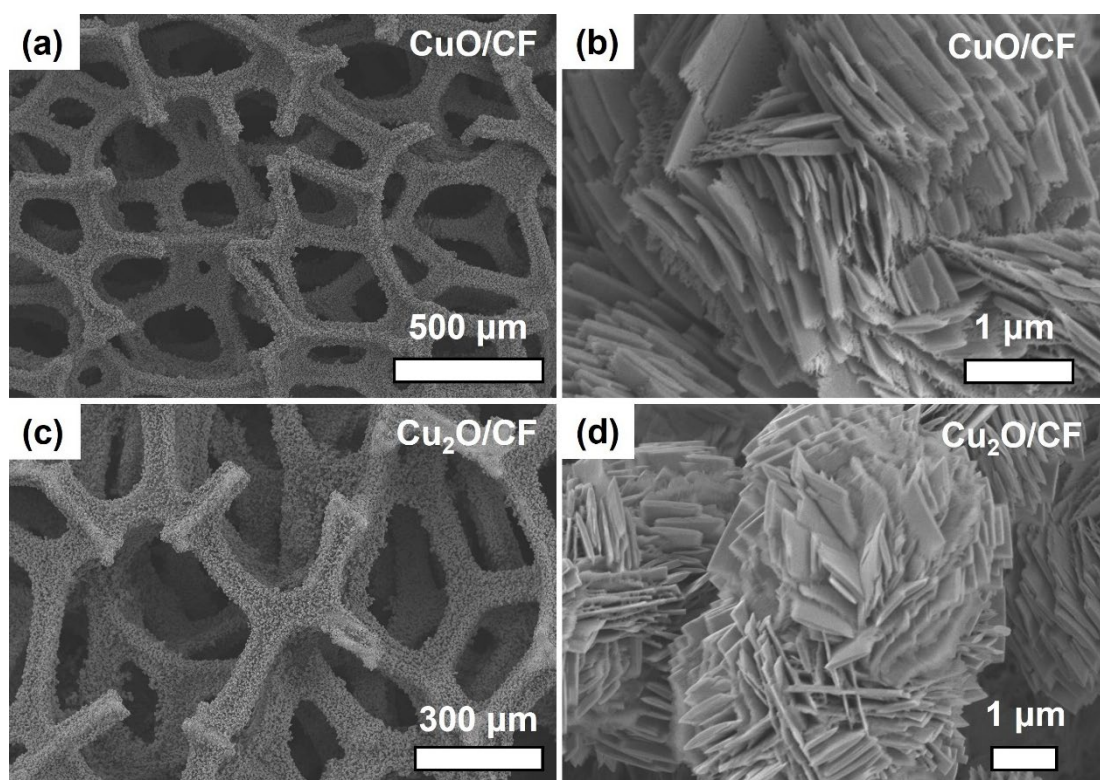

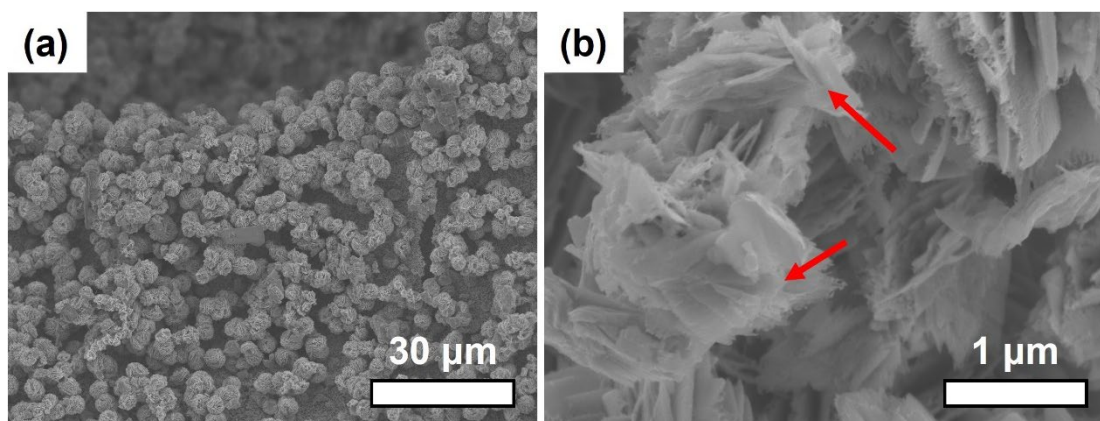**Figure 5.5**. SEM images of **(a,b)** CuO/CF and **(c,d)** Cu_2O/CF at **(a,c)** low and **(b,d)** high magnifications.

Figure 5.6. (a,b) SEM images of $Mo_2TiC_2/Cu_2O/CF$ composite at different magnifications.

X-ray diffraction (XRD) was conducted to examine the structural properties of the prepared electrode materials. **Figure 5.7** presents the XRD patterns of the Mo_2TiAlC_2 MAX phase and the exfoliated Mo_2TiC_2 MXene. The Mo_2TiAlC_2 MAX phase precursor depicts main diffraction peaks at 2θ values of 9.4°, 19.0°, and 28.6°, corresponding to the (002), (004), and (006) planes, respectively. After treating the MAX precursor with HF, these peaks shifted to lower angles at 6.6°, 13.2°, and 18.9°, corresponding to the (002), (004), and (006) planes, respectively, which aligns with previously reported data.[8, 10, 11] This shift towards lower angles indicates an increase in d-spacing and the c-lattice parameter due to the intercalation of water molecules and the attachment of surface terminal groups among the MXene sheets, which replace the A element.[12] The (002) peak of Mo_2TiC_2 MXene is more intense compared to the (002) peak of Mo_2TiAlC_2 MAX, suggesting that the selective etching of the "Al" layer and the attachment of surface functional groups reduced defects in the original Mo_2TiAlC_2 structure, thereby improving structural stability and overall crystallinity of Mo_2TiC_2. Additionally, the diffraction peaks between 35° and 45° correspond to a small fraction of unreacted MAX phase in the MXene sample.
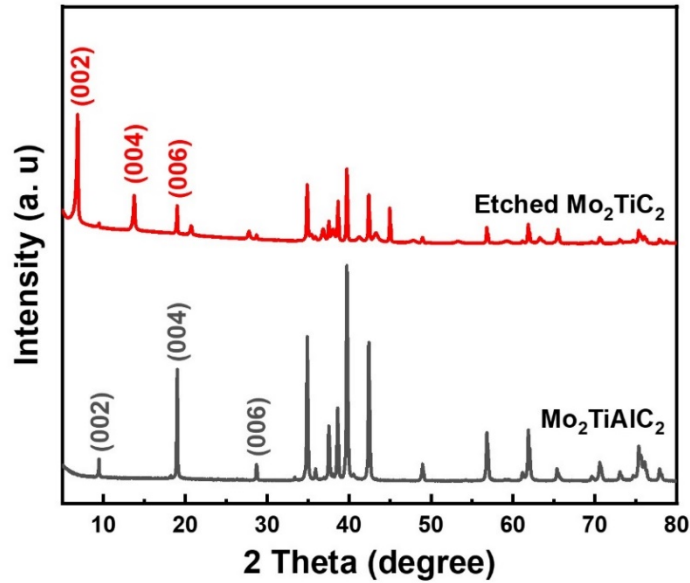
Figure 5.7. XRD patterns of Mo_2TiAlC_2 MAX phase and Mo_2TiC_2 MXene powders.

Figure 5.8 examines the XRD patterns of the CF, CuO/CF, Cu_2O/CF, and Mo_2TiC_2/Cu_2O/CF composite. The clean pure copper foam shows diffraction peaks at 2θ angles of 43.3°, 50.4°, and 74.1°, corresponding to the (111), (200), and (220) crystal planes of elemental copper (PDF #04-0836).[13] After surface oxidation, CuO/CF exhibits characteristic peaks corresponding to both CuO (PDF #48-1548) and $Cu(OH)_2$ (PDF #13-0420).[14] The formation of $Cu(OH)_2$ is due to the CuO lattice readily absorbing water molecules. Subsequently, Cu_2O/CF was obtained through reduction, and its XRD pattern comprises diffraction peaks at 36.4°, 42.3°, and 61.3°, ascribed respectively to the (111), (200), and (220) planes of the standard Cu_2O reference (PDF #05-0667).[15] After loading Mo_2TiC_2 MXene onto the Cu_2O nanoflowers, the XRD pattern did not display characteristic peaks of Mo_2TiC_2 MXene. This is because the peak intensity of the Mo_2TiC_2 MXene sheets is much lower than that of the Cu-based materials, thus being obscured.
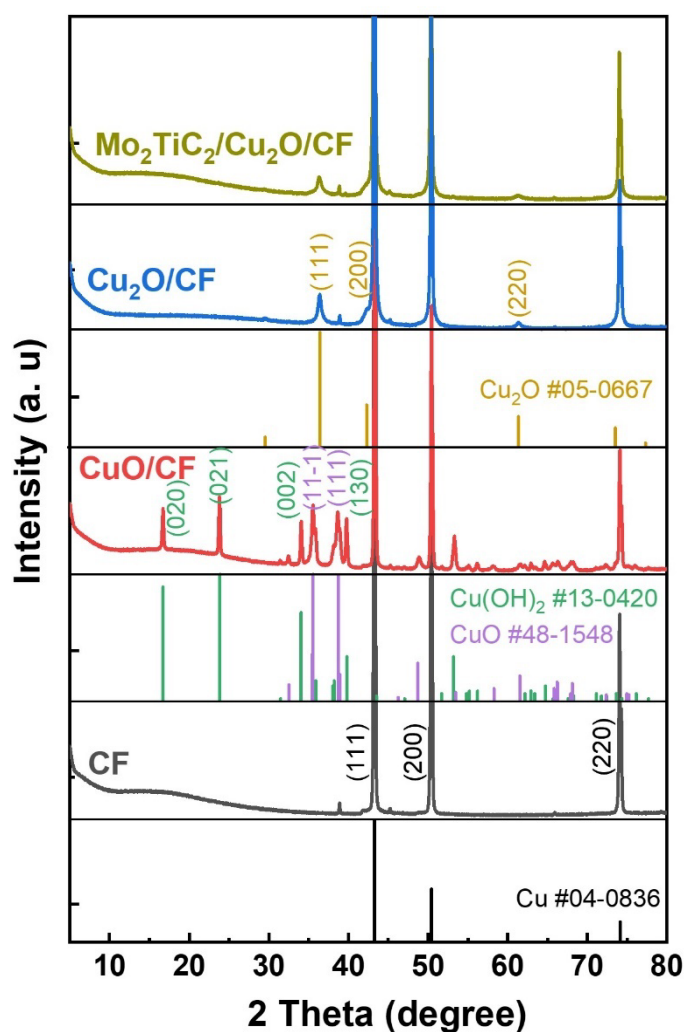
Figure 5.8. XRD patterns of CF, CuO/CF, Cu_2O/CF and Mo_2TiC_2/Cu_2O/CF composite.

5.2.2. Formaldehyde Oxidation Reaction (FOR)

The electrocatalytic FOR performance of the Mo_2TiC_2/Cu_2O/CF composite was evaluated using a standard three-electrode setup. **Figure 5.9** presents the linear sweep voltammetry (LSV) curves of the Mo_2TiC_2/Cu_2O/CF composite recorded in 1 M KOH with/without 1 M HCHO. When the electrolyte does not contain formaldehyde, the LSV curve of Mo_2TiC_2/Cu_2O/CF composite still retained the typical copper redox features

and showed the oxygen evolution reaction (OER). Initially, the oxidation peak at 0.57 V_{RHE} indicates the oxidation of Cu^0 to Cu^+, the peak at 1 V_{RHE} corresponds to the oxidation of Cu^+ to Cu^{2+}, and the peak at 1.32 V_{RHE} signifies the transition of Cu from +2 to higher oxidation states.[1] The increase in current density beyond 1.5 V_{RHE} is due to the oxygen evolution reaction (OER) with a potential of 1.69 V, which is required to drive a current density of 100 mA cm². Surprisingly, when the electrolyte contains 1 M HCHO, an ultra-low onset potential of -0.09 V_{RHE} was required for formaldehyde oxidation reaction (FOR), and a sharp increase in the current density occurred with further potential increase, achieving outstanding anodic oxidation performance with a current density of 100 mA cm^{-2} at an extremely low potential of 0.23 V_{RHE}, which represents a potential difference of 1.46 V compared to the traditional OER. This result revealed convincingly that $Mo_2TiC_2/Cu_2O/CF$ composite is an excellent electrocatalyst for FOR in alkaline electrolyte and more energy efficient than for OER.
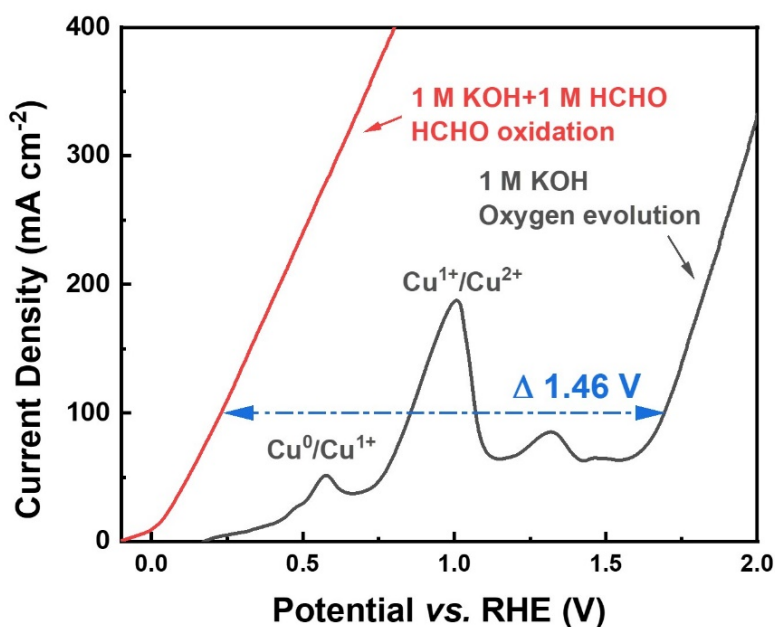

Figure 5.9. LSV curves of the $Mo_2TiC_2/Cu_2O/CF$ composite in 1 M KOH with/without 1 M HCHO at a scan rate of 5 mV s^{-1}.

The results in **Figure 5.10** clearly indicate that the current density declined upon decreasing the formadehyde concentration below 1 M, but even with only 0.1 M HCHO, the current density is significantly increased compared to when HCHO is completely absent, corresponding to the formaldehyde oxidation reaction (FOR). According to Faraday's law and reaction kinetics principles, the current density is proportional to the concentration of the reactant (formaldehyde).
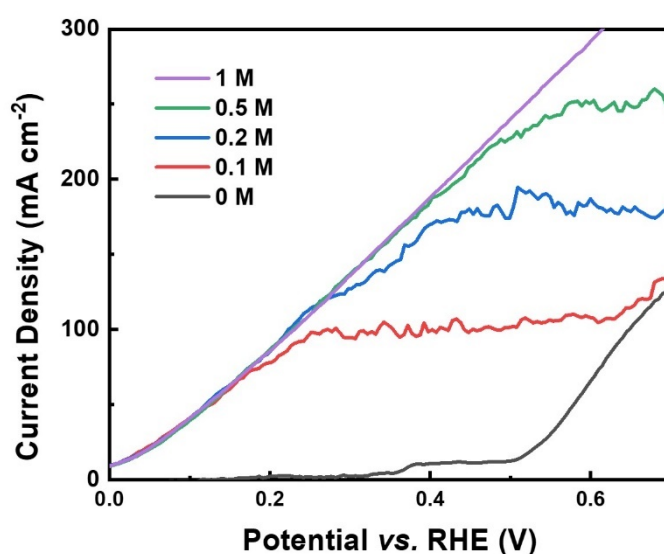

Figure 5.10. LSV curves of $Mo_2TiC_2/Cu_2O/CF$ composite for FOR in 1 M KOH containing different HCHO concentrations.

To compare the FOR behavior, **Figure 5.11(a)** depicts the LSV curves of various materials with a consistent electrode area. As the voltage increases, the pure copper foam electrode also displayed some FOR activity, indicating that Cu-based materials inherently possess good catalytic oxidation activity for formaldehyde, while Mo_2TiC_2 MXene/CF merely exhibited slight enhancement in activity. Additionally, Cu_2O/CF demonstrated higher FOR catalytic activity and required a potential of 0.24 V_{RHE} to drive 100 mA cm^{-2}, proving that Cu$^+$ owns greater FOR catalytic advantages compared

to Cu^0. $Mo_2TiC_2/Cu_2O/CF$ composite featured significantly improved catalytic activity, requiring only a potential of 0.13 V_{RHE} to drive 10 mA cm^{-2}. **Figure 5.11(b)** details the potentials required for various materials to achieve different current densities of 10, 50, and 100 mA cm^{-2}, further illustrating the catalytic performance advantage of $Mo_2TiC_2/Cu_2O/CF$ composite.
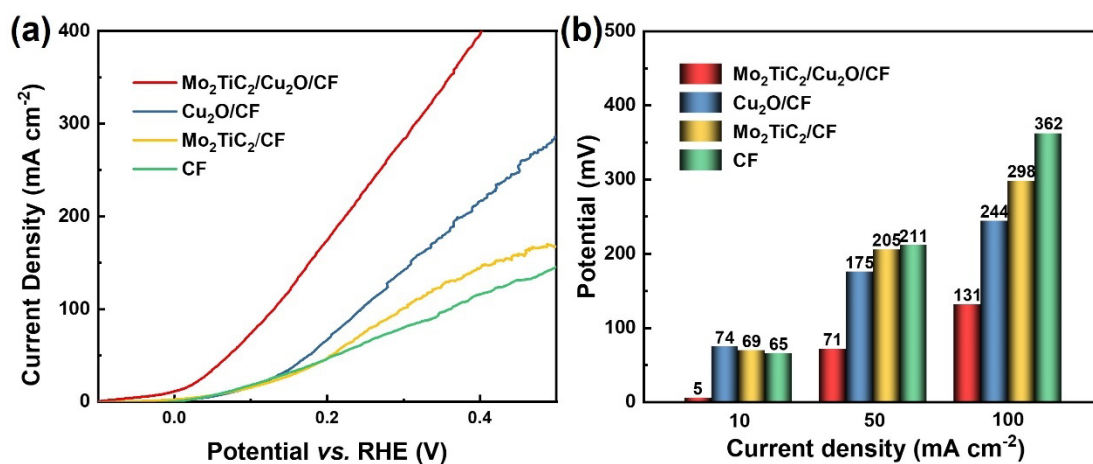

Figure 5.11. (**a**) LSV curves and (**b**) the required potentials of the $Mo_2TiC_2/Cu_2O/CF$ composite, Cu_2O/CF and Mo_2TiC_2 MXene/CF in 1 M KOH + 1 M HCHO.

The catalytic activity of $Mo_2TiC_2/Cu_2O/CF$ as an electrode material for FOR has been demonstrated. In order to deeply investigate the kinetic mechanism of the performance improvement of $Mo_2TiC_2/Cu_2O/CF$, we performed electrochemical impedance spectroscopy (EIS) tests. The starting position of the semicircle indicates the solution resistance (R_s), which theoretically is unrelated to the charge transfer properties of the catalyst. The semicircle at lower frequencies represents the charge transfer resistance (R_{ct}).[16, 17] It can be seen from the Nyquist plots in **Figure 5.12** that $Mo_2TiC_2/Cu_2O/CF$ featured the smallest radius (R_{ct} = 3.39 Ω) compared with pure

Cu$_2$O/CF (R$_{ct}$ = 18.75 Ω) and Mo$_2$TiC$_2$/CF (R$_{ct}$ = 36.92 Ω), revealing its remarkable electron transport capability (**Table 5.1**). After introducing Mo$_2$TiC$_2$ MXene, the charge transfer resistance significantly decreases, indicating that the addition of Mo$_2$TiC$_2$ MXene greatly enhances the charge transfer performance of the catalyst. This improvement is attributed to Mo$_2$TiC$_2$ MXene's unique atomic structure and large surface area.
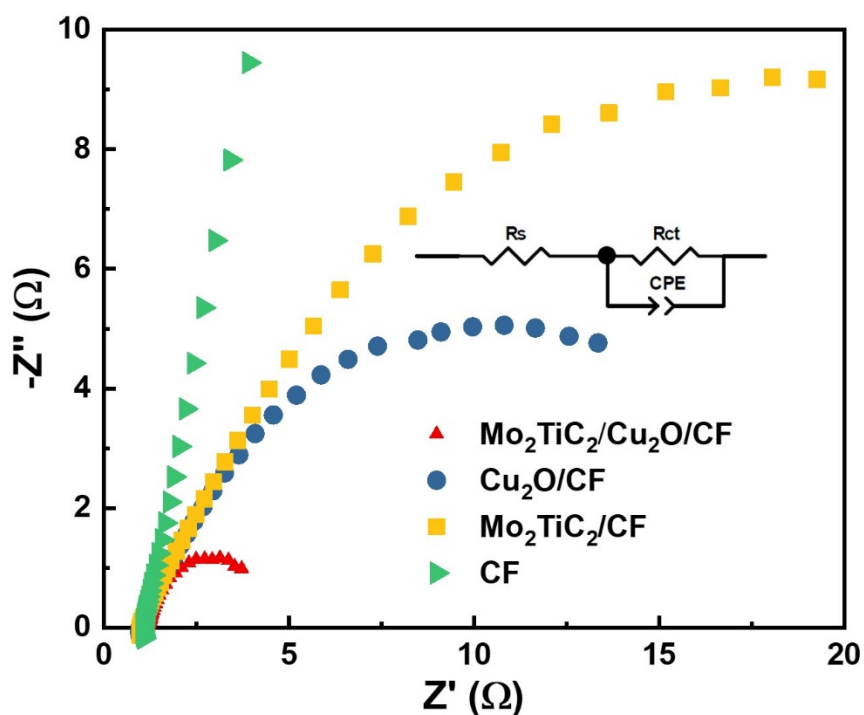

Figure 5.12. Nyquist plots of the Mo$_2$TiC$_2$/Cu$_2$O/CF, Cu$_2$O/CF, Mo$_2$TiC$_2$/CF and CF in the100 kHz to 0.01 Hz frequency range in 1M KOH + 1M HCHO. The insert is the equivalent circuit.

Table 5.1. Solution resistance (R_s) and charge transfer resistance (R_{ct}) values of $Mo_2TiC_2/Cu_2O/CF$, Cu_2O/CF, Mo_2TiC_2/CF and CF.

	R_s /Ω	R_{ct}/Ω
$Mo_2TiC_2/Cu_2O/CF$	1.18	3.39
Cu_2O/CF	0.96	18.75
Mo_2TiC_2/CF	0.95	36.92
CF	1.278	655.80

To further investigate the stability for FOR, chronoamperometry analysis was conducted on the $Mo_2TiC_2/Cu_2O/CF$ catalyst, as shown in **Figure 5.13(a)**. Initially, at an applied voltage of 0.13 V_{RHE}, the catalytic current density of $Mo_2TiC_2/Cu_2O/CF$ was approximately 100 mA cm^{-2}. Subsequently, the current density gradually decreased as the catalysis time increased, due to the formaldehyde in the electrolyte gradually being reduced to hydrogen and formate. After 7 hours, the current response was nearly zero, indicating that the formaldehyde in the electrolyte was almost completely decomposed.

The ^{1}H NMR before and after 7-hour electrolysis of electrolyte in **Figure 5.13(b)** confirmed this hypothesis. In the ^{1}H NMR spectrum, the characteristic peak of formate (HCOO$^-$) usually appears in the chemical shift range of about 8.3-8.5 ppm. This peak is produced by the hydrogen (H) in the formate. Since the hydrogen atom in formate is directly connected to the carbonyl group (C=O), it will show a singlet because it has no neighboring hydrogen atoms to couple with. After 7 hours of potentiostatic catalysis, the peak at 8.45 ppm significantly increased, indicating a substantial rise in the concentration of formate produced by formaldehyde oxidation. The characteristic peak of formate that appeared before the reaction began could be due to partial oxidation of formaldehyde in the aqueous solution caused by its instability in air. The methanol peak

at a chemical shift of 3.3 ppm is due to the presence of methanol used as a stabilizer in the purchased formaldehyde solution. The peak at 4.80 ppm originates from deuterium oxide (D_2O). This peak overlaps with the ^1H peak of formaldehyde. From the intensity change of this peak, it can be observed that the formaldehyde content significantly decreases after 7 hours of reaction. These results all demonstrate that the formaldehyde in the electrolyte is oxidized and decomposed into formate after a prolonged catalytic reaction. Furthermore, to analyze the carbon balance before and after catalysis, it is necessary to test the ^{13}C NMR spectrum of the electrolyte for quantitative analysis.
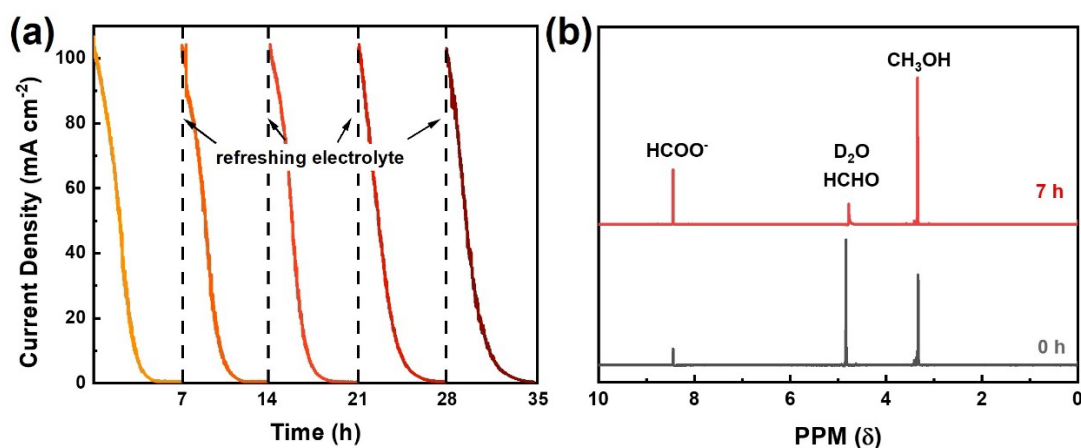

Figure 5.13. (**a**) Five consecutive 7-hour chronoamperometry cycles of FOR at 0.13 V_{RHE} of $Mo_2TiC_2/Cu_2O/CF$ in 1M KOH + 1M HCHO (the electrolyte was replaced every seven hours). (**b**) ^1H NMR spectra before and after 7-hour electrolysis of electrolyte by using $Mo_2TiC_2/Cu_2O/CF$.

It is worth noting that after five rounds of 7-hour potentiostatic catalysis, the rate of decrease in current response remained similar to the first round, nearly reaching zero within 7 hours. Furthermore, after 5×7 hours, its LSV curve showed only negligible decay compared to the initial curve (**Figure 5.14**), verifying the long-term stability of the $Mo_2TiC_2/Cu_2O/CF$ composite catalyst.
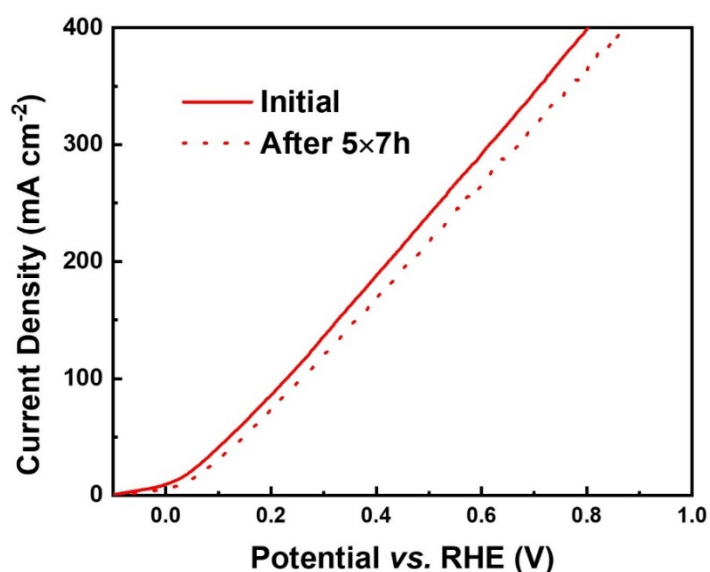
Figure 5.14. LSV curves of the $Mo_2TiC_2/Cu_2O/CF$ composite before and after long-term stability test.

5.2.3. HER and Overall Formaldehyde Electrolysis

Figure 5.15(a) depicts the LSV curves of different materials for HER without iR correction, including the commercial Pt/C catalyst. Pt/C casted on CF exhibited superior activity, whereas $Mo_2TiC_2/Cu_2O/CF$, Cu_2O/CF, Mo_2TiC_2/CF displayed similar activity and pure CF had related poor HER activity. Meanwhile, $Mo_2TiC_2/Cu_2O/CF$ MXene required an overpotential of 378 mV to attain a current density of 100 mA cm^{-2}, which is slightly enhanced as compared to pure Cu_2O/CF (402 mV at 100 mA cm^{-2}) (**Figure 5.15b**). Thus, similar to the FOR study, Mo_2TiC_2 MXene played a key role as an efficacious conductive framework or charge channels for HER. The long-term stability of $Mo_2TiC_2/Cu_2O/CF$ for HER is depicted in **Figure 5.16**. After 30 h of continuous catalysis under different constant potentials, the current density could still maintain 95.8% of its initial value under 100 mA cm^{-2}, which demonstrated its catalytic
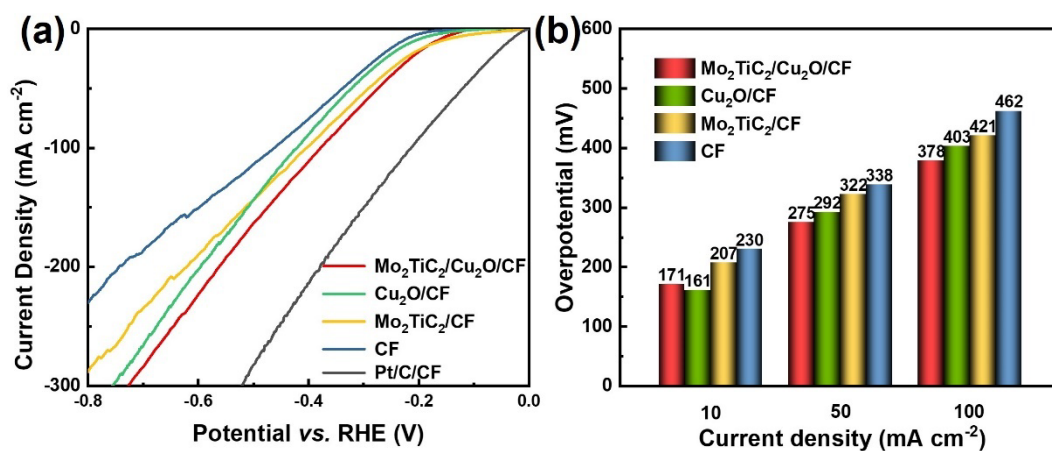
durability for HER.

Figure 5.15. Electrocatalytic performance for hydrogen evolution reaction. LSV curves of the $Mo_2TiC_2/Cu_2O/CF$, Cu_2O/CF, Mo_2TiC_2/CF and CF electrode in 1M KOH+1M HCHO at a scan rate of 5 mV s^{-1}.
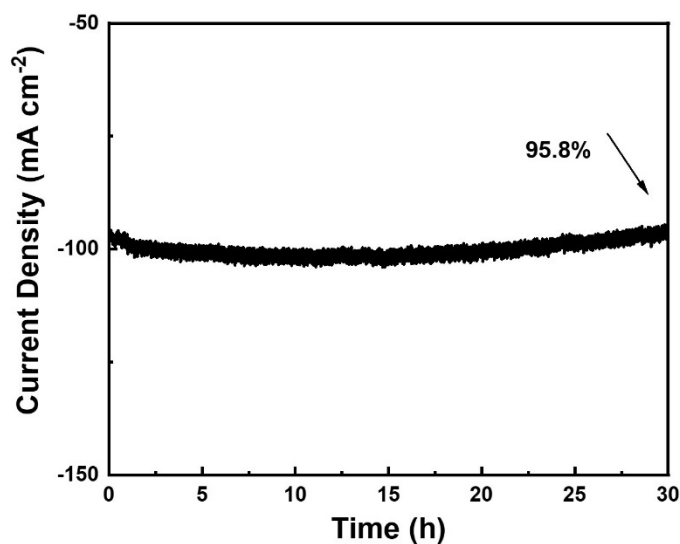

Figure 5.16. Current density *vs*. time curves of the $Mo_2TiC_2/Cu_2O/CF$ under the static potential of -0.2 V for 30 h.

Continuously, FOR and HER were conducted within a potential window (**Figure**

5.17). The potential difference between the cathode and anode was 1.61V at a current density of ±100 mA cm^{-2}. Considering the good HER and FOR activities of Mo$_2$TiC$_2$/Cu$_2$O/CF composites in 1M KOH + 1M HCHO, its potential as a bifunctional catalyst for total formaldehyde-containing water deserves further investigation. In order to achieve total water splitting, a two-electrode electrolyzer that produces H$_2$ gas simultaneously at both electrodes was constructed employing Mo$_2$TiC$_2$/Cu$_2$O/CF as both the anode and cathode (**Figure 5.18a**). The Mo$_2$TiC$_2$/Cu$_2$O/CF-based electrolyzer only required 1.62 V to drive a current density of 100 mA cm^{-2} in a 1 M KOH solution (**Figure 5.18b**), a value corresponding to the potential difference measured for HER and FOR at a current density of 100 mA cm^{-2} in a three-electrode system (**Figure 5.17**). In addition, for overall formaldehyde electrolysis, it required a cell voltage of only 0.36 V to drive 50 mA cm^{-2}, which is 1.49 V lower compared to that for pure water splitting recorded at the same current density. This results in significant savings in the energy consumption required for hydrogen production.
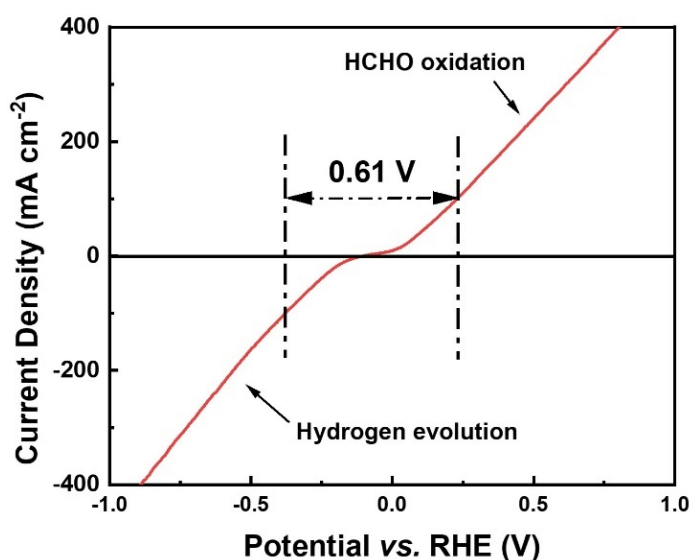

Figure 5.17. LSV curves of the Mo$_2$TiC$_2$/Cu$_2$O/CF for HER and FOR, respectively.
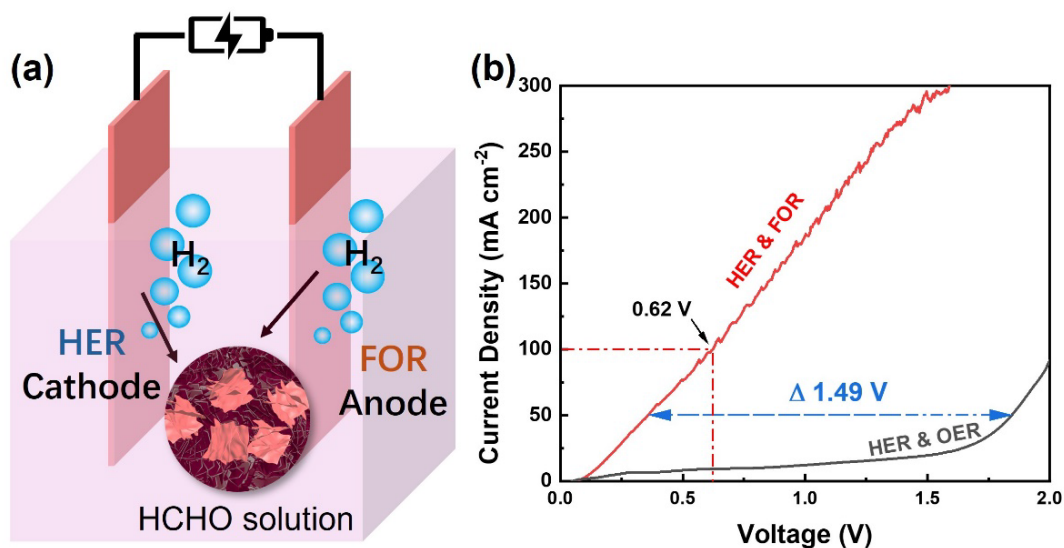
Figure 5.18. (**a**) Schematic of the overall water-splitting system. (**b**) Polarization curves of $Mo_2TiC_2/Cu_2O/CF$ (+, −) in 1M KOH + 1M HCHO in a two-electrode system for overall water splitting.

It is worth noting that although the HER performance of this catalyst allows it to be used as a bifunctional catalyst, if a more efficient hydrogen evolution catalyst is used for the cathode, the cell voltage could potentially be further reduced.

5.3 Conclusion

The study demonstrates the successful fabrication of $Mo_2TiC_2/Cu_2O/CF$ composites and their excellent catalytic activity for formaldehyde oxidation and hydrogen evolution reactions. These composites exhibit superior performance in electrochemical reactions, making them promising candidates for applications such as water splitting and environmental remediation. Overall, the study highlights the potential of $Mo_2TiC_2/Cu_2O/CF$ composites in advancing electrochemical technologies. Further, we will continue to collect and analyze the gaseous products produced by the positive and negative electrodes to determine the possibility of this strategy for twofold hydrogen production.

References

(1) Li, G.; Han, G.; Wang, L.; Cui, X.; Moehring, N. K.; Kidambi, P. R.; Jiang, D. E.; Sun, Y. Dual Hydrogen Production from Electrocatalytic Water Reduction Coupled with Formaldehyde Oxidation via a Copper-silver Electrocatalyst. *Nature Communications* **2023**, *14* (1), 525.

(2) Sun, X.; Ding, R. Recent Progress with Electrocatalysts for Urea Electrolysis in Alkaline Media for Energy-saving Hydrogen Production. *Catalysis Science & Technology* **2020**, *10* (6), 1567-1581.

(3) Zhu, D.; Zhang, H.; Miao, J.; Hu, F.; Wang, L.; Tang, Y.; Qiao, M.; Guo, C. Strategies for Designing More Efficient Electrocatalysts towards the Urea Oxidation Reaction. *Journal of Materials Chemistry A* **2022**, *10* (7), 3296-3313.

(4) Xiao, L.; Dai, W.; Mou, S.; Wang, X.; Cheng, Q.; Dong, F. Coupling Electrocatalytic Cathodic Nitrate Reduction with Anodic Formaldehyde Oxidation at Ultra-low Potential Over Cu_2O. *Energy & Environmental Science* **2023**, *16* (6), 2696-2704.

(5) Han, G.; Li, G.; Sun, Y. Electrocatalytic Dual Hydrogenation of Organic Substrates with a Faradaic Efficiency Approaching 200%. *Nature Catalysis* **2023**, *6* (3), 224-233.

(6) Li, M.; Wang, T.; Zhao, W.; Wang, S.; Zou, Y. A Pair-Electrosynthesis for Formate at Ultra-Low Voltage Via Coupling of CO_2 Reduction and Formaldehyde Oxidation. *Nano-micro Letters* **2022**, *14* (1), 211.

(7) Zhang, H.; Tan, L.; Zhang, Z.; Zhang, G.; Lu, J. Activated Carbon and Poly-o-anisidine(POA) Synergistic Supported Pt Nanoparticles as a Highly Efficient Catalyst for Electrocatalytic Oxidation of Formaldehyde. *Electrochimica Acta* **2021**, *388*, 138617.

(8) Ali, I.; Yousaf, M.; Sajid, I. H.; Hakim, M. W.; Rizwan, S. Reticulation of 1D/2D Mo_2TiC_2 MXene for Excellent Supercapacitor Performance. *Materials Today Chemistry* **2023**, *34*, 101766.

(9) Wang, W.; Feng, H.; Liu, J.; Zhang, M.; Liu, S.; Feng, C.; Chen, S. A Photo Catalyst of Cuprous Oxide Anchored MXene Nanosheet for Dramatic Enhancement of Synergistic Antibacterial Ability. *Chemical Engineering Journal* **2020**, *386*, 124116.

(10) Li, G.; Zhou, B.; Wang, P.; He, M.; Fang, Z.; Yuan, X.; Wang, W.; Sun, X.; Li, Z. High-Efficiency Oxygen Reduction to Hydrogen Peroxide Catalyzed by Oxidized Mo_2TiC_2 MXene. *Catalysts* **2022**, *12* (8), 850.

(11) Chen, X.; Li, R.; Li, B.; Wang, J.; Wang, T.; Yan, F.; Zhang, G. Achieving Ultra-high Ductility and Fracture Toughness in Molybdenum via Mo_2TiC_2 MXene Addition. *Materials Science and Engineering: A* **2021**, *818*, 141422.

(12) Naguib, M.; Unocic, R. R.; Armstrong, B. L.; Nanda, J. Large-scale Delamination of Multi-layers Transition Metal Carbides and Carbonitrides "MXenes". *Dalton Transactions* **2015**, *44* (20), 9353-9358.

(13) Betancourt-Galindo, R.; Reyes-Rodriguez, P. Y.; Puente-Urbina, B. A.; Avila-Orta, C. A.; Rodríguez-Fernández, O. S.; Cadenas-Pliego, G.; Lira-Saldivar, R. H.; García-Cerda, L. A. Synthesis of Copper Nanoparticles by Thermal Decomposition and Their Antimicrobial Properties. *Journal of Nanomaterials* **2014**, *2014*, 1-5.

(14) Wang, L.; Zhang, K.; Hu, Z.; Duan, W.; Cheng, F.; Chen, J. Porous CuO Nanowires as the Anode of Rechargeable Na-ion Batteries. *Nano Research* **2013**, *7* (2), 199-208.

(15) Zhang, M.; Chen, Z.; Wang, Y.; Zhang, J.; Zheng, X.; Rao, D.; Han, X.; Zhong, C.; Hu, W.; Deng, Y. Enhanced Light Harvesting and Electron-hole Separation for Efficient Photocatalytic Hydrogen Evolution over Cu_7S_4-enwrapped Cu_2O Nanocubes. *Applied Catalysis B: Environmental* **2019**, *246*, 202-210.

(16) Li, M.; Wang, Y.; Li, T.; Li, J.; Huang, L.; Liu, Q.; Gu, J.; Zhang, D. Hierarchical Few-layer Fluorine-free $Ti_3C_2T_X$ (T=O,OH)/MoS_2 Hybrid for Efficient Electrocatalytic Hydrogen Evolution. *Journal of Materials Chemistry A* **2021**, *9* (2), 922-927.

(17) Liang, X.; Yun, J.; Xu, K.; Xiang, H.; Wang, Y.; Sun, Y.; Yu, Y. A Multi-layered Ti_3C_2/Li_2S Composite as Cathode Material for Advanced Lithium-sulfur Batteries. *Journal of Energy Chemistry* **2019**, *39*, 176-181.

Chapter 6. Conclusion and perspectives

In this thesis, significant strides were made towards addressing the global energy crisis and environmental degradation by developing innovative electrocatalysts for hydrogen production *via* water electrolysis. The research focused on creating stable, efficient, and cost-effective MXene and MXene-based catalysts for water splitting, seawater electrolysis, and wastewater treatment.

Key achievements include the successful electrodeposition of RuO_2 particles onto Ti_3C_2 sheets supported on nickel foam (RuO_2-Ti_3C_2/NF). This structure demonstrated remarkable catalytic activity and stability in hydrogen evolution reaction (HER), oxygen evolution reaction (OER), and overall water splitting, even in challenging seawater conditions. The RuO_2-Ti_3C_2/NF catalyst showed good stability over 25 hours and nearly 100% Faradaic efficiency, providing a viable solution for energy generation in regions with limited freshwater resources.

Additionally, the synthesis of a Co_3O_4/Ti_3C_2 MXene composite under mild conditions yielded a highly efficient and stable electrocatalyst for both urea oxidation reaction (UOR) and HER in alkaline media. This composite outperformed its individual components by addressing issues such as insufficient active site exposure and particle agglomeration, offering a new approach for energy-efficient hydrogen production and urea-containing wastewater purification.

Finally, a novel Mo_2TiC_2 MXene cluster complex supported by Cu_2O nanoflowers was synthesized using a simple immersion method. This catalyst was effective in HER coupled with formaldehyde oxidation reaction, enabling hydrogen production at both the cathode and anode and producing formic acid, a valuable fuel, while reducing the overall electrical energy consumption.

Perspectives

The promising results from this thesis highlight the potential of MXene-based catalysts in various electrochemical applications. Future research should focus on the following areas:

Optimization and scaling: Further optimization of synthesis methods and catalyst compositions to enhance performance and scalability for industrial applications. This includes refining electrodeposition techniques, improving material stability, and developing cost-effective large-scale production methods.

Durability studies: Conducting long-term stability and durability tests under real-world conditions is crucial to ensure the practical viability and commercial adoption of these catalysts. This includes exploring the impact of different environmental factors and operational conditions on catalyst performance.

Broader applications: Expanding the scope of MXene-based catalysts to other electrochemical processes, such as carbon dioxide reduction, nitrogen fixation, and ammonia synthesis, could open new avenues for sustainable energy and environmental applications. This requires exploring the unique properties of MXenes and their interaction with various reactants.

Integration into systems: Integrating these catalysts into complete electrochemical systems, such as electrolyzers and fuel cells, and evaluating their performance in pilot-scale setups is essential for transitioning from laboratory research to real-world applications. Collaborations with industry partners can facilitate this transition and address practical challenges.

Advanced characterization techniques: Utilizing advanced characterization techniques to gain deeper insights into the structure-property relationships of MXene-based catalysts can help identify the key factors influencing their performance. Techniques such as *in situ*/operando spectroscopy, high-resolution electron microscopy,

and computational modeling can provide valuable information.

Environmental and economic impact: Assessing the environmental and economic impact of MXene-based catalysts in comparison to conventional catalysts is important for understanding their potential benefits and limitations. Life cycle analysis and cost-benefit analysis can provide a comprehensive evaluation of their sustainability and commercial viability.

Policy and regulatory considerations: Engaging with policymakers and regulatory bodies to promote the adoption of MXene-based technologies in sustainable energy and environmental applications is crucial. Developing standards and guidelines for the safe and efficient use of these materials can facilitate their acceptance and implementation.

By addressing these areas, the potential of MXene-based materials in contributing to a sustainable and carbon-free energy future can be fully realized. This work lays a strong foundation for the development of next-generation electrocatalysts, driving forward the vision of sustainable hydrogen production and environmental remediation. The ongoing advancements in MXene research promise to revolutionize the field of electrocatalysis, paving the way for cleaner, more efficient, and more sustainable energy solutions.

Publications

Yi Zhang, Zhaohui Zhang, Ahmed Addad, Qi Wang, Pascal Roussel, Mohammed A. Amin, Sabine Szunerits, and Rabah Boukherroub*. 0D/2D Co_3O_4/Ti_3C_2 MXene Composite: A Dual-Functional Electrocatalyst for Energy-Saving Hydrogen Production and Urea Oxidation. *ACS Appl. Energy Mater.* **2022** *5* (12), 15471-15482.

Yi Zhang, Zhaohui Zhang, Zhiran Yu, Ahmed Addad, Qi Wang, Pascal Roussel, Sabine Szunerits, and Rabah Boukherroub*. Ruthenium Oxide Nanoparticles Immobilized on Ti_3C_2 MXene Nanosheets for Boosting Seawater Electrolysis. *ACS Appl. Mater. Interfaces* **2023** *15* (50), 58345-58355.

Zhaohui Zhang, **Yi Zhang**, Alexandre Barras, Ahmed Addad, Pascal Roussel, Longcheng Tang, Mohammed A. Amin, Sabine Szunerits, and Rabah Boukherroub*. Preparation of Flower-Shaped Co-Fe Layer Double Hydroxide Nanosheets Loaded with Pt Nanoparticles by Corrosion Engineering for Efficient Electrocatalytic Water Splitting. *ACS Appl. Energy Mater.* **2022**, 5 (12), 15269-15281.

Zhaohui Zhang, Zhiran Yu, **Yi Zhang**, Alexandre Barras, Ahmed Addad, Pascal Roussel, Longcheng Tang, Mu. Naushad, Sabine Szunerits, and Rabah Boukherroub*. Construction of desert rose flower-shaped NiFe LDH-Ni_3S_2 heterostructures via seawater corrosion engineering for efficient water-urea splitting and seawater utilization. *J. Mater. Chem. A*, **2023**, 11, 19578.